Polymer-Schichtsilikat-Nanokomposite -

die Allrounder

Vom Lebensmittelregal bis in den Weltraum?

DISSERTATION

zur Erlangung des akademischen Grades eines

Doktors der Naturwissenschaften (Dr. rer. nat.)

an der Fakultät für Biologie, Chemie und Geowissenschaften

der Universität Bayreuth

vorgelegt von

Christoph Habel

aus Cham, Oberpfalz

Bayreuth, 2020

Die vorliegende Arbeit wurde in der Zeit von Oktober 2016 bis Mai 2020 in Bayreuth am Lehrstuhl für Anorganische Chemie I unter Betreuung von Prof. Dr. Josef Breu angefertigt.

Vollständiger Abdruck der von der Fakultät für Biologie, Chemie und Geowissenschaften der Universität Bayreuth genehmigten Dissertation zur Erlangung des akademischen Grades eines Doktors der Naturwissenschaften (Dr. rer. nat.).

Dissertation eingereicht am: 13.05.2020

Zulassung durch die Promotionskommission: 20.05.2020

Wissenschaftliches Kolloquium: 20.01.2021

Amtierender Dekan: Prof. Dr. Matthias Breuning

Prüfungsausschuss:

Prof. Dr. Josef Breu (Gutachter)

Prof. Dr. Andreas Greiner (Gutachter)

Prof. Dr. Rainer Schobert (Vorsitz)

JProf. Dr. Anna Schenk

„Arbeite klug, nicht hart.“

-Dr. Gregory House-

Meiner über alles geliebten Familie

Inhaltsverzeichnis

Abkürzungsverzeichnis

Å	Angstrøm (10^{-10} m)
Abb.	Abbildung
atm	physikalische Atmosphäre (1 atm = 1,10133 bar)
bzw.	beziehungsweise
cm	Zentimeter
D	Diffusivität
DSC	Dynamische Differenzkalometrie (*Differential Scanning Calorimetry)*
g	Gramm
Gl.	Gleichung
h	Stunde(n)
H	Höhe (Schichtsilikat)
L	Löslichkeit
L_d	mittlerer lateraler Durchmesser (Schichtsilikat)
m	Meter
MMT	Montmorillonit
NaHec	Natrium-Fluorohectorit ($[Na_{0,5}]^{Zw.}[Mg_{2,5}Li_{0,5}]^{Okt.}[Si_4]^{Tet.}O_{10}F_2$)
nm	Nanometer (10^{-9} m)
n	Avramiindex
OLED	Organische Leuchtdioden (*Light Emitting Diodes)*
OP	Sauerstoffpermeabilität (*Oxygen Permeability*)
OTR	Sauerstofftransmissionsrate (*Oxygen Transmission Rate*)
P	Permeabilität
PEG	Polyethylenglykol (*Polyethylenglycol*)

PET	Polyethylenterephthalat
PLA	Polymilchsäure (*Polylactid acid*)
PVA	Polyvinylalkohol
r.h.	Relative Luftfeuchtigkeit (*relative humidity*)
SAXS	Röntgenkleinwinkelstreuung (*Small-angle X-ray scattering*)
Tab.	Tabelle
TGA	Thermogravimetrische Analyse
u.a.	unter anderem
vol%	Volumenprozent (*volume%*)
WL	Wasserlage
WVP	Wasserdampfpermeabilität (*Water Vapor Permeability*)
WVTR	Wasserdampf Transmissionsrate (*Water Vapor Transmission Rate*)
wt%	Gewichtsprozent (*weight %*)
XRD	Röntgenbeugung (*X-Ray Diffraction*)
z.B.	zum Beispiel
α	Aspektverhältnis
ϕ	Volumenbruch
1D	1-dimensional
_	Leerstelle

1 Summary

Within the scope of this work, it was accomplished to produce (bio-) nanocomposites/hybrids based on synthetic layered silicates. These can be used in various low- and high-tech applications due to their versatile characteristics. The main focus was on the barrier properties of these polymeric layered silicate nanocomposites/hybrids. In addition to the determination of suitable manufacturing processes and the research of multi-functional properties, which are of interest for a wide range of applications, a deeper understanding of the influence of layered silicates as fillers on various resulting (composite/polymer) properties was gained.

The solvent route used in this work initially made it possible to produce delaminated layered silicate lamellae, polymeric dispersions. These dispersions can then be further processed by doctor blading or spray coating. In the course of this work, a combined production process of electrospinning and filtration was developed to reduce the production time and increase the drying efficiency. By creating a sandwich structure and subsequent hot pressing, it was possible to produce transparent nanocomposite membranes with improved mechanical and barrier properties.

As already mentioned, spray coating represents a further processing option. This was used in another project to produce a biopolymer layered silicate nanocomposite barrier coating. Especially in the field of food packaging, barrier properties play an important role in terms of food shelf life. Biopolymers, which are considered environmentally friendly alternatives for current petro-based commercial packaging materials, often do not show the desired properties. In this thesis, a water-based thin biopolymer nanocomposite coating was successfully produced, which makes the biopolymer-substrate a competitive sustainable alternative due to the resulting competitive barrier and optical properties, the predominant flexibility and the anti-colonization potential.

However, barrier properties do not only play a major role in the field of food packaging. Highly diffusive gases such as hydrogen, or even helium, are particularly important in the aerospace industry. A water-based high-barrier nanocomposite liner against helium and hydrogen has been developed, which can be used as a barrier coating in lighter-than-air vehicles or space technology. Additionally, the

flexibility and competitive barrier properties even outperform high barrier polymers. The developed system is particularly convincing due to its low application weight, which is of enormous relevance especially in lightweight construction applications.

In many fields of application, it is necessary that the above-mentioned barrier properties are maintained even at high humidity levels. For this purpose, copolymers with varying hydrophobic components are often used to control the swelling behavior and thus the barrier properties. Fillers can also change this swelling behavior. Within the scope of this work, a perfectly structured polymer hybrid was produced, which served as a model system to work out a detailed relationship between the filler content, the dependence of the barrier properties on the humidity and the impact of the confinement effect due to high filler contents.

But not only the impermeability of the layered silicates has a positive influence on the barrier properties. Crystalline areas in polymers are also considered impermeable to gases and water vapor. Using a water-based polymer, the interplay of the nucleation and confinement effect based on the filler content of the layered silicates could be worked out. By varying the filler content, it was thus possible to produce nanocomposites with tailor-made crystallinity.

The present work is a cumulative thesis. Therefore, all results are presented in the attached publications.

2 Zusammenfassung

Im Rahmen dieser Arbeit ist es gelungen (Bio-)Nanokomposite/Hybride basierend auf synthetischem Schichtsilikat herzustellen, welche aufgrund ihrer vielseitigen Eigenschaften in unterschiedlichsten *Lowtech*- und *Hightech*-Anwendungen Einsatz finden können. Der Hauptfokus lag hierbei auf den Barriereeigenschaften dieser Polymer-Schichtsilikat-Nanokomposite/-Hybride.

Neben dem Ermitteln geeigneter Herstellungsverfahren und dem Erforschen multifunktionaler Eigenschaften, welche für verschiedenste Anwendungsgebiete von Interesse sind, konnte weiterhin ein vertieftes Verständnis über den Einfluss von Schichtsilikaten als Füllstoff auf diverse resultierende (Komposit/Polymer-) Eigenschaften gewonnen werden.

Durch die in dieser Arbeit verwendete Lösemittelroute konnten zunächst Polymer-Schichtsilikat-Dispersionen hergestellt werden, in denen das Schichtsilikat delaminiert vorlag. Diese Dispersionen können darauf aufbauend unter anderem mittels Sprüh-, oder auch Rakelverfahren weiterverarbeitet werden. Im Zuge dieser Arbeit wurde ein kombiniertes Herstellungsverfahren aus *Electrospinning* und Filtration erarbeitet, um die Herstellungsdauer von Barrierematerialien zu senken und die Trocknungseffizienz zu steigern. Durch das Erstellen einer Sandwichstruktur und dem anschließenden Heißverpressen ist es hierbei gelungen transparente Nanokomposit-Membrane mit verbesserten Mechanik- und Barriereeigenschaften herzustellen.

Wie bereits erwähnt, stellt das Sprühverfahren eine weitere Applikationsmöglichkeit dar. Dies wurde angewandt, um in einem anderen Projekt eine Biopolymer-Schichtsilikat-Nanokomposit-Barrierebeschichtung herzustellen. Gerade im Bereich der Lebensmittelverpackungen spielt die Gasbarriere, bezüglich Lebensmittelhaltbarkeit, eine tragende Rolle. Biokunststoffe, welche als potenzielle, umweltfreundliche Alternativen zu den kommerziellen, petrobasierten Verpackungsmaterialien gelten, zeigen jedoch oftmals nicht die gewünschten Eigenschaften. In dieser Arbeit ist es gelungen, eine wasserbasierte und dünne Biopolymer-Nanokomposit-Beschichtung herzustellen, welche das Substratbiopolymer aufgrund der entstehenden Barriereeigenschaften und

optischen Eigenschaften, der Flexibilität und des Antikolonisationspotentials zu einer kompetitiven, zukunftsträchtigen Alternative werden lässt.

Doch nicht nur im Bereich der Lebensmittelverpackungen spielen Barriereeigenschaften eine mit entscheidende Rolle. Hochdiffusive Gase, wie Wasserstoff (H_2) oder auch Helium (He), sind gerade in der Luft- und Raumfahrttechnik von Bedeutung. So konnte ein wasserbasierter Liner mit Hochbarriereeigenschaften gegenüber H_2 und He entwickelt werden, welcher als Barrierebeschichtung im Bereich von *lighter-than-air*-Fahrzeugen oder der Raumfahrt Anwendung finden kann. Neben Merkmalen wie Flexibilität und kompetitiven Barriereeigenschaften, welche die Barrieren von Hochleistungspolymeren übertreffen, überzeugt dieses System vor allem durch das geringe Auftragsgewicht, was gerade bei Leichtbauanwendungen von enormer Relevanz ist.

In vielen Anwendungsbereichen ist es zudem erforderlich, dass die genannten Barriereeigenschaften auch bei höherer Luftfeuchtigkeit gewährleistet sind. Hierfür werden oftmals Copolymere mit variierenden hydrophoben Anteilen verwendet, um das Quellverhalten und damit die Barriereeigenschaften zu kontrollieren. Auch Füllstoffe können dieses Quellverhalten verändern. Im Zuge dieser Arbeit ist es gelungen ein perfekt strukturiertes Polymer-Hybrid herzustellen, welches als Modellsystem diente, um einen detaillierten Zusammenhang zwischen dem Füllstoffanteil, der Abhängigkeit der Barriereeigenschaften von der Luftfeuchtigkeit und dem Einfluss des, durch hohe Füllstoffanteile, entstehenden *Confinements*, herauszuarbeiten.

Doch nicht nur die Impermeabilität der Schichtsilikate hat einen positiven Einfluss auf die Barriereeigenschaften. Kristalline Bereiche in Polymeren gelten ebenfalls als undurchlässig für Gase und Wasserdampf. So konnte anhand eines wasserbasierten Polymers das Wechselspiel des Nukleations- und *Confinement*-Effekts basierend auf dem Füllstoffgehalt an Schichtsilikat herausgearbeitet werden. Durch Variation des Füllstoffgehaltes war es möglich Nanokomposite mit variierender Kristallinität herzustellen.

Bei dieser Arbeit handelt es sich um eine kumulative Dissertation. Daher werden die Ergebnisse, thematisch sortiert, in den angehängten Publikationen beschrieben.

3 Einleitung

3.1 Bedeutung von Kunststoffen im täglichen Leben

„Also, wenn die Frage ist, ob wir Kunststoffe aus unserer Welt wegdenken können: eigentlich nicht mehr. Wir haben uns eine kunststofforientierte Welt geschaffen. Wir haben gelernt, mit Kunststoffen umzugehen und diese zu nutzen. Kunststoffe haben viele technologische Neuerungen gebracht. Das heißt, ohne Kunststoffe wird es in Zukunft nicht mehr gehen. Wenn die Frage ist, ob wir so weitermachen können wie bisher: dann ein klares Nein! Wir müssen einiges verändern. […]“,

so Prof. Dr. Cordt Zollfrank (Biogenic Polymers, TUM Campus Straubing) in einem Interview 2019.[1] Diese Aussage von Professor Zollfrank fasst in wenigen Sätzen die aktuellen Diskussionen rund um den Bereich der Kunststoffwirtschaft zusammen. Aufgrund ihrer vielfältigen und maßgeschneiderten Eigenschaften (u.a. Barrierewirkung, Mechanik) sowie ihrem vergleichsweise geringen Gewicht und der einfachen Herstellung, sind Kunststoffe aus dem heutigen Leben nicht mehr wegzudenken.[2, 3] Seit den 1950er Jahren wurden bereits über 8 Milliarden

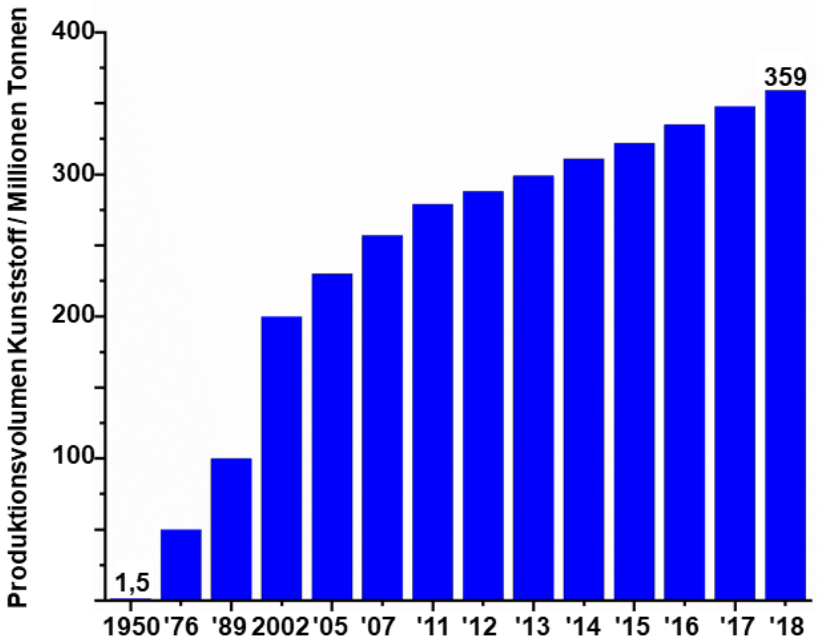

Abb. 1: Produktionsvolumen an Kunststoffen im zeitlichen Ablauf von 1950 bis 2018.[5, 6] (berücksichtigt: Thermoplasten, Duroplasten, Polyurethane, Beschichtungen, Klebstoffe, Dichtungsmittel und Polypropylen-Fasern; ausgenommen: Polyethylenterephthalat-, Polyamid- und Polyacryl-Fasern)

Tonnen[4-6] an Kunststoffen produziert und dieses Produktionsvolumen findet aktuell mit ca. 359 Millionen Tonnen pro Jahr sein Maximum (**Abb. 1**).[6]

In den unterschiedlichsten Bereichen, von Automobilindustrie, über Haushalt, alternativer und neuartiger Luft- und Raumfahrttechniken bis hin zu Lebensmittelverpackungen werden Kunststoffe sowohl in *Lowtech*-, als auch in *Hightech*-Anwendungen eingesetzt.[6-9] Der Großteil der produzierten Kunststoffe findet, mit fast 40 %, im Bereich (flexibler) Verpackungen und hierbei u.a. auch im Bereich der Lebensmittelverpackung Anwendung.[10] Trotz der angesprochenen Vorteile von Kunststoffen gehen auch einige Nachteile oder gar Gefahren durch deren Nutzung im Alltag einher. Nicht nur der entstehende Kunststoffverpackungsmüll, welcher sich im europäischen Durchschnitt auf über 20 kg pro Kopf pro Jahr (2016)[11] beläuft, stellt ein großes Problem dar, sondern auch die unsachgemäße Entsorgung dieses Mülls in die Natur.[12] Dies führt unweigerlich zu den in den Medien thematisierten Bildern der Kontamination der Umwelt. Eine Lösung hierfür erhofft man sich durch die Verwendung von Biokunststoffen, wobei zunächst klar abgegrenzt werden muss, wie dieser Begriff definiert ist. In die Klasse der Biokunststoffe fallen sowohl (teilweise) biobasiert produzierte als auch biologisch abbaubare Kunststoffe unabhängig der Rohstoffherkunft oder solche, die beide dieser Eigenschaften erfüllen (**Abb. 2**).[13, 14] Bei dieser weitgreifenden Definition ist jedoch Vorsicht geboten, da sie beim

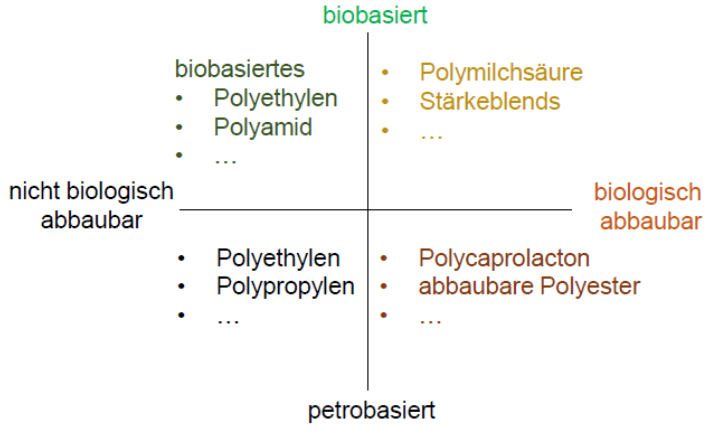

Abb. 2: Übersicht und Einteilung Industrie-relevanter Kunststoffe in verschiedene Klassen. Die Farben in den einzelnen Quadranten beschreiben die Mischung der Farben von petrobasiert (schwarz), biobasiert (grün), biologisch abbaubar (braun) und nicht biologisch abbaubar (schwarz). Somit werden alle aufgeführten Klassen an Kunststoffen unter Ausschluss des in schwarz aufgeführten Quadranten als Biokunststoffe bezeichnet. [*adapted from* [13,14]]

Verbraucher zu Verunsicherung und Diskussionsbedarf führen kann. Die offiziellen Definitionen „biologisch abbaubar“ oder auch „kompostierbar“ sind zum Teil deutlich vom umgangssprachlichen Gebrauch dieser Begriffe abzugrenzen, was die Vielzahl an unterschiedlichen Vorschriften und Normen in diesem Bereich verdeutlichen. Zur Veranschaulichung gibt **Tab. 1** einen exemplarischen Überblick über die diesbezüglich vorherrschenden Normen und deren Prüfanforderungen.[15] Die allgemein verwendeten Begriffe der Kompostierbarkeit und Bioabbaubarkeit sind demnach im Alltag mit Vorsicht zu behandeln. Weiterhin wird deutlich, dass diese Abbaubarkeit von verschiedenen Parametern wie Temperatur (aber auch Luftfeuchtigkeit oder Mikroorganismen) abhängig ist. Daher lässt der Begriff „bioabbaubar“ nicht direkt darauf schließen, dass diese Materialien keinen Beitrag zur Umweltverschmutzung leisten.[16]

Tab. 1: Übersicht* über vorherrschende Normen im Bereich „Bioabbaubarkeit“ und „Kompostierbarkeit“ und deren Prüfziel unter Angabe der Prüfanforderungen:[15]

Normen	Prüfziel	Prüfanforderungen
EN 13432	Industrielle Kompostierbarkeit	Vollständige biologische Abbaubarkeit; 90% Abbau (absolut oder bezogen auf Referenzsubstrat) nach ≤ 6 Monaten bei 58± 2°C
AS 5810 NF T 51-800	Gartenkompostierbarkeit	- Vollständige biologische Abbaubarkeit; 90% Abbau (absolut oder bezogen auf Referenzsubstrat) nach ≤ 6 Monaten bei < 30°C - Zersetzung im Bioabfall nach < 180 Tagen (< 10% des Restmaterials > 2 mm, 25 °C)
EN 17033	Bioabbaubarkeit in Boden (Mulchfolien)	Vollständige biologische Abbaubarkeit; 90% Abbau nach 24 Monaten bei 20-28°C
EN 13432 EN 14995	Bioabbaubarkeit in Süßwasser	Vollständige biologische Abbaubarkeit; 90% Abbau (absolut oder bezogen auf Referenzsubstrat) nach 56 Tagen bei 20-25°C
ASTM D7081 (zurückgezogen)	Bioabbaubarkeit in Meerwasser	Vollständige biologische Abbaubarkeit; 90% Abbau (absolut oder bezogen auf Referenzsubstrat) nach 6 Monaten

*diese Übersicht beinhaltet weder alle vorhandenen Normen noch die kompletten Prüfanforderungen, sondern zeigt exemplarisch, im Sinne einer didaktischen Reduktion, lediglich Ausschnitte

Eine intensive Studie, mit der Dauer von über einem Jahr, zur Abbaubarkeit von Kunststoffen, in Süß- und künstlich hergestelltem Meerwasser hat gezeigt, dass als „biologisch abbaubar“ deklarierte Polymere (u.a. Polycaprolacton (PCL)) zum Teil nahezu keinen Abbau zeigen. Demnach lässt der Begriff „bioabbaubar“ keinesfalls direkt auf einen Abbau in natürlicher Umgebung schließen, zeigt jedoch eine mögliche Richtung alternativer Kunststoffe auf.[16]

Nichtsdestotrotz können Biokunststoffe in bestimmten, sinnvollen Anwendungsbereichen, wie z.B. Lebensmittelverpackungen, als nachhaltige Alternativen zu kommerziellen, klassisch petrobasierten Kunststoffen eingesetzt werden.[17] Der Produktionsvolumenanteil von Biokunstoffen am Gesamtvolumen liegt jedoch bislang bei < 1%.[18] Ein Grund hierfür sind die im direkten Vergleich teilweise nicht kompetitiven Eigenschaften, welche unter anderem im Bereich der Barrierecharakteristika vorherrschen.[19, 20] Hierbei gilt es zu wissen, dass eben diese Barriereeigenschaften (u.a. gegenüber Sauerstoff und Wasserdampf) gerade in Lebensmittelverpackungen von entscheidender Bedeutung für die Haltbarkeit der Lebensmittel sind.[19, 21]

Doch diese Barrierematerialien spielen nicht nur in *Lowtech*-Bereichen wie Lebensmittelverpackungen eine entscheidende Rolle. Barriereverkapselungen sind der Schlüssel zu einem weiten Feld fortschrittlicher Technologien, wie der Verpackung von sauerstoff- und feuchtigkeitsempfindlichen Solarzellen auf Perowskitbasis oder hochsensibler, flexibler, organischer Leuchtdioden (FOLEDs).[22-26] Um eine zufriedenstellende Lebensdauer der jeweiligen Geräte zu gewährleisten, müssen extrem geringe Sauerstoff- und/oder Wasserdampftransmissionsraten gesichert sein, was sich als besonders herausfordernd darstellt.[27-29]

Hochdiffusive Gase wie Wasserstoff (H_2) und Helium (He) stellen eine ähnliche, wenn nicht sogar noch anspruchsvollere, aber nicht weniger relevante Herausforderung dar. Die Wasserstoffwirtschaft ist einer der wichtigsten Zweige einer auf Alternativ-Energiequellen basierenden Wirtschaft. In der Luftfahrt und im Verkehr bedarf es innovativer Leichtbauwerkstoffe für den Transport und die Lagerung dieses ansonsten vielversprechenden Treibstoffs.[30-35] In gleicher Weise erregen Leichtbaufahrzeuge viel Aufmerksamkeit, da sie den Weg zu effizienteren, neuartigen Konzepten von "Windmühlen" ebnen, die in Höhen bis zu Strahlströmen

arbeiten und den Magnus-Effekt nutzen.[36, 37] Solche Höhenplattformen sind zudem Voraussetzung für zukunftsorientierte Kommunikationsnetze, die auch an abgelegenen Orten rund um den Globus einen zuverlässigen und schnellen Internetzugang ermöglichen sollen (Projekt Loon).[38, 39] Für diese Anwendungen stellt die hohe Diffusivität von He eine große Herausforderung dar. Neben der Barriereeffizienz sind Flexibilität, mechanische Festigkeit und ein geringes Gewicht weitere Voraussetzungen für Barrierematerialien, die für diese Technologien in Betracht gezogen werden.[8]

Um dafür die Leistungscharakteristika von Polymeren bezüglich ihrer verschiedenen Eigenschaften zu verbessern, bieten sich verschiedene Arten von Füllstoffen und Verarbeitungstechniken an.[40-42]

Dadurch können nicht nur die mechanischen Kennzahlen[43-45] verbessert werden, sondern auch die Flammschutzeigenschaften[46, 47] und die bereits angesprochenen Barriereleistungen.[43, 48-50] Einen dieser möglichen Füllstoffe stellt die Klasse der Schichtsilikate dar, auf welchen basierend in den 1980er Jahren die ersten Polymer-Schichtsilikat-Nanokomposite hergestellt wurden.[51]

Kapitel 3.2 dieser Arbeit beschreibt zunächst den Aufbau von Schichtsilikaten, grenzt verschiedene Schichtsilikate voneinander ab (Kapitel 3.2.1) und beschreibt die Synthese und die Eigenschaften des in dieser Arbeit verwendeten Schichtsilikats (Kapitel 3.2.2 + 3.2.3). Darauf aufbauend wird in **Kapitel 3.3** genauer auf die Herstellungsarten (Kapitel 3.3.1), mögliche Applikationstechniken (Kapitel 3.3.2) und die Charakteristika von Polymer-Schichtsilikat-Nanokompositen (Kapitel 3.3.3) eingegangen, wobei die Hintergründe zur Barrierethematik im Fokus stehen. Abgerundet wird **Kapitel 3.3** mit den zugrundeliegenden Messmethoden (Kapitel 3.3.4).

Kapitel 3.4 beschreibt, basierend auf diesen Grundlagen, die Problemstellung dieser Arbeit. Auf die dort aufgeführten Forschungsfragen und die zu Grunde liegenden Ideen der einzelnen Publikationen wird in der Synopsis (**Kapitel 4**), welche einen zusammenführenden Leitfaden bietet, detailliert eingegangen. Die dazugehörigen Original-Publikationen sind in **Kapitel 6** aufgeführt.

3.2 Schichtsilikate: früher war alles besser? – Generationen im Vergleich

In diesem Kapitel werden die beiden betrachteten Generationen an Schichtsilikaten zunächst detailliert vorgestellt, um darauf aufbauend die Vorteile und damit einhergehenden potenziellen Anwendungsgebiete von Schichtsilikaten der zweiten Generation zu beleuchten.

Schichtsilikate der ersten (natürliche Schichtsilikate) und zweiten Generation (synthetische Schichtsilikate) im Vergleich:[52]

3.2.1 Struktur und Klassifizierung der betrachteten Schichtsilikate

Das in dieser Arbeit verwendete Tonmineral Hectorit gehört zur Familie der 2:1 Schichtsilikate. Diese Einteilung basiert auf dem strukturellen Aufbau, worin zwei Schichten eckenverknüpfter Tetraeder (Tet., SiO_4), über apikale Sauerstoffatome an eine Oktaederschicht (Okt.) ankondensiert sind (**Abb. 3**). Je nach Oktaederkation unterscheiden sich die Bezeichnungen. So kann die Oktaederschicht trioktaedrisch (alle Oktaederlücken besetzt, z.B. in Talk

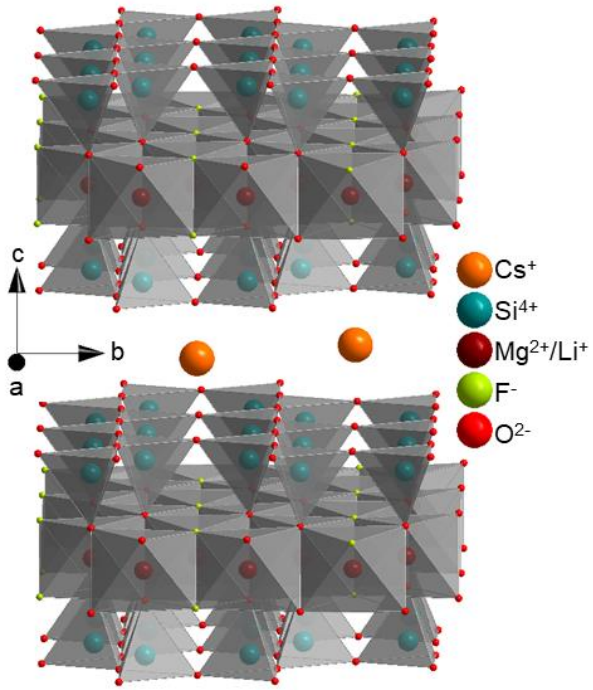

Abb. 3: Darstellung der 2:1 Schichtstruktur (Tetraeder-, und Oktaederschichten) zweier Fluorohectorit-Lamellen (Plättchen) mit Cäsium (orange) als Zwischenschichtkation. Dieses gleicht die negative Ladung der Schichten aus, welche durch partielle isomorphe Substitution von Mg^{2+} gegen Li^+ (lila) generiert wird.

$[Mg_3]^{Okt.}<Si_4>^{Tet.}O_{10}(OH)_2$) oder dioktaedrisch (nur 2/3 der Oktaederlücken besetzt, z.B. in Pyrophyllit $[Al_2\_]^{Okt.}<Si_4>^{Tet.}O_{10}(OH)_2$) sein.[52, 53] Durch isomorphe Substitution dieser Oktaederkationen durch niedervalentere Kationen entstehen bei Schichtsilikaten negative Schichtladungen, welche durch Kationen im Zwischenschichtraum zwischen den einzelnen Lamellen ausgeglichen werden (**Abb. 3**).[54] Mittels isomorpher Substitution lassen sich aus Talk und Pyrophyllit die im weiteren Verlauf gegenübergestellten Schichtsilikate Hectorit (Hec, partieller Austausch von Mg^{2+} gegen Li^{+}) und Montmorillonit (MMT, partieller Austausch von Al^{3+} gegen Mg^{2+}) ableiten. Diese weisen eine Schichtladung im Bereich von 0,2 und 0,6 pro Formeleinheit auf und sind der Klasse der sogenannten Smectite zuzuordnen.[52, 53]

3.2.2 Synthese des Natrium-Fluorohectorits

In dieser Arbeit wird ein synthetisch hergestellter Fluorohectorit mit einer Schichtladung von 0,5 pro Formeleinheit und Natrium als Zwischenschichtkation verwendet, wobei daraus die Summenformel $[Na_{0,5}]^{Zw.}[Mg_{2,5}Li_{0,5}]^{Okt.}[Si_4]^{Tet.}O_{10}F_2$ (NaHec) resultiert. Die Herstellung erfolgt mittels einer Schmelzsynthese bei 1750 °C in einem geschlossenen Molybdäntiegel über eine Stunde und einem anschließendem Temperschritt über einen Zeitraum von sechs Wochen bei 1045 °C.[55] Durch diese Art von Schmelzsynthese mit anschließender Hochtemperaturbehandlung erfolgt eine statistische isomorphe Substitution und somit entsteht ein sehr ladungshomogenes und phasenreines Schichtsilikat.[55] Die entsprechenden Taktoide (Stapel einzelner Lamellen/Plättchen) erreichen durch diesen Syntheseweg einen sehr großen mittleren lateralen Durchmesser L_d (≈ 20 µm).[55] Dies ist ein entscheidender Unterschied zu dem eben erwähnten, natürlich vorkommenden, MMT. Dieser weist, neben Phasenunreinheiten und Ladungsinhomogenität, weiterhin eine deutlich geringere laterale Ausdehnung als NaHec auf.[48, 53, 56]

Bleibt die Frage nach den Folgen dieser erhöhten Ladungshomogenität und der größeren lateralen Ausdehnung der Taktoide des verwendeten synthetischen Schichtsilikats NaHec im Vergleich zu MMT. Welche Auswirkungen hat das für potenzielle Anwendungen der Schichtsilikate als Füllstoff?

3.2.3 Maximierung des Aspektverhältnisses von Natrium-Fluorohectorit

Die Quellung von Schichtsilikaten in Wasser gilt als ein mögliches erstes Indiz für die Homogenität/Heterogenität der Ladungsverteilung und demnach der intrakristallinen Reaktivität von Schichtverbindungen.[56] Dabei wurde gezeigt, dass Schichtsilikate, welche durch eine Hochtemperatursynthese hergestellt werden, eine homogene Ladungsverteilung aufweisen.[55]

Eine kristalline Quellung von Schichtsilikaten ist bereits an feuchter Luft möglich. Abhängig von der Luftfeuchtigkeit können, ausgehend vom trockenen Schichtsilikat, 1, 2 oder auch bis zu 3 Wasserlagen (WL) in den Zwischenschichtraum eingelagert werden, wobei der Übergang zwischen den Hydratstufen vom Zwischenschichtkation abhängig ist.[56]

Die einzelnen Stufen dieser kristallinen Quellung durch Koordination von WL sind bei synthetischen Schichtsilikaten stark ausgeprägt. Bei dem in dieser Arbeit verwendeten NaHec zeigt sich dies durch scharfe, stufenweise Übergänge zwischen den Hydratstufen. Je nach Anzahl der Wasserlagen nimmt der Zwischenschichtabstand sukzessive von 0,96 nm (trocken) auf 0,124 nm (1 WL) und 0,155 nm (2 WL) zu.[55] Im Gegensatz dazu bilden sich in weniger ladungshomogenen Schichtsilikaten statistische Wechsellagerungen (simultane Bildung der unterschiedlichen Quellzustände) aus, wodurch der angesprochene scharfe Übergang nicht zu sehen ist.[56, 57]

Das Aufweiten des Schichtabstandes bei Schichtsilikaten ist vor allem bei deren Einsatz als Füllstoff in den Bereichen Mechanik[45] und Barriere[48] von entscheidender Bedeutung. Das hierbei mitentscheidende Aspektverhältnis α wird durch den Quotienten aus lateralem Durchmesser L_d und der Höhe H der betrachteten Taktoide/Plättchen beschrieben.[48, 58] Gerade im Bereich von Barriereanwendungen, wie in den folgenden Kapiteln detailliert beschrieben wird, ist eine Maximierung des Aspektverhältnis unabdingbar.[59] Diese Maximierung kann hierbei entweder durch Ausweiten des Durchmessers durch Angleichen der Synthese oder durch Verringern der Taktoidhöhe, der sogenannten Exfolierung, erfolgen.[56] Eine Möglichkeit die Taktoidhöhe der Schichtsilikate zu verringern, besteht in einem ersten Schritt aus der beschriebene kristallinen Quellung, welche die attraktiven Wechselwirkungen (Coulomb-Wechselwirkung, van der Waals, Wasserstoffbrückenbindungen) zwischen den einzelnen Lamellen schwächt.[56]

Aufbauend darauf können die Taktoide weiter zu geringeren Stapelhöhen durch mechanische Scherung (Mühle/Mikrofluidizer) exfoliert werden. Dabei kann jedoch ein teilweises Brechen der Taktoide nicht vollständig vermieden werden, wodurch wiederum ungewollt das Aspektverhältnis verringert wird.[56, 60]

Daher wird ein spontaner „Zerfall" der Stapel, eine „vollständige Exfolierung", Delaminierung[56, 61] genannt, ohne äußere mechanische Einflüsse bevorzugt. Diese hochskalierbare und vergleichsweise billige Route ist bei NaHec möglich, da dieser, wie wenige andere Schichtverbindungen (z.B. schichtförmige Titanate und Antimonphosphate, Graphenoxid), das seltene Phänomen der osmotischen Quellung zeigt.[62-65] Diese osmotische Quellung setzt ein, wenn die repulsiven Wechselwirkungen durch Hydratation zwischen den Schichten größer sind als die attraktiven.[66]

Stöter et al. haben die einzelnen Stufen dieser Quellung von NaHec im Detail untersucht.[66] Auf die beschriebene kristalline Quellung folgt demnach bei Zugabe von flüssigem, deionisiertem Wasser zunächst das Gouy-Chapman Regime, in welchem eine homogene, einphasige, lyotrop lamellare Phase, ein sogenannter Wigner-Kristall, vorliegt.[66] Durch weiteres Verdünnen mittels Zugabe von Wasser und dem damit verbundenen Anstieg des Zwischenschichtabstands entsteht beim Überschreiten der Debye-Länge ein nematisches Sol. Hier können die einzelnen Schichtsilikat-Plättchen gegeneinander verkippen, wobei die große laterale Ausdehnung die freie Drehbarkeit einschränkt. In hochverdünnten Suspensionen ist eine freie Drehbarkeit der einzelnen Plättchen möglich und man spricht von der sogenannten isotropen Phase.[66]

Die einzelnen Plättchen zeigen hierbei eine hohe Flexibilität[67] und weisen darüber hinaus ein Aspektverhältnis von ≈ 20 000 auf, was dem bis zu > 65 fachen von natürlichen Schichtsilikaten entspricht.[48] Daher eignen sie sich ideal zum Einbringen in Polymermatrizen zur Herstellung von Polymer-Schichtsilikat-Nanokompositen, mit besonderem Fokus in dieser Arbeit auf Anwendungen im Bereich von Barrieren.

3.3 Polymer-Schichtsilikat-Nanokomposite

3.3.1 Herstellungsarten

Polymer-Schichtsilikat-Nanokomposite können mittels verschiedener Verfahren hergestellt werden. Hier sind vor allem die Möglichkeiten der Schmelzcompoundierung, der *in-situ* Polymerisation und der lösemittelbasierten Route anzuführen (**Abb. 4**).[41, 68-70]

Die im großtechnischen Maßstab oft genutzte Methode der **Schmelzcompoundierung** wird vor allem für thermoplastische und elastomere Polymere verwendet. Hierbei hat sich industriell das vielseitig einsetzbare Extrusionsverfahren etabliert, wobei die Polymerschmelze und der Füllstoff compoundiert werden (**Abb. 4a**).[41, 71] Der große Vorteil der Schmelzverarbeitung ist das Vermeiden größerer Mengen an (gesundheitsschädlichen) Lösemitteln, was das Verfahren besonders für große industrielle Maßstäbe interessant macht.[41] Weiterhin ist eine große Bandbreite kommerzieller Polymere durch diese Methode verarbeitbar.[41] Es hat sich jedoch gezeigt, dass das Maximum des Füllstoffgehalts

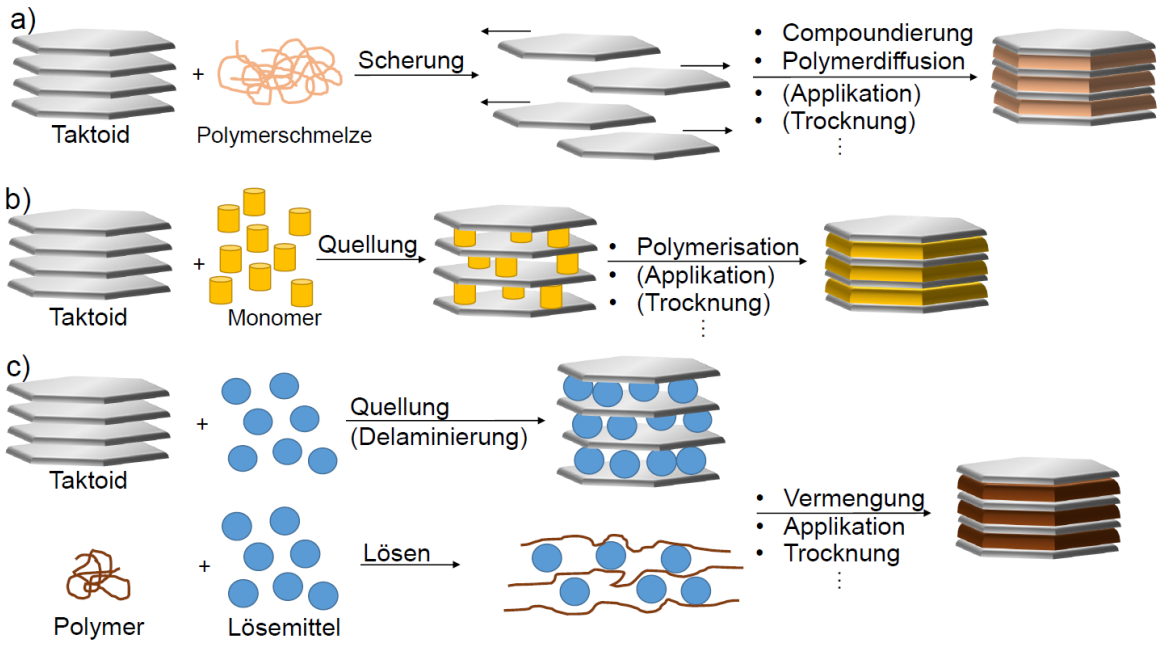

Abb. 4: Schematische Übersicht über die am weitesten verbreiteten Herstellungsarten von Polymer-Schichtsilikat-Nanokompositen. a) Schmelzcompoundierung, b) *in-situ*-Polymerisation, c) Lösemittelroute. Bei der in dieser Arbeit verwendeten Lösemittelroute lagen die Schichtsilikate bei Vermengung mit dem Polymer in delaminierter Form vor (siehe Kapitel 3.2). [*adapted from* [41] (*RSC Adv.,* 2014, *4*, 29393-29428) *by permission of* The Royal Society of Chemistry; https://doi.org/10.1039/C4RA01778A]

begrenzt ist, um eine homogene Verteilung der Schichtsilikate zu gewährleisten. Gerade die mechanische Scherung kann zum Brechen der Schichtsilikat-Taktoide führen und kann ein verringertes Aspektverhältnis zur Folge haben (siehe Kapitel 3.2).[56] Weiterhin ist es bei dieser Verarbeitungsmethode oftmals von Nöten, das Schichtsilikat in einem vorgeschalteten Schritt zu modifizieren, um die Kompatibilität zur Polymerschmelze und somit eine homogene Verteilung im Polymer sicherzustellen. Der Begriff der Modifizierung beschreibt hierbei den Austausch der Zwischenschichtkationen durch Oberflächenmodifikatoren zur Verbesserung der Kompatibilität zwischen dem hydrophileren Füllstoff und hydrophoberen Polymermatrizen.[72] Speziell bei der Verwendung von Biopolymeren sind die Prozessparameter besonders zu kontrollieren, da diese (u.a. Polymilchsäure, PLA) aufgrund der mechanische Scherung bzw. der vorliegenden Temperatur während des Prozesses abgebaut werden können.[41]

Die ***in-situ*-Polymerisation** beschreibt die Methode, mit welcher die ersten veröffentlichten Polymer-Schichtsilikat-Nanokomposite im Zuge des Toyota-Prozesses hergestellt wurden.[51] Bei diesem Verfahren wird das Schichtsilikat im reinen Monomer dispergiert, welches anschließend durch u.a. Hitze polymerisiert wird, wodurch verschiedene Polymer-Klassen (v.a. Duromere) verarbeitet werden können (**Abb. 4b**).[41, 69, 71, 73] Im Umkehrschluss muss berücksichtigt werden, dass die Polymerisation selbst durch das Schichtsilikat beeinflusst werden kann und die Kompatibilität zwischen Monomer und Schichtsilikat gewährleistet sein muss.[41]

Im Bereich von Beschichtungen bietet sich die **Lösemittelroute** an. Hierbei ist man in der Auswahl der möglichen Polymere beschränkt, da diese in einem industriell relevanten Lösemittel löslich sein müssen (**Abb. 4c**). Der große Vorteil dieser Methode ist jedoch, dass durch den vorgeschalteten Schritt der Quellung bzw. Delaminierung das Aspektverhältnis des Füllstoffs maximiert wird und der Füllstoffgehalt aufgrund des Arbeitens im Lösemittel ebenfalls maximiert werden kann (siehe Kapitel 3.2). Dies sind zwei essenzielle Bedingungen im Bereich von Barrierebeschichtungen. Ein weiterer entscheidender Vorteil ist zudem, dass auch Biopolymer-Nanokomposite-Dispersionen mit dieser Methode hergestellt werden können.[41] Diese Nanokomposit-Dispersionen können anschließend mittels verschiedener Verfahren (**Kapitel 3.3.2**) appliziert werden. Aus den genannten Gründen, stellt sich diese Route gerade in Bereichen von (Hoch-) Barrierebeschichtungen als höchst relevant dar.

3.3.2 Lösemittelbasierte Applikationstechniken

Polymer-Schichtsilikat-Nanokomposite können, wie bereits erwähnt, mittels unterschiedlicher Applikationstechniken auf verschiedenste Substrate aufgebracht werden. Alternativ können durch diese Methoden auch selbsttragende Filme hergestellt werden. Neben Dip-Coating oder Breitschlitzdüsen-Beschichtung sind vor allem das Rakel- und das Sprühverfahren weiterverarbeitende Applikationstechniken.[74] Auf diese wird im Folgenden unter Angabe der jeweiligen Vor- und Nachteile detailliert eingegangen.

Die **Rakelbeschichtung** kann durch eine Handrakel (Kastenrakel, Spiralrakel) bzw. eine automatisierte Rakel erfolgen. Hierbei wird die zu verwendende Dispersion auf das Substrat aufgegeben und mit Hilfe der Rakel über das Substrat gezogen und anschließend getrocknet. Neben der Forcierung einer Vorzugsorientierung des Füllstoffs ist der Zeitfaktor ein weiterer Vorteil dieser Art von Beschichtung, da das Verfahren schnell und einfach umzusetzen ist. Durch diese Art der Applikation bestehen jedoch neben Benetzungs- und Homogenitätsherausforderungen, vor allem bei der Trocknung potenzielle Problematiken. Durch die einmalige Applikation einer bestimmten Schichtdicke besteht bei der Trocknung ab zu dicken Beschichtungen mit guten Barriereeigenschaften die Gefahr einer Art Versiegelungseffekt. Dadurch kann im ungünstigsten Fall nicht das ganze Lösemittel beseitigt werden bzw. eine Blasenbildung einsetzen, wodurch die Barrierewirkung der Beschichtung stark gemindert werden kann.[49] Ein weiterer Nachteil dieses Verfahrens ist die Begrenzung auf planare Objekte.

Beim **Sprühverfahren** erfolgt eine Kombination aus Beschichtung und anschließender Trocknung in mehreren Zyklen. Der Nachteil dieses Verfahrens ist der Zeitfaktor, da durch die zyklische Deposition nur sehr dünne Schichten progressiv aufgebracht werden, womit bei dickeren Beschichtungen der Zeitfaktor eine Herausforderung darstellt.[75, 76] Der große Vorteil hierbei ist jedoch die homogene Trocknung der Schicht nach jedem Sprühzyklus, wodurch bereits während des Sprühprozesses ein Großteil des Lösemittels entfernt werden kann. Somit kann im Vergleich zum Rakelverfahren die Gefahr des Versiegelungseffekts gemindert werden. Weiterhin ist dieses Verfahren auch auf 3D Objekte übertragbar und somit in vielen potenziellen Anwendungsgebieten einsetzbar. Am Beispiel eines Polymer-Schichtsilikat-Nanokomposits konnte bereits gezeigt werden, dass durch

das Sprühverfahren eine bessere 1D Kristallinität erreicht werden kann als durch das Rakelverfahren. Weiterhin konnten in dieser Arbeit durch das Sprühverfahren weitaus bessere Barrierewerte erzielt werden.[77]

3.3.3 Charakteristika von Polymer-Schichtsilikat-Nanokompositen

Neben dem positiven Effekt von Schichtsilikaten als Füllstoff auf Polymermatrizen bezüglich mechanischer Eigenschaften und Flammschutzeigenschaften, stehen vor allem die Barriereeigenschaften im Fokus dieser Arbeit.

Für die Anwendungen ist hierbei die Transmissionsrate (*TR*) die entscheidende Kenngröße, welche in den Einheiten $cm^3\ m^{-2}\ day^{-1}\ bar^{-1}$ (Volumen (cm^3) pro Fläche (m^{-2}), pro Tag (day^{-1}(Tag)) bei bestimmten Druckverhältnissen (bar^{-1} oder atm^{-1}), u.a. bei Sauerstoff, Helium, Wasserstoff) bzw. $g\ m^{-2}\ day^{-1}$ (Masse (g) pro Fläche (m^{-2}) pro Tag (day^{-1}), bei Wasserdampf) angegeben werden.[76] **Abb. 5** zeigt die nötigen Transmissionsraten bezüglich Sauerstoff und Wasserdampf von Verpackungen verschiedenster Lebensmittel.[19] Im Vergleich dazu stellt das Einkapseln hochsensibler organischer LEDs (OLED) das anspruchsvollste Ziel im Bereich von Verpackungen dar. Hierbei sind Transmissionsraten von $< 10^{-5}\ cm^3\ m^{-2}\ day^{-1}\ bar^{-1}$ bzw. $10^{-6}\ g\ m^{-2}\ day^{-1}$ für Sauerstoff bzw. Wasserdampf erforderlich.[27]

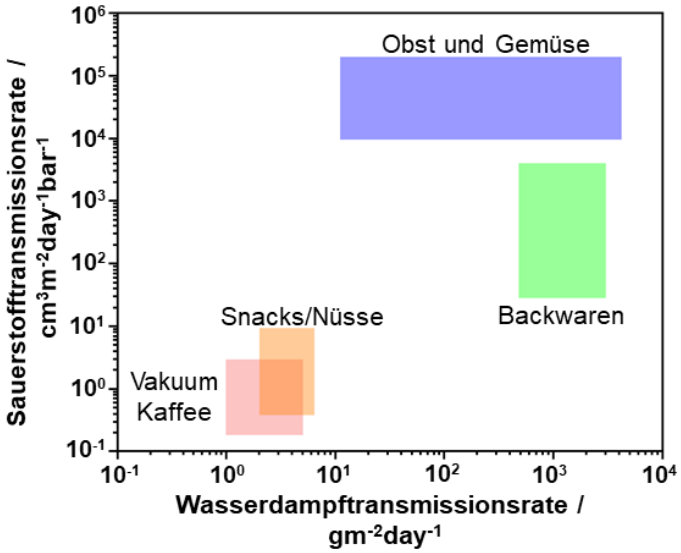

Abb. 5: Übersicht der Barriere-Anforderungen an ausgewählte Verpackungsmaterialien verschiedener Lebensmittelbereiche bezogen auf die Sauerstoff- und Wasserdampftransmissionsraten. [*adapted from* [19]]

Um verschiedene Materialien mit unterschiedlichen Dicken besser vergleichen zu können, wird der Begriff der Permeabilität *P* herangezogen. Das in diesem Bereich vorherrschende Permeations-Prinzip wird durch das Lösungs-Diffusion-Modell beschrieben. Hierbei wird der Prozess des Durchdringens einer Barriereschicht durch Gase oder auch Wasserdampf (Permeaten) bereits im 19. Jahrhundert von Graham untersucht und kann in folgende Schritte unterteilt werden:[78-80]

1. Adsorption des Permeaten an die Barriereschicht und (teilweise) Lösen in dieser
2. Diffusion des Permeaten durch die Barriereschicht
3. Desorption des Permeaten von der Barriereschicht

Dieser Prozess wird von den zwei Effekten der Diffusion (Diffusionskoeffizient *D*) und der Löslichkeit (*solubility*, Löslichkeitskoeffizient *S*) bestimmt, womit sich folgende Abhängigkeit ergibt (**Gl. 1**):[58, 79]

$$P = D \cdot S \qquad \textbf{Gl.1}$$

Die resultierende Permeabilität kann hierbei unter Einbeziehen des Ersten Fick´schen Gesetzes und dem Gesetz nach Henry in Abhängigkeit des Gleichgewichts-Masseflusses J_∞ beschrieben werden (**Gl. 2**):[58, 79, 81]

$$P = \frac{J_\infty \cdot d}{\Delta p} \qquad \textbf{Gl.2}$$

wobei *d* die Dicke der Barriereschicht beschreibt und die Triebkraft hierbei die Partialdruckdifferenz des Permeaten Δp darstellt.

Wie bereits beschrieben, sind die, für die Anwendungen, relevanten Werte die gemessenen Transmissionsraten *TR,* wobei der Zusammenhang in **Gl. 3** dargestellt ist:[81]

$$P = TR \cdot d \qquad \textbf{Gl.3}$$

Zur besseren Vergleichbarkeit der Permeabilitäten, werden diese auf eine bestimmte Dicke normiert, in dieser Arbeit 1 µm, womit die Permeabilitäten in dieser Arbeit mit den Einheiten cm^3 µm m^{-2} day^{-1} bar^{-1} (alternativ atm^{-1}, Sauerstoff, Helium, Wasserstoff) bzw. g µm m^{-2} day^{-1} bar^{-1} (alternativ atm^{-1}, Wasserdampf) beschrieben werden. Bei der Berechnung der Wasserdampf-Permeabilität ist dabei weiterhin zu beachten, dass der Druckunterschied durch den Wasserdampf bei den jeweiligen Messeinstellungen (Temperatur, Luftfeuchtigkeit) bestimmt wird.

Gerade in Bereichen von Beschichtungen ist es notwendig die Permeabilität der reinen Beschichtung ($P_{Beschichtung}$) zu ermitteln. Unter Einbeziehen der jeweiligen Dicken (d_{Gesamt}, $d_{Substrat}$, $d_{Beschichtung}$) als auch der experimentell ermittelten Transmissionsraten (TR_{Gesamt}, $TR_{Substrat}$) kann nach **Gl. 4** $P_{Beschichtung}$ berechnet werden:[82]

$$\frac{d_{Gesamt}}{P_{Gesamt}} = \frac{d_{Substrat}}{P_{Substrat}} + \frac{d_{Beschichtung}}{P_{Beschichtung}} \qquad \textbf{Gl.4}$$

Abzuleiten aus dem Lösungs-Diffusions-Modell kann die Permeabilität durch verschiedene Einflüsse verändert werden. Unpolare Gase wie Sauerstoff oder auch Helium lösen sich besser in hydrophoberen Polymeren, wohingegen Wasserdampf besser in hydrophilen Matrizen löslich ist. Dies hat einen Anstieg bzw. eine Abnahme der Permeabilität je nach Permeat-Polymer Kombination zur Folge. Darüber hinaus weisen sowohl der Diffusionskoeffizient als auch der Löslichkeitskoeffizient und somit auch die Permeabilität eine Temperaturabhängigkeit auf. Außerdem kann bei ansteigender Luftfeuchtigkeit Wasser als Weichmacher zum Anquellen der Polymermatrix führen und damit auch zum Ansteigen der Permeabilität. Doch auch die Polymereigenschaften selbst beeinflussen die Permeabilität. Eine vergrößerte Kristallinität des Polymers führt zu einer Verringerung der Permeabilität, da kristalline Bereiche als undurchlässig gelten.[79, 83]

Eine weitere Möglichkeit die Permeabilität zu verringern ist das Verwenden von Füllstoffen. Durch das Einbringen von schichtförmigen Verbindungen, wie dem hier verwendeten NaHec, entsteht ein sogenannter *tortuous path* (**Abb. 6a**).[58] Dadurch verlängert sich der effektive Weg der Gasmoleküle. Weiterhin wird durch das Einbringen auch die Löslichkeit des Gases in der Matrix verändert, wodurch sich durch die reguläre Anordnung von plättchenförmigen Füllstoffen in Polymermatrizen orthogonal zur Diffusionsrichtung, folgende Abänderungen bezüglich des Diffusions- und Löslichkeitskoeffizienten ergeben (**Abb. 6a**, **Gl. 5** + **Gl. 6**):[58, 84]

$$D_e = \frac{D_0}{f} \qquad \textbf{Gl.5}$$

$$S_e = S_0 \cdot (1-\phi) \qquad \textbf{Gl.6}$$

mit D_e und S_e als neue effektive Diffusivitäts- und Löslichkeitskoeffizienten nach Einbringen des Füllstoffs und D_0 und S_0 als Koeffizienten der reinen Matrix. ϕ

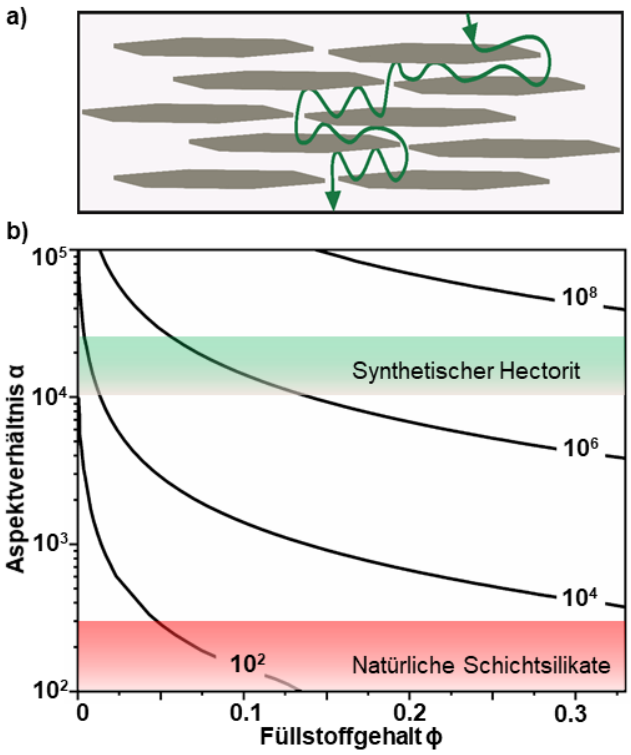

Abb. 6: Absenken der Permeabilität durch Einbringen von Schichtsilikat als Füllstoff. a) Verbildlichung des entstehenden *tortuous path* (grün). b) Darstellung der resultierenden Abhängigkeit der erreichbaren Barriere-Verbesserungsfaktoren (schwarze Linien) sowohl vom Füllstoffgehalt als auch dem Aspektverhältnis. Der Fokus liegt auf dem Vergleich von synthetischem Hectorit und natürlichen Schichtsilikaten.[48, 53, 81] [*adapted from* [48,81]]

beschreibt den Volumenanteil des Füllstoffs und *f* den Tortuositätsfaktor durch Einbringen des Füllstoffs. Der Tortuositätsfaktor *f* wird hierbei durch das Verhältnis des verlängerten Permeaten-Weges *d'* und der Barriereschichtdicke *d* beschrieben (**Gl. 7**).[58]

$$f = \frac{d'}{d} \qquad \textbf{Gl.7}$$

Aus den Gleichungen **Gl. 1**, **Gl. 5**, **Gl. 6** und **Gl. 7** ergibt sich somit **Gl. 8**:[58]

$$\frac{P_{Komposit}}{P_{Matrix}} = \frac{1-\phi}{f} \qquad \textbf{Gl.8}$$

Da jedes eingebrachte Füllstoffplättchen im Durchschnitt zur Hälfte des lateralen Durchmessers L_d zur Pfadverlängerung beiträgt, ergibt sich bei der Plättchenanzahl $\langle N \rangle$, welche durch $\langle N \rangle = d \cdot \phi / H$ (H = Plättchenschichtdicke) beschrieben wird, für *d'* (**Gl. 9**) und darauf aufbauend für *f* (**Gl. 10**):[58]

$$d' = d + \langle N \rangle \cdot \frac{L_d}{2} \qquad \textbf{Gl.9}$$

$$f = 1 + \frac{L_d}{2H} \cdot \phi \qquad \textbf{Gl.10}$$

Durch Kombination von **Gl. 8** und **Gl. 10** ergibt sich demnach für die Herleitung nach Nielsen (**Gl. 11**):[58]

$$\frac{P_{Komposit}}{P_{Matrix}} = \frac{1-\phi}{1+\frac{\alpha}{2}\cdot\phi} \qquad \textbf{Gl.11}$$

Demnach ist die Permeabilität der gefüllten Matrix neben dem Aspektverhältnis des Füllstoffs ebenfalls vom Füllstoffgehalt abhängig. Weiterhin ist die Permeabilität abhängig von der räumlichen Anordnung und der geometrischen Form des Füllstoffs.[59] Neben Nielsen haben viele weitere Experten in diesem Bereich Erweiterungen und Änderungen ermittelt, welche von Choudalakis und Gotsis zusammenfassend in einem Review detailliert und vergleichend hergeleitet wurden.[58] Halbverdünnte Systeme, bestehend aus Füllstoffen mit großem Aspektverhältnis werden durch das Cussler-Modell am genauesten beschrieben (**Gl. 12**):[59]

$$P_{rel} = \frac{P}{P_0} = \left(1+\mu\left(\frac{\alpha^2\phi^2}{1-\phi}\right)\right)^{-1} \qquad \textbf{Gl.12}$$

wobei P_{rel} = relative Permeabilität, P = Permeabilität des gefüllten Polymers, P_0 = Permeabilität der reinen Matrix, μ = geometrischer Faktor, abhängig von der Form des Füllstoffs (hier[81]: 4/9), α = Aspektverhältnis des Füllstoffs, ϕ = Füllstoffanteil ($\phi \ll 1/\alpha\cdot\phi > 1$)[81].

Der Einfluss eines Füllstoffes nach Cussler ist in **Abb. 6b** veranschaulicht. Gezeigt ist der theoretisch erreichbare Verbesserungsfaktor in Abhängigkeit des Füllstoffs und des Aspektverhältnisses. Selbst bei hohem Füllstoffgehalt an natürlichen Schichtsilikaten wie MMT, können Faktoren von > 10^4 nicht bewerkstelligt werden. Im Gegensatz dazu reichen bereits geringe Füllstoffanteile an synthetischem Hectorit mit sehr großem Aspektverhältnis, um diese Verbesserungen der Permeabilität zu erreichen. Weiterhin können mit hohen NaHec-Füllstoffanteilen in der Theorie Verbesserungsfaktoren von bis zu >10^6 erreicht werden, was gerade für Ultrahochbarriereanwendungen, wie den angesprochenen OLED-Verkapselungen, unabdingbar ist.[48]

3.3.4 Messmethoden

Zum Messen der jeweiligen Transmissionsraten bieten sich verschiedene Messmethoden an. Für Sauerstoffbarrieremessungen wurden die Messapparaturen der Firma Ametek GmbH (mocon) verwendet, welche exakt einstellbare Luftfeuchten und Temperaturen ermöglichen und darüber hinaus Messgrenzen von bis zu $5 \cdot 10^{-4}$ $cm^3\ m^{-2}\ day^{-1}$ gewährleisten. Dadurch ist es möglich auch Hochbarrierematerialien zu analysieren.[85] Das zugrundeliegende Messprinzip ist in **Abb. 7** veranschaulicht. Hierbei wird das, die Probe bereits durchdrungene, Testgas (Sauerstoff) von dem Trägergas (Formiergas) zum Coulox-Sensor transportiert. Dieser Sensor besteht aus einer Cadmium-Anode und einer Graphit-Kathode, wobei die ablaufenden Reaktionen ebenfalls in **Abb. 7** dargestellt sind. Der Coulox-Sensor verhält sich nach dem Faraday´schen Gesetz, womit durch den entstehenden Stromfluss auf die Menge an durchgedrungenen Sauerstoff zurückgerechnet werden kann.[85]

Eine weitere Möglichkeit der Messung von Transmissionsraten von Gasen bietet die manometrische Messung. Hierbei unterteilt die plane Probe eine Kammer in zwei Kammern, wobei diese jeweils evakuiert werden können. Durch den Druckanstieg bedingt durch die durchdringenden Gasmoleküle kann auf die Transmissionsraten

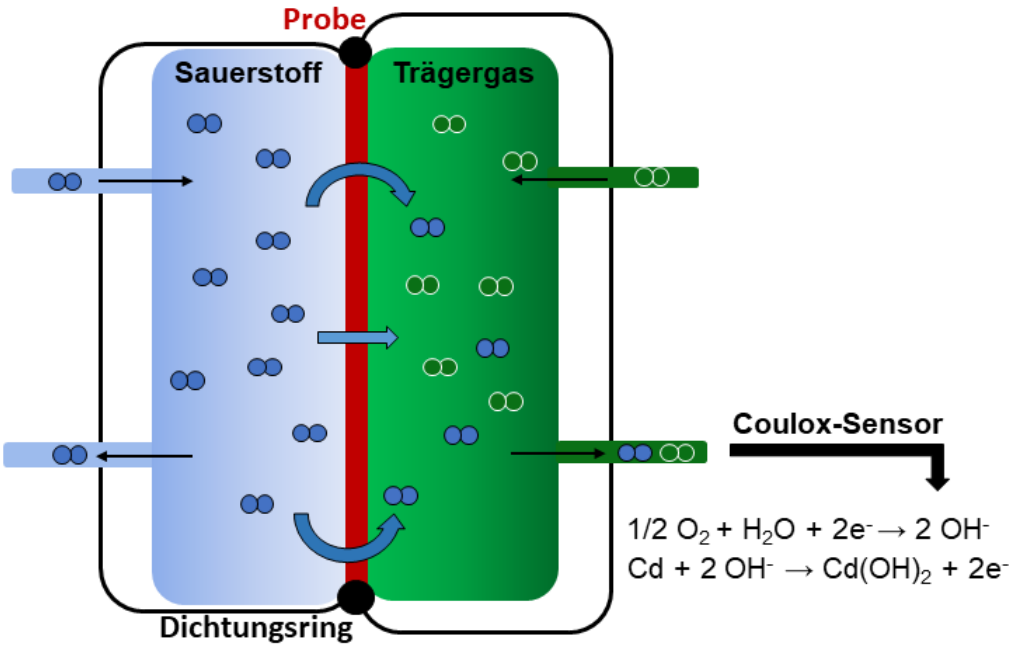

Abb. 7: Schematische Darstellung des Aufbaus des verwendeten Sauerstoffmessgeräts mittels Coulox-Sensor-Verfahren. [*adapted from* [85]]

zurückgerechnet werden. Diese Methode stellt sich als sehr flexibel einsetzbar dar und kann neben z.B. Stickstoff und Sauerstoff ebenfalls für hochdiffusive Gase wie Helium und Wasserstoff verwendet werden.[86]

Beim Messen der Wasserdampftransmissionsraten wurde ein innovatives Messgerät (hibarsens) der Firma Sempa Systems GmbH verwendet. Basierend auf einer laserspektroskopischen Spurengasanalyse ist dieses Gerät in der Lage Transmissionsraten im Bereich von 10^{-6} g m^{-2} day^{-1} zu detektieren und ist demnach unabdingbar um potenzielle OLED-Verkapselungsmaterialien zu testen.[87] Entscheidend ist hierbei, dass sich ein stabiler Wasserdampf-Diffusionsgradient innerhalb der Probe zwischen der „trockenen“ und der mit Wasserdampf beaufschlagten Seite einstellt. Dies erfordert ein Vorkonditionieren der Proben, da dieser Schritt einen essentiellen Anteil an der Gesamtmesszeit bei Hochbarrierematerialien hat.[88]

3.4 Problemstellung

Wie schon in **Kapitel 3.3** detailliert beschrieben können Schichtsilikate mittels geeigneter Methoden in Polymermatrizen eingebracht werden, um so Barrierematerialien für verschiedenste Anwendungen herzustellen.

Auf dem Prozessierungsweg vom reinen Schichtsilikat zum Nanokomposit können sich jedoch Herausforderungen und Problematiken ergeben, welche es zu lösen gilt. Weiterhin stellen die unterschiedlichen Anwendungsbereiche neben den Barriereeigenschaften weitere Anforderungen, die zu erfüllen sind. Einzelne dieser Herausforderungen, Problematiken und Anforderungen wurden im Zuge dieser Arbeit behandelt, welche im Folgenden unter Angabe der jeweils gestellten Forschungsfrage (F) aufgezeigt sind:

Die Lösemittelroute bietet sich zur Verarbeitung hochgefüllter Barrierematerialien mit Schichtsilikat als Füllstoff bevorzugt an, was bereits in **Kapitel 3.3** dargestellt wurde. Hierbei weisen die aktuell verwendeten Applikationsmethoden wie das Sprüh- oder auch Rakelverfahren Verbesserungspotentiale auf, weshalb im Zuge dieser Arbeit anhand folgender Leitfrage nach einer alternativen Methode geforscht wurde:

> (F1) Stellen sich neben den vielseitig verwendeten *state-of-the-art* Methoden weitere Techniken als sinnvoll und prozessierbar dar, um hochgefüllte Polymer-Schichtsilikat-Nanokomposite herzustellen?

Ebenfalls erläutert wurde bereits die Notwendigkeit von Barrierematerialien in den verschiedensten Einsatzbereichen, von *Lowtech*- bis hin zu *Hightech*-Anwendungen. Ein Großteil der verwendeten Kunststoffe wird in der Verpackungsindustrie eingesetzt. Aufgrund der bereits im Detail beschriebenen Umweltkontamination durch kommerzielle, petrobasierte Lebensmittelverpackungsmaterialien wurde im Rahmen dieser Arbeit folgende Fragestellung bearbeitet:

> (F2) Kann mit Schichtsilikaten als Füllstoff eine kompetitive, zukunftsträchtige Alternative zu kommerziellen Verpackungsmaterialien geschaffen werden?

Doch auch in hoch technologisierten Bereichen, wie der Luft- und Raumfahrt, werden Barrierematerialien gegenüber hochdiffusiven Permeaten, wie Helium und Wasserstoff, benötigt. Des Weiteren ist für Leichtbau-Anwendungen das Gewicht des Barriereliners von essenzieller Bedeutung. Diesbezüglich erweisen sich die *state-of-the-art* Barriereliner als ausbaufähig. In einer der Teilarbeiten dieser Dissertation wurde sich, auf diesen Anforderungen aufbauend, mit folgender Forschungsfrage im Detail beschäftigt:

> (F3) Können mit Hilfe von Schichtsilikaten auch in *Hightech*-Anwendungen mit hochdiffusiven Gasen kompetitive Alternativen zu *state-of-the-art* Barrierelinern realisiert werden?

Die genannten Barriereeigenschaften von Polymer-Schichtsilikaten beruhen auf dem Entstehen eines *tortuous path* durch das Einbringen der impermeablen Schichtsilikate in die Polymermatrix und dem damit verbundenen Herabsetzen der Diffusivität. Gerade hydrophile Polymermatrizen zeigen bei steigender Luftfeuchtigkeit das Phänomen der Quellung. Da viele der genannten Anwendungen jedoch auch bei höheren Luftfeuchtigkeiten eine kompetitive Barriereeigenschaft benötigen, wurde im Zuge dieses Projekts folgende Forschungsfrage gestellt und bearbeitet:

> (F4) Inwieweit hat ein variabler Füllstoffanteil an Schichtsilikat in der Polymermatrix neben dem Einfluss auf die Diffusivität der Permeaten, auch Auswirkungen auf die Quellbarkeit des Polymers im Zwischenschichtraum und inwieweit spielt das Polymer-*Confinement* zwischen den Schichten, basierend auf hohen Füllstoffanteilen, eine Rolle?

Doch nicht nur das Einbringen von impermeablen Füllstoffen erhöht die Barriereeigenschaften. Diese wird darüber hinaus durch Polymereigenschaften, wie der Kristallinität, beeinflusst. Kristalline Bereiche in Polymeren gelten als undurchdringbar für Gase oder Wasserdampf. Basierend darauf wurde anhand der folgenden Fragestellung ein Zusammenhang zwischen dem Einbringen von Schichtsilikat, der resultierenden Nanokomposit/Hybrid-Struktur, der auftretenden Effekte und der Nanokomposit/Hybrid-Kristallinität erarbeitet:

(F5) Welchen Einfluss können variierende Füllstoffanteile an Schichtsilikat auf die Struktur-Eigenschaftsbeziehung der entstehenden Nanokomposite/Hybride, mit Fokus auf deren Kristallinität, haben und welche Effekte sind dabei zu beobachten?

Die Synopsis (**Kapitel 4,** Schematische Übersicht **Abb. 8**) bietet einen zusammenführenden Leitfaden durch die einzelnen Forschungsfragen und geht detailliert auf die Problemstellungen, Lösungsansätze und Ergebnisse der einzelnen Arbeiten ein.

4 Synopsis

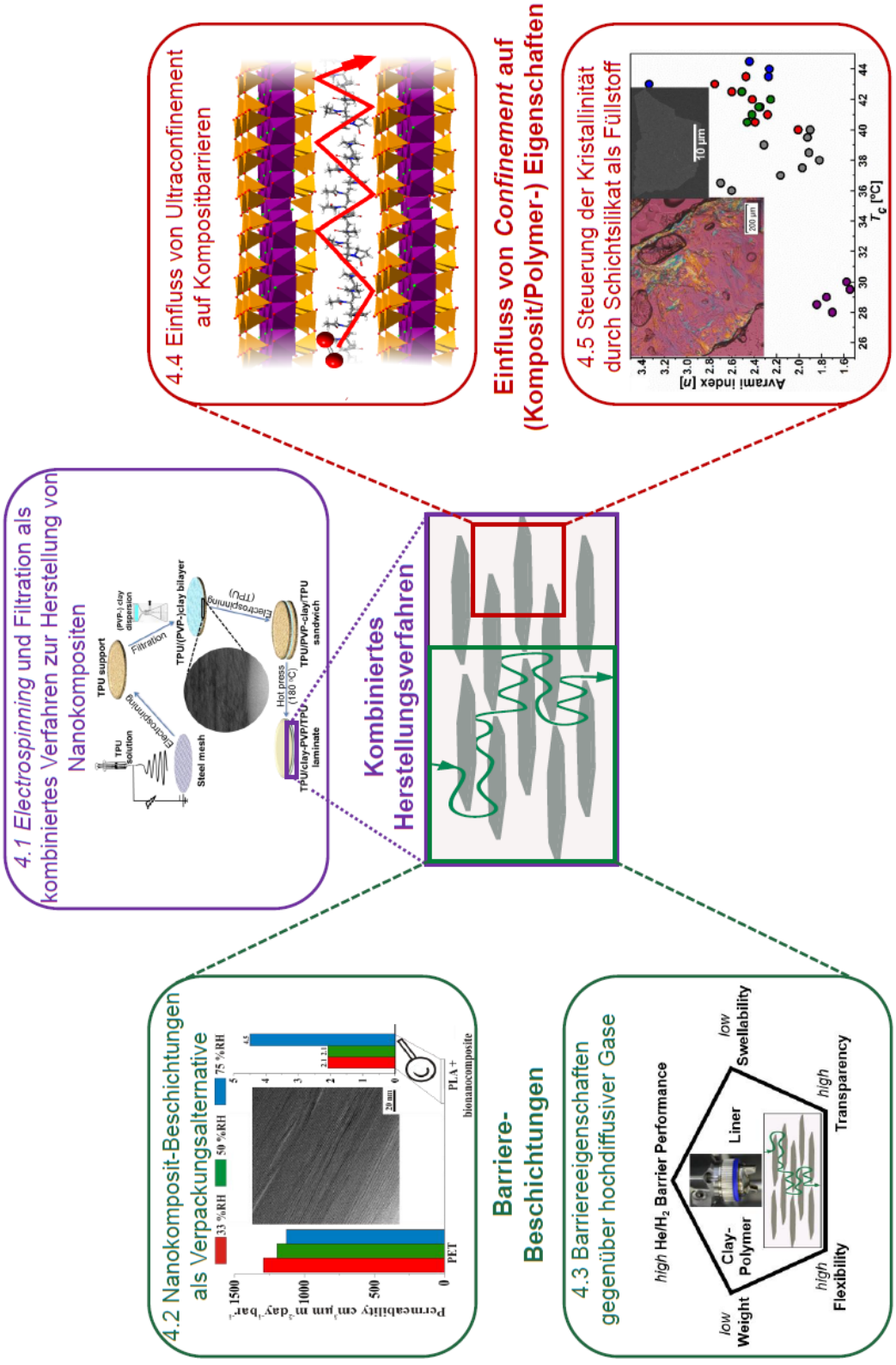

Abb. 8 Schematische Übersicht über die vorgestellten Publikationen dieser kumulativen Dissertation und deren genereller Zusammenhang. [*reprinting/reproduction permissions*: Kapitel 6]

Die vorliegende, kumulative Dissertation enthält 5 Publikationen. Diese behandeln die in **Kapitel 3.4** gestellten Forschungsfragen F und lassen sich in die drei Teilbereiche **Kombiniertes Herstellungsverfahren** von Polymer-Schichtsilikat-Nanokompositen (F1), dem Einsatz von synthetischen Hectorit als Füllstoff für **Barrierebeschichtungen** (F 2+3) und der Untersuchung des **Einflusses des *Confinements* auf (Komposit/Polymer-) Eigenschaften** (F 4+5) einteilen (**Abb. 8**).

Um den Zusammenhang zwischen den einzelnen Arbeiten noch einmal zu verdeutlichen, werden im Folgenden zunächst die Problemstellungen dieser Arbeit aufgegriffen, um anhand derer die Herangehensweisen darzulegen und die Ergebnisse in komprimierter Form aufzuzeigen.

Die Publikation, welche in **Kapitel 4.1** im Detail aufgearbeitet ist, basiert auf einem kombinierten Herstellungsverfahren aus *Electrospinning* und Filtration zur Herstellung von hoch gefüllten Polymer-Schichtsilikat-Nanokompositen. Sowohl das bereits in **Kapitel 3.3** beschriebene Sprüh-, als auch das Rakelverfahren weisen bestimmte Verbesserungspotenziale auf. Um die Herstellungsdauer und Trocknungseffizienz weiter zu senken bzw. zu steigern, wurden in diesem Gemeinschaftsprojekt mit dem Lehrstuhl für Makromolekulare Chemie die Kompetenzen in den Bereichen *Electrospinning* und dem Erstellen von Polymer-Nanokompositen mit anorganischen Füllstoffen kombiniert. Dadurch ist es gelungen Membranen mit verbesserten Mechanik- und Barriereeigenschaften herzustellen.

Um mit solchen, oder wie im folgenden Projekt mittels Sprühverfahren hergestellten, Polymer-Schichtsilikat-Nanokompositen im Bereich von Lebensmittelverpackungen Alternativen zu kommerziellen Produkten zu generieren, ist es notwendig vielfältige Eigenschaften zu gewährleisten. Dafür wurden unterschiedliche Expertisen (Makromolekulare Chemie, Mikrobiologie, Anorganische Chemie) gebündelt, um letztendlich eine GlycolChitosan-Schichtsilikat-Nanokomposit-Beschichtung herzustellen. Dieses in **Kapitel 4.2** im Detail betrachtete Nanokomposit-System weist neben kompetitiven Sauerstoff-Barriereeigenschaften, ebenfalls Transparenz, Flexibilität und Antikolonisationspotenziale gegenüber Biofilmbildnern auf, um eine Langlebigkeit der Schutzwirkung zu gewährleisten.

Doch nicht nur im Bereich von *Lowtech*-Anwendungen, wie bei Lebensmittelverpackungen, sind Barriereeigenschaften von enormer Relevanz. Neben Sauerstoff und Wasserdampf als Permeaten, gibt es Anwendungen in der Luft- und Raumfahrttechnik, welche eine Barriere gegenüber hochdiffusiven Gasen, wie Wasserstoff und Helium, erfordern. Die Arbeit, die im Detail in **Kapitel 4.3** beschrieben wird, fokussierte sich daher auf ein wasserbasiertes Polyvinylalkohol-Schichtsilikat-System, welches als Barrierebeschichtung im Bereich von *lighter-than-air*-Fahrzeugen oder der Raumfahrt dienen soll. Neben Eigenschaften wie Flexibilität und kompetitiven Barriereeigenschaften bietet sich diese Nanokomposit-Beschichtung aufgrund des geringen Auftragsgewichts für diese Anwendungen besonders an.

In den genannten Barriereanwendungen ist es oftmals erforderlich, dass die Barriereeigenschaften auch bei höheren Luftfeuchtigkeiten persistent bleiben. Wasserbasierte Systeme zeigen bei erhöhter Luftfeuchtigkeit ein erhöhtes Quellverhalten, wodurch die Barriereeigenschaften negativ beeinflusst werden. Durch Einbringen von Schichtsilikaten in die Polymermatrix kann dieses Quellverhalten beeinflusst werden.[76, 89] Das in **Kapitel 4.4** beschriebene perfekt strukturierte Polyvinylpyrrolidion-Schichtsilikat-Hybrid diente als Modellsystem, um den Zusammenhang zwischen dem Füllstoffanteil, der Abhängigkeit der Barrierewirkung von der Luftfeuchtigkeit und dem Einfluss des *Confinements* des Polymers im Zwischenschichtraum bei hohen Füllstoffgehalten, im Detail herauszuarbeiten.

Doch nicht nur Hectorit als Füllstoff kann die Barriereeigenschaften von Polymeren beeinflussen. Kristalline Bereiche in Polymeren gelten ebenfalls als undurchlässig für Gase und Dämpfe. In der lehrstuhlübergreifenden Arbeit mit Polymer-Kristallisationsexperten (**Kapitel 4.5**) lag der Fokus deshalb auf der Ermittlung der Abhängigkeit der resultierenden Kristallinität vom Füllstoffgehalt, der ausführlichen Erarbeitung der Struktur-Eigenschafts-Beziehung und dem Aufarbeiten des Gegenspiels der hierbei wirkenden Nukleations- und *Confinement*-Effekte.

In den folgenden **Kapiteln 4.1- 4.5** werden die Publikations-Inhalte im Detail beschrieben. Die zugehörigen Publikationen sind in **Kapitel 6** unter Angabe der jeweiligen persönlichen Beiträge aufgeführt.

4.1 *Electrospinning* und Filtration als kombiniertes Verfahren zur Herstellung von Nanokompositen

In **Kapitel 3.3.2** wurden bereits verschiedene lösemittelbasierte Applikationstechniken vorgestellt. Diese reichen von Rakelverfahren bis hin zu Sprühverfahren. Wie bereits beschrieben, weisen all diese Verfahren prozessspezifische Vor- und Nachteile auf. So besteht bei der Trocknung nach Rakelbeschichtung die Gefahr einer Art Versiegelungseffekt, wodurch nicht das ganze Lösemittel beseitigt werden kann bzw. sich Blasen bilden und somit die Barrierewirkung der Beschichtung stark gemindert werden kann.[49] Beim Sprühverfahren ergibt sich durch die Trocknung in Zyklen diese Problematik nicht, jedoch dauert der Prozess bei größeren Beschichtungsdicken deutlich länger.[77]

Im Zuge dieses Projekts wurde eine Verarbeitungsmethode entwickelt, welche diese Nachteile umgeht. Hierbei wird zunächst via *Electrospinning* als hochskalierbare Methode eine Trägermembran aus thermoplastischem Polyurethan (TPU) hergestellt.[90] Die Porendurchmesser belaufen sich hierbei auf 0,5 – 3,5 µm bei einer Porösität von ≈ 66%. Diese Trägermembran eignet sich daher bestens für die anschließende Filtration einer Polymer-Schichtsilikat (NaHec)-Nanokomposit-Dispersion. Hierbei wurde Polyvinylpyrrolidon (PVP) als Polymermatrix verwendet.

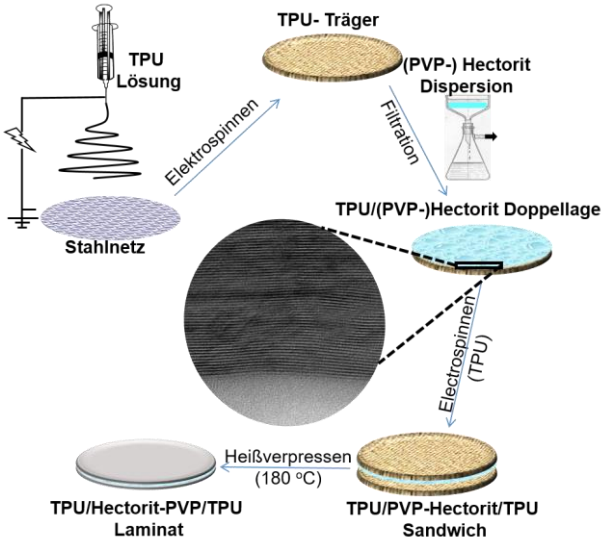

Abb. 9: Darstellung der entwickelten Verarbeitungsmethode zur Herstellung von Polymer-Schichtsilikat (NaHec)-Nanokompositen, welche *Electrospinning*, Filtration und Heißverpressen vereint. [Jian Zhu, Christoph Habel, Theresa Schilling, Andreas Greiner, Josef Breu, Seema Agarwal; Filter-Through Method of Making Highly Efficient Polymer-Clay Membranes; *Macromol. Mater. Eng.* 2019, *304* (7), 1800779. Copyright 2019 Wiley-VCH Verlag GmbH & Co. KGaA. *Reproduced with permission.*]

Nach dem Trocknen dieser Doppellage aus Trägermembran und gefilterter PVP-NaHec-Schicht wird erneut mittels *Electrospinning* eine weitere TPU-Schicht aufgebracht und das entstandene Sandwich bei 180°C zu einem Dreischicht-Laminat heißverpresst (**Abb. 9**). Die PVP-NaHec-Zwischenschicht weist eine nahezu perfekte Ordnung der einzelnen NaHec-Plättchen auf, welche mittels Röntgenbeugungsexperimente (XRD) belegt werden konnte.

Der NaHec-Anteil in der Zwischenschicht wurde hierbei variiert, um einen Einfluss dieser Komponente auf die resultierenden mechanischen Eigenschaften und auch Barriereeigenschaften zu untersuchen. Hierbei konnten kompetitive E-Moduli von bis zu 1117 MPa (29,5 wt% NaHec) bestimmt werden [Details: Originalpublikation in Kapitel 6.1 mit den dortigen Quellen (42-46)]. Darüber hinaus zeigen die Membranen eine Bruchdehnung von bis zu 487% (9,1 wt% NaHec) und kombinieren damit elastomere und thermoplastische Eigenschaften mit stark verbesserten E-Moduli. Weiterhin weisen die Membranen eine hohe Flexibilität auf, was durch Biegeversuche experimentell bestätigt wurde.

Das Einbringen von NaHec mit einem Aspektverhältnis von ≈ 20 000 beeinflusst zudem sowohl die Sauerstoff- als auch die Wasserdampfbarriereeigenschaften positiv. Durch den entstehenden *tortuous path* konnte beispielsweise die Sauerstoffpermeabilität (*oxygen permeability*, *OP*) hierbei im Vergleich zu ungefüllten Membranen um bis zu 98,8% auf eine *OP* von 185 $cm^3\ \mu m\ m^{-2}\ day^{-1}\ bar^{-1}$ (*OP* in Publikation in der Einheit $cm^3\ cm\ m^{-2}\ day^{-1}\ bar^{-1}$, 29,5 wt% NaHec, 50 %r.h.) verringert werden. Die resultierende Wasserdampfpermeabilität beläuft sich auf 7900 $g\ \mu m\ m^{-2}\ day^{-1}\ bar^{-1}$ (in der Publikation in der Einheit $g\ cm\ m^{-2}\ day^{-1}\ bar^{-1}$ angegeben, 9,1 wt% NaHec, 50 %r.h.).

Durch die Kombination der Vorteile eines maßgeschneiderten, porösen Trägermaterials und einer hochgefüllten Polymer-Schichtsilikat-Nanokomposit-Zwischenschicht, in der Schichtsilikate mit sehr großem Aspektverhältnis eingebettet sind, konnten somit flexible Membranen mit mechanischer Stabilität und konkurrenzfähigen Barriereeigenschaften hergestellt werden.

Somit stellt dieses Verfahren durch den modularen Aufbau eine sehr vielseitige, technisch gut umsetzbare Methode dar, hochgefüllte Polymer-Schichtsilikat-Nanokomposit-Membranen herzustellen.

4.2 Nanokomposit-Beschichtungen als Verpackungsalternative

Das steigende Problembewusstsein von Politik und Gesellschaft gegenüber der Thematik „Kunststoffe in der Umwelt“ wurde bereits in **Kapitel 3** im Detail beschrieben. Der Großteil der Polymere wird demnach in der für Endverbraucher relevanten (Lebensmittel-)Verpackungsindustrie verwendet und verlangt aufgrund der Naturbelastungsproblematik nach Alternativen.

Abb. 10 gibt einen Überblick, welche verschiedenen potenziellen Anforderungen an eine bioabbaubare/kompostierbare Lebensmittelverpackung gestellt werden müssen. Neben dem mechanischen Schutz vor Stößen und Vibrationen ist das Hauptmerkmal des Verpackungsmaterials eine wirksame Sauerstoffbarriere, die das Lebensmittel vor einem aeroben mikrobiellen Verderb und (bio)chemischen Reaktionen wie Fettoxidation schützt. Ausgehend von den Barrierefunktionen der Verpackung ergeben sich demnach mitunter die jeweiligen Mindesthaltbarkeitsdaten. Neben der Barriereeigenschaften ist es für den Schutz der Lebensmittel weiterhin erforderlich, dass eine Besiedelung der Verpackung durch Bakterien und Mikroben verhindert wird.[19, 91]

Gerade für den Endverbraucher sind auch die optischen Eigenschaften, wie z.B. Transparenz, von großer Bedeutung. In Bezug auf die übergeordnete Thematik

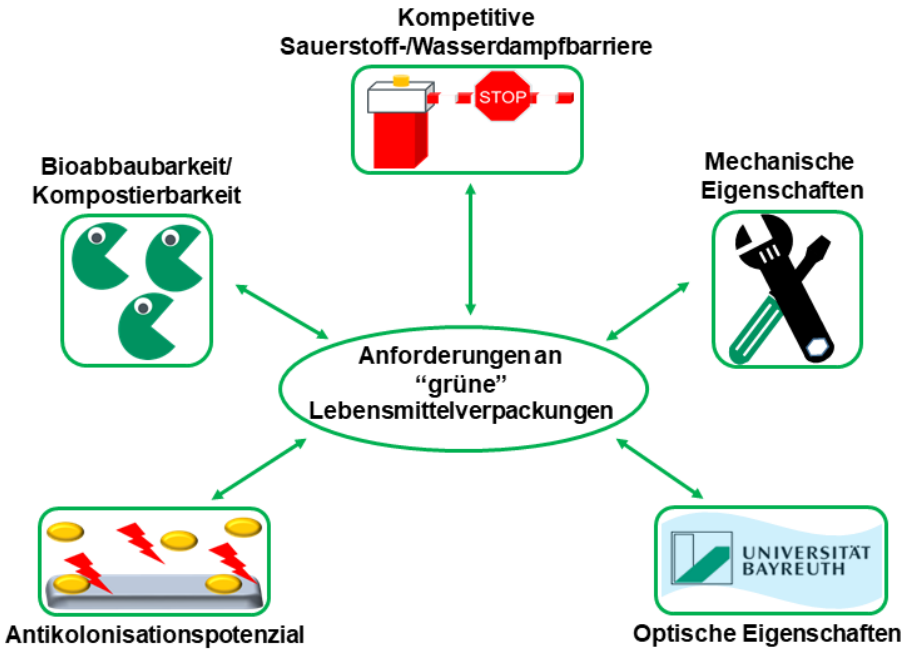

Abb. 10: Übersicht zu potenziellen Anforderungen an umweltschonende, alternative (hier beschrieben mit „grün“) Lebensmittelverpackungen.

Umweltschutz spielt weiterhin die Bioabbaubarkeit bzw. Kompostierbarkeit der Verpackungsmaterialien eine entscheidende Rolle. Biopolymere, wie PLA, welches durch die *FDA* (Behörde für Lebens- und Arzneimittel*, Food and Drug Administration, United States*) als sicher deklariert wurde, bieten eine biobasierte Alternative zu kommerziellen Verpackungsmaterialien, wie PET.[92-94] Letzteres kann bezogen auf die Barriereeigenschaften mit einer Sauerstoffpermeabilität von 1000 $cm^3\,\mu m\,m^{-2}\,day^{-1}\,bar^{-1}$ als eines der Standardmaterialien im Verpackungssektor gesehen werden.[19] Die Sauerstoffpermeabilität von PLA liegt etwa 20 Mal über dem des PETs. Das Ziel des Projekts war es daher, mittels einer Biopolymer-Schichtsilikat-Nanokomposit-Beschichtung PLA zu einer kompetitiven Alternative für PET zu gestalten.

Hierzu wurde eine wasserbasierte Dispersion aus GlycolChitosan (GlyChit) und Schichtsilikat (50 wt%, NaHec) hergestellt und eine 1,4 Mikrometer dicke Sprühbeschichtung auf ein PLA Substrat aufgebracht. Diese Beschichtung weist eine periodische Anordnung der NaHec-Plättchen auf welche jeweils durch 1,9 nm an GlyChit separiert sind. Dies lässt auf ein zweiphasiges Bionanokomposit aus 1D kristallinen, interkalierten Domänen als Hauptvolumen und partiell segregierten GlyChit als Minderheitsphase schließen. Durch Messung der Abhängigkeit des Zwischenschichtabstands von der Luftfeuchtigkeit konnte gezeigt werden, dass der Abstand bis zu einer Luftfeuchtigkeit von 43 %r.h. nahezu unverändert bleibt, was die bis zu dieser r.h. konstant bleibenden Sauerstoffpermeabilität unterstreicht. Erst bei hohen Luftfeuchtigkeiten (75 %r.h.) zeigte sich in den XRD-Messungen eine Zunahme des Zwischenschichtabstands von 1 nm, was eine starke Wasseraufnahme belegte.

Im Vergleich zu der gravierenden Luftfeuchtigkeits-Abhängigkeit der *OP* der ungefüllten GlyChit-Matrix zeigte sich für die *OP* der Nanokompositbeschichtung lediglich eine geringe Abhängigkeit. Dies bestätigte den Hydrophobisierungseffekt der Schichtsilikate auf die Polymermatrix (u.a. Kapitel 4.4), wobei sich die resultierende *OP* des mit dem Bionanokomposit beschichteten PLA-Substrats auf $< 5\ cm^3\,\mu m\,m^{-2}\,day^{-1}\,bar^{-1}$ (75 %r.h.) beläuft.

Weiterhin zeigte sich, dass sich die Beschichtung nicht vom Substrat ablöst und dass die beschichtete PLA-Folie sowohl im Vergleich zum unbeschichteten PLA als

auch zur klassischen PET-Folie bezüglich der optischen Eigenschaften kompetitiv ist.

Mittels Applikation von gramnegativen Biofilmbildnern (*Pseudonomas fluorescens* A506) konnte gezeigt werden, dass ein Antikolonisationseffekt durch die Beschichtung hervorgerufen wird. Im Vergleich zur PET- bzw. reinen PLA-Folie fand eine deutlich geringere Besiedelung durch den Biofilmbildner statt. Dies könnte darauf zurückzuführen sein, dass ein Teil der NH_2 -Gruppen im GlyChit in der Beschichtung protoniert vorliegt. Weiterhin konnte in ersten Testversuchen gezeigt werden, dass durch die nur einseitige Beschichtung eine enzymatische Abbaubarkeit des PLA von der unbeschichteten Seite her weiterhin stattfinden kann.

Im Rahmen dieser Arbeit ist es gelungen eine vollständig wasserbasierte Polymer-Schichtsilikat-Nanokomposit-Beschichtung auf ein PLA-Substrat aufzubringen, wodurch das System den Großteil der einzelnen aufgeführten potenziellen Anforderungspunkte an alternative Verpackungsmaterialien (**Abb. 10**) erfüllt.

4.3 Barriereeigenschaften gegenüber hochdiffusiver Gase

Nicht nur im Bereich der Lebensmittelverpackungen, wie in dem vorangegangen **Kapitel 4.2** beschrieben, spielen Barriereeigenschaften eine entscheidende Rolle. Auch in der Luftfahrt und im Verkehr werden für die Energiequelle Wasserstoff neue Leichtbauwerkstoffe für dessen Transport und Lagerung benötigt.[30, 31, 33, 35] In gleicher Weise erregen Leichtbaufahrzeuge viel Aufmerksamkeit, da sie den Weg zu effizienteren, neuartigen Konzepten von "Windmühlen" ebnen. Basierend auf solchen Höhenplattformen entstehen zudem innovative Kommunikationsnetze, die rund um den Globus Internetzugang ermöglichen sollen.[37-39] **Abb. 11** zeigt eine Übersicht verschiedener Anwendungen im Bereich Luft- und Raumfahrt, welche ultrahohe H_2- oder He- Barrieren erfordern. Diese hochdiffusiven Gase stellen demnach eine nicht weniger relevante Herausforderung hinsichtlich der Barrierewirkung dar. Neben der Barriereeffizienz sind Flexibilität und geringes Gewicht weitere Voraussetzungen für Barrierebeschichtungen, die im Bereich

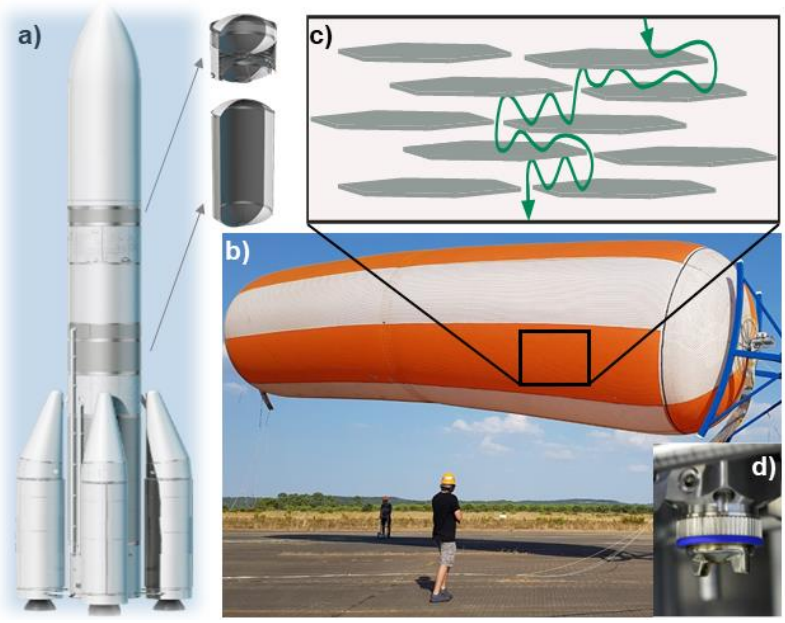

Abb. 11: Übersicht von Anwendungen, die eine ultrahohe, leichte H_2- oder He-Barriere erfordern: a) Ariane 6 Rakete mit den integrierten Tanksystemen (mit Genehmigung von MT Aerospace und ArianeGroup), b) Foto einer *lighter-than-air* Plattform (mit Genehmigung von Omnidea Lda.) c) Schema des *tortuous path* innerhalb des Nanokomposits, aufgebracht durch technische Verarbeitungsmethoden, wie Sprühbeschichtung (d)).
[*Reprinted with permission from ACS Nano* 2020, *14* (6), 7018-7024. Copyright 2020 American Chemical Society. https://pubs.acs.org/articlesonrequest/AOR-BKECUMPCU55IYSKPBVZX; *more informations:* https://helpfaqs.acs.org/2008/10/17/what-is-the-acs-articles-on-request-policy/]

dieser Technologien Anwendung finden sollen. Mechanische Festigkeit und hohe Ozonbeständigkeit sind ebenso von essenzieller Bedeutung.[8] Für stationäre/mobile (Wasserstoff-) Speicher stellen metallbeschichtete oder Hochleistungspolymer-beschichtete, faserummantelte Tanks den Stand der Technik dar.[95-98] Natürlich ist es gerade bei Leichtbauanwendungen in Luft- und Raumfahrt bzw. im Transportwesen wünschenswert, die Metallauskleidung durch ein leichtes, flexibles Barrierematerial zu ersetzen.

In diesem Projekt wurde deshalb ein Polymer-Schichtsilikat-Nanokomposit mit Polyvinylalkohol (PVA) als Polymermatrix und Schichtsilikat (NaHec, 50wt%) als Füllstoff hergestellt. Mittels SAXS-Messungen konnte gezeigt werden, dass die NaHec-Plättchen innerhalb der wasserbasierten Dispersion delaminiert vorliegen. Durch das Sprühverfahren wurde diese Dispersion auf eine Substratfolie aufgebracht, wobei durch die Trocknung eine Phasenseparation mittels XRD-Messungen zu beobachten war. Nichtsdestotrotz weisen die Barriereliner kompetitive Barriereeigenschaften auf. Dies wurde durch die Bestimmung der He- und H_2-Permeabilitäten (*HeP*, *H_2P*) bestätigt. Die ermittelten *HeP* und *H_2P* von 0,8 bzw. 0,6 $cm^3\,\mu m\,m^{-2}\,day^{-1}\,atm^{-1}$ bei 0 %r.h. unterbieten sogar die Barriereleistung von Hochbarrierepolymerlinern. Diese Permeabilitäten zeigen darüber hinaus einen insignifikanten Anstieg (Faktor < 1,5) bei einer Luftfeuchtigkeit von 75 %r.h. Darüber hinaus wurden zur Ermittlung der Ozon-Stabilität die Sauerstoffpermeabilität und zum Widerstand gegenüber Wasserdampf die Wasserdampfpermeabilität bestimmt, welche hierbei sogar die Leistungen von Hochbarrierepolymeren wie Ethylenvinylalkohol (EVOH) unterbieten. Ein weiterer entscheidender Aspekt in den beschriebenen Anwendungsbereichen ist das Auftragsgewicht. Hierzu wurde durch eine exemplarische Berechnung unter Einbeziehen der jeweiligen Permeabilitäten und Dichten eine deutliche Gewichtseinsparung von > 99,5 % pro m^2 im Vergleich zu EVOH aufgezeigt. [Details: Originalpublikation in Kapitel 6.3 mit den dortigen Quellen (23, 53, 54)]

Für alle Leichtbauanwendungen ist die einzigartige Kombination aus Flexibilität, optimierten Barriereeigenschaften und geringem Auftragsgsgewicht ein entscheidender Vorteil gegenüber Beschichtungen mit anderen Materialien. Darüber hinaus können die wasserbasierten Barriere-Beschichtungen durch großtechnische Verfahren wie Sprühbeschichtung auch auf 3D-Objekte aufgebracht werden.

4.4 Einfluss von *Ultraconfinement* auf Kompositbarrieren

Wie bereits in **Kapitel 3** beschrieben finden Polymere vor allem im Bereich von Lebensmittelverpackungen Anwendung. Neben dem mechanischen Schutz vor Vibrationen und Stößen fungieren die Verpackungsmaterialien primär als Sauerstoffbarriere, um die Lebensmittel vor aerobem, mikrobiell basiertem Verderben zu schützen.[19]

Die hierbei zugrundeliegende Permeabilität *P* wurde ebenfalls bereits in **Kapitel 3** erläutert. *P* wird demnach durch das Produkt aus Diffusivität *D* und Löslichkeit *S* beschrieben. *S* ist hierbei unter anderem abhängig von der Polarität der verwendeten Polymermatrizen. Demnach zeigen hydrophile Polymere, wie Polyvinylalkohol, bei geringen Luftfeuchtigkeiten exzellente Barriereeigenschaften gegenüber hydrophoben Gasen, wie Sauerstoff.[76]

Mit ansteigender Luftfeuchtigkeit, welche im Lebensmittelverpackungsbereich vorherrschen kann, fungiert die Luftfeuchtigkeit als Weichmacher, was zum Anquellen der Polymermatrix und in der Folge zu einem Anstieg der Sauerstoffpermeabilität führen kann.[99-101] In kommerziellen Verpackungsmaterialien wird unter anderem durch Variation des hydrophoben Anteils (Ethylen) in Copolymeren, wie z.B. in EVOH, die Luftfeuchtesensitivität gesenkt. Hierbei ist zu beachten, dass dies ab einem gewissen Grenzwert eine nichtlineare Abhängigkeit ist. Dieser Grenzwert kann durch den Ethylengehalt gesteuert werden.[83, 102]

Diese Sensitivität kann jedoch nicht nur durch Angleichen der Polarität verändert werden, sondern auch durch Compoundierung der Polymermatrix mit plättchenförmigen Füllstoffen. Diese reduzieren durch Bildung eines *tortuous path* nicht nur die Diffusivität, sondern führen zugleich zu einem Hydrophobisierungseffekt. In bereits veröffentlichten Arbeiten konnte gezeigt werden, dass durch Inkorporation von Schichtsilikaten die Grenzluftfeuchtigkeit, ab welcher die Sauerstoffbarriere einbricht, zu höheren Werten verschoben werden kann.[76, 100]

Eine systematische Untersuchung dieser Beobachtungen konnte bis dato jedoch noch nicht durchgeführt werden, da die betrachteten Nanokomposite Phasenseparationen, das heißt eine inhomogene Verteilung des Schichtsilikats in

der Polymermatrix, aufwiesen. Innerhalb dieses Projekts war es möglich mittels Polyvinylpyrrolidon (PVP) als Matrix und synthetischen NaHec als Füllstoff translatorisch homogene Hybridfilme mit unterschiedlichen Füllstoffgehalten herzustellen. XRD-Messungen zeigten hierbei rationale Serien. Eine Phasenseparation konnte weiterhin ausgeschlossen werden, da die experimentell bestimmten Zwischenschichtabstände von 2,3 nm (40 vol% NaHec) und 3 nm (31 vol% NaHec) exakt mit den theoretisch ermittelten Abständen übereinstimmen. Diese Hybridfilme weisen demnach eine vergleichbare strukturelle Qualität auf und erlaubten erstmals eine qualitative Untersuchung des Einflusses des *Confinements,* hervorgerufen durch die hohen Füllstoffanteile, auf die Barriereeigenschaften. Durch Messungen der Pulverdiffraktogramme in Abhängigkeit der Luftfeuchtigkeit konnte gezeigt werden, dass die Zunahmen der Zwischenschichtabstände der beiden Hybride mit steigender Luftfeuchtigkeit nur insignifikant voneinander abweichen (< 15%). Darauf aufbauend wurden die jeweiligen Sauerstoffpermeabilitäten (*OP*) der beiden Hybride bestimmt. Das für wasserbasierte Systeme bekannte Phänomen, dass kleine Mengen an

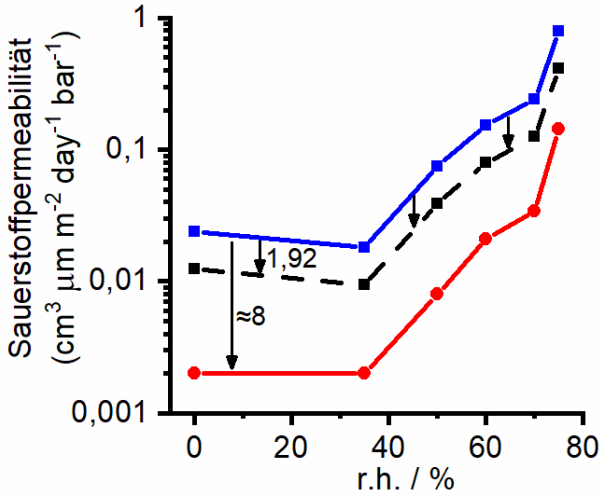

Abb. 12: Auftragung der Sauerstoffpermeabilitäten der unterschiedlich hoch gefüllten Hybride (rot: 40 vol%; blau: 31 vol%) gegen die Luftfeuchtigkeiten r.h.. Berechnungen auf Grundlage der Cussler Theorie würden eine Abnahme der *OP* mit steigendem Füllstoffanteil um einen Faktor von 1,92 ergeben (gestrichelte schwarze Linie). Die experimentellen Ergebnisse ergaben eine Abnahme um einen Faktor von ≈ 8.

[*Reproduced (translated) with permission from ACS Appl. Polym. Mater.* 2020, *2* (7), 3010-3015. Copyright 2020 American Chemical Society. https://pubs.acs.org/articlesonrequest/AOR-VTX6WSKFNED55Q5ARKE8;

***more informations*: https://helpfaqs.acs.org/2008/10/17/what-is-the-acs-articles-on-request-policy/]**

Wassermolekülen (geringe Luftfeuchtigkeiten) das freie Volumen im Polymer zunächst füllen und somit die *OP* zunächst mit steigender Luftfeuchtigkeit abnimmt, konnte auch für das vorliegende Polymer-Schichtsilikat-System gezeigt werden.[103,104] Bei höheren Wasseranteilen (höhere Luftfeuchtigkeiten) wirkt das Wasser dann als Weichmacher, was zu einem Anquellen der Polymermatrix und daraus resultierend zu einem Anstieg der *OP* führt. Durch die Messung der *OP* in Abhängigkeit der Luftfeuchtigkeit (0 %r.h. – 75 %r.h.) wurde herausgearbeitet, dass die Kurvenverläufe der *OP* in Abhängigkeit der r.h. kein unterschiedliches Verhalten für die unterschiedlich gefüllten Hybride aufzeigen. Dadurch konnte das nur gering unterschiedliche Quellverhalten, ermittelt durch die beschriebenen XRD-Messungen, bestätigt werden.

Durch theoretische Berechnungen, basierend auf dem Modell nach Cussler (**Gl. 12**) konnte weiterhin gezeigt werden, dass die Verringerung der *OP* durch die Erhöhung des Füllstoffgehalts größer ist (Faktor ≈ 8), als die Abschätzungen nach Cussler ergeben (Faktor: 1,92) (**Abb. 12**). Dies kann mit einer reduzierten Segmentmobilität im *confined space* in hochgefüllten Schichtsilikat-Systemen begründet werden, welche demnach die Diffusivität von kleinen Molekülen, wie Sauerstoff, herabsetzen könnte.[105]

Diese Ergebnisse sind, nach unserem Wissensstand, der erste eindeutige Beweis, dass neben den nichtlinearen Abhängigkeiten der *OP* nach Cussler (Füllstoffanteil, Aspektverhältnis), bei hohen Füllstoffgehalten und dem damit verbundenen starken *Confinement*, eine dadurch hervorgerufene, weitere, jedoch lineare, Abhängigkeit vorliegt.

4.5 Steuerung der Kristallinität durch Schichtsilikat als Füllstoff

Wie bereits mehrfach ausgeführt, führt die Impermeabilität der Schichtsilikate zu einer Verbesserung der Barriereeigenschaften von Polymermatrizen. Doch auch die Kristallinität der Polymermatrix selbst spielt für die Barriereeigenschaften eine entscheidende Rolle, da kristalline Bereiche, wie bereits in **Kapitel 3** beschrieben, als undurchlässig für Gase und Wasserdampf gelten. Aufgezeigt wurden bereits Arbeiten in welchen die Nanokomposite einen hohen Anteil an Schichtsilikaten enthalten, wodurch es vermehrt zu *Confinement*, der Einengung vom Polymer zwischen den Schichten, kommen kann.[106, 107] Dieser Einfluss kann zu enormen Unterschieden des Nanokomposits im Vergleich zum bulk-Material bezüglich isothermer Kristallisationskinetik und Kristallorientierung führen.[108] Bei Polymer-Füllstoff-Systemen, z.B. Polyethylenoxid (PEO) mit Kohlenstoff-Nanoröhren, wurde der Einfluss der Konzentration des Füllstoffs auf die Kristallisation des Polymers untersucht. So kann bei niedrigen Konzentrationen der Füllstoff als Nukleierungsmittel wirken und bei hohen Konzentrationen kann der beschriebene *Confinement*-Effekt auftreten.[109]

Das Hauptziel dieser Arbeit war die systematische Untersuchung des Einschlusseffekts des Füllstoffgehalts von Schichtsilikaten mit hohen Aspektverhältnissen (NaHec) auf die Struktur von Polyethylenglykol (PEG)-Nanokompositen. Dabei konnte mittels Kleinwinkelröntgenstreuung (SAXS) gezeigt werden, dass das Schichtsilikat in den ternären Dispersionen (Wasser, PEG, NaHec) delaminiert vorliegt. Durch den Trocknungsprozess entstehen Nanokomposite bei denen der Zwischenschichtabstand, gemessen durch Röntgenbeugung (XRD), unabhängig vom Füllstoffgehalt (20 wt%, 40 wt%, 60 wt%, 75 wt%) 0,81 nm beträgt, was auf eine partielle Phasenseparation in den geringer gefüllten Nanokompositen hinweist und demnach auf Biphasen-Systeme mit reinen PEG Domänen zwischen den interkalierten PEGHec-Phasen. Dies konnte durch Transmissionselektronenmikroskopie-Messungen bestärkt werden.

Diese Ergebnisse der strukturellen Analyse gehen einher mit den nicht-isothermischen DSC-Messungen (*Differential Scanning Calorimetry,* Dynamische Differenzkalometrie). Die Kristallisationstemperatur T_c nimmt zunächst bei einem Füllstoffgehalt von 20 wt% im Vergleich zu reinem PEG (22°C) stark zu, was auf einen Nukleationseffekt schließen lässt. Bei weiter steigendem Füllstoffanteil,

wirken sowohl der Nukleationseffekt, als auch der *Confinement*-Effekt, wobei letzterer die T_c verringert. Bei dem hochgefüllten PEGHec-System (75 wt%) zeigt sich der dominierende *Confinement*-Effekt durch eine T_c, welche sogar die von reinem PEG unterbietet. Die Berechnung der Kristallinität zeigte hierbei, dass mit einem ansteigenden Füllstoffgehalt die Kristallinität herabgesetzt wird. Mittels Selbstnukleierungsexperimenten konnte eine Nukleationseffizienz von Schichtsilikat von bis zu 67 % (20 wt% NaHec) bestimmt werden. Weitere kalorimetrische Experimente erlaubten einen vertieften Blick in die ablaufende isotherme Kristallisationskinetik und verdeutlichten die zwei ablaufenden Effekte. Bei geringen Füllstoffanteilen zeigt sich aufgrund des Nukleierungseffekts ein Beschleunigungseffekt auf die Gesamt-Kristallisationsrate, wohingegen das *Confinement* bei höheren Füllstoffgehalten zu einer Verminderung der Kristallisationsrate führt. Die erhaltenen isothermalen Kristallisationskinetik-Ergebnisse wurden darauf aufbauend mittels zweier Modelle ausgewertet, welche es erlaubten einen weiteren vertieften Einblick in die Struktur-Eigenschaftsbeziehung zu erhalten:

- Lauritzen-Hoffmann (LH) -Nukleations- und Wachstumsmodel[110, 111]
- Avrami-Gleichung

Zusammenfassend bestätigen beide Modelle die bereits beschriebenen kompetitiven Effekte, wobei hier nur kurz genauer auf die Avrami-Gleichung und den dadurch ermittelten Avrami-Index *n* eingegangen werden soll (**Gl. 13**):[107, 112, 113]

$$n = n_n + n_{gd} \qquad \textbf{Gl.13}$$

wobei n_n den Anteil am Index bezüglich Nukleation beschreibt (n_n=0 instantane Nukleation, n_n=1 sporadische Nukleation) und n_{gd} zeigt die Wachstumsdimensionalität (n_{gd} = 1 (1D Kristall), n_{gd} = 2 (Axialite, 2D) und n_{gd} = 3 (Sphärolithe, 3D)).

In **Abb. 13** wird die Abhängigkeit der Avrami-Indizes von der Kristallisationstemperatur veranschaulicht. Bei geringen Füllstoffgehalten bewegt sich der Avrami-Index aufgrund des Nukleationseffekts zunächst bei Werten zwischen 2,2 und 2,7, was der Bildung von instantan nukleierten Sphäroliten bzw. Axialiten entspricht. Durch einen ansteigenden Füllstoffanteil (75 wt%) sinkt der Avrami-Index aufgrund des zunehmenden *Confinement*-Effekts. Bei steigendem

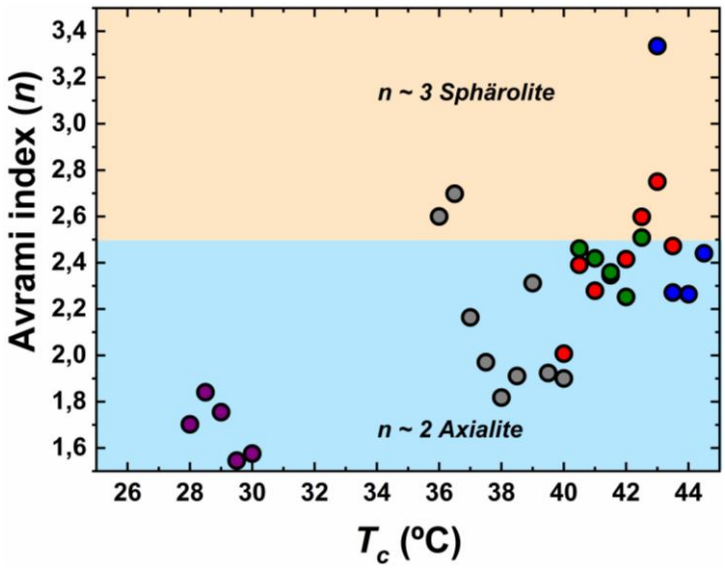

Abb. 13: Darstellung des Avrami-Index *n* gegen die Kristallisationstemperatur *Tc* bei variierenden Füllstoffanteilen (grau: reine Polmermatrix, rot: 20 wt% NaHec; blau: 40 wt% NaHec, grün: 60 wt% NaHec, lila: 75 wt% NaHec). [Christoph Habel, Jon Maiz, Jorge L. Olmedo-Martínez, Juan V. López, Josef Breu, Alejandro J. Müller; Competition between nucleation and confinement in the crystallization of poly(ethylene glycol)/ large aspect ratio hectorite composites; *Reproduced (translated) from Polymer* 2020, *202*, 122734. Copyright 2020 Elsevier Ltd.]

Einfluss des *Confinements* benötigen die Nanokomposite höhere Grade der Unterkühlung um zu kristallisieren.

Diese detaillierten Einblicke bezüglich des Einflusses von NaHec auf die Kristallisation von PEG ermöglichen die Synthese von PEG-Schichtsilikat-Nanokompositen mit maßgeschneiderter Kristallinität mit einem Füllstoff mit großem Aspektverhältnis.

Diese grundlegenden Ergebnisse sollen in aufbauenden Projekten helfen dieses System als bioabbaubare Alternative zu kommerziellen Verpackungsmaterialien zu untersuchen.

5 Literatur

1. Tagblatt, S., Zollfrank, C., **2019**, https://www.cs.tum.de/wir-muessen-einiges-veraendern (geprüft: 21.03.2021).

2. Andrady, A. L.; Neal, M. A., Applications and societal benefits of plastics. *Phil. Trans. R. Soc. B* **2009**, *364* (1526), 1977-1984.

3. Menges, G.; Haberstroh, E.; Michaeli, W.; Schmachtenberg, E., *Menges Werkstoffkunde Kunststoffe*. Carl Hanser Verlag GmbH Co KG: München, **2011**.

4. Geyer, R.; Jambeck, J. R.; Law, K. L., Production, use, and fate of all plastics ever made. *Sci. Adv.* **2017**, *3* (7), e1700782.

5. PlasticsEurope, *Daten und Fakten zu Kunststoff 2007.* Europe, P., **2008**, https://www.plasticseurope.org/de/resources/publications/218-daten-und-fakten-zu-kunststoff-2007 (geprüft: 21.03.2021).

6. PlasticsEurope, *Plastics - the facts 2017-2019: An analysis of European plastics production, demand and waste data* PlasticsEurope, **2017-2019**, https://www.plasticseurope.org/en/resources/publications (geprüft: 21.03.2021).

7. Soutis, C., Carbon fiber reinforced plastics in aircraft construction. *Mater. Sci. Eng. A* **2005**, *412* (1-2), 171-176.

8. Zhai, H.; Euler, A. Material Challenges for Lighter-Than-Air Systems in High Altitude Applications. In AIAA Meeting Paper (eISBN: 978-1-62410-067-3), AIAA 5th ATIO and 16th Lighter-Than-Air Sys Tech. and Balloon Systems Conferences, Arlington, Virgina, 26.09.2005 – 28.09.2005; American Institute of Aeronautics and Astronautics: Online, 2012; AIAA 2005-7488, 1-12.

9. Marsh, G., Composites strengthen aerospace hold. *Reinforc. Plast.* **2002**, *46* (7-8), 40-43.

10. PlasticsEurope, *Plastics-the facts 2019: An analysis of European plastics production, demand and waste data* PlasticsEurope, **2019**, https://www.plasticseurope.org/en/resources/publications (geprüft: 21.03.2021).

11. Fuhr, L.; Buschmann, R.; Freund, J., *Plastikatlas 2019: Daten und Fakten über eine Welt voller Kunststoff.* Heinrich-Böll-Stiftung; (BUND), Bund für Umwelt und Naturschutz Deutschland, **2019**, https://www.bund.net/service/publikationen/detail/publication/plastikatlas-2019/ (geprüft: 21.03.2021).

12. Jambeck, J. R.; Geyer, R.; Wilcox, C.; Siegler, T. R.; Perryman, M.; Andrady, A.; Narayan, R.; Law, K. L., Plastic waste inputs from land into the ocean. *Science* **2015**, *347* (6223), 768-771.

13. Beier, W., *Biologisch Abbaubare Kunststoffe.* Umweltbundesamt, **2009**, https://www.umweltbundesamt.de/publikationen (geprüft: 21.03.2021).

14. EuropeanBioplastics, https://www.european-bioplastics.org/bioplastics/materials/ (geprüft: 21.03.2021).

15. Burgstaller, M.; Potrykus, A.; Weißenbacher, J.; Kabasci, S.; Merrettig-Bruns, U.; Sayder, B., *Gutachten zur Behandlung biologisch abbaubarer Kunststoffe.* Bundesumweltamt, **2018**, https://www.umweltbundesamt.de/publikationen (geprüft: 21.03.2021).

16. Bagheri, A. R.; Laforsch, C.; Greiner, A.; Agarwal, S., Fate of so-called biodegradable polymers in seawater and freshwater. *Global Challenges* **2017**, *1* (4), 1700048.

17. EuropeanBioplastics, *Mythen und Fakten zu Biokunststoffen aufgeklärt.* EuropeanBioplastics, **2017**, https://www.european-bioplastics.org/mythen-und-fakten-zu-biokunststoffen-aufgeklart-german-only/ (geprüft: 21.03.2021).

18. EuropeanBioplastics, *Bioplastics Market Development Update 2019.* EuropeanBioplastics, **2019**, https://www.european-bioplastics.org/wp-content/uploads/2019/11/Report_Bioplastics-Market-Data_2019_short_version.pdf (geprüft: 21.03.2021).

19. Detzel, A.; Bodrogi, F.; Kauertz, B.; Bick, C.; Welle, F.; Schmid, M.; Schmitz, K.; Müller, K.; Käb, H., *Biobasierte Kunststoffe als Verpackung von Lebensmitteln.* Bundesministerium für Ernährung und Landwirtschaft (Auftraggeber) Fachagentur für Nachwachsende Rohstoffe (Projektträger): **2018**, https://www.ifeu.de/wp-content/uploads/Endbericht-Bio-LVp_20180612.pdf (geprüft: 21.03.2021).

20. Rhim, J.-W.; Ng, P. K., Natural biopolymer-based nanocomposite films for packaging applications. *Crit. Rev. Food Sci. and Nutr.* **2007**, *47* (4), 411-433.

21. Van Bree, I.; De Meulenaer, B.; Samapundo, S.; Vermeulen, A.; Ragaert, P.; Maes, K.; De Baets, B.; Devlieghere, F., Predicting the headspace oxygen level due to oxygen permeation across multilayer polymer packaging materials: A practical software simulation tool. *Innov. Food Sci. Emerg. Technol.* **2010**, *11* (3), 511-519.

22. Meng, L.; Zhang, Y.; Wan, X.; Li, C.; Zhang, X.; Wang, Y.; Ke, X.; Xiao, Z.; Ding, L.; Xia, R., Organic and solution-processed tandem solar cells with 17.3% efficiency. *Science* **2018**, *361* (6407), 1094-1098.

23. Bella, F.; Griffini, G.; Correa-Baena, J.-P.; Saracco, G.; Grätzel, M.; Hagfeldt, A.; Turri, S.; Gerbaldi, C., Improving efficiency and stability of perovskite solar cells with photocurable fluoropolymers. *Science* **2016**, *354* (6309), 203-206.

24. Uddin, A.; Upama, M. B.; Yi, H.; Duan, L., Encapsulation of Organic and Perovskite Solar Cells: A Review. *Coatings* **2019**, *9* (2), 65.

25. Seo, S.; Jeong, S.; Bae, C.; Park, N. G.; Shin, H., Perovskite Solar Cells with Inorganic Electron-and Hole-Transport Layers Exhibiting Long-Term (≈ 500 h) Stability at 85° C under Continuous 1 Sun Illumination in Ambient Air. *Adv. Mater.* **2018**, *30* (29), 1801010.

26. Park, M. H.; Kim, J. Y.; Han, T. H.; Kim, T. S.; Kim, H.; Lee, T. W., Flexible lamination encapsulation. *Adv. Mater.* **2015**, *27* (29), 4308-4314.

27. Kumar, R.; Auch, M.; Ou, E.; Ewald, G.; Jin, C. S., Low moisture permeation measurement through polymer substrates for organic light emitting devices. *Thin Solid Films* **2002**, *417* (1-2), 120-126.

28. Bryant, D.; Aristidou, N.; Pont, S.; Sanchez-Molina, I.; Chotchunangatchaval, T.; Wheeler, S.; Durrant, J. R.; Haque, S. A., Light and oxygen induced degradation limits the operational stability of methylammonium lead triiodide perovskite solar cells. *Energy Environ. Sci.* **2016**, *9* (5), 1655-1660.

29. Chaudhary, B.; Kulkarni, A.; Jena, A. K.; Ikegami, M.; Udagawa, Y.; Kunugita, H.; Ema, K.; Miyasaka, T., Poly (4-Vinylpyridine)-Based Interfacial

Passivation to Enhance Voltage and Moisture Stability of Lead Halide Perovskite Solar Cells. *ChemSusChem.* **2017**, *10* (11), 2473-2479.

30. Editorial, Hydrogen to the rescue. *Nat. Mater.* **2018**, *17*.

31. Society, R., Options for Producing Low-Carbon Hydrogen at Scale https://go.nature.com/2y1nHSZ (geprüft: 21.03.2021).

32. Hu, Y. H.; Zhang, L., Hydrogen storage in metal–organic frameworks. *Adv. Mater.* **2010**, *22* (20), E117-E130.

33. Assfour, B.; Leoni, S.; Seifert, G.; Baburin, I. A., Packings of carbon nanotubes–new materials for hydrogen storage. *Adv. Mater.* **2011**, *23* (10), 1237-1241.

34. Abdalla, A. M.; Hossain, S.; Nisfindy, O. B.; Azad, A. T.; Dawood, M.; Azad, A. K., Hydrogen production, storage, transportation and key challenges with applications: a review. *Energy Convers. Manag.* **2018,** *165*, 602-627.

35. Seayad, A. M.; Antonelli, D. M., Recent advances in hydrogen storage in metal-containing inorganic nanostructures and related materials. *Adv. Mater.* **2004,** *16* (9-10), 765-777.

36. Pavković, D.; Hoić, M.; Deur, J.; Petrić, J., Energy storage systems sizing study for a high-altitude wind energy application. *Energy* **2014**, *76*, 91-103.

37. Penedo, R. J.; Pardal, T. C.; Silva, P. M. S.; Fernandes, N. M.; Fernandes, T. R. C., High altitude wind energy from a hybrid lighter-than-air platform using the magnus effect. In *Airborne Wind Energy*, Springer: Heidelberg, 2013; pp 491-500.

38. d'Oliveira, F. A.; Melo, F. C. L. d.; Devezas, T. C., High-altitude platforms—Present situation and technology trends. *J. Aero. Technol. Manag.* **2016**, *8* (3), 249-262.

39. https://loon.com/press/ (geprüft: 21.03.2021).

40. Winey, K. I.; Vaia, R. A., Polymer nanocomposites. *MRS Bull.* **2007,** *32* (4), 314-322.

41. Unalan, I. U.; Cerri, G.; Marcuzzo, E.; Cozzolino, C. A.; Farris, S., Nanocomposite films and coatings using inorganic nanobuilding blocks (NBB): current applications and future opportunities in the food packaging sector. *RSC Advances* **2014**, *4* (56), 29393-29428.

42. Bhattacharya, M., Polymer nanocomposites—a comparison between carbon nanotubes, graphene, and clay as nanofillers. *Materials* **2016**, *9* (4), 262.

43. Eckert, A.; Rudolph, T.; Guo, J.; Mang, T.; Walther, A., Exceptionally Ductile and Tough Biomimetic Artificial Nacre with Gas Barrier Function. *Adv. Mater.* **2018**, *30* (32), 1802477.

44. Li, P.; White, K. L.; Lin, C.-H.; Kim, D.; Muliana, A.; Krishnamoorti, R.; Nishimura, R.; Sue, H.-j., Mechanical Reinforcement of Epoxy with Self-Assembled Synthetic Clay in Smectic Order. *ACS Appl. Mater. Interfaces.* **2014**, *6* (13), 10188-10195.

45. Ziadeh, M.; Weiss, S.; Fischer, B.; Förster, S.; Altstädt, V.; Müller, A. H.; Breu, J., Towards completely miscible PMMA nanocomposites reinforced by shear-stiff, nano-mica. *J. Colloid Interface Sci.* **2014**, *425*, 143-151.

46. Laufer, G.; Kirkland, C.; Cain, A. A.; Grunlan, J. C., Clay–chitosan nanobrick walls: completely renewable gas barrier and flame-retardant nanocoatings. *ACS Appl. Mater. Interfaces* **2012**, *4* (3), 1643-1649.

47. Edenharter, A.; Feicht, P.; Diar-Bakerly, B.; Beyer, G.; Breu, J., Superior flame retardant by combining high aspect ratio layered double hydroxide and graphene oxide. *Polymer* **2016**, *91*, 41-49.

48. Kunz, D. A.; Schmid, J.; Feicht, P.; Erath, J.; Fery, A.; Breu, J., Clay-based nanocomposite coating for flexible optoelectronics applying commercial polymers. *ACS nano* **2013**, *7* (5), 4275-4280.

49. Möller, M. W.; Kunz, D. A.; Lunkenbein, T.; Sommer, S.; Nennemann, A.; Breu, J., UV-Cured, Flexible, and Transparent Nanocomposite Coating with Remarkable Oxygen Barrier. *Adv. Mater.* **2012**, *24* (16), 2142-2147.

50. Priolo, M. A.; Holder, K. M.; Greenlee, S. M.; Grunlan, J. C., Transparency, Gas Barrier, and Moisture Resistance of Large-Aspect- Ratio Vermiculite Nanobrick Wall Thin Films. *ACS Appl. Mater. Interfaces.* **2012**, *4* (10), 5529-5533.

51. Okada, A.; Usuki, A., Twenty years of polymer-clay nanocomposites. *Macromolecular Materials and Engineering* **2006**, *292* (2), 220-220.

52. Fischer, B., Mikromechanische Wirkungsweise von Schichtsilikaten der zweiten Generation: ein neuartiger Nanofüllstoff zur Steigerung der Steifigkeit und Zähigkeit von PMMA. Universität Bayreuth, Bayreuth, **2018**.

53. Sattler, K., Polyethen-Schichtsilicat-Nanokomposite mit synthetischen Hectoriten In situ Polymerisation mittels geträgerter Metallocenkatalysatoren Doktorarbeit, Universität Bayreuth, Bayreuth, **2008**.

54. Lagaly, G.; Köster, H., *Tone und Tonminerale*. Steinkopff Verlag: Darmstadt, **1993**.

55. Stöter, M.; Kunz, D. A.; Schmidt, M.; Hirsemann, D.; Kalo, H.; Putz, B.; Senker, J.; Breu, J., Nanoplatelets of Sodium Hectorite Showing Aspect Ratios of≈ 20 000 and Superior Purity. *Langmuir* **2013**, *29* (4), 1280-1285.

56. Stöter, M.; Rosenfeldt, S.; Breu, J., Tunable exfoliation of synthetic clays. *Annu. Rev. Mater. Res.* **2015**, *45*, 129-151.

57. Ferrage, E.; Lanson, B.; Sakharov, B. A.; Geoffroy, N.; Jacquot, E.; Drits, V. A., Investigation of dioctahedral smectite hydration properties by modeling of X-ray diffraction profiles: Influence of layer charge and charge location. *Am. Mineral.* **2007**, *92* (10), 1731-1743.

58. Choudalakis, G.; Gotsis, A. D., Permeability of polymer / clay nanocomposites : A review. *Eur. Polym. J.* **2009**, *45* (4), 967-984.

59. Cussler, E.; Hughes, S. E.; Ward III, W. J.; Aris, R., Barrier membranes. *J. Membr. Sci.* **1988**, *38* (2), 161-174.

60. Cao, T.; Fasulo, P. D.; Rodgers, W. R., Investigation of the shear stress effect on montmorillonite platelet aspect ratio by atomic force microscopy. *Appl. Clay Sci.* **2010**, *49* (1-2), 21-28.

61. Daab, M., Quantitative Delaminierung zur Herstellung von Nanoschichten Struktur-inhärenter Dicke. Universität Bayreuth, Bayreuth, **2018**.

62. Liu, Y.; Xu, Z.; Gao, W.; Cheng, Z.; Gao, C., Graphene and other 2D colloids: liquid crystals and macroscopic fibers. *Adv. Mater.* **2017**, *29* (14), 1606794.

63. Davidson, P.; Penisson, C.; Constantin, D.; Gabriel, J.-C. P., Isotropic, nematic, and lamellar phases in colloidal suspensions of nanosheets. *Proc. Natl. Acad. Sci.* **2018**, *115* (26), 6662-6667.

64. Gabriel, J.-C. P.; Camerel, F.; Lemaire, B. J.; Desvaux, H.; Davidson, P.; Batail, P., Swollen liquid-crystalline lamellar phase based on extended solid-like sheets. *Nature* **2001**, *413* (6855), 504-508.

65. Wang, L.; Sasaki, T., Titanium oxide nanosheets: graphene analogues with versatile functionalities. *Chem. Rev.* **2014**, *114* (19), 9455-9486.

66. Rosenfeldt, S.; Stöter, M.; Schlenk, M.; Martin, T.; Albuquerque, R. Q.; Förster, S.; Breu, J., In-Depth Insights into the Key Steps of Delamination of Charged 2D Nanomaterials. *Langmuir* **2016**, *32* (41), 10582-10588.

67. Kunz, D. A.; Erath, J.; Kluge, D.; Thurn, H.; Putz, B.; Fery, A.; Breu, J., In-plane modulus of singular 2: 1 clay lamellae applying a simple wrinkling technique. *ACS Appl. Mater. Inter.* **2013**, *5* (12), 5851-5855.

68. Cui, Y.; Kumar, S.; Kona, B. R.; van Houcke, D., Gas barrier properties of polymer/clay nanocomposites. *RSC Advances* **2015**, *5* (78), 63669-63690.

69. Guo, F.; Aryana, S.; Han, Y.; Jiao, Y., A review of the synthesis and applications of polymer–nanoclay composites. *Appl. Sci.* **2018**, *8* (9), 1696.

70. Armentano, I.; Puglia, D.; Luzi, F.; Arciola, C. R.; Morena, F.; Martino, S.; Torre, L., Nanocomposites based on biodegradable polymers. *Materials* **2018**, *11* (5), 795-821.

71. Vasile, C., Polymeric nanocomposites and nanocoatings for food packaging: A review. *Materials* **2018**, *11* (10), 1834-1882.

72. Ziadeh, M., Towards Mechanical Reinforcement in Polymer Layered Silicates Nanocomposites of the Second Generation. University of Bayreuth, Bayreuth, **2014**.

73. Ratna, D.; Manoj, N. R.; Varley, R.; Singh Raman, R. K.; Simon, G. P., Clay-reinforced epoxy nanocomposites. *Polym. Int.* **2003**, *52* (9), 1403-1407.

74. Habibi, M.; Rahimzadeh, A.; Bennouna, I.; Eslamian, M., Defect-free large-area (25 cm2) light absorbing perovskite thin films made by spray coating. *Coatings* **2017**, *7* (3), 42.

75. Song, Y.; Gerringer, J.; Qin, S.; Grunlan, J. C., High oxygen barrier thin film from aqueous polymer/clay slurry. *Ind. Eng. Chem. Res.* **2018**, *57* (20), 6904-6909.

76. Tsurko, E. S.; Feicht, P.; Habel, C.; Schilling, T.; Daab, M.; Rosenfeldt, S.; Breu, J., Can high oxygen and water vapor barrier nanocomposite coatings be obtained with a waterborne formulation? *J. Membr. Sci.* **2017**, *540*, 212-218.

77. Tsurko, E. S.; Feicht, P.; Nehm, F.; Ament, K.; Rosenfeldt, S.; Pietsch, I.; Roschmann, K.; Kalo, H.; Breu, J., Large Scale Self-Assembly of Smectic Nanocomposite Films by Doctor Blading versus Spray Coating: Impact of Crystal Quality on Barrier Properties. *Macromolecules* **2017,** *50* (11), 4344-4350.

78. Stannett, V., The transport of gases in synthetic polymeric membranes—an historic perspective. *J. Membr. Sci.* **1978**, *3* (2), 97-115.

79. Siracusa, V., Food packaging permeability behaviour: A report. *Int. J. Polym. Sci.* **2012**, *2012* (https://doi.org/10.1155/2012/302029).

80. McKeen, L. W., *Permeability properties of plastics and elastomers Third Edition*. William Andrew Elsevier: **2012**.

81. Kunz, D. A., Schichtsilicate als effiziente Bausteine für funktionelle Nanokomposite. Universität Bayreuth, Bayreuth, **2013**.

82. Roberts, A.; Henry, B.; Sutton, A.; Grovenor, C.; Briggs, G.; Miyamoto, T.; Kano, M.; Tsukahara, Y.; Yanaka, M., Gas permeation in silicon-oxide/polymer (SiOx/PET) barrier films: role of the oxide lattice, nano-defects and macro-defects. *J. Membr. Sci.* **2002**, *208* (1-2), 75-88.

83. Maes, C.; Luyten, W.; Herremans, G.; Peeters, R.; Carleer, R.; Buntinx, M., Recent updates on the barrier properties of ethylene vinyl alcohol copolymer (EVOH): A review. *Polym. Rev.* **2018**, *58* (2), 209-246.

84. Nielsen, L. E., Models for the permeability of filled polymer systems. *J. Macromol. Sci. A* **1967**, *1* (5), 929-942.

85. mocon®, *OX-TRAN® Model 2/21 10x Modular System Operator's Manual: Revision A.*

86. GmbH, Brugger Feinmechanik, https://www.brugger-feinmechanik.com/de/produkte/permeationspruefung/gtt-gas-transmissions-tester/ (geprüft: 21.03.2021).

87. GmbH, Sempa Systems.; Fraunhofer IWS, HiBarSens 2.0 Making ultra-high barriermeasurements even better. http://www.hibarsens.com/wa_files/2402_20Datenblatt_20HiBarSens_20280218.pdf (geprüft: 21.03.2021).

88. GmbH, Sempa Systems, HiBarSens®PreConCellsMeasuring ultra barriers within hours. http://www.hibarsens.com/wa_files/2405_20Datenblatt_20PreConCells_20280218.pdf (geprüft: 21.03.2021).

89. Doblhofer, E.; Schmid, J.; Rieß, M.; Daab, M.; Suntinger, M.; Habel, C.; Bargel, H.; Hugenschmidt, C.; Rosenfeldt, S.; Breu, J., Structural Insights into Water-Based Spider Silk Protein–Nanoclay Composites with Excellent Gas and Water Vapor Barrier Properties. *ACS Appl. Mater. Interfaces* **2016**, *8* (38), 25535-25543.

90. Agarwal, S.; Burgard, M.; Greiner, A.; Wendorff, J., *Electrospinning: A Practical guide to nanofibers*. Walter de Gruyter GmbH & Co KG: Berlin/Boston, **2016**.

91. Bergmair, J.; Washüttl, M.; Wepner, B., *Prüfpraxis für Kunststoffverpackungen: Lebensmittel-, Pharma-und Kosmetikverpackungen*. Behr's Verlag DE: Hamburg, **2012**.

92. Jamshidian, M.; Tehrany, E. A.; Imran, M.; Jacquot, M.; Desobry, S., Poly-Lactic Acid: production, applications, nanocomposites, and release studies. *Compr. Rev. Food Sci. Food Saf.* **2010**, *9* (5), 552-571.

93. Auras, R., *Poly (lactic acid)*. Wiley Online Library: Hoboken, New Jersey, USA, **2010**.

94. Gupta, B.; Revagade, N.; Hilborn, J., Poly (lactic acid) fiber: an overview. *Progr. Pol. Sci.* **2007**, *32* (4), 455-482.

95. Liang, X.; King, D. M.; Groner, M. D.; Blackson, J. H.; Harris, J. D.; George, S. M.; Weimer, A. W., Barrier properties of polymer/alumina nanocomposite membranes fabricated by atomic layer deposition. *J. Membr. Sci.* **2008**, *322* (1), 105-112.

96. Murray, B. R.; Leen, S. B.; Semprimoschnig, C. O.; Brádaigh, C. M. Ó., Helium permeability of polymer materials as liners for composite overwrapped pressure vessels. *J. Appl. Polym. Sci.* **2016**, *133* (29), 43675.

97. Kezirian, M.; Johnson, K.; Phoenix, S. Composite Overwrapped Pressure Vessels (COPV): Flight Rationale for the Space Shuttle Program. In AIAA SPACE Forum (eISBN: 978-1-60086-953-2), AIAA SPACE 2011 Conference & Exposition, Long Beach, California, 27.09.2011 – 29.09.2011; American Institute of Aeronautics and Astronautics: Online, **2012**, AIAA 2011-7363, 1-12.

98. Barth, R. R.; Simmons, K. L.; San Marchi, C., Polymers for hydrogen infrastructure and vehicle fuel systems. *Sandia Report* **2013,** *SAND2013-8904*.

99. Mo, C.; Yuan, W.; Lei, W.; Shijiu, Y., Effects of temperature and humidity on the barrier properties of biaxially-oriented polypropylene and polyvinyl alcohol films. *J. Appl. Packag. Res.* **2014**, *6* (1), 40-46.

100. Grunlan, J. C.; Grigorian, A.; Hamilton, C. B.; Mehrabi, A. R., Effect of clay concentration on the oxygen permeability and optical properties of a modified poly (vinyl alcohol). *Journal of Applied Polymer Science* **2004,** *93* (3), 1102-1109.

101. Robertson, G. L., *Food packaging: principles and practice*. CRC press (Taylor and Francis group): Boca Raton, London, New York, **2013**.

102. EVAL Europe N.V., http://www.evalevoh.com/en/eval-properties/barrier-to-oxygen/relative-humidity.aspx (geprüft: 21.03.2021).

103. Wang, J.; Gardner, D. J.; Stark, N. M.; Bousfield, D. W.; Tajvidi, M.; Cai, Z. Moisture and Oxygen Barrier Properties of Cellulose Nanomaterial-Based Films. *ACS Sustain. Chem. Eng.* **2017**, *6* (1), 49-70

104. Muramatsu, M.; Okura, M.; Kuboyama, K.; Ougizawa, T.; Yamamoto, T.; Nishihara, Y.; Saito, Y.; Ito, K.; Hirata, K.; Kobayashi, Y., Oxygen permeability and free volume hole size in ethylene–vinyl alcohol copolymer film: temperature and humidity dependence. *Radiat. Phys. Chem.* **2003**, *68*, 561-564.

105. Eckert, A.; Abbasi, M.; Mang, T.; Saalwächter, K.; Walther, A., Structure, Mechanical Properties, and Dynamics of Polyethylenoxide/Nanoclay Nacre-Mimetic Nanocomposites. *Macromolecules* **2020**, *53* (5), 1716-1725.

106. Wang, Z.; Rolle, K.; Schilling, T.; Hummel, P.; Philipp, A.; Kopera, B. A.; Lechner, A. M.; Retsch, M.; Breu, J.; Fytas, G., Tunable thermoelastic anisotropy in hybrid Bragg stacks with extreme polymer confinement. *Angew. Chem.* **2020**, *132* (3), 1302-1310.

107. Michell, R. M.; Mueller, A. J., Confined crystallization of polymeric materials. *Prog. Polym. Sci.* **2016**, *54*, 183-213.

108. Arias-Trujillo, J.; Matías-Sanchez, A.; Cantero, B.; López-Querol, S., Effect of polymer emulsion on the bearing capacity of aeolian sand under extreme confinement conditions. *Constr. Build. Mater.* **2020**, *236*, 117473.

109. Müller, A. J.; Arnal, M. L.; Trujillo, M.; Lorenzo, A. T., Super-nucleation in nanocomposites and confinement effects on the crystallizable components within

block copolymers, miktoarm star copolymers and nanocomposites. *Eur. Polym. J.* **2011**, *47* (4), 614-629.

110. Lorenzo, A. T.; Müller, A. J.; Lin, M.-C.; Chen, H.-L.; Jeng, U.-S.; Priftis, D.; Pitsikalis, M.; Hadjichristidis, N., Influence of macromolecular architecture on the crystallization of (PCL2)-b-(PS2) 4-miktoarm star block copolymers in comparison to linear PCL-b-PS diblock copolymer analogues. *Macromolecules* **2009**, *42* (21), 8353-8364.

111. Trujillo, M.; Arnal, M. L.; Müller, A. J.; Mujica, M. A.; de Navarro, C. U.; Ruelle, B.; Dubois, P., Supernucleation and crystallization regime change provoked by MWNT addition to poly (ε-caprolactone). *Polymer* **2012**, *53* (3), 832-841.

112. Michell, R. M.; Blaszczyk-Lezak, I.; Mijangos, C.; Mueller, A. J., Confinement effects on polymer crystallization: From droplets to alumina nanopores. *Polymer* **2013**, *54* (16), 4059-4077.

113. Müller, A. J.; Balsamo, V.; Arnal, M. L., Nucleation and crystallization in diblock and triblock copolymers. In *Block Copolymers II*, Springer: **2005**; pp 1-63.

6. Ergebnisse

6.1 *Electrospinning* und Filtration als kombiniertes Verfahren zur Herstellung von Nanokompositen

Jian Zhu†, Christoph Habel†, Theresa Schilling, Andreas Greiner*, Josef Breu*, Seema Agarwal*

† J.Z. und C.H.: zu gleichen Teilen beigetragen (*equally contributed*).

Filter-Through Method of Making Highly Efficient Polymer-Clay Nanocomposite Membranes

Macromol. Mater. Eng. **2019**, *304* (7), 1800779.

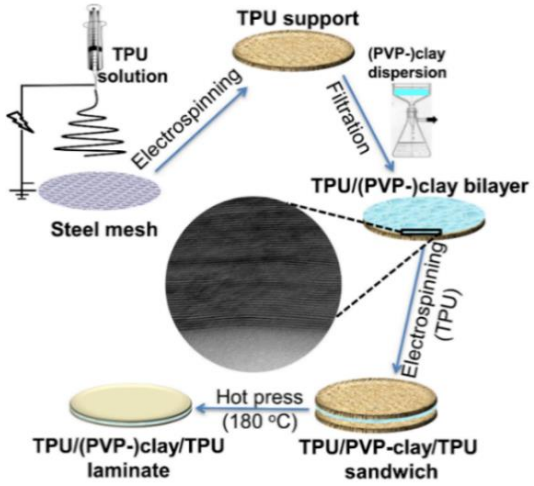

https://doi.org/10.1002/mame.201800779

Bayerisches Polymer Institut und Fakultät für Chemie, Universität Bayreuth, Universitätsstraße 30, Bayreuth, 95447, Germany

*E-Mail: agarwal@uni-bayreuth.de, greiner@uni-bayreuth.de, josef.breu@uni-bayreuth.de

Darstellung des Eigenanteils: Das Konzept der Publikation von experimenteller Seite wurde zusammen mit *Dr. J. Zhu, Prof. Dr. S. Agarwal*, *Prof. Dr. J. Breu*, und *Prof. Dr. A. Greiner,* von mir erarbeitet. Die Experimente und Messungen wurden von *Dr. J. Zhu* und mir durchgeführt. *T. Schilling* hat die Schichtsilikat-Dispersionen hergestellt. Die Publikation wurde hauptsächlich von mir und *Dr. J. Zhu* verfasst und mit *Prof. Dr. S. Agarwal*, *Prof. Dr. J. Breu*, und *Prof. Dr. A. Greiner* zur Einreichung überarbeitet. Mein Eigenanteil beträgt ca. 45%.

FULL PAPER

Polymer-Clay Nanocomposites

Macromolecular Materials and Engineering
www.mme-journal.de

Filter-Through Method of Making Highly Efficient Polymer-Clay Nanocomposite Membranes

Jian Zhu, Christoph Habel, Theresa Schilling, Andreas Greiner, Josef Breu,* and Seema Agarwal**

Electrospun filter with hierarchical pore structure and variable pore diameter is used for the first time in making a flexible, strong, and high gas-barrier membrane. A versatile, technical, benign processing method for the fabrication of highly filled (>25 wt%) efficient gas-barrier polymer membrane with perfectly aligned synthetic high-aspect ratio layered silicate (clay) of variable and considerable thickness (up to 5 µm) is presented. This process combines advantageous features of an electrospun substrate like high porosity, variable pore size (typically <5 µm), thermoplasticity and of an aqueous suspension of a synthetic clay consisting of single 1 nm thick layers with a huge median lateral extension (>10 µm) in a layered structure. By simple and fast filtration, a gas-barrier self-assembled layer of variable and appropriate thickness is obtained on a mechanically stable thermoplastic electrospun filter support that subsequently can be laminated adhesively or via hot pressing, even in a multilayer structure, if required. The resulting composite membranes are flexible, strong, transparent, and show enhanced gas-barrier properties.

1. Introduction

Electrospun porous thermoplastic membranes have been extensively studied and used as air (high efficiency particulate air [HEPA], ultra-low particulate air [ULPA]) and for bacterial filtration.[1–3] The hierarchical porous structure with small and variable pore size and high specific surface area provides efficient filtration. The focus of such studies was purification of air and water by removing particulate living and nonliving impurities. To the best of our knowledge, we show a novel aspect of particulate filtration through electrospun thermoplastic porous membranes for the first time in making flexible, strong polymer membranes with enhanced gas-barrier properties. The novelty is based on the high-aspect ratio delaminated melt synthesized layered silicate (clay)[4] that is self-assembled in a polymer matrix as a barrier-layer between two electrospun membranes by filtration (filter-through method) and subsequently hot-pressed[5] which leads to enhanced gas-barrier properties.

Nanosheets of layered materials like clay (e.g., Na-hectorite [Hec]),[6–9] or graphene oxide (GO)[10,11] are the most promising fillers for the fabrication of polymer nanocomposite barrier coatings.[12–16] Barrier is of prime importance in applications spanning from automotive, furniture, construction, food, or optoelectronic packaging.[13,14,17–19] According to Cussler, the barrier improvement factor is nonlinearly dependent on both aspect ratio and filler content. Consequently, it is most efficient and material-saving to apply fillers with the highest aspect ratio accessible and at the maximum filler level that can be processed.[20] Melt synthesized hectorites come in diameters of up to 20 µm and moreover can be utterly delaminated into 1 nm thick nanosheets by repulsive osmotic swelling simply by immersing them into water.[4,21–23] The suspensions obtained represent viscous liquid crystalline (nematic) phases because the huge aspect ratio blocks isotropic rotation.[24–26] The nematic phases can, however, easily be mixed with water-soluble polymers without triggering any reaggregation. As a consequence of the nematic character only dilute polymer/clay suspensions can be applied for coatings. The final filler content of the dried coating is determined by the polymer/clay ratio. Removal of large amounts (>95 vol%) of the dispersion medium (here water), represents a serious challenge. In particular, if the coating is applied on an impermeable substrate, typically a polyethylene terephthalate (PET) foil, evaporation can only occur at the suspension/air interface while concomitantly both filler and polymer are increasingly concentrated. Consequently, a steadily improving barrier to further evaporation is building up with time.

These drying obstacles limit the coating thickness that can be obtained in one coating step to less than 2 µm and the drying moreover has to be conducted very carefully at moderate temperatures (<80 °C) and slowly (typically >48 h). Otherwise suspension medium is getting trapped in the barrier coating

J. Zhu, Prof. A. Greiner, Prof. S. Agarwal
Macromolecular Chemistry II
Bavarian Polymer Institute and Bayreuth Center for Colloids and Interfaces
University of Bayreuth
Universitätsstraße 30, Bayreuth 95447, Germany
E-mail: greiner@uni-bayreuth.de; agarwal@uni-bayreuth.de
C. Habel, T. Schilling, Prof. J. Breu
Bavarian Polymer Institute and Department of Inorganic Chemistry
University of Bayreuth
Universitätsstraße 30, Bayreuth 95447, Germany
E-mail: Josef.Breu@uni-bayreuth.de
The ORCID identification number(s) for the author(s) of this article can be found under https://doi.org/10.1002/mame.201800779.

DOI: 10.1002/mame.201800779

ADVANCED SCIENCE NEWS
www.advancedsciencenews.com

Macromolecular Materials and Engineering
www.mme-journal.de

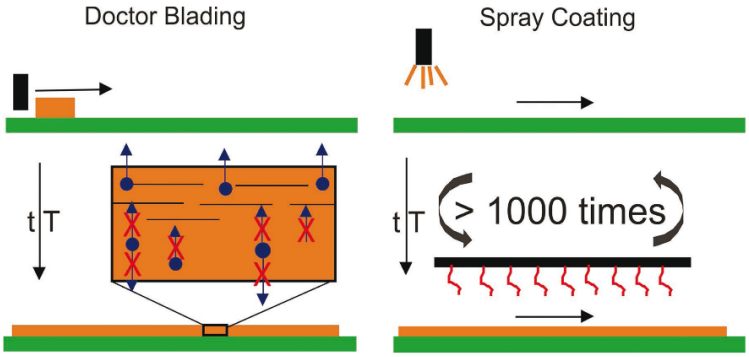

Scheme 1. Disadvantages of the two main state-of-the art solution based processing techniques. Doctor blading suffers of the self-sealing effect that potentially traps suspension medium if not dried slowly at moderate temperatures. Spray coating of multiple layers can be automated but nevertheless is time consuming for coatings of appreciable thickness.

and will eventually trigger blistering that completely ruins barrier.[27] Alternatively, coatings can be applied by spraying multiple layers with intermediate drying of individual applications. Both processing methods yield polymer/clay nanocomposite coatings showing (ultra-) high gas barriers.[13,14,17,18,27]

Moreover, the compatibility between the coating dispersion and the substrate is critical.[28,29] In particular with doctor blading the wettability often poses a problem that requires a primer or additives.[16] In summary, both doctor blading and spray coating represent rather time-consuming processing methods (**Scheme 1**) retarding mass production and widespread application in particular in low margin (commodity) applications like food packaging.

Here we present a new simple and upscalable, technical benign processing method to fabricate clay self-assembled coatings via filtration of the clay aqueous dispersion on an electrospun, thermoplastic nonwoven support **Scheme 2**, step (1). Electrospinning is a simple and robust processing technique to produce fibers with adjustable diameters that can be deposited to form porous, nonwoven supports.[30–32] Fabrication of infinite tracks with areas up to 2000 m^2 day^{-1} represents no problem.[33,34] The porosity of the nonwoven substrate can be tuned to optimize filtration efficiency. Wetting of the porous support represents no problem. The dispersion medium is removed concomitantly by evaporation at the top and filtration at the bottom reducing the drying time drastically (Scheme 2, Step (2)).

While in principle any polymer that can be electrospun may be considered as porous support,[35] here we chose thermoplastic polyurethane (TPU). TPU shows good chemical resistance, abrasion resistance, high elasticity, and great shock absorption. TPU films and coatings are applied in various fields, like automotive, furniture, and construction.[36–39] For food packaging, however, the stiffness and strength and the gas permeability properties of TPU have to be improved. This is achieved by applying a polyvinylpyrrolidone (PVP)-Hec barrier sandwich layer between the TPU membranes.

For reasons of simplicity we here laminate with a second electrospun TPU nonwoven (Scheme 2, Step (3)). The thermoplastic nature of TPU allows lamination of the porous TPU/PVP-Hec sandwich by hot pressing which concomitantly densifies the TPU (Scheme 2, Step (4)).

2. Results and Discussion

2.1. Processing Route

Electrospinning of a TPU solution provides fibrous nonwoven supports by random deposition of fibers with an average fiber diameter of 840 nm (**Figure 1**a). The pore diameter is in the range of 0.5–3.5 µm with maximum pore diameters being around 2.4 µm (Figure 1b) which is considerably smaller than the typical diameter of Hec nanosheets (≈20 µm) (Figure S1, Supporting Information).[4]

The porosity of the TPU support is ≈66%, which makes TPU electrospun support an excellent candidate for coating with PVP-Hec nanocomposites via filtration. Because of the huge aspect ratio of Hec nanosheets (20 000) upon filtration through the pores of the nonwoven TPU support they self-assemble perfectly aligned (textured) to the surface of the support. The sample after filtration is designated as bilayer TPU/PVP-Hec. The PVP fills the gaps between the individual Hec nanosheets. The large absolute diameter of the Hec nanosheets is prerequisite to this coating process. Natural montmorillonite[40] (diameter <0.3 µm) passes almost completely through the filter and no homogenous continuous layer is built (Figure S2, Supporting Information).

Contrary to montmorillonite, with large aspect ratio Hec a homogeneous

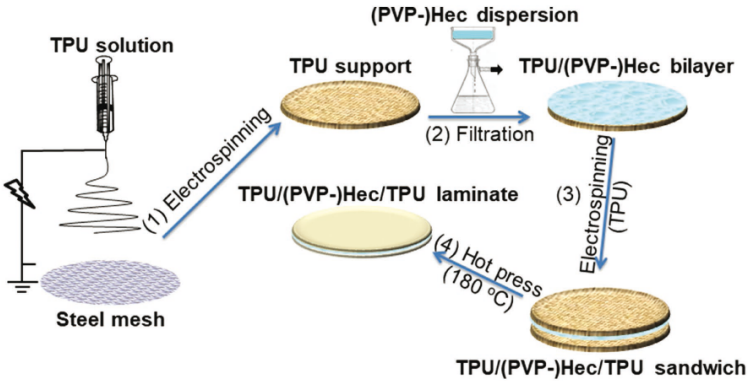

Scheme 2. Fabrication procedure of TPU/PVP-Hec/TPU laminates.

ADVANCED SCIENCE NEWS
www.advancedsciencenews.com

Macromolecular Materials and Engineering
www.mme-journal.de

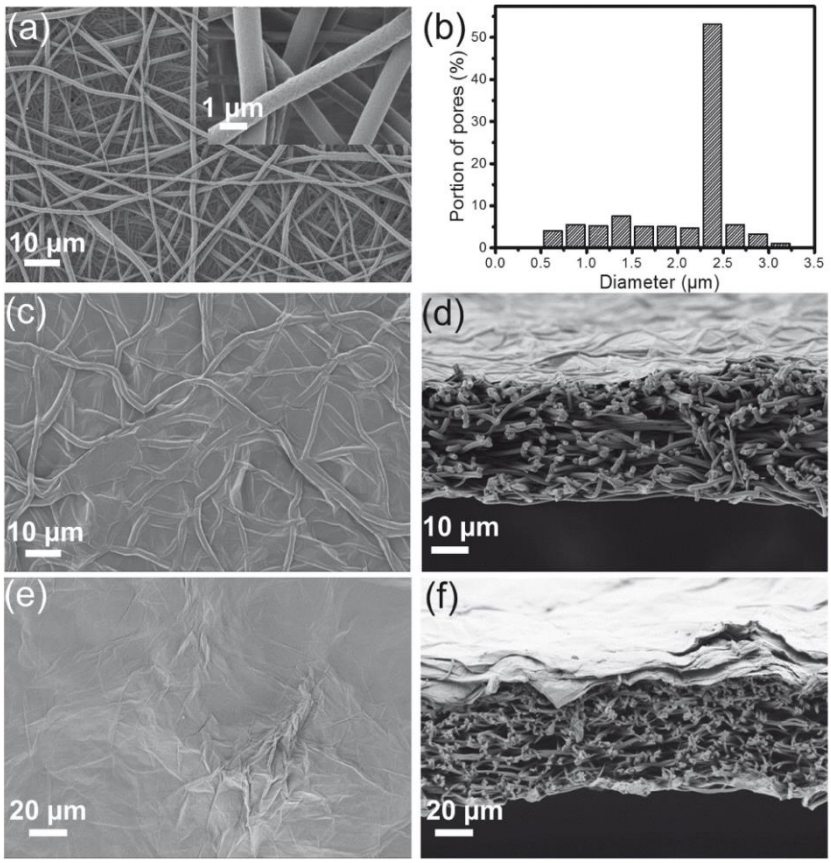

Figure 1. a) Scanning electron microscope (SEM) images and b) pore size distribution of the electrospun TPU support. Dependency of the surface roughness and coating thickness on the Hec content in the filtration suspension (2 mg) c,d) and 65 mg e,f) per 100 mL water, respectively.

deposition of the clay nanosheets on the surface of the TPU support is observed (Figure 1c–f). For fabrication of barrier coatings, suspensions having different amounts of PVP-Hec (constant ratio of PVP:Hec/40:60 wt%) were coated on the porous TPU support by filtration. Even low amounts of Hec (as low as 2 mg 100 mL^{-1} in the filtration dispersion) provide a compact and uniform layer of the Hec nanosheets on the TPU fibrous supports (Figure 1c). The PVP fills the gaps between the individual Hec nanosheets. The surface of the nanocomposite coating becomes smoother with increasing amount of PVP-Hec in the dispersion filtered on the TPU support (Figure S3, Supporting Information).

SEM micrographs of cross sections of the TPU/PVP-Hec bilayer indicate a thickness of the PVP-Hec coatings in the range of around 60 to 5000 nm for the samples prepared by filtration of suspensions with Hec concentrations, 2 to 65 mg 100 mL^{-1} suspensions, respectively (Figure 1d,f). Clearly, the thickness of the PVP-Hec nanocomposite coating can be adjusted over a wide range by varying the amount of Hec in the suspension deposited on the porous TPU support (Figure S4, Supporting Information). The thickness of the PVP-Hec layer changes little during the hot press process (**Figure 2**a,b).

The PVP-Hec nanocomposite coatings supported on TPU non-woven obtained by filtration can subsequently be laminated. For simplicity and as a proof of principle we here laminated with a second nonwoven TPU layer. For this, a second TPU non-woven is casted onto the bilayer via electrospinning. Subsequently the sandwich is laminated by hot pressing at 180 °C for 10 min. This sandwich-like structure could be obtained with almost any other second polymer film. This will allow fabricating barrier membranes meeting mechanical and gas-barrier property requirements in various fields of application. In this proof of principle, the second outer-layer is also TPU. The PVP-Hec nanocomposite coating is opaque due to a certain surface roughness of the highly filled composite resulting in surface scattering. Consequently, after lamination via hot pressing a transparent nanocomposite membrane is obtained (Figure 2c,d). The transmittance was found to be in the range of 60–80% while the thickness of the PVP-Hec coating had a negligible influence on the transmittance (Figure 2e; Table S1, Supporting Information). The dense three-layer laminates obtained

ADVANCED SCIENCE NEWS
www.advancedsciencenews.com

Macromolecular Materials and Engineering
www.mme-journal.de

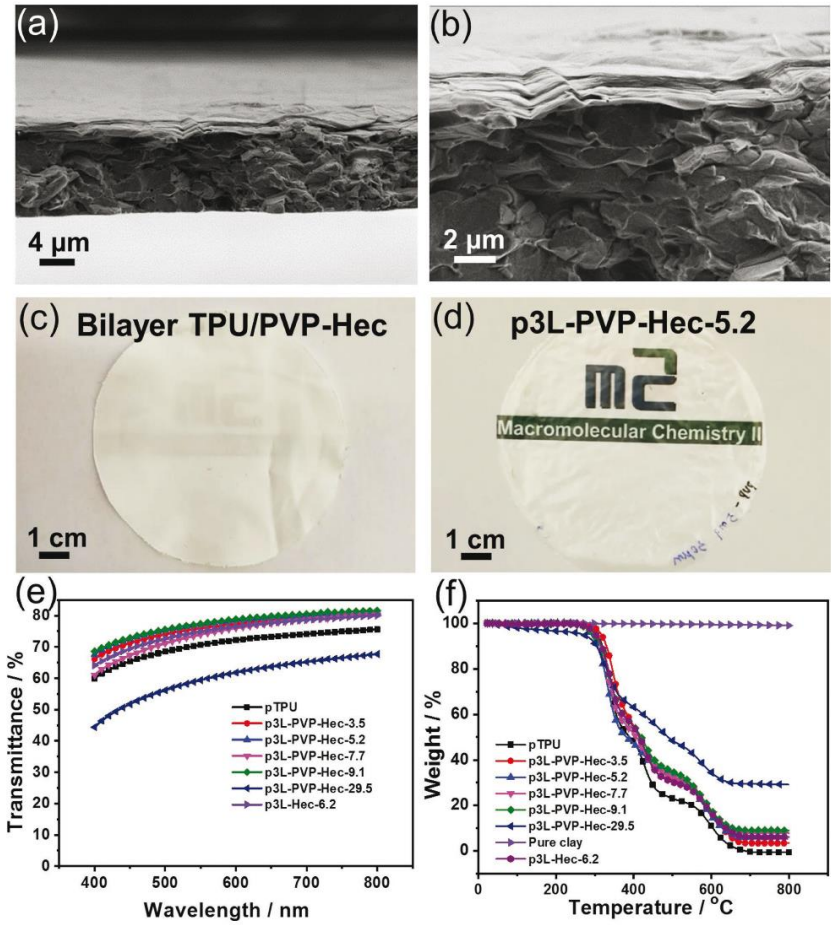

Figure 2. a) and b) show SEM pictures of cross section of bilayer-TPU/PVP-Hec after hot pressing (sample from 20 mg per 100 mL suspension). c) is the photo of TPU/PVP-Hec membrane before hot pressing and d) is the photo of final laminate after hot pressing. e) The transmittances of the final laminate between the wavelengths of 400–800 nm. f) Thermogravimetric analysis (TGA) curves of TPU and composite membrane.

after hot pressing are referred to as p3L-PVP-Hec-X where X gives the Hec content (wt%) in the resulting laminate. The three-layer laminates with Hec content from 3.5 to 29.5 wt% were obtained (Figure 2f; Table S1, Supporting Information).

2.2. Crystallinity of PVP-Hec Coatings

The Hec and PVP-Hec coatings obtained via filtration represent smectic crystals as evidenced by X-ray diffraction (XRD). The neat electrospun TPU support (Scheme 2, after Step (1)) shows an amorphous halo centered at $2\theta = 20°$ (**Figure 3**a). With pure Hec coatings a sharp diffraction peak was observed at $2\theta_{001} = 7.23°$ (Figure 3a) which corresponds to mono-hydrated sodium cations in the interlayer space with a typical d-spacing of 1.22 nm.[41] PVP-Hec dispersions filtrated on a nonwoven TPU layer showed a sharp and rational *001*-series with the *001* diffraction peak being observed at $2\theta_{001} = 3.96°$. This corresponds to a d-spacing of 2.26 nm (Figure 3a, Scheme 2 after Step (2)) and indicates that in the nanocomposite coating adjacent Hec nanosheets (0.96 nm) are separated by equivalent volumes (1.3 nm) of PVP.

The rational *001*-series with sharp peaks indicates a well ordered smectic crystallinity of the PVP-Hec coatings with translational homogeneity of the nanocomposite. The nearly perfect order of equidistantly arranged Hec nanosheets is furthermore not affected by the final hot pressing step as shown in the transmission electron microscopy (TEM) image of the cross section (Figure 3b).

2.3. Mechanical Properties

Even a pure clay coating sandwiched between two TPU layers (p3L-Hec-6.2) already increased the modulus dramatically without affecting the tensile stress at break significantly as compared to neat hot-pressed TPU support (pTPU) (Table S2,

ADVANCED SCIENCE NEWS
www.advancedsciencenews.com

Macromolecular Materials and Engineering
www.mme-journal.de

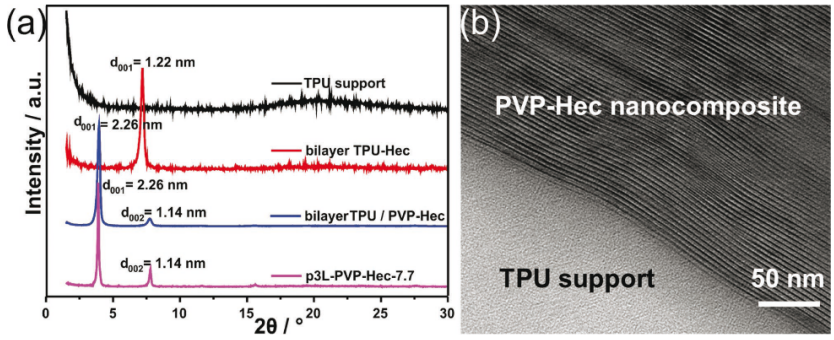

Figure 3. a) XRD patterns of the neat pressed TPU support, Hec coating (bilayer TPU-Hec), and PVP-Hec coating on the TPU support (bilayer TPU/PVP-Hec) and the final hot-pressed laminate after the hot pressing (p3L-PVP-Hec-7.7); b) TEM image of the alignment of the clay nanoplatelets in the interlayer PVP-Hec nanocomposite (p3L-PVP-Hec-9.1).

Supporting Information; **Figure** 4a). Nevertheless, by comparison of pure Hec coatings with PVP-Hec coatings of comparable amount of Hec, it can be seen that the elasticity modulus (E-Modulus) is sigificantely higher. With increasing Hec content in the laminates, the tensile modulus increases by up to a factor of >60 as compared to the neat TPU (17 MPa). With 29.5 wt% of Hec an E-Modulus of 1117 MPa was observed (p3L-PVP-Hec-29.5, Figure 4a). More interestingly, with a polymer matrix separating the adjacent clay nanosheets, the laminates are significantely less brittle than for pure Hec coatings. Without any polymer matrix (p3L-Hec-6.2), there is a huge reduction of the strain at break of about 40% (from 564% to 351%) as compared to the neat TPU matrix (pTPU). For p3L-PVP-Hec-9.1, using PVP-Hec, this is lowered to a 15% reduction.

Furthermore, this modulus is even much higher than other TPU-clay nanocomposites mentioned in literature with comparable clay contents, like TPU/laponite, TPU/dopamine-modified clay, PU/vermiculite, or TPU/organoclay (Figure 4b).[42–45] Moreover, the resulting E-Modulus of samples even outperform low-density polyethylene (LDPE) and rather is found to be in the range of polyamide (PA 6).[46] With a strain at break of up to 487% (p3L-PVP-Hec-9.1) the sandwich-like nanocomposite laminate combines elastomeric and thermoplastic behavior with much improved moduli while the strength of all nanocomposite laminates is little affected by the incorporation of the PVP-Hec coating at all filler contents below 10 wt%. The nanocomposite laminate is flexible even with high amount of clay (p3L-PVP-Hec-29.5), as revealed by bending test (Figure S5, Supporting Information). The laminate did not develop any cracks even after bending for 10 000 times.

2.4. Oxygen and Water Vapor Transmission Rate

In particular for food packaging, the oxygen transmission rate (OTR) is the crucial parameter. As already mentioned, platelet fillers like graphene oxide or layered silicates may be used to improve the barrier properties of polymer matrices against different gases and molecules. According to Cussler the resulting gas barrier of a polymer (permeability nanocomposite: P, neat matrix: permeability P_0 and geometrical factor μ) with layered materials is dependent in a nonlinear manner on the filler content (ϕ, vol% ratio) and the aspect ratio (α) of the filler (Equation (1)).[47]

$$P_{\text{rel}} = \frac{P}{P_0} = \left(1 + \mu\left(\frac{\alpha^2 \phi^2}{1-\phi}\right)\right)^{-1} \quad (1)$$

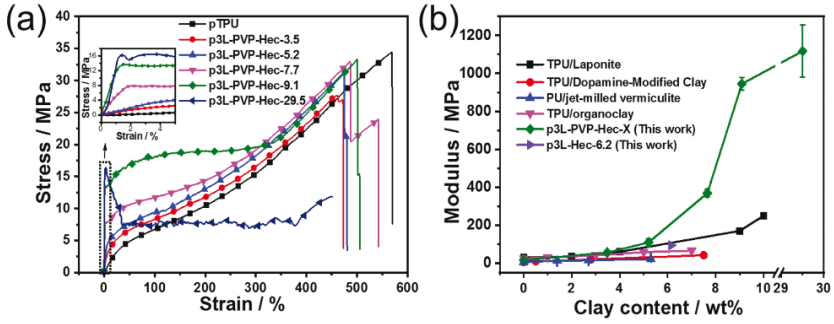

Figure 4. a) Stress–strain curves of the neat hot-pressed TPU (pTPU) compared to the laminates with the nanocomposite interlayer. b) Comparison of the elasticity modulus of the laminates of this work and the TPU nanocomposites of other research groups.

ADVANCED SCIENCE NEWS
www.advancedsciencenews.com

Macromolecular Materials and Engineering
www.mme-journal.de

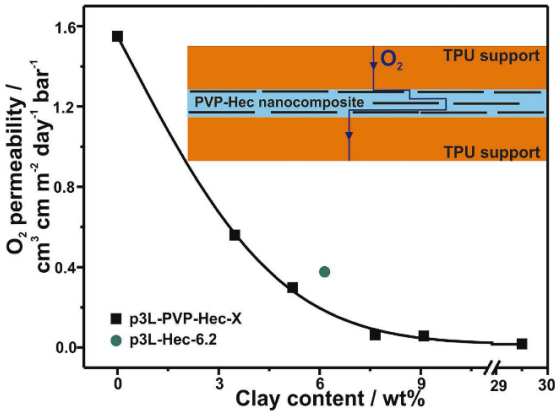

Figure 5. Oxygen permeability of p3L-PVP-Hec-X laminate membranes changes with different amounts of clay (X) at 50% RH. A laminate with a pure clay coating is shown for comparison. The "tortuous pathway" created by incorporation of delaminated Hec nanosheets into a PVP matrix is also illustrated.

The permeability is the measured transmission rate normalized to a certain thickness which allows comparison with other materials of different thicknesses. Herein, the overall laminate thickness (TPU support+ PVP-Hec nanocomposite+ TPU support) is used for this calculation. Caused by the huge aspect ratio of the melt synthesized Hec nanosheets the permeability decreased with incorporation of both, pure Hec coatings and PVP-Hec nanocomposite coatings as interlayer into the laminated membrane (**Figure 5**). By filling the gaps between the inorganic nanosheets in the filtered interlayer with a polymer matrix, the barrier properties are greatly improved as compared to the pure Hec coating. Moreover, the permeability steadily decreases with increasing amounts of delaminated Hec nanoplatelets in the interlayer nanocomposite (Table S3, Supporting Information; Figure 5). This is due to the elongation of the tortuous path in the interlayer, realized with a homogenous dispersion of the Hec nanoplatelets in the polymer matrix (inset in Figure 5). The increased amount of Hec is realized with the filtration of thicker interlayers, which occurs with filtration of nanocomposite dispersion with an increased overall solid content. A remarkable reduction of the oxygen permeability of 98.8% with a filler content of 29.5 wt% (0.0185 cm^3 cm m^{-2} day^{-1} bar^{-1}, p3L-PVP-Hec-29.5) for the laminate as compared to the neat TPU matrix (1.55 cm^3 cm m^{-2} day^{-1} bar^{-1}, pTPU) was observed at 50% RH.

The reduction of the oxygen barrier compared to the neat polymer matrix (up to >80 times) is higher than in other published PU clay nanocomposites and furthermore, the resulting overall permeability rates are much lower (Table S3, Supporting Information).[48,49] We carried out measurements at 50% RH and even at elevated RH of 75%. Even at 75% RH the permeability of p3L-PVP-Hec-29.5 just slightly increases to 0.024 cm^3 cm m^{-2} day^{-1} bar^{-1}. Moreover, the laminates outperform commercially used packaging materials like polyethylene therephthalate (PET) or low-density polyethylene (LDPE) (Table S2, Supporting Information).[46,50,51] Furthermore, also the water vapor transmission rate (WVTR) could be reduced by a factor of >35 to a resulting water vapor permeability of 0.79 g cm m^{-2} day^{-1} bar^{-1} (50% RH, p3L-PVP-Hec-9.1).

3. Conclusions

The proposed processing method enables fabrication of light weight barrier membranes by a scalable, fast, and simple filtration. Any porous thermoplastic electrospun support can be used. The porosity of the support greatly accelerates fabrication of a barrier coating from a dilute dispersion of delaminated nanosheets mixed with a soluble polymer matrix.

This fast processing technique releases time-constraints encountered by other solution based processing methods of coatings like doctor blading or spray coating. It therefore offers a great potential to deliver highly filled nanocomposite coatings via a mechanically stable support that subsequently may be laminated with a variable third layer. This offers flexibility with respect to the overall performance of the resulting barrier membrane. Hot pressing as used in this work is just one example that may be replaced by any other lamination approach.

The amount of Hec can easily be varied and with increasing Hec content barrier performance (98.8% reduction of oxygen permeability) and tensile moduli (by a factor of >60) of the laminates improve a great deal, while elongation at break is affected little.

4. Experimental Section

Materials: Thermoplastic polyurethane (TPU, Desmopan DP 2590, Bayer Materials Science, M_w: 88 900), polyvinyl pyrrolidone (PVP, M_w: 40 000, Sigma-Aldrich), were used as received. The Na-Hectorite ($[Na_{0.5}]^{inte}{}^{r}[Mg_{2.5}Li_{0.5}]^{oct}[Si_4]^{tet}O_{10}F_2$) (Hec) was synthesized via melt synthesis according to an established literature procedure.[4] The clay platelets show aspect ratios of ≈20 000 which has been proven by statistic light scattering (SLS) and atomic force microscopy (AFM).[4] Natural montmorillonite (MMT) was used for comparison (BYK GmbH). *N*,*N*-Dimethylformamide (DMF, 99.9%), tetrahydrofuran (THF, ≥99.9%), and *n*-butyl alcohol were purchased from Sigma-Aldrich and used without purification.

Preparation of the TPU/PVP-Hec Composite Membranes: The electrospinning solution was prepared by dissolution of TPU in mixed solvents of DMF and THF (volume ratio 80/20). The concentration of the TPU solution was 16 wt%. A circular 325-mesh stainless steel wire mesh (diameter 6.4 cm, area 43 cm^2) was used as the collector with the distance of 20 cm to the tip of needle for collecting spun fibers. The applied voltage was 16 kV. Electrospun TPU fibrous membrane deposited on the steel mesh obtained from spinning 0.4 mL solution was used as the filter for Hec suspension. Hec suspension was prepared by dispersing 1 g Na-Hectorite (Hec) in 199 mL deionized water and stirring vigorously for 3 days to form a 0.5 wt% suspension. The PVP-Hec dispersion was obtained by adding certain amounts of PVP powder in Hec suspension and stirring for another 12 h. The mass ratio (wt%) of Hec to PVP was controlled to 6:4. The TPU/PVP-Hec/TPU laminates were fabricated by vacuum filtration combined with hot pressing. For example, PVP-Hec dispersion, 100 mL diluted suspension with definite amount of Hec (2, 5, 10, 20, and 65 mg per 100 mL water, PVP:Hec wt% ratio always 4:6) was filtered through an electrospun TPU membrane. The PVP-Hec layer was sandwiched between the TPU fibrous membranes by spinning another 0.4 mL TPU on top of the PVP-Hec layer. At last, the sandwich-like structure was peeled from the mesh and pressed with a load of 15 000 pound at 180 °C for 10 min to get transparent p3L-TPU-PVP-Hec-X membranes. X is the amount of Hec in the final composite as determined by TGA. A pure TPU film and a p3L-TPU-Hec film were used for comparison.

ADVANCED SCIENCE NEWS
www.advancedsciencenews.com

Macromolecular Materials and Engineering
www.mme-journal.de

Characterization: The pore size distribution of the TPU fibrous membranes was tested with a pore size meter (PSM 165, Topas GmbH). The porosity of the TPU membranes was confirmed by *n*-butyl alcohol absorption method. A TPU membrane with the size of 10 mm × 20 mm was dried completely and weighed. After immersing it in *n*-butyl alcohol for 2 h, the sample was weighed again. The porosity was calculated using the following equation.

$$\text{Porosity} = \frac{W - W_0}{\rho * V_0} \quad (2)$$

where W_0, V_0 are the weight and volume of pristine TPU mat and W is the weight after putting in *n*-butyl alcohol, ρ = density *n*-butyl alcohol. Differential scanning calorimetry (DSC) was adopted to measure the thermal transitions of TPU membrane. The morphology of the TPU membrane, PVP-Hec layered on TPU membrane, the cross section of the bilayer-TPU/PVP-Hec membranes, and the diameter of the clay nanosheets were observed by scanning electron microscope (SEM, Zeiss Leo 1530). The macrostructure of the PVP-Hec coated TPU membrane was checked by XRD using nickel filtered Cu Kα radiation (λ = 1.54187 Å) on a Bragg-Brentano-type diffractometer (XPERT-PRO, PANalytical B.V.). The transparency was measured by a UV–vis spectrophotometer (V-630, JASCO). The ordered structure of PVP-Hec layer was observed by transmission electron microscopy (TEM), after preparing the samples via cryo ion-slicing (Cryo Ion Slicer IB-09060CIS (JEOL GmbH, Germany)). The samples for the UV–vis measurement were cut to the size of 1 cm × 4 cm and stuck on a glass plate of the same size. The glass plate without sample was tested as the blank. The precise contents of Hec in the p3L-TPU-PVP-Hec-X membranes were determined via thermogravimetric analysis (TGA, TG 209 F1 Libra) in air at heating rate of 10 °C min^{-1}). Mechanical properties were determined by stress-strain tests on a testing machine (Zwick/Roell, BT1-FR0.5TN. D14). The samples for the tensile measurement were cut to size of 3 mm × 40 mm. The tensile speed applied to the samples was 5 mm min^{-1} and the pristine effective tensile length is 10 mm. The slope of the linear region of the stress–strain curves was used to determine the elasticity modulus. All the tests for each sample were measured for at least five times and statistically averaged. Flexibility was determined by bending test using Zwick/Roell machine. Oxygen transmission rates (OTRs) of the specimens were determined on a Mocon Ox-Tran 2/21 (Mocon Inc., Minneapolis, USA) at room temperature and 50% and 75% relative humidity (RH). A mixture of 95% N_2 and 5% H_2 (Linde Formiergas 95/5) was used as carrier gas and 100% O_2 (Linde Sauerstoff 3.5) as permeant. The effective sample area was controlled to 5 cm^2 by covering with aluminum masks (type MO025-493, Mocon Inc.). WVTRs were determined on a HiBarSens HBS 2.0 HT (Sempa Systems GmbH, Dresden, Germany). The lower detection limit is 1×10^{-6} g m^{-2} day^{-1}. At 23 °C water vapor partial pressure at 100% RH is 0.02811 bar. Thereby at 50% RH water vapor partial pressure is 0.01405 bar. The partial pressure is needed to convert WVTR into water vapor permeability (WVP).

Supporting Information

Supporting Information is available from the Wiley Online Library or from the author.

Acknowledgements

J.Z. and C.H. contributed equally to this work. The authors thank Florian Puchtler for producing the synthetic hectorite and Marco Schwarzmann for preparing the samples via ion-slicing of the samples and the SEM and TEM measurements. Furthermore, C.H. and T.S. would like to thank the Elite Network Bavaria for financial and other support. The work was supported by the German Science Foundation (DFG) within the collaborative research project SFB 840.

Conflict of Interest

The authors declare no conflict of interest.

Keywords

clays, electrospinning, filter-through, gas barriers, nanocomposites

Received: December 20, 2018
Revised: February 27, 2019
Published online:

[1] H. Gao, Y. Yang, O. Akampumuza, J. Hou, H. Zhang, X. Qin, *Environ. Sci.: Nano* **2017**, *4*, 864.
[2] H. Souzandeh, B. Molki, M. Zheng, H. Beyenal, L. Scudiero, Y. Wang, W.-H. Zhong, *ACS Appl. Mater. Interfaces* **2017**, *9*, 22846.
[3] H. Ma, B. S. Hsiao, B. Chu, *J. Membr. Sci.* **2014**, *452*, 446.
[4] M. Stöter, D. A. Kunz, M. Schmidt, D. Hirsemann, H. Kalo, B. Putz, J. Senker, J. Breu, *Langmuir* **2013**, *29*, 1280.
[5] M. Morits, T. Verho, J. Sorvari, V. Liljeström, M. A. Kostiainen, A. H. Gröschel, O. Ikkala, *Adv. Funct. Mater.* **2017**, *27*, 1605378.
[6] M. W. Möller, T. Lunkenbein, D. A. Kunz, H. Kalo, M. Schieder, J. Breu, *Z. Anorg. Allg. Chem.* **2010**, *636*, 2113.
[7] H. Kalo, M. W. Möller, M. Ziadeh, D. Dolejš, J. Breu, *Appl. Clay Sci.* **2010**, *48*, 39.
[8] C.-H. Zhou, Z.-F. Shen, L.-H. Liu, S.-M. Liu, *J. Mater. Chem.* **2011**, *21*, 15132.
[9] C.-W. Chiu, J.-J. Lin, *Prog. Polym. Sci.* **2012**, *37*, 406.
[10] T. Szabó, A. Szeri, I. Dékány, *Carbon* **2005**, *43*, 87.
[11] S. Eigler, A. Hirsch, *Angew. Chem., Int. Ed.* **2014**, *53*, 7720.
[12] Y. Cui, S. Kundalwal, S. Kumar, *Carbon* **2016**, *98*, 313.
[13] E. Doblhofer, J. Schmid, M. Rieß, M. Daab, M. Suntinger, C. Habel, H. Bargel, C. Hugenschmidt, S. Rosenfeldt, J. Breu, *ACS Appl. Mater. Interfaces* **2016**, *8*, 25535.
[14] D. A. Kunz, J. Schmid, P. Feicht, J. Erath, A. Fery, J. Breu, *ACS Nano* **2013**, *7*, 4275.
[15] A. Eckert, T. Rudolph, J. Guo, T. Mang, A. Walther, *Adv. Mater.* **2018**, *30*, 1802477.
[16] Y. Song, J. Gerringer, S. Qin, J. C. Grunlan, *Ind. Eng. Chem. Res.* **2018**, *57*, 6904.
[17] J. J. Kochumalayil, M. Bergenstråhle-Wohlert, S. Utsel, L. Wågberg, Q. Zhou, L. A. Berglund, *Biomacromolecules* **2013**, *14*, 84.
[18] M. A. Priolo, K. M. Holder, D. Gamboa, J. C. Grunlan, *Langmuir* **2011**, *27*, 12106.
[19] E. S. Tsurko, P. Feicht, F. Nehm, K. Ament, S. Rosenfeldt, I. Pietsch, K. Roschmann, H. Kalo, J. Breu, *Macromolecules* **2017**, *50*, 4344.
[20] F. Ding, J. Liu, S. Zeng, Y. Xia, K. M. Wells, M.-P. Nieh, L. Sun, *Sci. Adv.* **2017**, *3*, e1701212.
[21] S. Rosenfeldt, M. Stöter, M. Schlenk, T. Martin, R. Q. Albuquerque, S. Förster, J. Breu, *Langmuir* **2016**, *32*, 10582.
[22] M. Daab, N. J. Eichstaedt, C. Habel, S. Rosenfeldt, H. Kalo, H. Schießling, S. Förster, J. Breu, *Langmuir* **2018**, *34*, 8215.
[23] M. Daab, N. J. Eichstaedt, A. Edenharter, S. Rosenfeldt, J. Breu, *RSC Adv.* **2018**, *8*, 28797.
[24] L. J. Michot, I. Bihannic, S. Maddi, S. S. Funari, C. Baravian, P. Levitz, P. Davidson, *Proc. Natl. Acad. Sci. U. S. A.* **2006**, *103*, 16101.
[25] Y. Mori, K. Togashi, K. Nakamura, *Adv. Powder Technol.* **2001**, *12*, 45.
[26] H. Hemmen, N. I. Ringdal, E. N. De Azevedo, M. Engelsberg, E. L. Hansen, Y. Méheust, J. O. Fossum, K. D. Knudsen, *Langmuir* **2009**, *25*, 12507.

ADVANCED SCIENCE NEWS
www.advancedsciencenews.com

Macromolecular Materials and Engineering
www.mme-journal.de

[27] M. W. Möller, D. A. Kunz, T. Lunkenbein, S. Sommer, A. Nennemann, J. Breu, *Adv. Mater.* **2012**, *24*, 2142.
[28] F. Carosio, A. Di Pierro, J. Alongi, A. Fina, G. Saracco, *J. Colloid Interface Sci.* **2018**, *510*, 142.
[29] A. J. Svagan, A. Åkesson, M. Cárdenas, S. Bulut, J. C. Knudsen, J. Risbo, D. Plackett, *Biomacromolecules* **2012**, *13*, 397.
[30] A. Greiner, J. H. Wendorff, *Angew. Chem., Int. Ed.* **2007**, *46*, 5670.
[31] S. Jiang, Y. Chen, G. Duan, C. Mei, A. Greiner, S. Agarwal, *Polym. Chem.* **2018**, *9*, 2685.
[32] S. Agarwal, A. Greiner, J. H. Wendorff, *Prog. Polym. Sci.* **2013**, *38*, 963.
[33] Y. Ding, H. Hou, Y. Zhao, Z. Zhu, H. Fong, *Prog. Polym. Sci.* **2016**, *61*, 67.
[34] H. Hou, W. Xu, Y. Ding, *J. Jiangxi Norm. Univ., Nat. Sci.* **2018**, *42*, 551.
[35] S. Agarwal, M. Burgard, A. Greiner, J. Wendorff, *Electrospinning: A Practical Guide to Nanofibers*, Walter de Gruyter GmbH, Berlin **2016**.
[36] S. Pandey, K. K. Jana, V. K. Aswal, D. Rana, P. Maiti, *Appl. Clay Sci.* **2017**, *146*, 468.
[37] H. Kim, Y. Miura, C. W. Macosko, *Chem. Mater.* **2010**, *22*, 3441.
[38] A. Mishra, B. P. D. Purkayastha, J. K. Roy, V. K. Aswal, P. Maiti, *Macromolecules* **2010**, *43*, 9928.
[39] M. Joshi, B. Adak, B. Butola, *Prog. Mater. Sci.* **2018**, *97*, 230.
[40] C. Anthony, S. Durand-Vidal, P. Turq, J. Brendle. *J. Colloid Interface Sci.* **2005**, *285*, 719.
[41] H. Kalo, W. Milius, J. Breu, *RSC Adv.* **2012**, *2*, 8452.
[42] S. M. Liff, N. Kumar, G. H. McKinley, *Nat. Mater.* **2007**, *6*, 76.
[43] S. L. Phua, L. Yang, C. L. Toh, S. Huang, Z. Tsakadze, S. K. Lau, Y.-W. Mai, X. Lu, *ACS Appl. Mater. Interfaces* **2012**, *4*, 4571.
[44] Y. Qian, C. I. Lindsay, C. Macosko, A. Stein, *ACS Appl. Mater. Interfaces* **2011**, *3*, 3709.
[45] D. Sheng, J. Tan, X. Liu, P. Wang, Y. Yang, *J. Mater. Sci.* **2011**, *46*, 6508.
[46] T. R. Crompton, *Physical Testing of Plastics*, Smithers Rapra, Akron, OH **2012**.
[47] E. Cussler, S. E. Hughes, W. J. WardIII, R. Aris, *J. Membr. Sci.* **1988**, *38*, 161.
[48] G. L. Yuan, W. M. Li, S. Yin, F. Zou, K. C. Long, Z. F. Yang, *J. Appl. Polym. Sci.* **2009**, *114*, 1964.
[49] J. M. Herrera-Alonso, E. Marand, J. C. Little, S. S. Cox, *J. Membr. Sci.* **2009**, *337*, 208.
[50] K. S. Miller, J. Krochta, *Trends Food Sci. Technol.* **1997**, *8*, 228.
[51] U. Edlund, Y. Z. Ryberg, A.-C. Albertsson, *Biomacromolecules* **2010**, *11*, 2532.

Supporting Information

for *Macromol. Mater. Eng.,* DOI: 10.1002/mame.201800779

Filter-Through Method of Making Highly Efficient Polymer-Clay Nanocomposite Membranes

Jian Zhu, Christoph Habel, Theresa Schilling, Andreas Greiner,* Josef Breu,* and Seema Agarwal*

Supporting Information

Filter-through method of making highly efficient polymer-clay nanocomposite membranes

Jian Zhu, Christoph Habel, Theresa Schilling, Andreas Greiner, Josef Breu*, Seema Agarwal**

J. Zhu, Prof. A. Greiner, Prof. S. Agarwal,
Macromolecular chemistry II, Bavarian Polymer Institute and Bayreuth Center for Colloids and Interfaces, University of Bayreuth, Universitätsstraße 30, Bayreuth, 95447, Germany
E-mail: greiner@uni-bayreuth.de, agarwal@uni-bayreuth.de

C. Habel, T. Schilling, Prof. J. Breu
Bavarian Polymer Institute and Department of Inorganic Chemistry, University of Bayreuth, Universitätsstraße 30, Bayreuth, 95447, Germany
E-mail: Josef.Breu@uni-bayreuth.de
† These authors contributed equally to this work.

Figures and Tables

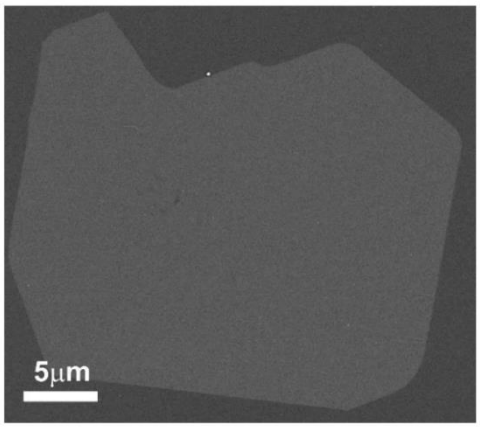

Figure S1. SEM image of a Hec platelet. The diameter is >20 µm.

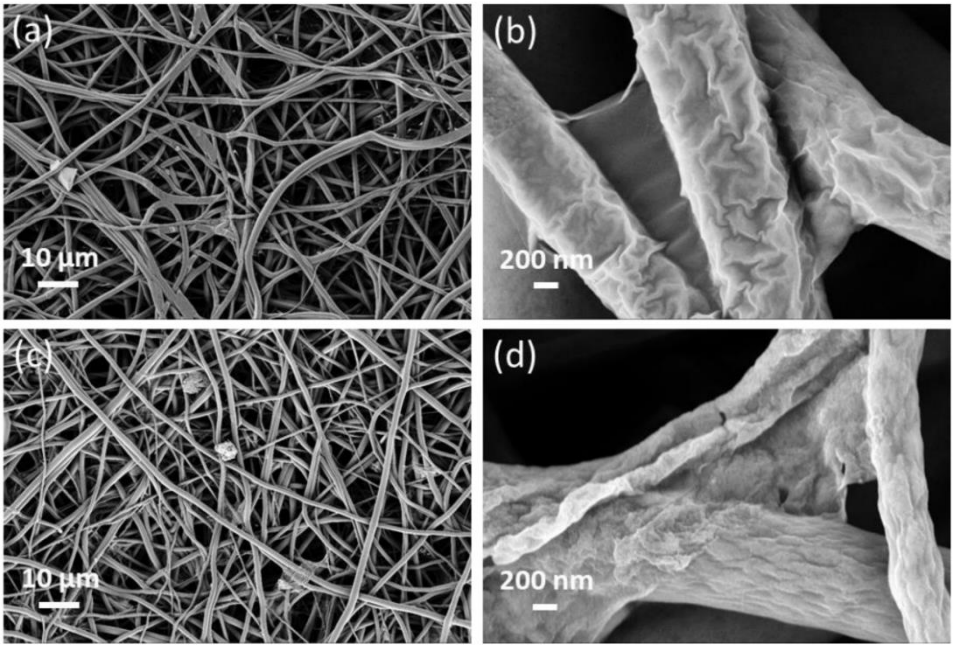

Figure S2. Filtration of MMT with concentration of 0.2 mg ml^{-1}(a, b) and 0.65 mg ml^{-1} (c, d) through electrospun TPU non-woven. MMT did not make a layer but seems to either wrap around the TPU fibers or passed through the filter due to its small diameter.

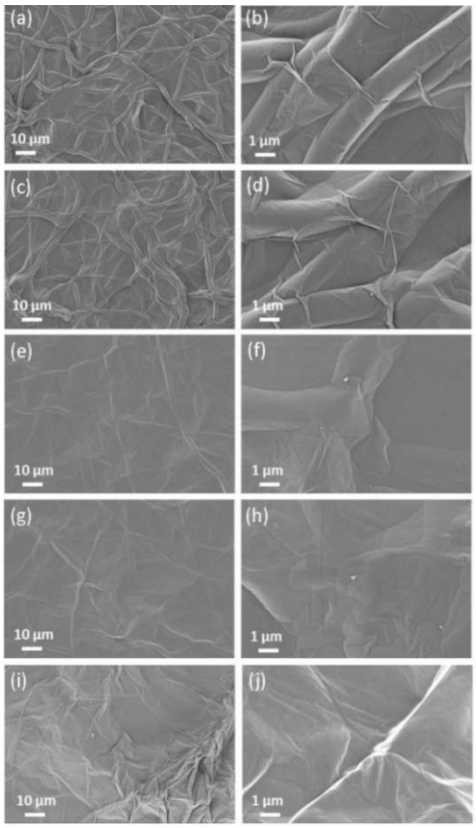

Figure S3. SEM images of PVP-clay deposited on the surface of TPU support. The amount of clay was 2 mg (a, d), 5 mg (c, d), 10 mg (e, f), 20 mg (g, h) and 65 mg (i, j) per 100 ml water in the suspension, respectively.

3

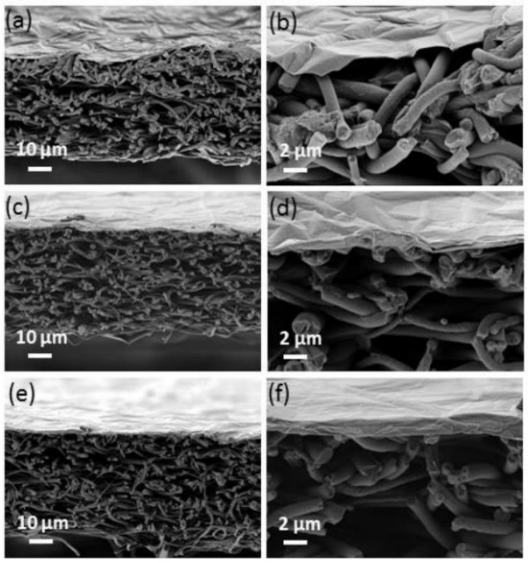

Figure S4. SEM images of cross section of bilayer TPU/PVP-Hec membrane with different amounts of Hec coating. The amount of Hec in the suspension filtered through TPU was 2 mg (**Figure 1**), 5mg (a, b), 10 (c, d), 20 mg (e, f) and 65 mg (**Figure 1**) per 100 ml, corresponding to the average thickness of PVP-Hec layers around 60nm, 160nm, 70nm, 1200nm and 5000 nm, respectively.

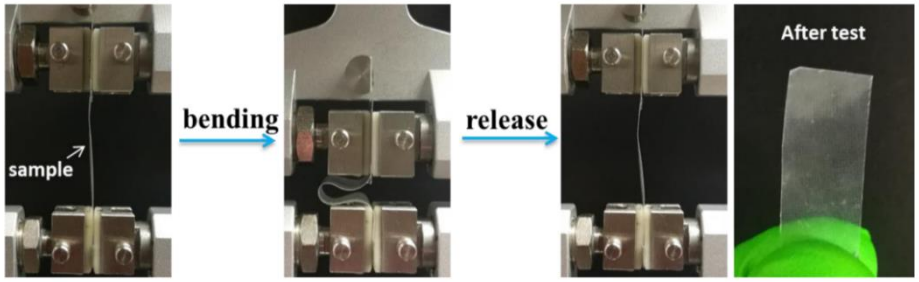

Figure S5. Bending test of p3L-PVP-Hec-29.5 laminate.

Table S1. Summary of the transparent properties and thermal properties of laminates with different amounts of clay (p3L-PVP-Hec-X, X describes the Hec content).

Samples	Transmittance at 600 nm (%)	Content of Hec from TGA (wt%)
pTPU	72	0
p3L-PVP-Hec-3.5	77	3.5
p3L-PVP-Hec-5.2	79	5.2
p3L-PVP-Hec-7.7	76	7.7
p3L-PVP-Hec-9.1	79	9.1
p3L-PVP-Hec-29.5	62	29.5
p3L-PVP-Hec-6.2	77	6.2

Table S2. Mechanical properties (Strength, E-Modulus, Strain at break) of the neat pressed TPU support (pTPU) in comparison with the laminates with different amounts of clay (p3L-PVP-Hec-X, X describes the Hec content).

Samples	Strength (MPa)	E-modulus (MPa)	Strain at break (%)
pTPU	37±1.6	17±1.6	564±13.7
p3L-PVP-Hec-3.5	28±0.4	56±3.7	474±20.3
p3L-PVP-Hec-5.2	30±2.3	110±19	464±28.8
p3L-PVP-Hec-7.7	29±3.6	369±19.6	464±18.6
p3L-PVP-Hec-9.1	33±3.5	945±34.1	487±21.6
p3L-PVP-Hec-29.5	17±0.7	1117±138	471±21
p3L-PVP-Hec-6.2	27±2.0	17±1.6	564±13.7

Table S3. OTRs (dry or 50% RH, room temperature) and calculated permeabilities (overall thickness of the laminates) of the neat TPU matrix and the nanocomposite foils in dependency of the Hec content and comparing the Oxygen Permeability (OP) of films reported in literature. [1-4]

Samples	Overall thickness (µm)	OTR (cm^3 m^{-2} day^{-1} bar^{-1})	OP (cm^3 cm m^{-2} day^{-1} bar^{-1}) [a]
pTPU	**35**	**442.5**	**1.55**
p3L-PVP-Hec-3.5	**34**	**165.1**	**0.56**
p3L-PVP-Hec-5.2	**34**	**106.8**	**0.299**
p3L-PVP-Hec-7.7	**30**	**20.9**	**0.063**
p3L-PVP-Hec-9.1	**36**	**16**	**0.058**
p3L-PVP-Hec-29.5	**50**	**3.7**	**0.0185**
p3L-PVP-Hec-6.2	**34**	**110.5**	**0.377**
PU*	**56**	**753**	**4.22**
PU*+8 wt% MMT	**57**	**166**	**0.93**
PU**	-	-	**59.8**
PU**+28 wt% Cloisite	-	-	**3.3**
LDPE	-	-	18.7
PET	38	-	0.146
HDPE	-	-	4.27
Polyester	-	-	0.156

[a] In order to assist comparability, some of the values are recalculated to the same unit.

References

[1] G. L. Yuan, W. M. Li, S. Yin, F. Zou, K. C. Long, Z. F. Yang, *J. Appl. Polym. Sci.* **2009**, 114, 1964.

[2] J. M. Herrera-Alonso, E. Marand, J. C. Little, S. S. Cox, *J. Membr. Sci.* **2009**, 337, 208.

[3] K. S. Miller, J. Krochta, *Trends Food Sci. Tech.* **1997**, 8, 228.

[4] U. Edlund, Y. Z. Ryberg, A.-C. Albertsson, Barrier films from renewable forestry waste, *Biomacromolecules* **2010**, 11, 2532.

6.2 Nanokomposit-Beschichtungen als Verpackungsalternative

Christoph Habel[1], Marius Schöttle[1], Matthias Daab[1], Natalie J. Eichstaedt[1], Daniel Wagner[1], Hadi Bakhshi[1], Seema Agarwal[1], Marcus A. Horn[2], Josef Breu[1,*]

High-Barrier, Biodegradable Food Packaging

Macromol. Mater. Eng. **2018**, *303* (10), 1800333.

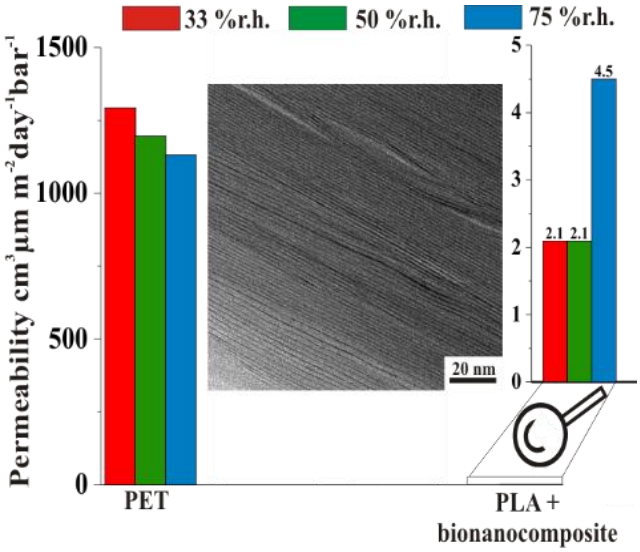

https://doi.org/10.1002/mame.201800333

[1] Bayerisches Polymer Institut und Fakultät für Chemie, Universität Bayreuth, Universitätsstraße 30, Bayreuth, 95447, Germany
[2] Institut für Mikrobiologie, Universität Hannover, Herrenhäuser Straße 2, Hannover, 30419, Germany

*E-Mail: josef.breu@uni-bayreuth.de

Darstellung des Eigenanteils: Das Konzept der Publikation wurde von *Prof. Dr. J. Breu* und mir erarbeitet. Von mir wurden alle Experimente, deren Auswertungen und deren Interpretation (Ausnahme Kolonisationsmessung, enzymatischer Abbau) durchgeführt. Die Kolonisationsmessungen wurden von *Prof. Dr. M. A. Horn* und seinem Team durchgeführt und von *Prof. Dr. M. A. Horn* ausgewertet und diskutiert. *Dr. H. Bakhshi* führte die enzymatischen Abbau-Tests durch, welche mit *Prof. Dr. S. Agarwal* wissenschaftlich ausgewertet und diskutiert wurden. *M. Schöttle* und *Dr. M. Daab* trugen zur wissenschaftlichen Diskussion bei. *N. J. Eichstaedt* und *D. Wagner* prüften die Reproduzierbarkeit innerhalb eines Masterpraktikums. Die Publikation wurde von mir geschrieben und mit *Prof. Dr. S. Agarwal*, *Prof. Dr. M. A. Horn* und *Prof. Dr. J. Breu* zur Einreichung überarbeitet. Mein Eigenanteil beträgt ca. 80%.

COMMUNICATION

PLA Food Packaging

Macromolecular Materials and Engineering
www.mme-journal.de

High-Barrier, Biodegradable Food Packaging

*Christoph Habel, Marius Schöttle, Matthias Daab, Natalie J. Eichstaedt, Daniel Wagner, Hadi Bakhshi, Seema Agarwal, Marcus A. Horn, and Josef Breu**

Biodegradable, high-barrier, flexible and transparent food packaging are required to replace current multilayered, metal- or halogen-containing packaging that is nonrecyclable and nondegradable. An "all-green" solution for food packaging made of a polylactic acid (PLA) foil (25 µm) furnished with a glycol chitosan-clay nanocomposite coating (1.4 µm) is presented here that surpasses state-of-the-art high-performance materials like metallized poly(ethylene terephthalate) or poly(vinylidene chloride) even at harsh conditions (OTR = 0.17 cm^3 m^{-2} day^{-1} bar^{-1} at 75% relative humidity). While the barrier side of the foil inhibits bacterial colonization, the uncoated PLA side assures biodegradability. Such a Janus feature in combination with the superb barrier performance renders this waterborne bio-nanocomposite coating a valuable alternative to conventional less eco-friendly food packaging materials.

The food packaging market in Europe is predicted to grow to a market volume of about 38.2 million tons in 2022. Moreover, it is a dynamically changing market where canning or metallized foils are increasingly replaced by transparent flexible packaging.[1] Consumers prefer lightweight convenient packaging assuring a long shelf life and allowing to visually inspect the product. From a waste management perspective, high-barrier, multilayer, flexible, and transparent biodegradable food packaging is highly sought after to replace current multilayered, metal- or halogen-containing packaging that is nonrecyclable and nondegradable. The environmental trade-offs of such eco-friendly materials have recently been positively evaluated.[2] Sustainability is also an increasingly important issue for consumers and therefore in Europe, the demand for bioplastics in the packaging industry is expected to increase by more than 15% p.a. over the next few years.[1] Biodegradable packaging materials, however, suffer from inherent shortcomings like low-barrier properties that severely limit the best before date. Barrier coatings are therefore decisive. Additionally, they are susceptible to microorganisms, resulting in one hand in good biodegradability, which on the other hand might be disadvantageous for food preservation. Consequently, the market share of biopolymers is currently still below 1%.[3,4]

The poor barrier performance for oxygen is closely related to swelling of biopolymers with water vapor at increasing relative humidity (RH) levels rendering them inappropriate for long shelf life packaging.[5,6] Neat polyethylene terephthalate (PET) represents the low performance standard in flexible food packaging with oxygen permeabilities of 1000 cm^3 µm m^{-2} day^{-1} bar^{-1}. State-of-the-art high-performance packaging materials like laminates of ethylene vinyl alcohol copolymers and polyethylene (EVOH/PE), poly(vinylidene chloride) (PVDC), or metallized PET typically warrant oxygen permeabilities <50 cm^3 µm m^{-2} day^{-1} bar^{-1}.[7]

Polylactic acid (PLA) is biocompatible, biodegradable and is available from renewable agricultural resources.[8] Furthermore, PLA is generally recognized as safe (GRAS) by the United States Food and Drug Administration (FDA).[9,10] The permeability of PLA is 20 times higher than PET and even more than two orders of magnitude higher than the above listed high-performance materials. Even at low RH and room temperature, the barrier properties are too bad to apply neat PLA in food packaging. The situation with all other biopolymers is similar. Establishing biopolymers in the high-performance packaging market inevitably will require compounding with barrier pigments like layered silicates as first pointed out by Darder et al.[11] Low aspect-ratio fillers like natural montmorillonite have been shown to significantly reduce the permeability of biodegradable chitosan-nanocomposites at 0% RH.[12] The barrier of biopolymers is, however, very sensitive to moisture and for PLA-nanocomposite coatings, it was found to break down by a factor of 45 when increasing the water vapor concentration from 20% to 80% RH.[13]

We have recently shown, that high-aspect ratio synthetic fluorohectorite waterborne polymer formulations are accessible that show a barrier improvement by a factor of 10^4 even at a RH of 75%. Such reduction levels correspond to potential extensions of best before dates for dry food like flour to more than 1000 days.[14,15]

C. Habel, M. Schöttle, M. Daab, N. J. Eichstaedt, D. Wagner, Dr. H. Bakhshi, Prof. S. Agarwal, Prof. J. Breu
Department of Chemistry
Bavarian Polymer Institute
University of Bayreuth
Universitätsstraße 30, Bayreuth 95447, Germany
E-mail: Josef.Breu@uni-bayreuth.de
Prof. M. A. Horn
Institute of Microbiology
University of Hannover
Herrenhäuser Straße 2, Hannover 30419, Germany
The ORCID identification number(s) for the author(s) of this article can be found under https://doi.org/10.1002/mame.201800333.

DOI: 10.1002/mame.201800333

ADVANCED SCIENCE NEWS
www.advancedsciencenews.com

Macromolecular Materials and Engineering
www.mme-journal.de

Since the effect of clay-compounding on biodegradation is unclear, we apply a biopolymer barrier coating to a biodegradable PLA foil. This leaves one PLA surface accessible to microbes warranting the well-known good biodegradation. As matrix for the barrier coating, we chose glycol chitosan (GlyChit), because chitosan and GlyChit were shown to exhibit antimicrobial properties.[16,17] Because of its antimicrobial property, chitosan is often used in medical applications.[18,19] GlyChit is soluble in water allowing environmentally benign water-based processing.

Numerous publications exist in the field of biopolymers focusing on barrier properties[12,13,20] or antibacterial characteristics.[21,22] However, very little work has been done concerning systems that combine the two features.[23] Dual functional (antibacterial and biodegradable) polymers with antibacterial units covalently attached to the biodegradable polyesters were also studied in the recent years as promising materials for packaging besides biomedical applications. But, these materials were never tested for barrier properties for packaging applications.[24]

Here, we present an "all-green" alternative to commercially available packaging materials like PET. Moreover, multifunctionality of a GlyChit-hectorite bio-nanocomposite is central to concomitantly assure barrier, optical transparency and anticolonization activity.

For applications, absolute transmission rates are the relevant figures. Transmission rates are; however, largely influenced by the thickness of barrier coatings and even the transmission rate of the substrate. The performance of barrier coatings can therefore only be compared if transmission rates are converted into permeabilities, whereby it is generally assumed that the rate is inversely proportional to the thickness.[25] Nevertheless, for real-life applications, like food packaging, the absolute transmission rates are the decisive characteristics.

PLA foils themselves show permeabilities of about 20 000 cm^3 µm m^{-2} day^{-1} bar^{-1} against hydrophobic gases like oxygen at room temperature and RH of 33–75% as relevant for food packaging. The bad barrier translates into short shelf life-time of packaged food and therefore PLA foils cannot compete with commercially established PET foils. The latter shows a permeability of about 1000 cm^3 µm m^{-2} day^{-1} bar^{-1}, which complies with the upper limit for flexible packaging materials tolerated in food applications.[26] Moreover, the rise of convenience food packaged in single person servings, urges the market toward high-performance materials warranting oxygen transmission rates <1 cm^3 m^{-2} day^{-1} bar^{-1}.[7] If PLA foils are ever to become a feasible alternative in the flexible packaging market, the overall permeability must be decreased by at least a factor of 10^3 with a suitable coating.

Permeability is governed by the solubility of permeates in the polymer matrix and the diffusivity of these permeates through the matrix. Water soluble or just polar polymers tend to be sensitive to humidity, in particular, at elevated RH levels >50%. Water molecules dissolving in the barrier film act as plasticizer and the enhanced segment mobility significantly increases permeability for O_2.

As suggested by Cussler, incorporation of flexible, crystalline, layered ceramic fillers effectively reduce permeability.[27] The tortuous path of the permeate increases nonlinearly with aspect ratio α and volume content φ of the platy filler (Equation (1)).

$$P_{rel} = \frac{P}{P_0} = \left(1 + \mu\left(\frac{\alpha^2\phi^2}{1-\phi}\right)\right)^{-1} \quad (1)$$

The improvement of the barrier properties is reflected by the inverse of $P_{rel.}$ which is named barrier improvement factor (BIF).

Synthetic fluorohectorite (NaHec) repulsively delaminates when immersed into water. At solid contents of typically 0.5 wt%, the separation of singular clay platelets is ≈200 nm and therefore the rotation of the platelets is sterically hindered because of the huge average aspect ratios of 20 000.[28] Suspensions of such concentrations therefore are not isotropic but rather represent liquid crystalline, nematic phases. For preparing water-borne coatings, such clay suspensions were mixed with an aqueous solution (1 wt%) of GlyChit which subsequently was spray-coated on the PLA substrate (for details see nanocomposite foils fabrication, Supporting Information) with resulting foil thicknesses of 1.4 µm (**Scheme 1**).

The barrier foils were highly flexible and sufficiently stable for packaging. No delamination of the coating was observed when repeatedly bending the barrier foil to a radius of $r < 1$ cm (Figure S1, Supporting Information). At 33% RH, a GlyChit-NaHec coating as thin as 1.4 µm reduces the oxygen transmission rate (OTR) as compared to the neat PLA substrate foil by four orders of magnitude to 0.08 cm^3 m^{-2} day^{-1} bar^{-1} (**Table 1**). Moreover, this superb performance is not hampered at all by increasing the water vapor concentration to 50% RH, even at 75% RH the bio-nanocomposite packaging material (PLA+GlyChit-NaHec) still outperforms neat PET by a factor of 180.

PLA+GlyChit-NaHec even outperforms less eco-friendly, nondegradable high-performance materials like metallized PET foils (OTR < 2 cm^3 m^{-2} day^{-1} bar^{-1}) or PVDC (OTR < 10 cm^3 m^{-2} day^{-1} bar^{-1}) at 50% RH and room temperature.

An unfilled GlyChit coating showed much smaller reductions. Moreover, the performance of unfilled GlyChit is very sensitive

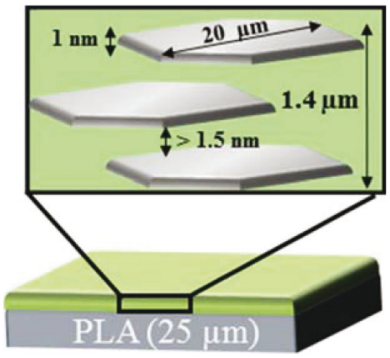

Scheme 1. Schematic representation of the architecture of the resulting coating (1.4 µm thickness) on the PLA substrate. The clay nanoplatelets are separated by the polymer matrix glycol chitosan (green).

ADVANCED SCIENCE NEWS
www.advancedsciencenews.com

Macromolecular Materials and Engineering
www.mme-journal.de

Table 1. Oxygen transmission rates of different coatings and substrates as a function of RH.

	RH [%]	PET	PLA	PLA+GlyChit	PLA+ GlyChit-NaHec
		Overall thickness [µm]			
		35.5 ± 0.1	25 ± 0.7	27.5 ± 0.3	26.4 ± 0.1
OTR cm^3 m^{-2} day^{-1} bar^{-1}	33	36.4	903.6	62.6	0.08
	50	33.7	874.2	166.3	0.08
	75	31.9	864.8	653.5	0.17

to moisture. The OTR increases by more than one order of magnitude when increasing the RH from 33% to 75%. Since ISO 14663-2 defines 65% RH as a standard for food packaging, we refrain from reporting irrelevant 0% RH values but focus on a range of RH (50% and 75% RH) enclosing this standard.

Apparently, the clay filler not only reduces the permeability of the bio-nanocomposite but it also greatly reduces the sensitivity of the performance on water vapor concentrations. This "hydrophobization effect" has already been observed and discussed in previous papers with other nonbiodegradable, waterborne polymer matrices.[14,15]

As pointed out above, comparison of barrier performance is greatly facilitated by converting transmission rates into permeabilities (**Figure 1**). The resulting permeabilities are then normalized to a packaging foil thickness of 1 µm.

Spray coating of pure GlyChit on PLA foils reduces the permeability by 92% at 33% RH (1700 cm^3 µm m^{-2} day^{-1} bar^{-1}) which, however, still is insufficient regarding food packaging applications. As already mentioned, Grunlan et al. produced clay–polymer nanocomposites with low-aspect ratio fillers, like montmorillonite. Applying a tedious layer-by-layer processing, Grunlan et al. obtained oxygen permeabilities of <0.03 cm^3 cm cm^{-2} s^{-1} Pa^{-1} (equal to 2.6 cm^3 µm m^{-2} day^{-1} bar^{-1}). The values were, however, only recorded at irrelevant and misleading conditions (0% RH).[12] Because of the strong and highly nonlinear dependency of the permeability on increasing RH, these values cannot be extrapolated to conditions relevant for food packaging.[13] As already mentioned, in this line unfilled GlyChit is also prone to swelling and, thereby the permeabilities increase drastically. At 75% RH, the GlyChit coating causes a reduction by less than 18% (17900 cm^3 µm m^{-2} day^{-1} bar^{-1}). Quite surprisingly, with the incorporation of NaHec as filler, however, not only the gas barrier is improved drastically but moreover, the sensitivity of the oxygen permeability to water vapor is greatly eased. At 33% RH the permeability is as low as 2.1 cm^3 µm m^{-2} day^{-1} bar^{-1} reflected in a huge barrier improvement factor of 10^4 compared to neat PLA. In a recent publication by Walther et al. on water soluble polymer clay nanocomposites (50 wt% montmorillonite/poly(vinyl amine)/poly(vinylalcohol)) oxygen permeabilities of 0.005 cm^3 mm m^{-2} day^{-1} atm^{-1} (equal to 5 cm^3 µm m^{-2} day^{-1} bar^{-1}) were reported at 45% RH.[29] GlyChit-NaHec coatings clearly outperform this value even at the significantly more challenging 75% RH (4.5 cm^3 µm m^{-2} day^{-1} bar^{-1} corresponding to a barrier improvement factor of over 4×10^3). Since the dependency of the permeability on RH is known to be highly nonlinear and shows threshold values with sudden discontinuous jumps of permeability, it is moreover important to measure above the standard value of 65% RH defined in ISO 14663-2.

The low moisture-sensitivity of the bio-nanocomposite might be related to the smectic nature of the coating. The coating comprises large 1D crystalline domains (**Figure 2**).

With X-ray diffraction (Figure 2a), a rational series of basal reflections (d_{001} = 28.7 Å) is observed corresponding to a periodic arrangement of 9.6 Å thick silicate layers being separated by 19.1 Å of GlyChit volume. Assuming a density of 1.5 g cm^{-3} and 2.7 g cm^{-3} for GlyChit and NaHec, respectively, 50 wt% filler content of the bio-nanocomposite translates to 36 vol%. Consequently, for a 1D crystalline, translationally homogeneous bio-nanocomposite, we would expect a basal spacing of 27 Å which is significantly lower than the observed value. This would suggest that the bio-nanocomposite is biphasic being comprised of 1D crystalline intercalated domains as majority phase and partially segregated GlyChit volumes as minority phase (Figure 2b). The segregated polymer volumes are small and therefore will not show bulk properties but rather still experience the confined space. This might explain why both the intercalated and the segregated domains are much less sensitive to swelling than bulk GlyChit.

Interestingly, the bio-nanocomposite still swells significantly at elevated humidity but there seems to be a lower threshold pressure for the onset of this swelling. Prior to measurement, the samples were equilibrated 24 h above saturated K_2CO_3 (43% RH) and another

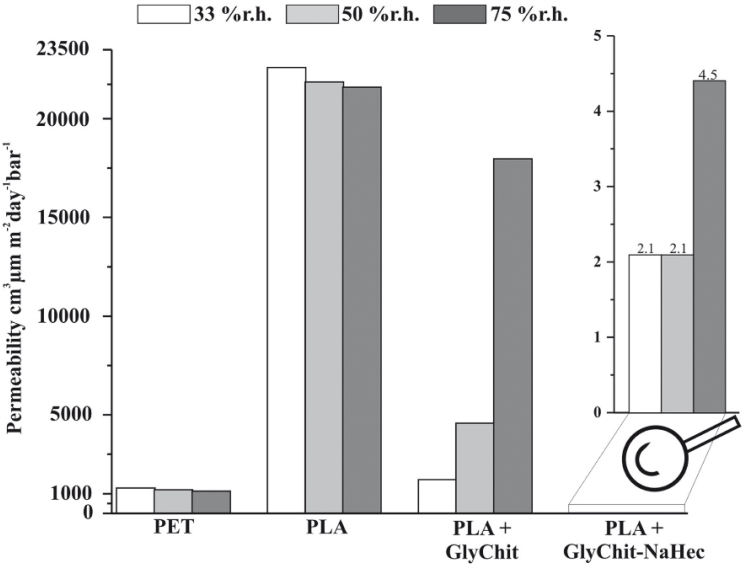

Figure 1. Permeabilities of different coatings and substrates as a function of RH.

ADVANCED SCIENCE NEWS
www.advancedsciencenews.com

Macromolecular Materials and Engineering
www.mme-journal.de

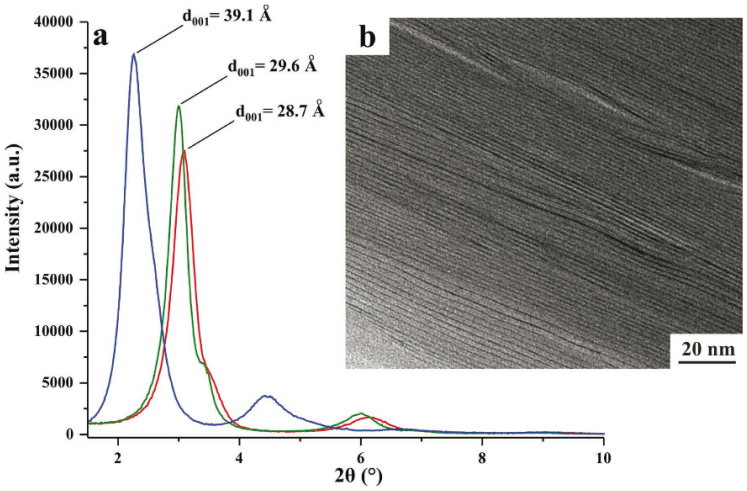

Figure 2. a) PXRD of the GlyChit-NaHec coating at different relative humidities (red = 0% RH, green = 43% RH, blue = 77% RH), b) transmission electron micrograph of the GlyChit-NaHec coating (dark: single silicate layers; light: GlyChit).

24 h above saturated NaCl (77% RH) salt solutions. The basal spacings increase little up to 43% RH (Figure 2a) which is in line with OTR remaining little affected up to 50% RH. At 77% RH, the basal spacing, however, jumps by 1 nm indicating significant water uptake, which goes along with a doubling of the permeability. It is surprising that this moisture-related increase, however, is still very low compared with the unfilled GlyChit. Incorporation of the nanofiller apparently causes a significant hydrophobization of the neat polymer matrix.

Protonated chitosan foils have been shown to significantly inhibit the growth of mesophilic bacteria, psychrotrophic yeasts, and molds.[30] Disruption of cell wall integrity has been suggested as a possible mode of chitosan action. Such antimicrobial properties of chitosan have been applied for decades in food, medical, and textile industries.[31] We used *Pseudomonas fluorescens* A506, a potent biofilm former, as a gram-negative model organism to examine colonizability of polymer and nanocomposite surfaces. The colonization potentials of neat PET and PLA foils were similar. However, the GlyChit and GlyChit-NaHec-coated PLA were less colonized (Kruskal–Wallis, p(same) < 0.001; Mann–Whitney pair wise with Bonferroni correction, p < 0.001) (**Figure 3**). A potential explanation for this observation might be the cationic charge density of chitosan. At the pH of the buffer, 23% of available $-NH_2$ in GlyChit were determined to be protonated by potentiometric titration.

Customers clearly prefer transparent food packaging rendering optical properties economically important (**Figure 4**). The overall transmittance of the coated PLA foil is comparable to neat PLA foil and even higher than the neat PET reference foil. Haze and clarity of the bio-nanocomposite-coated PLA (PLA+GlyChit-NaHec) are slightly increased and decreased, respectively. The biodegradable barrier-coated foils clearly are appropriate for transparent, flexible food packaging.

Spray-coating of biopolymer-based nanocomposite coatings made of GlyChit and a large aspect ratio synthetic fluorohectorite on a PLA substrate yields transparent and flexible packaging foils that in respect to barrier performance are competitive to state-of-the-art high-performance materials like metallized PET, EVOH/PE laminates, or PVDC. Despite being waterborne, this is true even in moist air (75% RH) because the incorporation of the nanofiller reduced moisture sensitivity to a great deal. Waterborne formulations will allow for environmentally benign processing. These bio-nanocomposite foils, moreover, show bifunctional surface properties: The readily colonizable uncoated

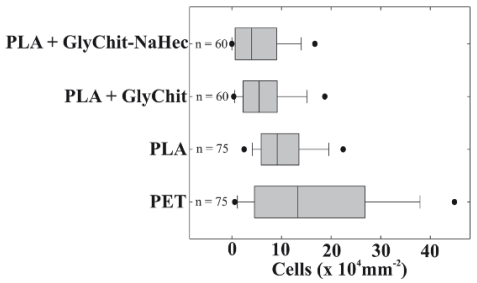

Figure 3. Counts of attached cells on polymer or nanocomposite surfaces after 24 h of incubation; *n* indicates the number of areas that were counted in total. The boundary of the box closest to zero indicates the 25th percentile, a line within the box marks the median, and the boundary of the box farthest from zero indicates the 75th percentile. The error bars above and below the box indicate the 90th and 10th percentiles. Filled circles indicate outliers.

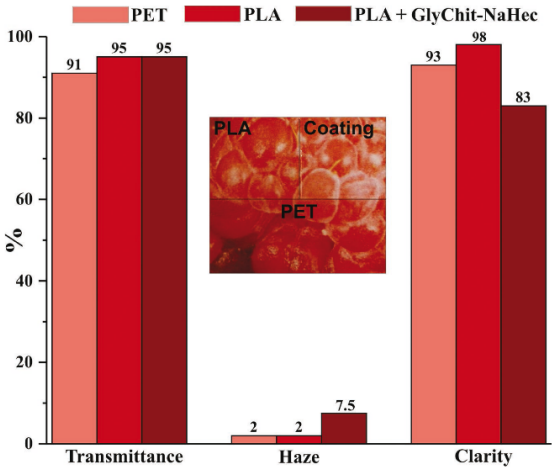

Figure 4. Optical properties (transmittance, haze, clarity) of PET foils, PLA foils, and coated PLA foils. The inset shows an image of a raspberry covered with neat PLA and PET substrates and the coated PLA foil.

ADVANCED SCIENCE NEWS
www.advancedsciencenews.com

Macromolecular Materials and Engineering
www.mme-journal.de

neat PLA side assures biodegradability, while the GlyChit-NaHec coating showed reduced bacterial colonization. This will reduce biofilm formation on the food side and this way might help to reduce food spoilage and pathogenic microorganisms. The coating approach leaves one PLA surface accessible warranting the well-known good biodegradation. Preliminary results obtained by immersing the barrier foils in phosphate buffered saline (PBS) containing esterase and NaN_3 confirm this Janus nature. The PLA side was degraded while the GlyChit-NaHec-coating was not attacked (Figure S2, Supporting Information). The combination of superb barrier performance and control of microbiota makes this bio-nanocomposite foil an attractive green alternative to commercially established food packaging materials. The results are promising and require further detailed studies with respect to the activity against fungi, other bacteria (using standard test procedures), in growth-supportive, and nongrowth-supportive media to ascertain antimicrobial activity. The biodegradability of the composite foils under controlled and environmental conditions will also be studied to check influence on degradability of PLA. Compost collected from homes and grocery stores was recently established as a previously unknown source of microplastic pollution, which most likely is tied to food packaging.[32] The food packaging material proposed here certainly has the potential to greatly reduce or eliminate microplastic pollution through this terrestrial pathway.

Supporting Information

Supporting Information is available from the Wiley Online Library or from the author.

Acknowledgements

The authors thank Florian Puchtler for producing the synthetic clay, Marco Schwarzman for the electron microscopy measurements, Patrick Simmons for conducting the colonization assays, Patrick Hummel for the helium pycnometer tests, and Thomas Brüser as well as Lena Hoffmann for providing *P. fluorescens* A506. Furthermore, C.H. and M.S. would like to thank the Elite Network Bavaria for financial and other support. This work was supported by the German Science Foundation (DFG) within the collaborative research project SFB 840. The Supporting Information was edited after initial online publication October 15, 2018.

Conflict of Interest

The authors declare no conflict of interest.

Keywords

biopolymers, food packaging, gas permeability, layered silicates, nanocomposites

Received: June 4, 2018
Revised: July 27, 2018
Published online: September 4, 2018

[1] Ceresana, Market Study: Food Packaging—Europe, www.ceresana.com/en/market-studies/packaging/food-packaging-europe/ (accessed: 2018).
[2] L. S. Dilkes-Hoffman, J. L. Lane, T. Grant, S. Pratt, P. A. Lant, B. Laycock, *J. Clean. Prod.* **2018**, *180*, 325.
[3] PlasticsEurope, *Plastics–The facts 2017: An analysis of European plastics production, demand and waste data* **2017**, pp. 1–44.
[4] European Bioplastics, *Bioplastics market data*, **2017**, pp. 1–4.
[5] J.-W. Rhim, P. K. Ng, *Crit. Rev. Food Sci. Nutr.* **2007**, *47*, 411.
[6] S. Wang, L. Shen, Y. Tong, L. Chen, I. Phang, P. Lim, T. Liu, *Polym. Degrad. Stab.* **2005**, *90*, 123.
[7] J. Lange, Y. Wyser, *Packag. Technol. Sci.* **2003**, *16*, 149.
[8] M. Jamshidian, E. A. Tehrany, M. Imran, M. Jacquot, S. Desobry, *Compr. Rev. Food Sci. Food Saf.* **2010**, *9*, 552.
[9] R. Auras, *Poly (Lactic Acid)*, Wiley Online Library, Hoboken, NJ **2010**.
[10] B. Gupta, N. Revagade, J. Hilborn, *Progr. Pol. Sci.* **2007**, *32*, 455.
[11] M. Darder, M. Colilla, E. Ruiz-Hitzky, *Chem. Mater.* **2003**, *15*, 3774.
[12] G. Laufer, C. Kirkland, A. A. Cain, J. C. Grunlan, *ACS Appl. Mater. Interfaces* **2012**, *4*, 1643.
[13] A. J. Svagan, A. Åkesson, M. Cárdenas, S. Bulut, J. C. Knudsen, J. Risbo, D. Plackett, *Biomacromolecules* **2012**, *13*, 397.
[14] E. S. Tsurko, P. Feicht, C. Habel, T. Schilling, M. Daab, S. Rosenfeldt, J. Breu, *J. Membr. Sci.* **2017**, *540*, 212.
[15] E. Doblhofer, J. Schmid, M. Rieß, M. Daab, M. Suntinger, C. Habel, H. Bargel, C. Hugenschmidt, S. Rosenfeldt, J. Breu, *ACS Appl. Mater. Interfaces* **2016**, *8*, 25535.
[16] M. Aider, *LWT Food Sci. Technol.* **2010**, *43*, 837.
[17] B. S. Inbaraj, T. Y. Tsai, B. H. Chen, *Sci. Technol. Adv. Mater.* **2012**, *13*, 015002.
[18] M. N. R. Kumar, *React. Funct. Polym.* **2000**, *46*, 1.
[19] R. Jayakumar, D. Menon, K. Manzoor, S. Nair, H. Tamura, *Carbohydr. Polym.* **2010**, *82*, 227.
[20] Y. Kasirga, A. Oral, C. Caner, *Polym. Compos.* **2012**, *33*, 1874.
[21] R. C. Goy, D. D. Britto, O. B. Assis, *Polímeros* **2009**, *19*, 241.
[22] M. Friedman, V. K. Juneja, *J. Food Prot.* **2010**, *73*, 1737.
[23] A. Giannakas, M. Vlacha, C. Salmas, A. Leontiou, P. Katapodis, H. Stamatis, N.-M. Barkoula, A. Ladavos, *Carbohydr. Polym.* **2016**, *140*, 408.
[24] a) H. Wang, M. Langner, S. Agarwal, *Polym. Eng. Sci.* **2016**, *56*, 1146; b) H. Bakhshi, S. Agarwal, *J. Mater. Chem. B* **2017**, *5*, 6827; c) L. Tan, S. Maji, C. Mattheis, M. Zheng, Y. Chen, E. Caballero-Diaz, P. Rivera Gil, W. J. Parak, A , Greiner, S. Agarwal, *Macromol. Biosci.* **2012**, *12*, 1068.
[25] V. Siracusa, *Int. J. Polym. Sci.* **2012**, *2012*, 1687.
[26] U. Edlund, Y. Z. Ryberg, A.-C. Albertsson, *Biomacromolecules* **2010**, *11*, 2532.
[27] E. L. Cussler, S. E. Hughes, W. J. Ward, R. Aris, *J. Membr. Sci.* **1988**, *38*, 161.
[28] M. Stöter, D. A. Kunz, M. Schmidt, D. Hirsemann, H. Kalo, B. Putz, J. Senker, J. Breu, *Langmuir* **2013**, *29*, 1280.
[29] A. Eckert, T. Rudolph, J. Guo, T. Mang, A. Walther, *Adv. Mater.* **2018**, *30*, 1802477.
[30] M. D. R. Moreira, M. Pereda, N. E. Marcovich, S. I. Roura, *J. Food Sci.* **2011**, *76*, 54.
[31] M. Kong, X. G. Chen, K. Xing, H. J. Park, *Int. J. Food Microbiol.* **2010**, *144*, 51.
[32] N. Weithmann, J. N. Möller, M. G. J. Löder, S. Piehl, C. Laforsch, R. Freitag, *Sci. Adv.* **2018**, *4*, eaap8060.

Supporting Information

for *Macromol. Mater. Eng.,* DOI: 10.1002/mame.201800333

High-Barrier, Biodegradable Food Packaging

Christoph Habel, Marius Schöttle, Matthias Daab, Natalie J. Eichstaedt, Daniel Wagner, Hadi Bakhshi, Seema Agarwal, Marcus A. Horn, and Josef Breu*

Supporting Information

for *Macromol. Mater. Eng.*, DOI: 10.1002/mame.201800333

High-Barrier, Biodegradable Food Packaging

Christoph Habel, Marius Schöttle, Matthias Daab, Natalie J. Eichstaedt, Daniel Wagner, Hadi Bakhshi, Seema Agarwal, Marcus A. Horn, Josef Breu*

Experimental

Materials

Sodium hectorite $[Na_{0.5}]^{inter}[Mg_{2.5}Li_{0.5}]^{oct}[Si_4]^{tet}O_{10}F_2$ (NaHec) was synthesized via melt synthesis according to an established literature procedure. The material featured a cation exchange capacity (CEC) of 1.27 mmol g^{-1}.[1]

1g of Glycol chitosan (GlyChit; Sigma Aldrich, Germany) with a polymerization degree of ≥ 400 (crystalline, 73% deacetylated) was dissolved in 99 ml of Millipore water.

Polylactic acid (PLA) films with a thickness of 25 µm were applied as substrates (Pütz GmbH & Co. Folien KG) and corona treated polyethylene terephthalate (PET) (36 µm) films were used as reference material (Bleher KG, Germany).

Nanocomposite films fabrication

Preparation of glycol chitosan-clay nanocomposite (GlyChit-NaNaHec was delaminated by immersing it into Millipore water (1g, 0.5 wt%) and this was mixed with a 1wt% GlyChit solution in a 1:1 (wt%) ratio. The total solid content was then adjusted to 0.7 wt% by adding Millipore water. After homogenization of the dispersion by using a silent crusher (2 minutes, 12000 rpm) the dispersion was transferred to a speedmixer (Hauschild & Co. KG) to remove gas bubbles under vacuum (5 minutes, 100 mbar) and to further improve the dispersion quality. The dispersion was then spray coated (SATA 4000 LAB HVLP 1.0 mm spray gun,

SATA GmbH & Co. KG, Germany) onto a PLA substrate film. After each spray cycle (80 cycles in sum) the sample was dried under an IR lamp at 30 °C for 80 seconds. A detailed description of the spray coating process is given in a previous paper. [2] The neat GlyChit solutions were prepared using Millipore water (final solid content of 0.7 wt%) and treated the same way as described above for the nanocomposite films.

Nanocomposites characterization

Oxygen transmission rates (OTR) were measured on a Mocon OX-TRAN 2/21 XL instrument (Minneapolis, USA) with a lower detection limit of 0.0005 $cm^3\ m^{-2}\ day^{-1}\ bar^{-1}$. The measurements were conducted at 23 °C and r.h. of 33%, 50% and 75%.

Thin cross sections of the nanocomposite coatings were prepared with an Ion Slicer EM-09100IS (JEOL GmbH, Germany) and transmission electron micrographs (TEM) were obtained on a JEM-2200 FS (JEOL GmbH, Germany). The total thickness of the resulting foils was determined as mean value of 10 measurements with a high accuracy digimatic micrometer (Mitutoyo, Japan) with a measuring range of 0-25 mm and a resolution of 0.0001 mm. X-ray diffraction (XRD) patterns were recorded with nickel filtered Cu-Kα radiation (λ = 1.54187 Å) on a Bragg-Brentano-type diffractometer (XPERT-PRO, PANalytical B.V.) equipped with an X'Celerator Scientific RTMS detector. All patterns were analyzed using Panalytical's Highscore Plus software. The degrees of deacetylation and of protonation of the $-NH_2$ groups of GlyChit were determined via potentiometric titration.[3] Transmittance, Clarity, and Haze were measured on a BYK-Gardner Haze-Gard Plus. The shown graphs are representative of five individual measurements.

The density of glycol chitosan was determined with a helium pyknometer (Quantacrome Instruments, USA; Ultrapyc 1200e, test gas helium 5.0). With the sample cell used, the estimated error is below 0.03 %.

Colonization assays

Pseudomonas fluorescens strain A506[4] is a very potent biofilm former and was used as a model organism to evaluate microbial colonization potentials on polymer films. A506 was grown in M63 medium composed of 3 gl^{-1} KH_2PO_4, 7 gl^{-1} K_2HPO_4, 10 gl^{-1} $(NH_4)2SO_4$, 1 mM $MgCl_2$, 2 gl^{-1} glucose, and 5 gl^{-1} casaminoacids, pH 7. Precultures (5 ml M63 in 10 ml tubes inoculated with an A506 colony) were grown over night for 16 h at 25 °C and used to inoculate 10 ml Hungate tubes with 3 ml oxic M63 medium at 1%. Films were cut into pieces of 1 x 4 cm, UV sterilized for 2 min, and placed into the Hungate tubes and fixed at the tube wall with coatings facing to the center of the tube. Controls remained uninoculated. Tubes were incubated over night for 24 h on a tube roller at room temperature. Tubes were then placed on ice to stop growth, films were washed 3 times in sterile 0.9% NaCl solution, films were cut, placed on glass slides, and mounted with 30 µl of a fluorescent dye solution [10 µl ascorbic acid 1 M, 10 µl DAPI (4',6-diamidino-2-phenylindoldihydrochlorid 1 mgl^{-1}), 140 µl Moviol Mounting Medium (2.4 g Moviol, 6 ml glycerol, 6 ml ddH_2O, 14 ml phosphate buffered (10 mM) saline pH 7.4)] for 30 min on ice prior to fluorescence microscopy with a Zeiss (Jena, Germany) Axioskop equipped with Filter Set 02 (excitation filter G 365, beam splitter FT 395, emission filter LP 420). DAPI stained cells on 60-75 areas of 52.5 μm^2 on at least three films were counted and cell densities per mm^2 calculated. Data was evaluated by non-parametric statistics, i.e. Kruskal-Wallis test for equal medians and Man-Whitney pair wise test with Bonferroni correction using the software PAST 3.20.[5]

Figures

Figure S1. GlyChit-NaHec coated on a PLA substrate rolled around a pen showing sufficient delamination stability of the barrier film.

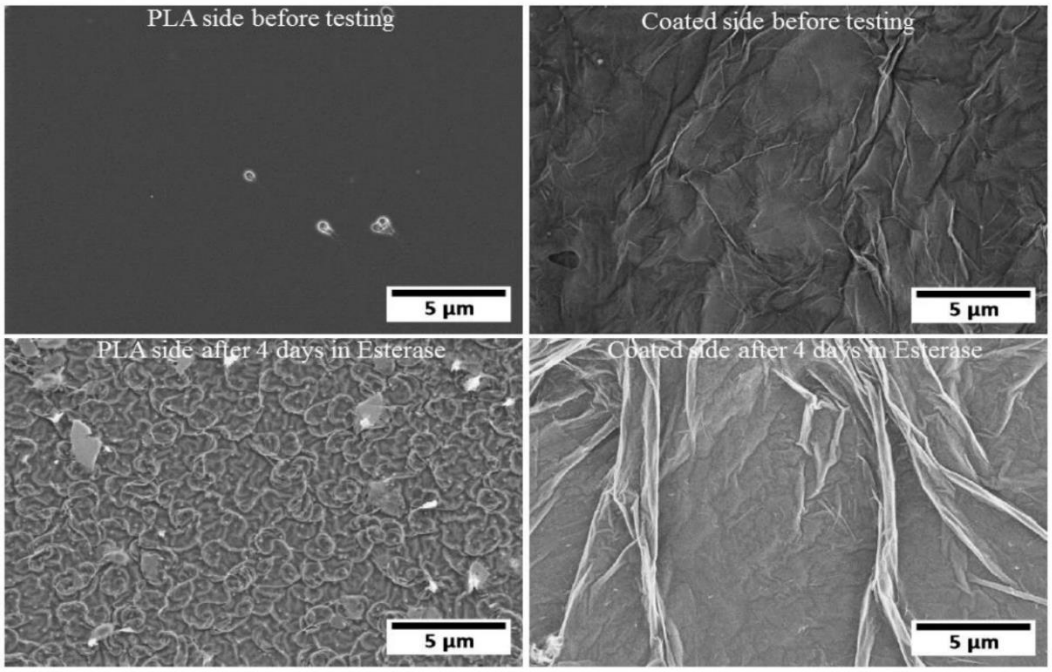

Figure S2. As a preliminary test for degradation barrier foils were immersed in 10 ml of a PBS (Phosphate buffered saline, pH = 7.4) containing esterase (0.5 gl^{-1}) and NaN3 (0.05 gl^{-1}) and placed in a shaking incubator (rotation at 50 r.p.m., 37 °C, 4 days. The test confirmed the Janus nature: The PLA side (left side, before and after testing) was degraded while the side of the GlyChit-coating (right side, before and after testing) was not attacked.

References

[1] M. Stöter, D. A. Kunz, M. Schmidt, D. Hirsemann, H. Kalo, B. Putz, J. Senker, J. Breu, *Langmuir* **2013,** *29*, 1280.
[2] E. S. Tsurko, P. Feicht, C. Habel, T. Schilling, M. Daab, S. Rosenfeldt, J. Breu, *J. Membr. Sci.* **2017,** *540*, 212.
[3] E. S. de Alvarenga, *Biotechnology of biopolymers*, IntechOpen Limited, London, United Kingdom, **2011**.
[4] M. Wilson, S. E. Lindow, Phytopathology, **1993**, *83*, 117.
[5] Ø. Hammer, D. Harper, P. Ryan, *Palaeontol. Electronica* **2001,** *4*, 9.

6.3 Barriereeigenschaften gegenüber hochdiffusiver Gase

Christoph Habel[1], Evgeny S. Tsurko[1], Renee L. Timmins[1], Julia Hutschreuther[2], Raphael Kunz[1], Dominik Schuchardt[1], Sabine Rosenfeldt[1], Volker Altstädt[2], Josef Breu[1,*]

Lightweight Ultra-High Barrier Liners for Helium and Hydrogen

Reprinted with permission from
ACS Nano **2020**, *14* (6), 7018-7024.

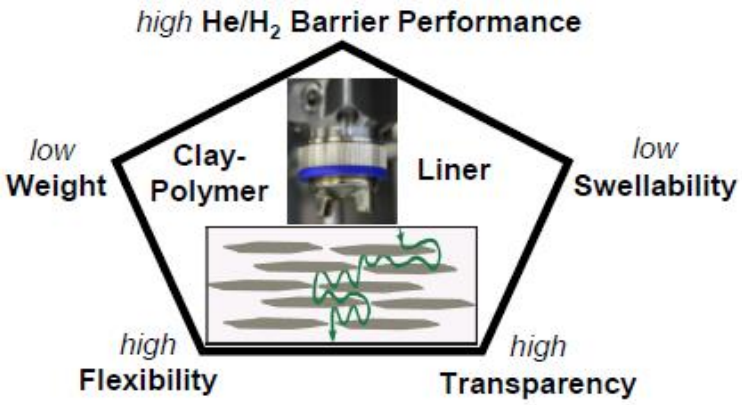

https://pubs.acs.org/articlesonrequest/AOR-BKECUMPCU55IYSKPBVZX

(*more informations:* https://helpfaqs.acs.org/2008/10/17/what-is-the-acs-articles-on-request-policy/)

[1] Bayerisches Polymer Institut und Fakultät für Chemie, Universität Bayreuth, Universitätsstraße 30, Bayreuth, 95447, Germany

[2] Lehrstuhl für Polymere Werkstoffe, Universität Bayreuth, Universitätsstraße 30, Bayreuth, 95447, Germany

*E-Mail: josef.breu@uni-bayreuth.de

Darstellung des Eigenanteils: Das Konzept der Arbeit wurde von *Prof. Dr. J. Breu* und mir erarbeitet. Von mir wurden die Auswertungen und deren Interpretation, die Messungen (Ausnahme SAXS) und alle Experimente durchgeführt. Die SAXS Messungen wurden von *Dr. S. Rosenfeldt* und *Dominik D. Schuchardt* durchgeführt und zusammen mit mir ausgewertet. Die Publikation wurde von mir geschrieben und mit *R. L. Timmins, J. Hutschreuther, Dr. S. Rosenfeldt, Prof. Dr. V. Altstädt* und *Prof. Dr. J. Breu* zur Einreichung überarbeitet. *Dr. E. Tsurko* und *R. Kunz* haben zur wissenschaftlichen Diskussion beigetragen. Mein Eigenanteil beträgt ca. 80%.

ACSNANO
www.acsnano.org

ARTICLE

Lightweight Ultra-High-Barrier Liners for Helium and Hydrogen

Christoph Habel, Evgeny S. Tsurko, Renee L. Timmins, Julia Hutschreuther, Raphael Kunz, Dominik D. Schuchardt, Sabine Rosenfeldt, Volker Altstädt, and Josef Breu*

Cite This: *ACS Nano* 2020, 14, 7018−7024 Read Online

ACCESS | Metrics & More | Article Recommendations | Supporting Information

ABSTRACT: **Upcoming efficient air-borne wind energy concepts and communication technologies applying lighter-than-air platforms require high-performance barrier coatings, which concomitantly and nonselectively block permeation not only of helium but also of ozone and water vapor. Similarly, with the emergence of green hydrogen economy, lightweight barrier materials for storage and transport of this highly diffusive gas are very much sought-after, particularly in aviation technology. Here the fabrication of ultraperformance nanocomposite barrier liners by spray coating lamellar liquid crystalline dispersions of high aspect ratio (∼20 000) silicate nanosheets mixed with poly(vinyl alcohol) on a PET substrate foil is presented. Lightweight nanocomposite liners with 50 wt % filler content are obtained showing helium and hydrogen permeabilities as low as 0.8 and 0.6 cm^3 μm m^{-2} day^{-1} atm^{-1}, respectively. This exhibits an improvement up to a factor of 4×10^3 as compared to high-barrier polymers such as ethylene vinyl alcohol copolymers. Furthermore, ozone resistance, illustrated by oxygen permeability measurements at elevated relative humidity (75% r.h.), and water vapor resistance are demonstrated. Moreover, the technically benign processing by spray coating will render this barrier technology easily transferable to real lighter-than-air technologies or irregular- and concave-shaped hydrogen tanks.**

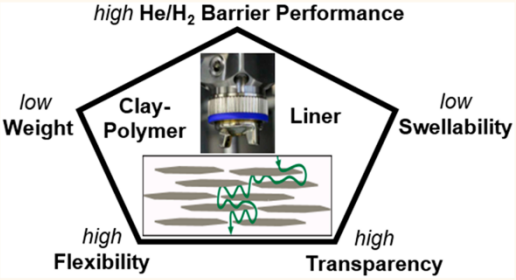

KEYWORDS: *clay nanosheets, liner, helium barrier, lighter-than-air technology, hydrogen economy*

Ultra-high-barrier encapsulation is key to the broad field of advanced technologies such as the packaging for oxygen- and moisture-sensitive perovskite-based solar cells or organic light-emitting diodes.[1−5] Such applications are most challenging because of the extremely low transmission rates required to ensure acceptable device lifetimes.[6,7] Highly diffusive gases such as hydrogen (H_2) and helium (He) pose another relevant and similar, if not more severe, challenge. The hydrogen economy is one of the most important branches of an economy based on renewable energy sources.[8−11] For aviation and transport applications, it requires alternative lightweight materials for transportation and storage of this otherwise promising fuel (Figure 1a).[12,13] Along the same lines, lighter-than-air vehicles attract much attention since they are of paramount importance for concepts regarding more efficient "windmills", which work at altitudes up to the region of jet streams and utilize the Magnus effect (Figure 1b).[14,15]

Such high-altitude platforms are likewise a prerequisite for upcoming communication networks that provide reliable and fast Internet access to everybody around the globe, even in isolated areas (Project Loon).[16,17] For these applications, the high diffusivity of He represents a crucial challenge, as permeability limits the duration of stay and/or the altitude at which equipment can be placed in the atmosphere. Besides barrier efficiency, being flexible and lightweight are additional prerequisites for barrier coatings suitable for these technologies. Mechanical strength and high ozone resistance are further specifications to be considered.[18] In this work, we measured the oxygen permeability as a representation of the ozone permeation into the liner material.

For rigid composite overwrapped pressure vessels (COPVs)[19] and hydrogen tanks in mobile applications, carbon fiber reinforced resin tanks are state-of-the-art. The necessary gas barrier is ensured by a metallic liner (type III) or polymeric

Received: February 25, 2020
Accepted: May 6, 2020
Published: May 6, 2020

https://dx.doi.org/10.1021/acsnano.0c01633
ACS Nano 2020, 14, 7018−7024

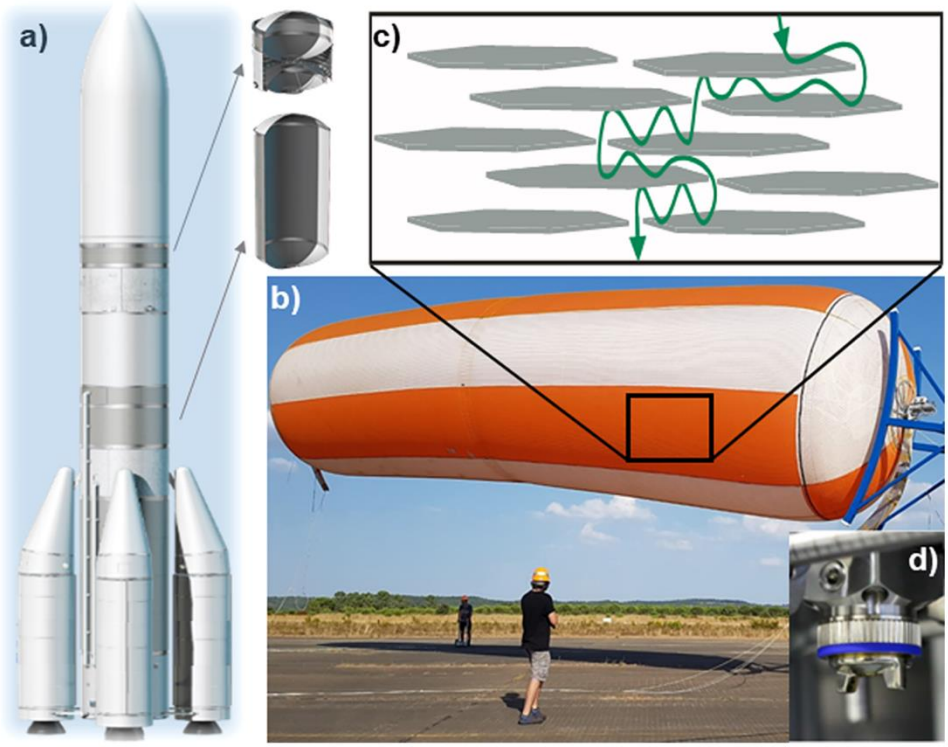

Figure 1. Applications requiring ultrahigh, lightweight, and flexible H_2 or He barrier liners: (a) Picture of Ariane 6 rocket with the integrated H_2 tank system (provided with permission from MT Aerospace and ArianeGroup). (b) Photo of Omnidea's lighter-than-air "wind mill" (provided with permission from Omnidea Lda.). (c) Scheme of the tortuous path created by impermeable, closely packed silicate nanosheets. (d) Technically benign processing *via* spray coating applying airbrush nozzles.

liners (type IV).[20] However, for aerospace applications, in particular, it is highly desired to replace the metal liner by a lightweight barrier material.[21] Metalized polymers, polymers with a titanium or aluminum liner, and neat high-barrier polymers represent the classical high-performance barrier materials. Best-performing polymeric materials are polyvinyl difluoride, polyester, polyamide, and ethylene vinyl alcohol copolymers (EVOH). For the latter, a 20 μm film, for instance, shows a He transmission rate as high as 160 $cm^3\ m^{-2}\ day^{-1}\ atm^{-1}$.[18,21−23]

Permeability can be hampered either by slowing down diffusion or by reducing the solubility of the permeate in the barrier material. Addressing the latter approach, more polar polymer materials such as EVOH or poly(vinyl alcohol) (PVA) limit the solubility of nonpolar gases such as oxygen, He, and H_2 and therefore demonstrate a great barrier of hydrophobic gases.[23−25] The performance is, however, great only at low relative humidity (r.h.). This is because polar polymers "swell" with water vapor and the water uptake at elevated r.h. leads to a drastic increase of permeability not only of water vapor but also of nonpolar gases such as oxygen, and thereby potentially also for He and H_2.[24,26] For instance, it has been shown by Grunlan *et al.* that the oxygen permeability (OP) of a PVA film increases by >500% when going from 0% to 55% r.h., resulting in an absolute oxygen transmission rate (OTR) for a 6 μm thick film of 3.1 $cm^3\ m^{-2}\ day^{-1}\ atm^{-1}$.[24] Clearly, the sensitivity to water vapor must be carefully evaluated, considering that great barriers reported at 0% r.h. do not necessarily represent solutions for real-world applications. Compounding with clay fillers not only reduces the permeability of the polymer matrix but has also been shown to reduce the sensitivity of the barrier to elevated r.h. significantly.[24]

The permeability of polymer films can be reduced in a nonselective manner by elongating the diffusion path of permeates *via* the incorporation of platy, crystalline, and therefore impermeable inorganic fillers.[22,27−33] This tortuous path approach has long been established by Cussler *et al.* (Figure 1 c) and is highly nonlinear with respect to both the filler content and the aspect ratio of the platy filler (eq 1).[34] Thus, for ultrahigh barriers, both should be pushed to the maximum.

$$P_{rel} = \frac{P}{P_0} = \left(1 + \mu\left(\frac{\alpha^2\phi^2}{1-\phi}\right)\right)^{-1} \quad (1)$$

with P = permeability of the filled polymer matrix, P_0 = permeability of the neat polymer matrix, ϕ = filler content (volume fraction), α = aspect ratio of the filler ($\alpha = \frac{d}{h}$; diameter d, height h) of the filler, and μ = geometrical factor related to the shape of the filler.[7,34]

The synthetic clay sodium fluorohectorite (NaHec, $[Na_{0.5}]^{inter}[Mg_{2.5}Li_{0.5}]^{oct}[Si_4]^{tet}O_{10}F_2$) belongs to a handful of layered compounds that exhibit the rare phenomenon of osmotic swelling,[35] with layered titanates,[36] layered antimony phosphates,[37,38] or graphene oxide[39] being other prominent examples. Osmotic swelling is a thermodynamically allowed

https://dx.doi.org/10.1021/acsnano.0c01633
ACS Nano 2020, 14, 7018−7024

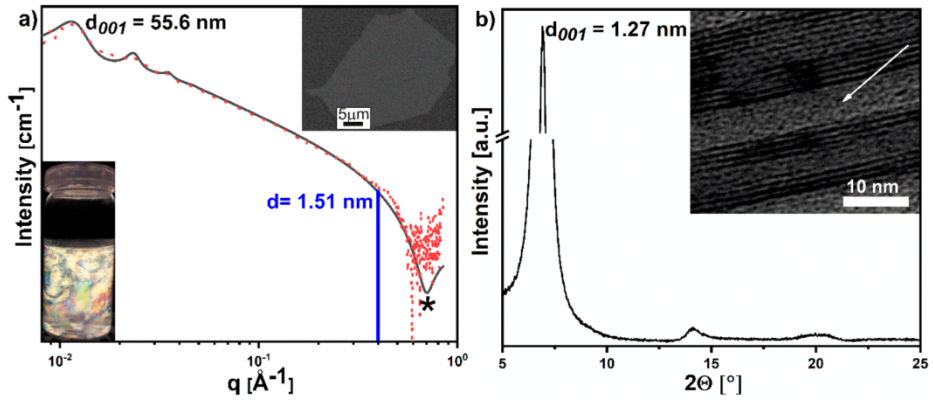

Figure 2. (a) SAXS pattern indicating a perfectly homogeneous NaHec/PVA suspension with individual NaHec nanosheets being uniformly separated to 55.6 nm. The observed minimum (star) corresponds to the thickness of single delaminated clay nanosheets (red dots: measurement, black line: fit). The insets show birefringence of the nematic clay suspension between cross polarizers and a scanning electron microscope (SEM) image of an individual NaHec nanosheet with a huge diameter of ~20 μm. (b) XRD pattern of the nanocomposite film indicating phase segregation upon drying. The inset shows a transmission electron microscope (TEM) image of the NaHec nanocomposite liner with perfectly aligned PVA intercalated domains and segregated PVA domains (white arrow).

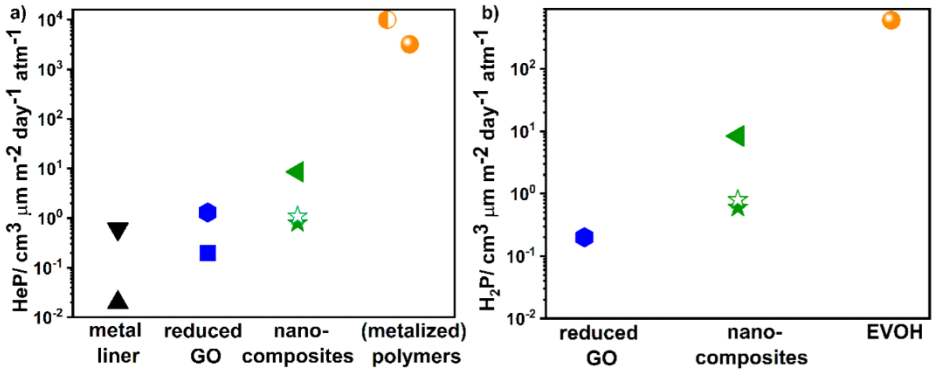

Figure 3. Comparison of different commercial and published barrier liners with respect to their helium (a) and hydrogen (b) permeabilities. The stars mark the NaHec nanocomposite with filled and unfilled symbols referring to 0% and 75% r.h., respectively. In blue: neat reduced GO with different thicknesses ■: 100 nm thickness, ⬢: 30 nm),[27] In black: titanium (▲) and aluminum as liner (▼).[21] In green: published layered silicate nanocomposite (◀).[22] In orange: state-of-the-art high-performance (metalized) polymers, such as aluminized polyurethane[22] (Al. PU, ◐) and EVOH[23] (●).

process[40] and consequently allows for a gentle, yet complete, delamination preserving the diameter from the nondelaminated state. This way, quantitative NaHec nanosheets with 1 nm thickness and a median diameter of 20 μm are obtained simply by immersing the synthesized material into deionized water. Contrary to graphene oxide (GO) sheets, for which it has been long established that holes are formed by overoxidation,[41−45] NaHec nanosheets are perfectly crystalline and free of structural and in-plane[46] defects. In this work we present a flexible, lightweight NaHec nanocomposite coating with commercial poly(vinyl alcohol) (PVA) as polymer matrix with exceptional helium and hydrogen barrier properties.

RESULTS AND DISCUSSION

Due to the large aspect ratio of ~20 000, rotation of the NaHec nanosheets is hindered, and the suspensions obtained by osmotic delamination represent nonisotropic, nematic phases.[47] Even the very dilute suspensions of NaHec applied here (0.125 wt % corresponding to 0.05 vol %) represent lamellar liquid crystalline phases[48] with cofacial nanosheets separated to >200 nm by strong electrostatic repulsion. This facilitates diffusion of PVA into the interlayer galleries, yielding perfectly homogeneous ternary nematic dispersions, as evidenced by small-angle X-ray scattering (SAXS, Figure 2a). To improve sensitivity, this SAXS pattern was recorded with a concentrated gel (total solid content 4.5 wt %), yielding a separation of 55.6 nm. The most important feature of the SAXS data is the lack of a peak at 1.51 nm (blue line in Figure 2a), which would indicate hydrated NaHec nanosheets being restacked.

Here we fabricated an ultrahigh He and H_2 barrier coating with 50 wt % filler content (NaHec) by applying this ternary aqueous dispersion with 0.25 wt % overall solid content (NaHec + PVA in H_2O) on a 36 μm polyethylene terephthalate (PET) substrate (details of the coating process are given in the Methods part) by spray coating (Figure 1d), resulting in a coating thickness of 1.5 μm. The X-ray diffraction pattern (XRD, Figure 2b) of the nanocomposite film showed one characteristic broad peak of semicrystalline PVA at $2\theta = 20°$.[49] With a filler content

https://dx.doi.org/10.1021/acsnano.0c01633
ACS Nano 2020, 14, 7018−7024

of 50 wt % (30 vol %) and a uniform distribution of 1 nm thick NaHec nanosheets into PVA, the expected separation of the nanosheets is 2.3 nm, corresponding to a d_{001} of 3.3 nm. Thus, the XRD pattern with the most prominent peak at 1.27 nm suggested phase segregation occurred during removal of the solvent (indicated by the arrow in Figure 2b), which fortunately had no adverse effect on the tortuous path created (Figure 1c), as evidenced by transmission rate measurements.

For the real application benchmarks, transmission rate requirements must be met. Depending on the particular material and the processing, the minimum thickness required to fabricate liners varies in order to obtain a product devoid of pinholes and having more or less tolerance to stress/strain caused by distortions typically encountered in the field. Transmission rates scale with thickness of the barrier liner applied. However, meeting the required benchmarks by increasing applied liner thickness beyond the described threshold minimum consequently makes the liners more brittle, less transparent, and, most considerably, heavier. Permeabilities normalized to 1 μm liner thickness (HeP, H_2P) are therefore the more appropriate value for comparison. The PET substrate is highly permeable for both He and H_2, with HeP and H_2P values as high as 62 640 and 31 100 cm^3 μm m^{-2} day^{-1} atm^{-1} (published units[27] were converted to cm^3 μm m^{-2} day^{-1} atm^{-1}), respectively. The NaHec nanocomposite liner showed permeabilities as low as 0.8 and 0.6 cm^3 μm m^{-2} day^{-1} atm^{-1} (Figure 3a,b). Additionally, the 1.5 μm thin coating is highly flexible due to intercalated PVA mechanically decoupling adjacent nanosheets (Figure S1). Moreover, please note that to the best of our knowledge all values reported in the literature have been measured at 0% r.h., a condition implausible in the targeted applications. For this reason, we investigated transmission rate measurements additionally to 0% r.h. at an elevated and realistic environmental r.h. of 75%. Despite being water-born, the HeP and H_2P values of the nanocomposite increased only slightly when going from 0% to 75% r.h. to 1.1 and 0.8 cm^3 μm m^{-2} day^{-1} atm^{-1}, respectively.

The NaHec nanocomposite far outperforms both high-performance polymers and metalized polymers as well as published nanocomposite liners.[22,23] Applying a rather low aspect ratio filler, montmorillonite, Grunlan *et al.*[22] were able to obtain encouraging results with a polyelectrolyte matrix. The permeability (HeP) at 0% r.h. of their best-published clay nanocomposite films, however, is expectedly 1 order of magnitude higher compared to the NaHec system that has been reported here. Measurements at more realistic humidities are lacking. Given the high hygroscopy of the polyelectrolyte matrix, a drastic breakdown of performance is likely at elevated r.h.

Other platy materials, such as neat GO films, have been successfully applied as gas barrier materials.[50] As reported by Joshi *et al.*[50] GO laminates are only vacuum-tight in the dry state. In contact with water, GO laminates act as molecular sieves by blocking penetration of molecules with radii larger than 4.5 Å.[50] This is due to overoxidation of graphitic layers caused by the harsh conditions of GO synthesis, leading to structural defects in the plane of the GO nanosheets.[41,42,44,45] The excellent performance of GO-based barrier films is thus limited to 0% r.h., as any increase of the interlayer gallery by swelling[42,51] triggers a significant increase in permeabilities at ambient humidities. Once the gallery between adjacent GO nanosheets swells large enough to allow lateral He/H_2 diffusion, self-standing GO films become selectively permeable for He/H_2 rather than blocking diffusion.[52]

The detrimental swelling can be eliminated by chemical reduction to reduced GO (rGO). These coatings made of neat rGO outperform NaHec nanocomposites at 0% r.h., in particular when applied in less defect-prone 100 nm thicknesses (Figure 3).[27] Obviously, the reduction step further adds to the production cost of the material. Another drawback of both, neat GO and rGO, nanosheets barrier coatings is the lack of mechanical decoupling by soft polymer interlayers, which will render them more brittle and prone to cracking when twisted or stretched.

As already described, for rigid COPVs[19] and hydrogen tanks in mobile applications, carbon fiber reinforced resin tanks are state-of-the-art. The necessary gas barrier is ensured by a metallic liner (type III) or polymeric liners (type IV).[20] However, even lightweight metals have relatively high densities (Ti: 4.5 gcm^{-3}, Al: 2.7 gcm^{-3}), and a rather thick liner is required to reduce pinholes. When using high barrier polymers such as EVOH or one of the other already mentioned polymers, the resulting tanks might be lighter, which is advantageous in both aviation and mobile applications. Nevertheless, much thicker barrier liners as compared to type III are also required with these materials to ensure adequate hydrogen permeabilities.

In applications such as lighter-than-air ballonets, which will be continuously distorted by gusts of wind, the flexibility of the barrier liner is of prime interest. Aluminizing the polymer matrix is one of the state-of-the-art procedures to ensure the barrier properties. Nevertheless, an aluminum barrier liner would have to be >40 times thicker and thereby much heavier than the NaHec nanocomposite liner to ensure the same helium barrier performance.[22,27] Moreover, metal liners of such thickness are brittle and prone to crack formation in applications that require flexibility.

Clearly, when considering collectively all material properties relevant for lighter-than-air platforms and lightweight H_2 barriers in a spider chart, the NaHec nanocomposite evolves as the most appropriate material available (Figure 4). The variables included in the spider chart are discussed point-to-point in detail in the following:

1. As shown, NaHec nanocomposite barrier liners show an ultrahigh He and H_2 barrier significantly better than

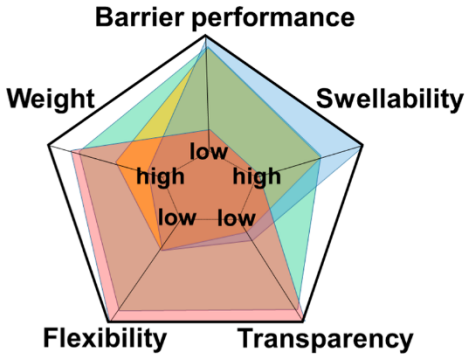

Figure 4. Qualitative comparison of the presented NaHec nanocomposite liner (green) and different commercial (metal liner: blue; high barrier polymers: red) and published all-inorganic barrier liners (rGO:yellow) with respect to properties relevant for lighter-than-air platforms and lightweight H_2 barriers. The bigger the area within the colored network, the more suitable the barrier material.

https://dx.doi.org/10.1021/acsnano.0c01633
ACS Nano 2020, 14, 7018−7024

published composite or high-performance polymer barriers.

2. In outdoor applications, barrier liners are inevitably exposed to various environmental factors. Water vapor and the sensitivity of the barrier to moisture are accordingly crucial. Therefore, we measured transmission rates not only at 0% r.h. but additionally at 75% r.h. (Figure 3). Quite promising results indicated moisture-related plasticization triggered only an insignificant increase by a factor <1.5 for both HeP and H_2P, with resulting permeabilities of 1.1 and 0.8 $cm^3\ \mu m\ m^{-2}\ day^{-1}\ atm^{-1}$, respectively. Furthermore, the water vapor resistance was demonstrated by a very low water vapor permeability of 2.4 g $\mu m\ m^{-2}\ day^{-1}\ atm^{-1}$ which far outperforms even hydrophobic types of EVOH (44 mol % ethylene, >660 g $\mu m\ m^{-2}\ day^{-1}\ atm^{-1}$, in original units as cited in the publication: $>10^{-12}$ g cm $cm^{-2}\ s^{-1}\ cmHg^{-1}$).[53] Moreover, the ozone resistance is of prime priority in air technologies. Oxygen transmission rates reported here have been measured at an elevated relative humidity of 75% to represent ozone permeation. The NaHec nanocomposite barrier liner showed excellent barrier properties with an oxygen permeability of $<7.5 \times 10^{-2}\ cm^3\ \mu m\ m^{-2}\ day^{-1}\ atm^{-1}$. This 1.5 μm thick coating undoubtedly outperforms high-performance EVOH (27 mol % ethylene, >6 $cm^3\ \mu m\ m^{-2}\ day^{-1}\ atm^{-1}$).[54]
3. NaHec nanocomposite coatings showed high flexibility and good wettability on the substrate, which was demonstrated by repeatedly wrapping the films around a tube ($r \sim 2.5$ cm) prior to measuring transmission rates (Figure S1). No crack formation or delamination of the coating from the substrate could be observed.
4. NaHec nanocomposites are comparatively lightweight as demonstrated by the following thought experiment:

   How thick would an EVOH barrier layer have to be to achieve comparable helium barrier performance compared to the nanocomposite liner?

   The EVOH barrier liner would have to be 0.4 cm thick to match the barrier properties of a 1 μm thin NaHec nanocomposite coating. Taking the densities of the different materials into account, this would correspond to 4.8 kg of EVOH (1.2 g cm^{-3}) per m^2, whereas a NaHec nanocomposite (~ 1.7 g cm^{-3}) would only amount to 1.7 g per m^2 for the same performance. Clearly, in lightweight applications, the NaHec nanocomposite would be advantageous. Similarly, the density of the NaHec nanocomposite is 1.6 and 2.6 times lower than Al and Ti, respectively.
5. Although transparency is not relevant for the particular applications in mind, it is included in this comparison for the sake of completeness. Compared to other liners, such as GO or rGO coatings, which become opaque, the transparency is not affected significantly for NaHec nanocomposites.[27] This is due to the perfectly parallel alignment of the clay nanosheets on any flat substrate.[25,30]

CONCLUSION

In summary, applying nematic suspensions of large aspect ratio synthetic clay by technical benign spray coating, NaHec nanocomposite liners have been prepared. These liners showed ultrahigh gas barrier properties with helium and hydrogen permeabilities in dry conditions as low as 0.8 and 0.6 $cm^3\ \mu m\ m^{-2}\ day^{-1}\ atm^{-1}$, respectively, which were not significantly affected by elevated r.h. This exceptional performance is attributed to NaHec as a nanofiller with a huge aspect ratio of ~20 000 as obtained by the thermodynamically allowed delamination *via* osmotic swelling. The resulting nematic suspensions allow fabricating an optimal tortuous path. For all lightweight applications, this combination of flexibility, transparency, and low application weight is required to meet barrier specifications, rendering this nanocomposite barrier liner superior to other materials that suffer from brittleness or high densities (Figure 4). Moreover, this waterborne barrier liner can be applied by technically benign processing such as spray coating[30] or slot-die coating.[55] Proper engineering of the spray coating including optimization of the nozzle will allow increasing the concentration of the nanocomposite dispersion and thus greatly reduce the number of spraying cycles.

METHODS

Materials. The employed $[Na_{0.5}]^{inter}[Mg_{2.5}Li_{0.5}]^{oct}[Si_4]^{tet}O_{10}F_2$ (NaHec) was obtained by melt synthesis followed by annealing according to an established literature procedure. The material featured a cation exchange capacity (CEC) of 1.27 mmol g^{-1}.[7,47,56,57] PVA Mowiol 20−98 (M_w = 125 000, 98.0−98.8 mol % hydrolysis) (Sigma-Aldrich, Germany) was used as polymer. A 10 g amount of PVA was dissolved in 90 g of Millipore water by heating at 95 °C for 4 h to obtain a 10 wt % solution. A corona-treated PET (36 μm) film was used as substrate (Bleher KG, Germany).

Fabrication of Nanocomposite Liners. Dried NaHec powder was first delaminated in an appropriate amount of Millipore water (0.5 wt %) and was then mixed dropwise with a PVA solution (10 wt %). Millipore water was added to adjust an overall solid content of 0.25 wt %, and the dispersion was stirred overnight. Spray coating has been performed with diluted dispersions (0.25 wt % overall solid content) by a fully automated spray coating system. This system was equipped with an SATA 4000 LAB HVLP 1.0 mm spray gun (SATA GmbH & Co. KG, Germany; 4 bar). The drying time was set to 120 s, the drying temperature to 50 °C, and the cycle number to 200. The number of cycles needed was determined by the rather low concentration chosen because of the viscosity of the nematic suspensions increasing rapidly with concentration. Afterward the nanocomposite coatings were dried at 80 °C (10^{-3} bar).

Nanocomposite Characterization. XRD patterns were obtained using nickel-filtered Cu Kα radiation (λ = 1.541 87 Å) on a Bragg−Brentano-type diffractometer (Empyrean) equipped with a Pixcel detector. All patterns were analyzed using Panalytical's Highscore Plus software.

All SAXS data were measured using the SAXS system "Ganesha AIR" (SAXSLAB, Denmark). The X-ray source of this laboratory-based system is a rotating anode F (copper, MicoMax 007HF, Rigaku Corporation, Japan). The data are recorded by a position-sensitive detector (PILATUS 300 K, Dectris). To cover the range of scattering vectors between 0.002 and 0.85 $Å^{-1}$, different detector positions were used. The measurements of the dispersions were performed in 1 mm glass capillaries (Hilgenberg, Germany) at room temperature. To improve the detection limit of the in-house machine, the dispersions (NaHec+PVA+H_2O) were first concentrated to ~4.5 wt % by centrifugation. The birefringence of the dispersions was evaluated with a self-made cross polarizer.

The diameters of the NaHec platelets were measured *via* scanning electron microscopy (SEM, Zeiss Leo 1530). Thin cross sections of the nanocomposite coatings were prepared with an Ion Slicer EM-09100IS (JEOL GmbH, Germany), and transmission electron micrographs (TEM) of the NaHec nanocomposite liner were obtained on a JEM-2200 FS (JEOL GmbH, Germany).

Oxygen transmission rates were determined on a Mocon OX-TRAN 2/21 instrument with a lower detection limit of 0.05 $cm^3\ m^{-2}\ day^{-1}\ atm^{-1}$. A mixture of 95% nitrogen and 5% hydrogen was used as carrier gas, and pure oxygen (>99.95%, Linde Sauerstoff

https://dx.doi.org/10.1021/acsnano.0c01633
ACS Nano 2020, 14, 7018−7024

3.5) as permeate gas. The measurements were conducted at 23 °C and 75% r.h.

Water vapor transmission rates were measured on a HiBarSens HBS 2.0 HT (Sempa Systems GmbH, Dresden, Germany) with a lower detection limit of 1×10^{-6} g m^{-2} day^{-1} at 23 °C and 75% r.h. For calculation of the water vapor permeability, the water vapor partial pressure has to be taken into account. At 100% r.h. it is 0.02811 bar, and thereby at 75% r.h. 0.021 bar. Helium and hydrogen transmission rates (HeTR, H_2TR) were measured applying the pressure difference method. Prior to measurement the nanocomposite films were wrapped around a tube (radius ∼ 2.5 cm) to demonstrate their flexibility (see also Figure S1). HeTR were measured with a gas transmission tester of the company Brugger Feinmechanik GmbH (measurement limit: 0.5 cm^3 m^{-2} day^{-1} atm^{-1}; resolution: 0.1 cm^3 m^{-2} day^{-1} atm^{-1}), and, moreover, HeTR and H_2TR were measured by Permlab. The relative humidity of 75% was set with a sulfuric acid solution (DIN 50008-2). The thickness of the PET substrate was measured with a high-accuracy Digimatic micrometer (Miitutoyo, Japan) with a measuring range of 0−25 mm and a resolution of 0.0001 mm, and the thicknesses of the resulting coated substrates were additionally measured by Permlab on nine different spots in the permeability area of 80 cm^2 according to DIN 53370.

ASSOCIATED CONTENT

Supporting Information

The Supporting Information is available free of charge at https://pubs.acs.org/doi/10.1021/acsnano.0c01633.

Figure S1: Wrapped PET foil coated with a NaHec nanocomposite liner (PDF)

AUTHOR INFORMATION

Corresponding Author

Josef Breu − *Bavarian Polymer Institute and Department of Chemistry, University of Bayreuth, Bayreuth 95447, Germany;* orcid.org/0000-0002-2547-3950; Phone: +49 921 55 2530; Email: Josef.Breu@uni-bayreuth.de; Fax: +49 921 55 2788

Authors

Christoph Habel − *Bavarian Polymer Institute and Department of Chemistry, University of Bayreuth, Bayreuth 95447, Germany*

Evgeny S. Tsurko − *Bavarian Polymer Institute and Department of Chemistry, University of Bayreuth, Bayreuth 95447, Germany*

Renee L. Timmins − *Bavarian Polymer Institute and Department of Chemistry, University of Bayreuth, Bayreuth 95447, Germany*

Julia Hutschreuther − *Department of Polymer Engineering, University of Bayreuth, Bayreuth 95447, Germany*

Raphael Kunz − *Bavarian Polymer Institute and Department of Chemistry, University of Bayreuth, Bayreuth 95447, Germany*

Dominik D. Schuchardt − *Bavarian Polymer Institute and Department of Chemistry, University of Bayreuth, Bayreuth 95447, Germany*

Sabine Rosenfeldt − *Bavarian Polymer Institute and Department of Chemistry, University of Bayreuth, Bayreuth 95447, Germany*

Volker Altstädt − *Department of Polymer Engineering, University of Bayreuth, Bayreuth 95447, Germany*

Complete contact information is available at: https://pubs.acs.org/10.1021/acsnano.0c01633

Notes

The authors declare no competing financial interest.

ACKNOWLEDGMENTS

The authors thank Florian Puchtler for synthesis of the synthetic clay and Marco Schwarzmann for SEM and TEM measurements and Ion Slicer preparation. We appreciate the support of the Keylab for Optical and Electron Microscopy of the Bavarian Polymer Institute (BPI). The authors want to thank the companies MT Aerospace/ArianeGroup and Omnidea Lda. for pictures of Ariane 6 and the lighter-than-air platform, respectively. This work was supported by the German Science Foundation (DFG) within the collaborative research project SFB 840.

REFERENCES

(1) Meng, L.; Zhang, Y.; Wan, X.; Li, C.; Zhang, X.; Wang, Y.; Ke, X.; Xiao, Z.; Ding, L.; Xia, R. Organic and Solution-Processed Tandem Solar Cells with 17.3% Efficiency. *Science* **2018**, *361*, 1094−1098.

(2) Bella, F.; Griffini, G.; Correa-Baena, J.-P.; Saracco, G.; Grätzel, M.; Hagfeldt, A.; Turri, S.; Gerbaldi, C. Improving Efficiency and Stability of Perovskite Solar Cells with Photocurable Fluoropolymers. *Science* **2016**, *354*, 203−206.

(3) Uddin, A.; Upama, M. B.; Yi, H.; Duan, L. Encapsulation of Organic and Perovskite Solar Cells: A Review. *Coatings* **2019**, *9*, 65−81.

(4) Seo, S.; Jeong, S.; Bae, C.; Park, N. G.; Shin, H. Perovskite Solar Cells with Inorganic Electron-and Hole-Transport Layers Exhibiting Long-Term (≥ 500 h) Stability at 85° C under Continuous 1 Sun Illumination in Ambient Air. *Adv. Mater.* **2018**, *30*, 1801010.

(5) Park, M. H.; Kim, J. Y.; Han, T. H.; Kim, T. S.; Kim, H.; Lee, T. W. Flexible Lamination Encapsulation. *Adv. Mater.* **2015**, *27*, 4308−4314.

(6) Lewis, J. Material Challenge for Flexible Organic Devices. *Mater. Today* **2006**, *9*, 38−45.

(7) Kunz, D. A.; Schmid, J.; Feicht, P.; Erath, J.; Fery, A.; Breu, J. Clay-Based Nanocomposite Coating for Flexible Optoelectronics Applying Commercial Polymers. *ACS Nano* **2013**, *7*, 4275−4280.

(8) Editorial, Hydrogen to the Rescue. *Nat. Mater.* **2018**, *17*, 565.

(9) Society, R. Options for Producing Low-Carbon Hydrogen at Scale. https://go.nature.com/2y1nHSZ (accessed October 31, 2019).

(10) Hu, Y. H.; Zhang, L. Hydrogen Storage in Metal-Organic Frameworks. *Adv. Mater.* **2010**, *22*, E117−E130.

(11) Assfour, B.; Leoni, S.; Seifert, G.; Baburin, I. A. Packings of Carbon Nanotubes-New Materials for Hydrogen Storage. *Adv. Mater.* **2011**, *23*, 1237−1241.

(12) Abdalla, A. M.; Hossain, S.; Nisfindy, O. B.; Azad, A. T.; Dawood, M.; Azad, A. K. Hydrogen Production, Storage, Transportation and Key Challenges with Applications: A Review. *Energy Convers. Manage.* **2018**, *165*, 602−627.

(13) Seayad, A. M.; Antonelli, D. M. Recent Advances in Hydrogen Storage in Metal-Containing Inorganic Nanostructures and Related Materials. *Adv. Mater.* **2004**, *16*, 765−777.

(14) Pavković, D.; Hoić, M.; Deur, J.; Petrić, J. Energy Storage Systems Sizing Study for a High-Altitude Wind Energy Application. *Energy* **2014**, *76*, 91−103.

(15) Penedo, R. J.; Pardal, T. C.; Silva, P. M. S.; Fernandes, N. M.; Fernandes, T. R. C. High Altitude Wind Energy from a Hybrid Lighter-Than-Air Platform Using the Magnus Effect. In *Airborne Wind Energy*; Springer: Heidelberg, 2013; pp 491−500.

(16) d'Oliveira, F. A.; Melo, F. C. L. d.; Devezas, T. C. High-Altitude Platforms—Present Situation and Technology Trends. *J. Aero. Technol. Manag.* **2016**, *8*, 249−262.

(17) Loon. Press. https://loon.com/press/ (accessed January 25, 2020).

(18) Zhai, H.; Euler, A. Material Challenges for Lighter-Than-Air Systems in High Altitude Applications. In *AIAA Meeting Paper (eISBN: 978-1-62410-067-3), AIAA 5th ATIO and 16th Lighter-Than-Air Sys Tech. and Balloon Systems Conferences*; American Institute of Aeronautics and Astronautics, 26.09.2005−28.09.2005; Arlington, VA: Online, 2012; AIAA 2005-7488, pp 1−12.

https://dx.doi.org/10.1021/acsnano.0c01633
ACS Nano 2020, 14, 7018−7024

(19) Kezirian, M.; Johnson, K.; Phoenix, S. Composite Overwrapped Pressure Vessels (COPV): Flight Rationale for the Space Shuttle Program. In *AIAA SPACE Forum (eISBN: 978-1-60086-953-2), AIAA SPACE 2011 Conference & Exposition*; American Institute of Aeronautics and Astronautics, 27.09.2011−29.09.2011; Long Beach, CA: Online, 2012, AIAA 2011-7363, pp 1−12.
(20) Barth, R. R.; Simmons, K. L.; San Marchi, C. Polymers for Hydrogen Infrastructure and Vehicle Fuel Systems. *Sandia Report* 2013, SAND2013-8904.
(21) Murray, B. R.; Leen, S. B.; Semprimoschnig, C. O.; Brádaigh, C. M. Ó. Helium Permeability of Polymer Materials as Liners for Composite Overwrapped Pressure Vessels. *J. Appl. Polym. Sci.* **2016**, *133*, 43675.
(22) Tzeng, P.; Lugo, E. L.; Mai, G. D.; Wilhite, B. A.; Grunlan, J. C. Super Hydrogen and Helium Barrier with Polyelectolyte Nanobrick Wall Thin Film. *Macromol. Rapid Commun.* **2015**, *36*, 96−101.
(23) EVAL Europe N.V. Permeating Gas. http://www.evalevoh.com/en/eval-properties/permeating-gas.aspx (accessed January 30, 2020).
(24) Grunlan, J. C.; Grigorian, A.; Hamilton, C. B.; Mehrabi, A. R. Effect of Clay Concentration on the Oxygen Permeability and Optical Properties of a Modified Poly (Vinyl Alcohol). *J. Appl. Polym. Sci.* **2004**, *93*, 1102−1109.
(25) Tsurko, E. S.; Feicht, P.; Habel, C.; Schilling, T.; Daab, M.; Rosenfeldt, S.; Breu, J. Can High Oxygen and Water Vapor Barrier Nanocomposite Coatings Be Obtained with a Waterborne Formulation? *J. Membr. Sci.* **2017**, *540*, 212−218.
(26) Mo, C.; Yuan, W.; Lei, W.; Shijiu, Y. Effects of Temperature and Humidity on the Barrier Properties of Biaxially-Oriented Polypropylene and Polyvinyl Alcohol Films. *J. Appl. Packag. Res.* **2014**, *6*, 40−46.
(27) Su, Y.; Kravets, V.; Wong, S.; Waters, J.; Geim, A.; Nair, R. Impermeable Barrier Films and Protective Coatings Based on Reduced Graphene Oxide. *Nat. Commun.* **2014**, *5*, 1−5.
(28) Möller, M. W.; Lunkenbein, T.; Kalo, H.; Schieder, M.; Kunz, D. A.; Breu, J. Barrier Properties of Synthetic Clay with a Kilo-Aspect Ratio. *Adv. Mater.* **2010**, *22*, 5245−5249.
(29) Möller, M. W.; Kunz, D. A.; Lunkenbein, T.; Sommer, S.; Nennemann, A.; Breu, J. UV-Cured, Flexible, and Transparent Nanocomposite Coating with Remarkable Oxygen Barrier. *Adv. Mater.* **2012**, *24*, 2142−2147.
(30) Tsurko, E. S.; Feicht, P.; Nehm, F.; Ament, K.; Rosenfeldt, S.; Pietsch, I.; Roschmann, K.; Kalo, H.; Breu, J. Large Scale Self-Assembly of Smectic Nanocomposite Films by Doctor Blading *versus* Spray Coating: Impact of Crystal Quality on Barrier Properties. *Macromolecules* **2017**, *50*, 4344−4350.
(31) Eckert, A.; Rudolph, T.; Guo, J.; Mang, T.; Walther, A. Exceptionally Ductile and Tough Biomimetic Artificial Nacre with Gas Barrier Function. *Adv. Mater.* **2018**, *30*, 1802477.
(32) Yang, Y. H.; Bolling, L.; Priolo, M. A.; Grunlan, J. C. Super Gas Barrier and Selectivity of Graphene Oxide-Polymer Multilayer Thin Films. *Adv. Mater.* **2013**, *25*, 503−508.
(33) Yoo, B. M.; Shin, H. J.; Yoon, H. W.; Park, H. B. Graphene and Graphene Oxide and Their Uses in Barrier Polymers. *J. Appl. Polym. Sci.* **2014**, *39628*, 1−23.
(34) DeRocher, J. P.; Gettelfinger, B. T.; Wang, J.; Nuxoll, E. E.; Cussler, E. Barrier Membranes with Different Sizes of Aligned Flakes. *J. Membr. Sci.* **2005**, *254*, 21−30.
(35) Lerf, A. Storylines in Intercalation Chemistry. *Dalton Trans.* **2014**, *43*, 10276−10291.
(36) Wang, L.; Sasaki, T. Titanium Oxide Nanosheets: Graphene Analogues with Versatile Functionalities. *Chem. Rev.* **2014**, *114*, 9455−9486.
(37) Davidson, P.; Penisson, C.; Constantin, D.; Gabriel, J.-C. P. Isotropic, Nematic, and Lamellar Phases in Colloidal Suspensions of Nanosheets. *Proc. Natl. Acad. Sci. U. S. A.* **2018**, *115*, 6662−6667.
(38) Gabriel, J.-C. P.; Camerel, F.; Lemaire, B. J.; Desvaux, H.; Davidson, P.; Batail, P. Swollen Liquid-Crystalline Lamellar Phase Based on Extended Solid-Like Sheets. *Nature* **2001**, *413*, 504−508.
(39) Liu, Y.; Xu, Z.; Gao, W.; Cheng, Z.; Gao, C. Graphene and Other 2D Colloids: Liquid Crystals and Macroscopic Fibers. *Adv. Mater.* **2017**, *29*, 1606794.
(40) Daab, M.; Eichstaedt, N. J.; Edenharter, A.; Rosenfeldt, S.; Breu, J. Layer Charge Robust Delamination of Organo-Clays. *RSC Adv.* **2018**, *8*, 28797−28803.
(41) Eigler, S.; Hirsch, A. Chemistry with Graphene and Graphene Oxide—Challenges for Synthetic Chemists. *Angew. Chem., Int. Ed.* **2014**, *53*, 7720−7738.
(42) Dimiev, A. M.; Eigler, S. *Graphene Oxide: Fundamentals and Applications*; John Wiley & Sons, Inc.: Chichester, West Sussex, 2017; pp 3−224.
(43) Hofmann, U.; König, E. Untersuchungen über Graphitoxyd. *Z. anorg. allg. Chem.* **1937**, *234*, 311−336.
(44) Feicht, P.; Eigler, S. Defects in Graphene Oxide as Structural Motifs. *ChemNanoMat* **2018**, *4*, 244−252.
(45) Feicht, P.; Biskupek, J.; Gorelik, T. E.; Renner, J.; Halbig, C. E.; Maranska, M.; Puchtler, F.; Kaiser, U.; Eigler, S. Brodie's or Hummers' Method: Oxidation Conditions Determine the Structure of Graphene Oxide. *Chem. - Eur. J.* **2019**, *25*, 8955−8959.
(46) Kunz, D.; Erath, J.; Kluge, D.; Thurn, H.; Putz, B.; Fery, A.; Breu, J. In-Plane Modulus of Singular 2:1 Clay Lamellae Applying a Simple Wrinkling Technique. *ACS Appl. Mater. Interfaces* **2013**, *5*, 5851−5855.
(47) Stöter, M.; Kunz, D. A.; Schmidt, M.; Hirsemann, D.; Kalo, H.; Putz, B.; Senker, J.; Breu, J. Nanoplatelets of Sodium Hectorite Showing Aspect Ratios of ≥ 20 000 and Superior Purity. *Langmuir* **2013**, *29*, 1280−1285.
(48) Rosenfeldt, S.; Stöter, M.; Schlenk, M.; Martin, T.; Albuquerque, R. Q.; Förster, S.; Breu, J. In-Depth Insights into the Key Steps of Delamination of Charged 2D Nanomaterials. *Langmuir* **2016**, *32*, 10582−10588.
(49) Gaume, J.; Taviot-Gueho, C.; Cros, S.; Rivaton, A.; Therias, S.; Gardette, J.-L. Optimization of PVA Clay Nanocomposite for Ultra-Barrier Multilayer Encapsulation of Organic Solar Cells. *Sol. Energy Mater. Sol. Cells* **2012**, *99*, 240−249.
(50) Joshi, R.; Carbone, P.; Wang, F. C.; Kravets, V. G.; Su, Y.; Grigorieva, I. V.; Wu, H.; Geim, A. K.; Nair, R. R. Precise and Ultrafast Molecular Sieving through Graphene Oxide Membranes. *Science* **2014**, *343*, 752−754.
(51) Hofmann, U.; Frenzel, A. Quellung von Graphit und die Bildung von Graphitsäure. *Ber. Dtsch. Chem. Ges. B* **1930**, *63*, 1248−1262.
(52) Nair, R.; Wu, H.; Jayaram, P.; Grigorieva, I.; Geim, A. Unimpeded Permeation of Water through Helium-Leak-Tight Graphene-Based Membranes. *Science* **2012**, *335*, 442−444.
(53) Zhang, Z.; Britt, I. J.; Tung, M. A. Permeation of Oxygen and Water Vapor through EVOH Films as Influenced by Relative Humidity. *J. Appl. Polym. Sci.* **2001**, *82*, 1866−1872.
(54) EVAL Europe N.V. Relative Humidity. http://www.evalevoh.com/en/eval-properties/barrier-to-oxygen/relative-humidity.aspx (accessed January 29, 2020).
(55) Ding, X.; Liu, J.; Harris, T. A. A Review of the Operating Limits in Slot Die Coating Processes. *AIChE J.* **2016**, *62*, 2508−2524.
(56) Breu, J.; Seidl, W.; Stoll, A. J.; Lange, K. G.; Probst, T. U. Charge Homogeneity in Synthetic Fluorohectorite. *Chem. Mater.* **2001**, *13*, 4213−4220.
(57) Kalo, H.; Möller, M. W.; Ziadeh, M.; Dolejš, D.; Breu, J. Large Scale Melt Synthesis in an Open Crucible of Na-Fluorohectorite with Superb Charge Homogeneity and Particle Size. *Appl. Clay Sci.* **2010**, *48*, 39−45.

https://dx.doi.org/10.1021/acsnano.0c01633
ACS Nano 2020, 14, 7018−7024

Supporting Information

Lightweight Ultra-High-Barrier Liners for Helium and Hydrogen

Christoph Habel[1], Evgeny S. Tsurko[1], Renee L. Timmins[1], Julia Hutschreuther[2], Raphael Kunz[1], Dominik D. Schuchardt[1], Sabine Rosenfeldt[1], Volker Altstädt[2], and Josef Breu[1,*]

[1] Bavarian Polymer Institute and Department of Chemistry, University of Bayreuth, Universitätsstraße 30, Bayreuth, 95447, Germany

[2] Department of Polymer Engineering, University of Bayreuth, Universitätsstraße 30, Bayreuth, 95447, Germany

*Corresponding Author

E-Mail address: Josef.Breu@uni-bayreuth.de, Tel: +49 921 55 2530, Fax: +49 921 55 2788

Figure

Figure S1. Wrapped PET foil (radius ~2.5 cm) coated with NaHec nanocomposite liner, showing no delamination of the substrate and no crack formation.

6.4 Einfluss von *Ultraconfinement* auf Kompositbarrieren

Theresa Schilling†, Christoph Habel†, Sabine Rosenfeldt, Maximilian Röhrl, Josef Breu*

† T.S. und C.H.: zu gleichen Teilen beigetragen (*equally contributed*).

Impact of Ultraconfinement on Composite Barriers

Reprinted with permission from
ACS Appl. Polym. Mater. **2020**, *2* (7), 3010-3015.

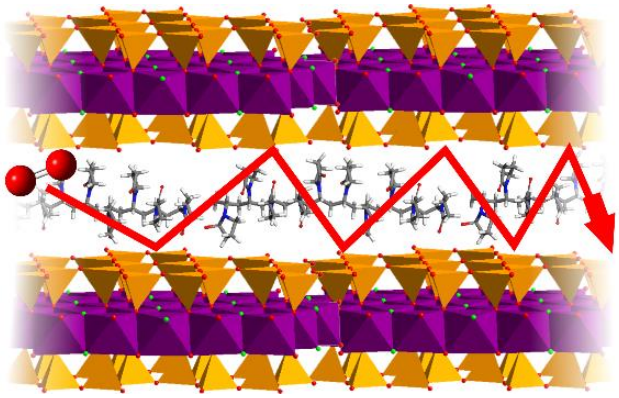

https://pubs.acs.org/articlesonrequest/AOR-VTX6WSKFNED55Q5ARKE8

(*more informations:* https://helpfaqs.acs.org/2008/10/17/what-is-the-acs-articles-on-request-policy/)

Bayerisches Polymer Institut und Fakultät für Chemie, Universitätsstraße 30, Bayreuth, 95447, Germany

*E-Mail: josef.breu@uni-bayreuth.de

Darstellung des Eigenanteils: Das Konzept der Publikation wurde von *Prof. Dr. J. Breu*, *T. Schilling* und mir erarbeitet. Von mir wurden die Barrieremessungen durchgeführt, ausgewertet und interpretiert. Die Hybridfilme wurden von *T. Schilling* präpariert und analysiert. Die SAXS-Messungen wurden durch *Dr. S. Rosenfeldt* durchgeführt. Maximilian Röhrl reproduzierte die Barrieremessungen und trug zur wissenschaftlichen Diskussion bei. Die Publikation wurde von *T. Schilling* und mir geschrieben und zusammen mit *Prof. Dr. J. Breu* zur Einreichung überarbeitet. Mein Eigenanteil beträgt ca. 45%.

ACS APPLIED POLYMER MATERIALS

pubs.acs.org/acsapm Article

Impact of Ultraconfinement on Composite Barriers

Theresa Schilling,† Christoph Habel,† Sabine Rosenfeldt, Maximilian Röhrl, and Josef Breu*

Cite This: ACS Appl. Polym. Mater. 2020, 2, 3010−3015 Read Online

ACCESS | Metrics & More | Article Recommendations | Supporting Information

ABSTRACT: Flexible optoelectronic packaging is required to provide an ultrahigh barrier to oxygen under ambient conditions, meaning at a relative humidity above 50%. Many polymeric packaging materials, however, adsorb water vapor and the consequential softening is detrimental for the barrier properties. Despite its importance, systematic studies on the impact of the relative humidity (RH) on the oxygen permeability (OP) of clay nanocomposite barriers and convincing evidence for a potential hydrophobization due to compounding with nanosheets are scarce. Especially at filler contents greater than 30 vol %, as required for ultrahigh barriers, a severe confinement is imposed on interlayered polymer and thus its permeability properties are expected to be significantly modified as compared to the bulk. A systematic study of the relation between permeability and RH requires nanocomposite films that differ in filler content but at the same time are comparable with respect to aspect ratio, filler type, quality of texture, and one-dimensional crystallinity. By applying water-soluble polyvinylpyrrolidone (PVP) and ultrahigh-aspect-ratio synthetic clay (sodium fluorohectorite), we were able to prepare hybrid samples that meet these requirements for the first time. By spray coating, the components self-assemble into hybrid films of one-dimensional crystalline Bragg stacks. Two such hybrid films with filler contents of 31 and 40 vol % were fabricated. Indeed, the filler content was found to greatly affect the dependence of the oxygen permeability on RH. Comparing the performance of these two films, the OP in the 40 vol % sample was four times lower than would be expected because of the increase in filler content. To the best of our knowledge, this is the first convincing evidence for a pronounced confinement effect on the permeability.

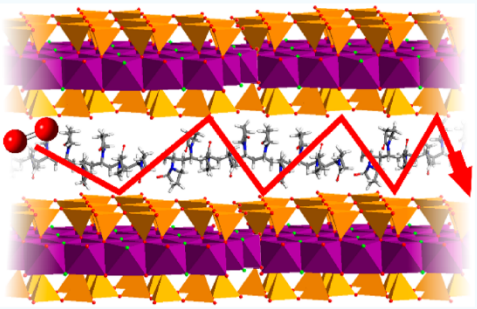

KEYWORDS: *clay, hybrid films, swelling, Cussler, oxygen permeability, ultraconfinement*

INTRODUCTION

Although having prominent uses in the electronics, automotive, and building sectors, nearly 40% of polymers are consumed in the packaging sector.[1] Besides mechanical protection against shocks and vibrations, the main application-relevant feature of packaging material is the oxygen barrier that protects food from aerobic microbial spoilage and biochemical reactions like fat oxidation.[2] Best-before dates of packed food strongly correlate with the barrier performance of the packaging. Optoelectronic devices are even more sensitive to oxygen, leading to barrier requirements being orders of magnitude higher than for food packaging.

In general, the permeability (P) of the barrier coating is given by $P = SD$, where S and D are solubility and diffusivity constants of the permeates, respectively.[3] S depends on the affinity of permeates to the matrix wherein polar molecules are generally more soluble in polar than in nonpolar matrices and vice versa. At low relative humidity (RH), hydrophilic polymers possess excellent barrier properties for hydrophobic permeates like oxygen (see poly(vinyl alcohol) (PVA)[4] in Figure 1). However, at ambient conditions, the packaging will swell with water vapor, which inevitably leads to an increase in oxygen permeability (OP)[5,6] because dissolved water mole-

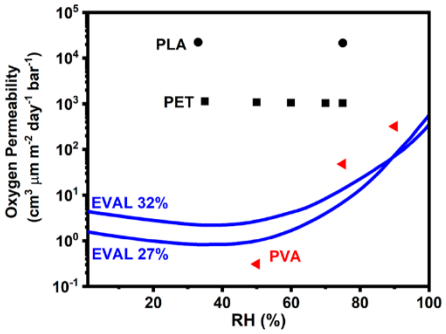

Figure 1. Nonlinear dependence of oxygen permeability of two EVAL types (% corresponds to the ethylene content).[15] Polyethylene terephthalate (PET, own measurement), PVA,[4] and polylactic acid (PLA)[16] values are giving for comparison.

Received: April 29, 2020
Accepted: May 28, 2020
Published: June 12, 2020

cules act as softener and increase segment mobility.[7] Alternatively, D can be reduced by the incorporation of crystalline, and thus impermeable, fillers like layered silicates (clay), which increase the diffusion path (tortuous pathway). For semidiluted systems with high-aspect-ratio fillers, Cussler's theory[8] predicts that D depends nonlinearly on the aspect ratio (α) and volume fraction (ϕ) of the filler (eq 1).

$$P_{rel} = \frac{P}{P_0} = \left(1 + \mu\left(\frac{\alpha^2\phi^2}{1-\phi}\right)\right)^{-1} \quad (1)$$

with P = permeability of the filled polymer matrix, P_0 = permeability of the neat polymer matrix, ϕ = filler content (volume fraction), α = aspect ratio ($\alpha = d/h$, diameter d, height h) of the filler, and μ = geometrical factor of the filler depending on its shape.

Cussler's theory assumes that confinement of the polymer matrix, interlayered between clay nanosheets, does not alter its properties. In particular, it is assumed that the permeability of interlayered and bulk polymer is the same. At filler contents greater than 30 vol %, as required for ultrahigh barriers, the confinement of the polymer is, however, quite severe: Given a thickness of a single clay nanosheet of 1 nm and an equidistant arrangement as required for a homogeneous nanocomposite, the slit between adjacent nanosheets at 31 vol % is as narrow as 2 nm. This easily falls beneath the interlayered polymer's radius of gyration. Clearly, such a severe confinement is expected to significantly alter the polymer properties as compared to the bulk properties. In the literature, the impact of the confinement on the segment mobility,[9] glass transition temperature,[10−12] and viscosity[13] was proven. In this paper, we will now investigate the role of polymer confinement on permeability.

In commercial packaging materials, the moisture sensitivity of the barrier performance is compensated by laminating the hydrophilic polymer with a more hydrophobic polymer.[14] Alternatively, the hydrophobicity can be tuned via copolymerization. For instance, copolymers like poly(ethylene-*co*-vinyl alcohol) (EVOH) or laminates of it with polyethylene are widely used high-performance polymers for flexible barrier packaging with low OP.[15]

The moisture sensitivity of EVOH barrier films can be tuned by adjusting the ratio of the two monomers (Figure 1).[15,17,18] More hydrophilic EVOH (f.e. EVAL with an ethylene content of 27%) show lower OP at low and medium RH but at the same time are more sensitive to increasing RH. Consequently, at some RH values, the barrier performance of a more hydrophobic EVOH (f.e. EVAL with an ethylene content of 32%) becomes superior. To meet the requirements of a particular application with given RH specification, the ethylene content has to be adjusted. Quite counterintuitively, both EVAL types show a minor but significant decrease in OP between 0 and 40% RH (Figure 1). This phenomenon has been attributed to adsorption of water molecules filling up of free volume, thus leading to a reduced OP due to a lower diffusity.[19,20]

Clays not only reduce permeability in a nonselective manner via the tortuous path mechanism but also have been claimed to hydrophobize polar, water-soluble polymer matrices. It has been shown that the critical RH, where swelling followed by a significant loss of oxygen barrier sets in, can be shifted to higher RH by compounding with sodium montmorillonite.[6,21,22] Choudalakis and Gotsis have suggested that this might be related to a modification of the structure and/or the crystallinity of the polymer matrix and a change of the free volume.[23] The incorporation of clay into a spider silk matrix was shown to increase the amount of crystalline ß-sheet domains in addition to a reduction in free volume and sensitivity to water.[24] This hydrophobization effect was furthermore observed for a PVA-modified clay nanocomposite[4] where swelling was shown to be retarded, resulting in low oxygen transmission rates at elevated RH. The swelling of nanocomposite films with a one-dimensional (1D) regular stacking (Bragg stacks) of polymer (polyethylenimine and poly(acrylic acid)) and a synthetic sodium fluorohectorite was found to be influenced by the quality of 1D crystallinity. The better ordered, the better the barrier observed at 38 °C and 90% RH.[25] Because of partial phase segregation, the volume of polymer matrix in the smectic domains was, however, invariant to the filler content. Consequently, this segregation did not allow for a systematic study on the impact of the volume ratio of clay to polymer matrix on the dependence of OP on RH.

With polyvinylpyrrolidone (PVP) as polymer matrix, phase segregation is not observed and 1D periodically homogeneous nanocomposite films (Bragg stacks) are obtained. These Bragg stack films represent a model system, which allow us to realize two different polymer confinements (with polymer contents of 31 vol % and 40 vol %) without affecting the 1D crystallinity, quality of texture, aspect ratio, or filler type. These materials allow, for the first time, a study on the swelling behavior of PVP in the confined space of two 1D crystalline Bragg stack films with varying clay content. Moreover, the impact of the confinement effect and the moisture sensitivity on the OP is studied and compared for two otherwise comparable nanocomposites.

EXPERIMENTAL SECTION

Materials. The synthetic clay sodium fluorohectorite (Hec, $[Na_{0.5}]^{inter}[Mg_{2.5}Li_{0.5}]^{oct}[Si4]^{tet}O_{10}F_2$) was obtained via melt synthesis followed by long-term annealing, according to an established procedure.[26,27] PVP (M_w = 40 000 g mol^{-1}) was provided by Sigma-Aldrich.

Film Preparation and Characterization. The as-synthesized Hec was delaminated by immersing it into Millipore water (0.2 vol %). PVP was dissolved in Millipore water (0.8 vol %) and added in the desired volume ratio. The suspension was mixed for at least 1 day in an overhead shaker. The quality of the suspension, in terms of homogeneity, was crosschecked by small-angle X-ray scattering (SAXS).

The nanocomposite films sprayed on a PET foil (36 μm, Bleher Folientechnik, Germany) were prepared by employing a fully automatic spray coating system. Every spraying cycle is followed by a drying cycle of 90 s at a temperature of 55 °C. The films were characterized by X-ray diffraction (XRD), transmission electron microscopy (TEM), and thermogravimetric analysis (TGA). Oxygen transmission rates (OTR) were measured on a Mocon OX-TRAN 2/21 (XL) instrument (Minneapolis, USA). Additional information about the sample preparation and characterization methods can be found in Sections S1 and S2.

RESULTS AND DISCUSSION

Synthetic sodium fluorohectorite (Hec, $[Na_{0.5}]^{inter}[Mg_{2.5}Li_{0.5}]^{oct}[Si_4]^{tet}O_{10}F_2$) is an excellent material for barrier applications. Hec shows the rare phenomenon of osmotic swelling. By immersing the Hec crystals into deionized water, osmotic swelling allows for complete and gentle delamination of the Hec crystals into 1 nm thick nanosheets while preserving the large diameter of 20 μm.[27] This way,

https://dx.doi.org/10.1021/acsapm.0c00456
ACS Appl. Polym. Mater. 2020, 2, 3010−3015

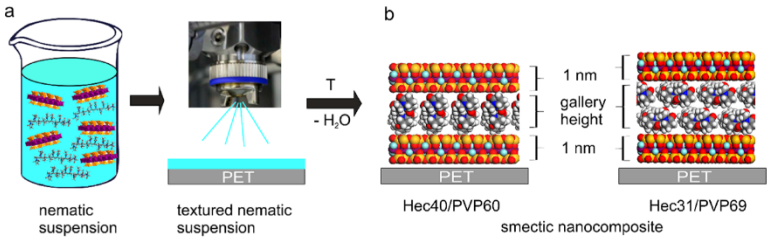

Figure 2. Schematic of the processing method of the perfectly ordered Hec/PVP Bragg stack film. (a) Homogeneous ternary nematic dispersion comprising Hec, PVP, and water. The ternary dispersion spray coated on a corona-treated PET foil. (b) Upon drying, the components self-assemble into a hybrid film where PVP chains are confined in the interlayer space between two 1 nm thick nanosheets. The gallery heights are 1.3 and 2.0 nm for Hec40/PVP60 and Hec31/PVP69, respectively. The observed gallery heights correspond to a monolayer and a bilayer of PVP for Hec40/PVP60 and Hec31/PVP69, respectively.

highly flexible platy fillers with high aspect ratio (>20 000) are obtained without needing brute force sonication or purification. Because of the large aspect ratio, rotation of the nanosheets in suspension is hindered. Therefore, even very dilute suspensions of Hec (<1 vol %) form nematic phases.[28]

As reported for titanate nanosheets,[29] dilute aqueous dispersions of negatively charged Hec nanosheets adopt a cofacial arrangement because of strong electrostatic repulsion. In this nematic state, adjacent clay nanosheets are not only held in a coherent cofacial geometry but are also separated to long distances determined by the clay content, typically exceeding 50 nm.[28] Mixing this Hec dispersion with different amounts of an aqueous PVP solution allows the polymer to diffuse between adjacent Hec sheets (Figure 2a), yielding a perfectly homogeneous nematic hybrid phase consisting of water, Hec, and PVP, as verified by a basal series being observed in the SAXS traces (Figure 3).

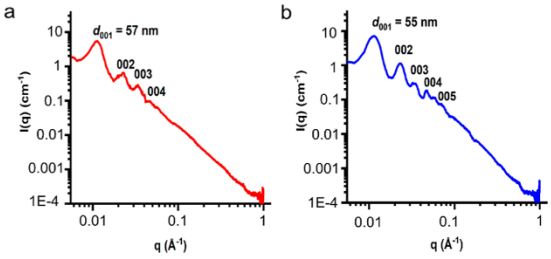

Figure 3. One-dimensional SAXS pattern of the concentrated gel sample (a) Hec40/PVP60 and (b) Hec31/PVP69. The varying layer separations observed are related to the clay content of the suspension rather than the Hec/PVP ratio.

Because of the transverse flexibility[30] of the 1 nm thin clay sheets and the huge aspect ratio of ~20 000, upon spray coating and subsequent drying the components self-assembled into 1D crystalline (Bragg-stack or smectic film[31]) nanocomposite films aligned parallel to the substrate (Figure 2b). At high filler content, the confinement of the polymer chains reaches a point where the height of the gallery between the nanosheets is the same order of magnitude as the molecular size of a polymer chain. Because the polymer matrix will always try to arrange itself in a dense packing between the nanosheets, only distinct polymer volumes, which depend on the diameter of a given polymer chain, allow for a regular stacking. The packing/size requirements and volume ratios match only for particular filler contents (31 and 40 vol %). Only then may homogeneous, 1D crystalline nanocomposite films (Figure 4)[25,31] be obtained, resulting in gallery heights (PVP layer thickness) of 1.3 and 2.0 nm, respectively. Here, the two samples were denoted as Hec31/PVP69 and Hec40/PVP60, with the numbers indicating the volume fractions, as crosschecked by TGA (Figure S1 and Table S1).

The XRD patterns of the hybrid films show rational 00*l* series with sharp and intense basal reflections up to the ninth order (Figure 4a, b). According to Meuring's rules,[32] the quality of the 1D crystalline order is further confirmed by a low coefficient of variation[32] and a small full width at half-maximum (Table S1). For Hec/PVP nanocomposites, phase segregation can safely be ruled out as the observed gallery heights were in accordance with the volume ratios (for details, see the Supporting Information) applied for fabricating the films. This perfect periodic homogeneity over large areas is further confirmed by TEM micrographs (Figure 4c, d). The nanocomposite films therefore may alternatively be considered as single-phase hybrid materials, of which we recently characterized the thermomechanical coupling.[33]

The two nanocomposite films with a filler content of 31 and 40 vol % are comparable in terms of crystalline order, homogeneity, type of polymer matrix and filler, aspect ratio of the filler, and the quality of texture but differ solely in the filler content. By comparing these two well-defined hybrid materials, the influence of the confinement on the moisture sensitivity can be systematically evaluated. Given the 1D crystallinity, the monitoring of swelling is particularly easy. With stepwise increase in the RH, both hybrid films swelled significantly as indicated by increasing gallery height (Figure 5a). Normalizing the increase to the gallery height at 0% RH showed that the water uptake is almost identical for both films (Figure 5b). For the less-filled hybrid film (Hec31/PVP69), the relative change in PVP volume is slightly higher than for the more-filled hybrid film (Hec40/PVP60), but only differs by less than 15%.

This observation is somewhat in contrast to a literature report,[34] where a more pronounced swelling was suggested when PVP was deposited alternating with montmorillonite clay via layer by layer (LbL) deposition. The LbL films, however, represent laminates of pure clay layers alternating with pure polymer layers, a segregated structure quite different from the hybrids investigated here. Comparing the swelling behavior of Hec40/PVP60 and Hec31/PVP69 suggested that increasing the Hec content reduces water vapor adsorption of the hybrid films slightly.

https://dx.doi.org/10.1021/acsapm.0c00456
ACS Appl. Polym. Mater. 2020, 2, 3010−3015

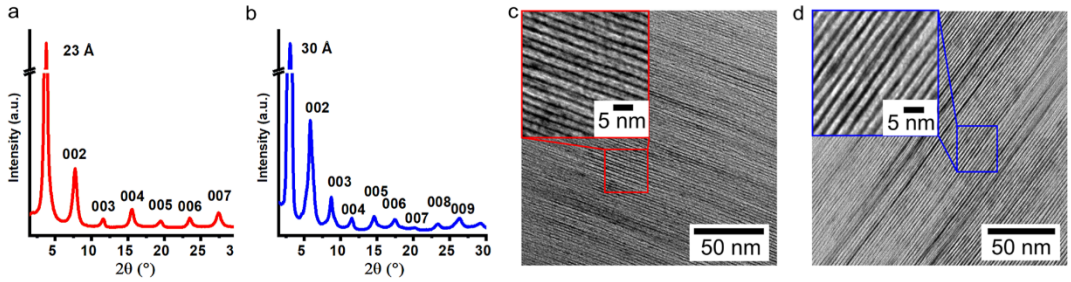

Figure 4. XRD patterns and microscopic images of the 1D periodically homogeneous nanocomposite films. XRD pattern of (a) Hec40/PVP60 and (b) Hec31/PVP69 with a rational series of 001-reflections up to the ninth order. Cross-sectional TEM images of (c) Hec40/PVP60 and (d) Hec31/PVP69 confirm the perfect translationally periodic homogeneity over large areas.

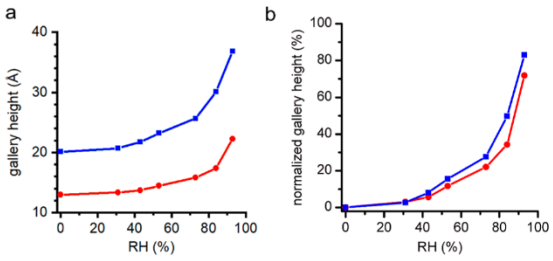

Figure 5. Study of the swelling behavior. (a) Absolute gallery height as a function of RH (red = Hec40/PVP60, blue = Hec31/PVP69). (b) Increase of the gallery height, normalized to the value at 0% RH, as a function of RH (red = Hec40/PVP60, blue = Hec31/PVP69).

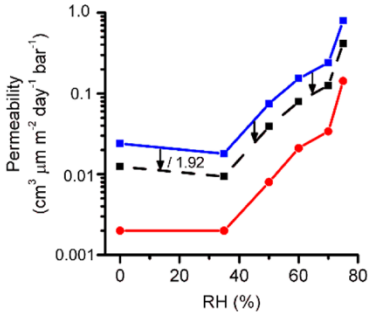

Figure 6. Oxygen permeability in logmarithic scaling of Hec40/PVP60 (red) and Hec31/PVP69 (blue) as a function of RH. According to Cussler's theory, the OP of Hec31/PVP69 should be reduced by a factor of 1.92 because of the increase in the filler content from 31 to 40 vol % (displayed as dashed black line).

Oxygen transmission rates (OTR) measured at various RH are, however, the much more sensitive probe for moisture sensitivity (Table S2). For applications, absolute OTR are the relevant features. However, transmissions rates are largely influenced by the thickness of the barrier coatings and even the transmission rate of the substrate. Therefore, the performance of the barrier coatings can only be compared by converting transmission rates into OP. For conversion, it is generally assumed that the rate is inversely proportional to the thickness (2.1 and 3.0 μm for Hec40/PVP60 and Hec31/PVP69, respectively).[35] Upon conversion of OTR values into OP values, the contribution of the PET substrate is subtracted according to Roberts et al.[36]

For water-soluble polymers, the sensitivity to RH, and consequently the deterioration of the barrier, is a well-known adverse phenomenon, as discussed in the Introduction.[5,6,37] However, as also discussed in the Introduction, up to a certain threshold value (<35% RH) the OP slightly decreases (Figure 6), as previously observed for EVAL[15] (Figure 1) and cellulose films.[19] Although both hybrid films adsorb water commencing at low RH, as indicated by the increasing gallery height (Figure 5a), initially the adsorbed water has no negative impact on the OP. The offset of swelling and breakdown of the barrier has been reported before. Wang et al.[19] and Muramatsu et al.[20] suggested that at the early stages of swelling, the adsorbed water is filling the free volume in the system, and thus leads to a lower diffusivity.[20] Above this threshold value (>35% RH), the permeability of Hec31/PVP69 increased from 0.024 (0% RH) to 0.796 cm^3 μm m^{-2} day^{-1} bar^{-1} (75% RH) and of Hec40/PVP60 from 0.002 (0% RH) to 0.143 cm^3μm m^{-2} day^{-1} bar^{-1} (75% RH).

Throughout the complete RH range, the OP of the more-filled hybrid film (Hec40/PVP60) was reduced by a factor of around 8. Because aspect ratio (α), geometrical factor (μ), and permeability of the neat polymer matrix (P_0) are the same for both nanocomposite films, according to Cussler's theory, the permeability is expected to be reduced by only a factor of 1.92 (see Section S3 for details) when increasing the filler content from 31 vol % (Hec31/PVP69) to 40 vol % (Hec40/PVP60) (Figure 6). The relative reduction observed in OP between Hec31/PVP69 and Hec40/PVP60 clearly cannot be attributed to the effect of increasing filler content as predicted by Cussler's theory. The effect is actually a factor of ≈4 larger than what is expected from Cussler's theory. As both hybrid films are identical except for the filler content, we propose this factor to be due to the differing confinement of the interlayered polymer sandwiched between the Hec nanosheets. Wang et al.[33] recently proposed, that the gallery height of the Hec/PVP hybrid film of 1.3 and 2 nm is related to the principle axes of 1.0 and 1.3 nm of the PVP chain itself. The gallery heights of Hec40/PVP60 and Hec31/PVP69 are consistent to a monolayer and a bilayer (Figure 2b), respectively. As recently suggested by Eckert et al.,[9] the segment mobility of a polymer chain within the confined space is significantly reduced. This is expected to diminish the diffusivity of low-molecular-weight components like oxygen and thus reduce the OP. This observation suggests that besides the nonlinear dependence of diffusivity on the aspect ratio and the volume fraction of filler considered by Cussler, additionally,

https://dx.doi.org/10.1021/acsapm.0c00456
ACS Appl. Polym. Mater. 2020, 2, 3010−3015

a linear effect of confinement exists at high filler content and thus severe confinement.

CONCLUSION

Periodically ordered Hec/PVP hybrid films represent model systems perfectly suited to study the impact of confinement on oxygen permeability. The model system allows for fabrication of nanocomposite films that are identical regarding homogeneity, crystallinity, and type and aspect ratio of filler, but that differ in filler content. Ranging from 0% to 75% of RH, the offset in permeability of these two films is much greater than what could be attributed to the increase of tortuous path predicted by Cussler's theory. This observation is attributed to the reduction of segment mobility by severe polymer confinement as encountered in highly filled homogeneous nanocomposites.

ASSOCIATED CONTENT

Supporting Information

The Supporting Information is available free of charge at https://pubs.acs.org/doi/10.1021/acsapm.0c00456.

Detailed information about the film preparation and characterization with instrumental details; a table with an overview of the OTR and OP values and the approximation of Cussler's equation (PDF)

AUTHOR INFORMATION

Corresponding Author

Josef Breu − *Bavarian Polymer Institute and Department of Chemistry, University of Bayreuth, Bayreuth 95447, Germany*; orcid.org/0000-0002-2547-3950; Email: josef.breu@uni-bayreuth.de

Authors

Theresa Schilling − *Bavarian Polymer Institute and Department of Chemistry, University of Bayreuth, Bayreuth 95447, Germany*

Christoph Habel − *Bavarian Polymer Institute and Department of Chemistry, University of Bayreuth, Bayreuth 95447, Germany*

Sabine Rosenfeldt − *Bavarian Polymer Institute and Department of Chemistry, University of Bayreuth, Bayreuth 95447, Germany*

Maximilian Röhrl − *Bavarian Polymer Institute and Department of Chemistry, University of Bayreuth, Bayreuth 95447, Germany*

Complete contact information is available at: https://pubs.acs.org/10.1021/acsapm.0c00456

Author Contributions

†T.S. and C.H. contributed equally to this work. The manuscript was written through contributions of all authors. All authors have given approval to the final version of the manuscript. T.S. explored and optimized the Hec/PVP system and fabricated and characterized the Hec/PVP films. C.H. conducted and analyzed the OTR measurements to obtain the oxygen permeabilities.

Funding

This work was supported by the German Science Foundation (DFG) within the collaborative research projects SFB 840 and SFB 1357.

Notes

The authors declare no competing financial interest.

ACKNOWLEDGMENTS

The authors thank Florian Puchtler for producing the synthetic clay and Marco Schwarzmann for the transmission electron microscopy images. Moreover, we thank Renee Timmins for proofreading the manuscript. T.S. and C.H. thank the Elite Network of Bavaria for financial and other support. We appreciate the support of the Keylab for Optical and Electron Microscopy of the Bavarian Polymer Institute (BPI).

REFERENCES

(1) *Plastics—The Facts 2018: An Analysis of European Plastics Production, Demand and Waste Data*; PlasticsEurope: Brussels, Belgium, 2018.

(2) Akelah, A. Polymers in Food Packaging and Protection. In *Functionalized Polymeric Materials in Agriculture and the Food Industry*; Springer: Boston, 2013; pp 293−347.

(3) Sabu, T.; Kuruvilla, J.; Malhotra, S. K.; Goda, K.; Sreekala, M. S. *Polymer Composites*; Wiley−VCH: Weinheim, Germany, 2013; Vol. 2.

(4) Tsurko, E. S.; Feicht, P.; Habel, C.; Schilling, T.; Daab, M.; Rosenfeldt, S.; Breu, J. Can high oxygen and water vapor barrier nanocomposite coatings be obtained with a waterborne formulation? *J. Membr. Sci.* **2017**, *540*, 212−218.

(5) Mo, C.; Yuan, W.; Lei, W.; Shijiu, Y. Effects of Temperature and Humidity on the Barrier Properties of Biaxially-oriented Polypropylene and Polyvinyl Alcohol Films. *J. Appl. Packag. Res.* **2014**, *6*, 40−46.

(6) Grunlan, J. C.; Grigorian, A.; Hamilton, C. B.; Mehrabi, A. R. Effect of clay concentration on the oxygen permeability and optical properties of a modified poly(vinyl alcohol). *J. Appl. Polym. Sci.* **2004**, *93*, 1102−1109.

(7) Robertson, G. L. *Food Packaging: Principles and Practice*; Taylor & Francis Group: Boca Raton, FL, 2006.

(8) Cussler, E. L.; Hughes, S. E.; Ward, W. J.; Aris, R. Barrier membranes. *J. Membr. Sci.* **1988**, *38*, 161−174.

(9) Eckert, A.; Abbasi, M.; Mang, T.; Saalwächter, K.; Walther, A. Structure, Mechanical Properties, and Dynamics of Polyethylenoxide/Nanoclay Nacre-Mimetic Nanocomposites. *Macromolecules* **2020**, *53*, 1716−1725.

(10) Zhang, C.; Guo, Y.; Priestley, R. D. Glass Transition Temperature of Polymer Nanoparticles under Soft and Hard Confinement. *Macromolecules* **2011**, *44*, 4001−4006.

(11) Qin, X.; Xia, W.; Sinko, R.; Keten, S. Tuning Glass Transition in Polymer Nanocomposites with Functionalized Cellulose Nanocrystals through Nanoconfinement. *Nano Lett.* **2015**, *15*, 6738−44.

(12) Kang, E.; Graczykowski, B.; Jonas, U.; Christie, D.; Gray, L. A. G.; Cangialosi, D.; Priestley, R. D.; Fytas, G. Shell Architecture Strongly Influences the Glass Transition, Surface Mobility, and Elasticity of Polymer Core-Shell Nanoparticles. *Macromolecules* **2019**, *52*, 5399−5406.

(13) Johnson, K. J.; Glynos, E.; Maroulas, S.-D.; Narayanan, S.; Sakellariou, G.; Green, P. F. Confinement Effects on Host Chain Dynamics in Polymer Nanocomposite Thin Films. *Macromolecules* **2017**, *50*, 7241−7248.

(14) López-Rubio, A.; Hernández-Muñoz, P.; Gimenez, E.; Yamamoto, T.; Gavara, R.; Lagarón, J. M. Gas barrier changes and morphological alterations induced by retorting in ethylene vinyl alcohol-based food packaging structures. *J. Appl. Polym. Sci.* **2005**, *96*, 2192−2202.

(15) Kuraray Relative Humidity. http://www.evalevoh.com/en/eval-properties/barrier-to-oxygen/relative-humidity.aspx (accessed 2020-01-29).

(16) Habel, C.; Schöttle, M.; Daab, M.; Eichstaedt, N. J.; Wagner, D.; Bakhshi, H.; Agarwal, S.; Horn, M. s. A.; Breu, J. High-Barrier, Biodegradable Food Packaging. *Macromol. Mater. Eng.* **2018**, *303*, 1800333.

https://dx.doi.org/10.1021/acsapm.0c00456
ACS Appl. Polym. Mater. 2020, 2, 3010−3015

(17) Lange, J.; Wyser, Y. Recent Innovations in Barrier Technologies for Plastic Packaging - a Review. *Packag. Technol. Sci.* **2003**, *16*, 149−158.
(18) Zhang, Z.; Britt, I. J.; Tung, M. A. Permeation of oxygen and water vapor through EVOH films as influenced by relative humidity. *J. Appl. Polym. Sci.* **2001**, *82*, 1866−1872.
(19) Wang, J.; Gardner, D. J.; Stark, N. M.; Bousfield, D. W.; Tajvidi, M.; Cai, Z. Moisture and Oxygen Barrier Properties of Cellulose Nanomaterial-Based Films. *ACS Sustainable Chem. Eng.* **2018**, *6*, 49−70.
(20) Muramatsu, M.; Okura, M.; Kuboyama, K.; Ougizawa, T.; Yamamoto, T.; Nishihara, Y.; Saito, Y.; Ito, K.; Hirata, K.; Kobayashi, Y. Oxygen permeability and free volume hole size in ethylene−vinyl alcohol copolymer film: temperature and humidity dependence. *Radiat. Phys. Chem.* **2003**, *68*, 561−564.
(21) Song, Y.; Gerringer, J.; Qin, S.; Grunlan, J. C. High Oxygen Barrier Thin Film from Aqueous Polymer/Clay Slurry. *Ind. Eng. Chem. Res.* **2018**, *57*, 6904−6909.
(22) Ding, F.; Liu, J.; Zeng, S.; Xia, Y.; Wells, K. M.; Nieh, M. P.; Sun, L. Biomimetic nanocoatings with exceptional mechanical, barrier, and flame-retardant properties from large-scale one-step coassembly. *Sci. Adv.* **2017**, *3*, e1701212.
(23) Choudalakis, G.; Gotsis, A. D. Free volume and mass transport in polymer nanocomposites. *Curr. Opin. Colloid Interface Sci.* **2012**, *17*, 132−140.
(24) Doblhofer, E.; Schmid, J.; Riess, M.; Daab, M.; Suntinger, M.; Habel, C.; Bargel, H.; Hugenschmidt, C.; Rosenfeldt, S.; Breu, J.; Scheibel, T. Structural Insights into Water-Based Spider Silk Protein-Nanoclay Composites with Excellent Gas and Water Vapor Barrier Properties. *ACS Appl. Mater. Interfaces* **2016**, *8*, 25535−43.
(25) Tsurko, E. S.; Feicht, P.; Nehm, F.; Ament, K.; Rosenfeldt, S.; Pietsch, I.; Roschmann, K.; Kalo, H.; Breu, J. Large Scale Self-Assembly of Smectic Nanocomposite Films by Doctor Blading versus Spray Coating: Impact of Crystal Quality on Barrier Properties. *Macromolecules* **2017**, *50*, 4344−4350.
(26) Breu, J.; Seidl, W.; Stoll, A. J.; Lange, K. G.; Probst, T. U. Charge Homogeneity in Synthetic Fluorohectorite. *Chem. Mater.* **2001**, *13*, 4213−4220.
(27) Stöter, M.; Kunz, D. A.; Schmidt, M.; Hirsemann, D.; Kalo, H.; Putz, B.; Senker, J.; Breu, J. Nanoplatelets of sodium hectorite showing aspect ratios of approximately 20,000 and superior purity. *Langmuir* **2013**, *29*, 1280−1285.
(28) Rosenfeldt, S.; Stöter, M.; Schlenk, M.; Martin, T.; Albuquerque, R. Q.; Förster, S.; Breu, J. In-Depth Insights into the Key Steps of Delamination of Charged 2D Nanomaterials. *Langmuir* **2016**, *32*, 10582−10588.
(29) Sano, K.; Kim, Y. S.; Ishida, Y.; Ebina, Y.; Sasaki, T.; Hikima, T.; Aida, T. Photonic water dynamically responsive to external stimuli. *Nat. Commun.* **2016**, *7*, 12559.
(30) Kunz, D. A.; Erath, J.; Kluge, D.; Thurn, H.; Putz, B.; Fery, A.; Breu, J. In-plane modulus of singular 2:1 clay lamellae applying a simple wrinkling technique. *ACS Appl. Mater. Interfaces* **2013**, *5*, 5851−5855.
(31) Wong, M.; Ishige, R.; White, K. L.; Li, P.; Kim, D.; Krishnamoorti, R.; Gunther, R.; Higuchi, T.; Jinnai, H.; Takahara, A.; Nishimura, R.; Sue, H. J. Large-scale self-assembled zirconium phosphate smectic layers via a simple spray-coating process. *Nat. Commun.* **2014**, *5*, 3589.
(32) Moore, D. M.; Reynolds, R. C.; M, D. *X-ray Diffraction and the Identification and Analysis of Clay Minerals*; Oxford University Press: Oxford, U.K., 1997.
(33) Wang, Z.; Rolle, K.; Schilling, T.; Hummel, P.; Philipp, A.; Kopera, B. A. F.; Lechner, A. M.; Retsch, M.; Breu, J.; Fytas, G. Tunable Thermoelastic Anisotropy in Hybrid Bragg Stacks with Extreme Polymer Confinement. *Angew. Chem., Int. Ed.* **2020**, *59*, 1286−1294.
(34) Holder, K. M.; Priolo, M. A.; Secrist, K. E.; Greenlee, S. M.; Nolte, A. J.; Grunlan, J. C. Humidity-Responsive Gas Barrier of Hydrogen-Bonded Polymer−Clay Multilayer Thin Films. *J. Phys. Chem. C* **2012**, *116*, 19851−19856.
(35) Siracusa, V. Food Packaging Permeability Behaviour: A Report. *Int. J. Polym. Sci.* **2012**, *2012*, 1687−1697.
(36) Roberts, A. P.; Henry, B. M.; Sutton, A. P.; Grovenor, C. R. M.; Briggs, G. A. D.; Miyamoto, T.; Kano, M.; Tsukahara, Y.; Yanaka, M. Gas permeation in silicon-oxide/polymer (SiOx/PET) barrier films: role of the oxide lattice, nano-defects and macro-defects. *J. Membr. Sci.* **2002**, *208*, 75−88.
(37) Tang, M. C.; Agarwal, S.; Alsewailem, F. D.; Choi, H. J.; Gupta, R. K. A model for water vapor permeability reduction in poly(lactic acid) and nanoclay nanocomposites. *J. Appl. Polym. Sci.* **2018**, *135*, 46506.

https://dx.doi.org/10.1021/acsapm.0c00456
ACS Appl. Polym. Mater. 2020, 2, 3010−3015

Supporting Information

Impact of Ultraconfinement on Composite Barriers

Theresa Schilling,[‡1] *Christoph Habel,*[‡1] *Sabine Rosenfeldt,*[1] *Maximilian Röhrl,*[1] *Josef Breu*[1*]

[1]Bavarian Polymer Institute and Department of Chemistry, University of Bayreuth, Universitätsstraße 30, 95447 Bayreuth, Germany

[‡] equal contribution

KEYWORDS: clay, hybrid films, swelling, Cussler, oxygen permeability, ultraconfinement

* Corresponding author

E-Mail: Josef.Breu@uni-bayreuth.de

Section S1. Materials and Film preparation

Materials

The synthetic clay sodium fluorohectorite (Hec, $[Na_{0.5}]^{inter}[Mg_{2.5}Li_{0.5}]^{oct}[Si4]^{tet}O_{10}F_2$) was synthesized via melt synthesis followed by long-term annealing, according to an established procedure.[1-2] The material featured a cation exchange capacity of 1.27 mmol g^{-1}. PVP (Mw = 40000 g mol^{-1}) was provided by Sigma Aldrich.

Film preparation

For repulsive delamination by osmotic swelling,[2-3] the synthetic Hec was immersed into Millipore water (0.2 vol%). The aqueous PVP solution (0.8 vol%) was added in the desired weight ratio. This dispersion of Hec and PVP was homogenized by mixing for at least 1 day in the overhead shaker (Figure 2a).

The barrier coatings were prepared by spray coating. The fully automatic spray coating system was equipped with a SATA 4000 LAB HVLP 1.0 mm spray gun (SATA GmbH & Co. KG, Germany). Dispersions were sprayed on a corona-treated polyethylene terephthalate (PET) foil (36 µm, Bleher Folientechnik, Germany). The spraying and nozzle pressure were set constant at values of 2 and 4 bar, respectively. The thickness of the dispersion layer applied in one spraying step is ≈ 2 µm, which corresponds to ≈ 20 nm dry nanocomposite film thickness (Figure 3c). For drying the dispersion layer, the sample was stopped under infrared lamps until evaporation of the solvent was complete. After every spraying cycle, a drying cycle of 90 s with a temperature of 55 °C took place. The spraying/drying cycle was repeated 80 times. Afterwards, the film was dried at 100 °C for 3 days under vacuum (10^{-3} bar).

Section S2. Dispersion and Film Characterization

Small angle X-ray scattering. Homogeneity of the dispersions was crosschecked by small angle X-ray scattering (SAXS) measurements using the small-angle X-ray system "Ganesha AIR" (SAXSLAB, Denmark). The X-ray source of this laboratory-based system is a rotating anode (copper, MicroMax 007HF, Rigaku Corporation, Japan). The data were recorded by a position sensitive detector (PILATUS 300 K, Dectris). To cover the range of scattering vectors between 0.02-0.85 $Å^{-1}$, different detector positions were used. The measurements of the dispersions were done in 1 mm glass capillaries (Hilgenberg, code 4007610, Germany) at room temperature. To improve the detection limit of the in-house machine, the dispersions were first concentrated to ≈ 10 wt% by centrifugation.

Thermogravimetric analysis. To rule out compositional changes during spray coating, these ratios were cross-checked (Table S1) by thermogravimetric analysis (TGA), using a Linseis STA PT 1600 (Linseis Messgeräte GmbH, Germany). Changes in mass observed upon heating in synthetic air up to 800 °C were attributed to the combustion of PVP. (Figure S1).

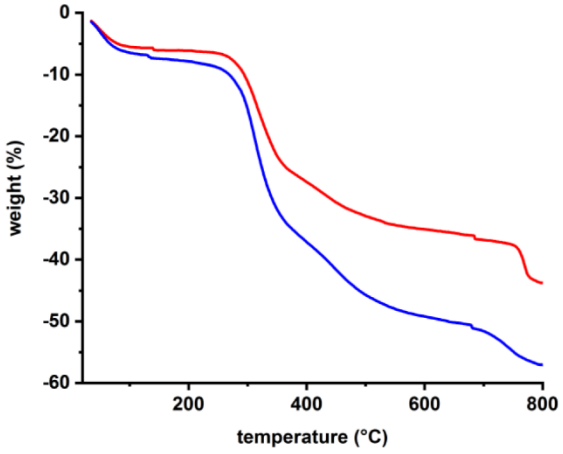

Figure S1. TGA curves of Hec40/PVP60 (red) and Hec31/PVP69 (blue). The weight loss below 200 °C corresponds to the water.

X-ray diffraction. XRD patterns of the films were recorded in Bragg-Brentano-geometry on an Empyrean diffractometer (PANalytical B.V.; the Netherlands) using Cu K_α radiation (λ = 1.54187 Å). The films were placed on glass slides (Menzel-Gläser; Thermo Scientific). Prior to measurements at 0% RH, samples were dried at 100 °C for one week in a vacuum chamber (10^{-3} bar). For the measurements of XRD patterns at varying RH, the samples were equilibrated for 1 week above saturated $MgCl_2$ $6H_2O$ (32% RH), K_2CO_3 (43% RH), $Mg(NO_3)_2$ (53% RH), NaCl (75% RH) KCl (84% RH) and KNO_3 (94% RH), respectively.

Calculation of the nominal gallery height:

Ruling out phase segregation

While XRD would be blind for segregated amorphous polymer volumes, it is, however, representative for the bulk of the nanocomposite films, since the X-ray beam is sampling large areas. Moreover, a more detailed evaluation of the XRD trace, including the crystallographic analysis for potential defects, renders it conclusive for ruling out phase segregation: The XRD pattern showed a rational *00l*-series characterized by a low coefficient of variation (Figure 4), emphasizing that the hybrid film is periodically homogenous over long ranges (more precisely: > the coherence length of the X-ray beam, which is typically 50 nm). In addition, the periodicity of the Hec/PVP film can be calculated via the volume fraction of PVP and Hec. In a 1D ordered Bragg film, the latter corresponds to the thickness of the Hec platelet. As calculated and observed gallery heights are identical (Table S1), within experimental certainty, phase segregation can be ruled out. The segregated polymer volume would be “missing” in the galleries and would not allow for such a perfect agreement.

Assuming PVP and Hec densities of 1.2 g cm^{-3} and 2.7 g cm^{-3}, respectively, nominal gallery height can be calculated for the various volume ratios (nominal gallery height in Table S1).[4] They agree reasonably with those obtained from XRD measurements (observed gallery height

in Table S1). The gallery height corresponds to the *d*-spacing minus the Hec platelet height of 0.96 nm.

Table S1. Overview of the structural and chemical characterization at 0 % RH.

sample	nominal Hec:PVP ratio [wt%]	nominal Hec:PVP ratio [vol%]	PVP content * [wt%]	PVP content ** [vol%]	Nominal gallery height [nm]	Observed gallery height [nm]	CV [%]	FWHM [°2θ]
Hec40/PVP60	60:40	40:60	38	58	1.3	1.3	1.3	0.3
Hec31/PVP69	50:50	31:69	49	68	2.0	2.0	1.0	0.3

CV: coefficient of variation; FWHM: full width at half maximum

* determined by TGA (Fig. S2); ** calculated with the PVP content determined by TGA;

Transmission electron microscopy. Transmission electron microscopy (TEM) images were taken on a JEOL JEM-2200FS (JEOL GmbH, Germany) at an acceleration voltage of 200 kV. Cross-section pictures of the self-supporting films were prepared with a Cryo Ion Slicer IB-09060CIS (JEOL, Germany).

Oxygen transmission rates. Oxygen transmission rates (OTR) were measured on a Mocon OX-TRAN 2/21 and a Mocon OX-TRAN 2/21 XL instrument (Minneapolis, USA) with a lower detection limit of 0.05 $cm^3m^{-2}\,day^{-1}\,bar^{-1}$ and 0.0005 $cm^3m^{-2}\,day^{-1}\,bar^{-1}$, respectively. The measurements were conducted at 23 °C and RH of 0%, 35%, 50%, 60%, 70% and 75%. All films were carefully conditioned at the relevant RH until the samples reached equilibrium.

Table S2. Overview of the oxygen transmission rates and oxygen permeabilities.

RH (%)	Hec40/PVP60 (2.1 µm)	Hec31/PVP69 (3.0 µm)	Hec40/PVP60 (2.1 µm)	Hec31/PVP69 (3.0 µm)
	OTR (cm^3 m^{-2} day^{-1} bar^{-1})		OP (cm^3 µm m^{-2} day^{-1} bar^{-1})	
0	0.001	0.008	0.002	0.024
35	0.001	0.006	0.002	0.018
50	0.004	0.025	0.008	0.075
60	0.010	0.051	0.021	0.153
70	0.016	0.080	0.034	0.240
75	0.068	0.263	0.143	0.796

Profilometer. The thickness of the films was measured with a Veeco Dektak 150 Surface Profiler (Veeco Instruments, USA). Six measurements were taken at different spots of the films and averaged.

Section S3. Approximation of Cussler's equation

$$\frac{P_1}{P_2} = \frac{1+\mu\frac{\alpha^2\phi_2{}^2}{1-\phi_2}}{1+\mu\frac{\alpha^2\phi_1{}^2}{1-\phi_1}}$$

With α = const.=20000, μ = const.= 4/9, 0.3≤ ϕ ≤ 0.4 → $\alpha^2 \cdot \mu > 177000000$:

→ Equation simplified to

$$\frac{P_1}{P_2} = \frac{\mu\frac{\alpha^2\phi_2{}^2}{1-\phi_2}}{\mu\frac{\alpha^2\phi_1{}^2}{1-\phi_1}} = \frac{\frac{\phi_2{}^2}{1-\phi_2}}{\frac{\phi_1{}^2}{1-\phi_1}}$$

For ϕ_1= 0.31 and ϕ_2= 0.4: $\frac{P_1}{P_2}$ = **1.92**

References

(1) Breu, J.; Seidl, W.; Stoll, A. J.; Lange, K. G.; Probst, T. U. Charge Homogeneity in Synthetic Fluorohectorite. *Chem. Mater.* **2001,** *13*, 4213-4220.

(2) Stöter, M.; Kunz, D. A.; Schmidt, M.; Hirsemann, D.; Kalo, H.; Putz, B.; Senker, J.; Breu, J. Nanoplatelets of sodium hectorite showing aspect ratios of approximately 20,000 and superior purity. *Langmuir* **2013,** *29*, 1280-1285.

(3) Rosenfeldt, S.; Stöter, M.; Schlenk, M.; Martin, T.; Albuquerque, R. Q.; Förster, S.; Breu, J. In-Depth Insights into the Key Steps of Delamination of Charged 2D Nanomaterials. *Langmuir* **2016,** *32*, 10582-10588.

(4) Tsurko, E. S.; Feicht, P.; Nehm, F.; Ament, K.; Rosenfeldt, S.; Pietsch, I.; Roschmann, K.; Kalo, H.; Breu, J. Large Scale Self-Assembly of Smectic Nanocomposite Films by Doctor Blading versus Spray Coating: Impact of Crystal Quality on Barrier Properties. *Macromolecules* **2017,** *50*, 4344-4350.

6.5 Steuerung der Kristallinität durch Schichtsilikat als Füllstoff

Christoph Habel[1,†], Jon Maiz[2,†], *Jorge L. Olmedo-Martínez[2]*, Juan V. López[3], Josef Breu[1*], Alejandro J. Müller[2,4*]

† C.H. und J.M.: zu gleichen Teilen beigetragen (*equally contributed*).

Competition between nucleation and confinement in the crystallization of poly(ethylene glycol)/ large aspect ratio hectorite nanocomposites

Reprinted from
Polymer **2020**, *202*, 122734.

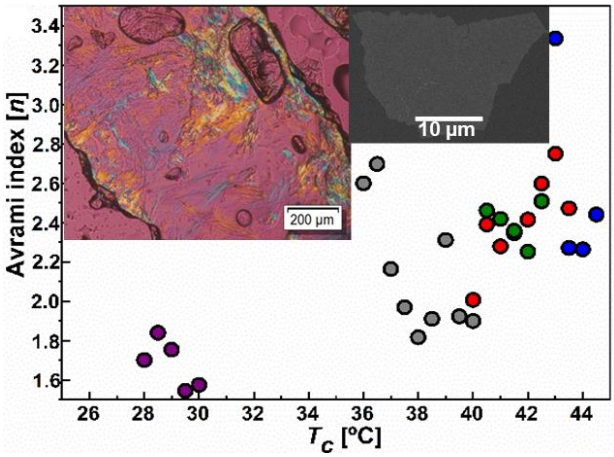

https://doi.org/10.1016/j.polymer.2020.122734

[1] Bayerisches Polymer Institut und Fakultät für Chemie, Universität Bayreuth, Universitätsstraße 30, Bayreuth, 95447, Germany

[2] POLYMAT und Abteilung Polymerwissenschaft und Technologie, Fachbereich Chemie, Universität des Baskenlandes UPV/EHU, Paseo Manuel de Lardizábal 3, 20018 Donostia-San Sebastián, Spain

[3] Polymergruppe USB, Abteilung Materialwissenschaft, Simón Bolívar Universität, Apartado 89000, Caracas 1080-A, Venezuela

[4] IKERBASQUE, Baskische Stiftung für Wissenschaft, Bilbao, Spain

*E-Mail: alejandrojesus.muller@ehu.es, josef.breu@uni-bayreuth.de

Darstellung des Eigenanteils: Das Konzept der Arbeit wurde von *Prof. Dr. A. J. Müller, Prof. Dr. J. Breu, Dr. J. Maiz* und mir erarbeitet. Von mir wurden die Proben hergestellt, die XRD und die PLOM-Messungen ausgeführt und ausgewertet. Die DSC-Messungen wurden von *Dr. J. Maiz* durchgeführt und ausgewertet. *Juan V. López* hat die isothermalen Kristallisationsmessungen durchgeführt. Die Publikation wurde von mir geschrieben und von *Dr. J. Maiz, J. Olmedo-Martínez, Prof. J. Breu* und *Prof. A. J. Müller* zur Einreichung überarbeitet. Mein Eigenanteil beträgt ca. 45%.

Polymer 202 (2020) 122734

Contents lists available at ScienceDirect

Polymer

journal homepage: http://www.elsevier.com/locate/polymer

Competition between nucleation and confinement in the crystallization of poly(ethylene glycol)/ large aspect ratio hectorite nanocomposites

Christoph Habel [a,1], Jon Maiz [b,1], Jorge L. Olmedo-Martínez [b], Juan V. López [c], Josef Breu [a,**], Alejandro J. Müller [b,d,*]

[a] Bavarian Polymer Institute and Department of Chemistry, University of Bayreuth, Universitätsstraße 30, Bayreuth, 95447, Germany
[b] POLYMAT and Polymer Science and Technology Department, Faculty of Chemistry, University of the Basque Country UPV/EHU, Paseo Manuel de Lardizábal 3, 20018, Donostia-San Sebastián, Spain
[c] USB Polymer Group, Department of Materials Science, University Simón Bolívar, Apartado 89000, Caracas, 1080-A, Venezuela
[d] IKERBASQUE, Basque Foundation for Science, Bilbao, Spain

ARTICLE INFO

Keywords:
Hectorite/PEG nanocomposites
Nucleation
Confinement

ABSTRACT

The overall crystallization kinetics of polymer nanocomposites is determined by nucleation and crystal growth, both of which are greatly affected by confinement. Heterogeneous nucleation is influenced by the interphase area between filler and polymer matrix. Starting with a homogeneous lamellar lyotropic aqueous dispersion of a mixture containing polyethylene glycol (PEG) and varying amounts of a high aspect ratio layered silicate (hectorite, Hec), nanocomposite films were casted containing a systematic variation of the degree of PEG confinement. This is achieved by a partial phase segregation upon drying, where independent of filler content, a thermodynamically stable, 1-dimensional crystalline hybrid with a constant volume of intercalated PEG (0.81 nm corresponding to a fraction of 75 wt% and 55 vol%, respectively) is formed. This intercalated hybrid phase is incorporated into segregated PEG domains. The kinetics of the thermodynamically driven segregation is dependent on the PEG volume available in surplus of the hybrid. Due to the very large lateral extension of the Hec, the segregated domains are increasingly two dimensional. As evidenced by transmission electron micrographs and powder X-ray diffraction, the segregation produces composite structures where, in dependency of filler content, PEG slabs of different thickness are separated by domains of the intercalated hybrid material. The crystallization behavior of these bi-phasic materials was investigated by Differential Scanning Calorimetry (DSC) and Polarized Light Optical Microscopy (PLOM). DSC results reveal a competition between the nucleating effect of Hec, which was particularly important at low amounts, and the confinement of PEG at higher filler loadings. Applying a self-nucleation protocol, the nucleation efficiency of the hectorite was shown to be up to 67%. The isothermal crystallization kinetics accelerated at low Hec contents (nucleation) up to a maximum, and then decreased as Hec content increased (confinement). Additionally, a clear correlation between filler content and the Avrami index was obtained supporting the increase in confinement as filler loading increased.

1. Introduction

Polymeric nanocomposites are remarkable materials, because of their morphology, properties, and the large variety of existing nanofillers [1–3]. Furthermore, these nanofillers can improve many properties of the matrix, such as mechanical, fire retardancy, barrier quality, thermal resistance, and conductivity [4–7]. When the nanofiller content increases beyond a percolation threshold, normally, confinement effects can develop [8].

Polymers can be confined in one dimension (ultra-thin films, nanolayers, nanoscopic phases within block copolymers), two dimensions (nanocylinders in AAO templates or strongly segregated block copolymers), or three dimensions (3D micro or nano domains within blends, block copolymers, etc.) [9]. The behavior of polymers in

* Corresponding author. POLYMAT and Polymer Science and Technology Department, Faculty of Chemistry, University of the Basque Country UPV/EHU, Paseo Manuel de Lardizábal 3, 20018, Donostia-San Sebastián, Spain.
** Corresponding author. Bavarian Polymer Institute and Department of Chemistry, University of Bayreuth, Universitätsstraße 30, Bayreuth, 95447, Germany.
E-mail addresses: josef.breu@uni-bayreuth.de (J. Breu), alejandrojesus.muller@ehu.es (A.J. Müller).
[1] These authors contributed equally to this work.

https://doi.org/10.1016/j.polymer.2020.122734
Received 3 April 2020; Received in revised form 10 June 2020; Accepted 15 June 2020
Available online 25 June 2020

restricted space can be dramatically different than in bulk [10], in particular when nanodomains reach sizes comparable to the radius of gyration of the chains. Thermal transitions in confined polymers change according to the level of confinement, as well as crystal orientation.

Nucleation and crystallization depend on the size and number of crystallizable domains or microdomains. When the number of micro or nanodomains is similar to the number of heterogeneities present in a bulk polymer, the crystallization of the confined material can undergo a process known as fractionated crystallization. Here, crystallization during cooling from the melt at distinct supercoolings can be divided into several exotherms. The different crystallization peaks are due to the different populations of confined microdomains that have different nucleation mechanisms. Typically, the nucleation changes from heterogeneous at high temperatures (where one or more exotherms can correspond to heterogeneities that have different activation energies) to surface or homogeneous nucleation at very high supercoolings, close to vitrification, due to increases in the degree of confinement or decreases in the size of the microdomain. If the number of microdomains is several orders of magnitude higher than the number of available heterogeneities in the bulk material, the crystallization occurs in a single crystallization peak that corresponds to surface or homogeneous nucleation [8].

Polyethylene oxide (PEO) and its low lower molecular weight equivalent, known as polyethylene glycol (PEG), are known to be water-soluble and non-ionic polymers of great interest in several fields of application. Beside their use as drug delivery systems, they are mainly used as hydrogels, wound healing materials, tissue engineering, and in the field of cell culture [11–14]. Moreover, they have been studied in confined systems, for example with carbon nanotubes (CNT), with silica, in block copolymers, and blends [15,16]. In the case of polymer-filler systems, for example, the effect of the concentration of the filler on the crystallization of polyethylene oxide (PEO) [17], polyethylene (PE), and polycaprolactone (PCL) with carbon nanotubes has been studied. At low concentrations, the filler can act as a nucleating agent, whereas at high concentrations a confinement effect may occur [18].

Recently, Wen et al. studied the confined crystallization of methoxypolyethylene glycol (MPEG) grafted to silica as a function of grafting density and molecular weight. They showed that confinement is stronger for lower molecular weight grafted MPEG. Their results demonstrated how the crystallization temperature (T_c) and the crystallinity of grafted MPEG chains reduces with decreases in grafting density. They also fitted their results to the Avrami equation and found that the Avrami index had a value of n ≈ 3 for neat MPEG as the material formed instantaneous spherulites. Instead, for MPEG-g-SiO_2, the Avrami index was less than 1 (at high silica loadings). This result showed that the overall crystallization kinetics was dominated by nucleation, a typical finding of confined crystallization [19].

The main objective of this work is to study the nucleation and confinement effect from a layered silicate with high aspect ratio on PEG and the dependancy of this on the filler content. The used silicate polymer dispersions and the resulting composites are characterized via Small Angle X-Ray Scattering (SAXS) and X-Ray Diffraction (XRD) techniques, respectively. Furthermore, the influence of the resulting structures on the crystallization kinetics of PEG is investigated by DSC measurements. Additionally, the nucleating efficiency of the synthesized layered silicate on PEG were estimated by self-nucleation studies and confirmed by polarized light optical microscopy (PLOM). A potential application for these materials could be food packaging, as low molecular PEG is known to be biocompatible and biodegradable [20].

2. Experimental section

2.1. Materials and samples preparation

Sodium hectorite $[Na_{0.5}]^{inter}[Mg_{2.5}Li_{0.5}]^{oct}[Si_4]^{tet}O_{10}F_2$ (Hec) was prepared by employing a synthesis procedure from the melt, previously reported in the literature [21,22]. The material features a cation exchange capacity (CEC) of 1.27 mmol g^{-1} and a temperature stability of up to 800 °C [23]. Polyethylene glycol (PEG, Mw = 1450 g mol^{-1}) was provided by Sigma Aldrich (Germany). Hec was immersed into Millipore water (1 wt%) for its delamination, and this suspension was added dropwise during stirring to a 1–5 wt% PEG solution in the weight ratios (wt%) PEG:Hec 80:20, 60:40, 40:60 and 25:75 and shaken overnight to improve dispersion quality. Afterwards, the dispersions were cast into Teflon containers and dried (room temperature and 40–80 °C (10^{-3} bar)). The different samples are labeled as PEGHec-X with X describing the filler content of Hec in wt%. For comparison, a neat PEG sample was used.

2.2. Characterization

Structural Characterization. PEGHec composites were thinly cut with an Ion Slicer EM-09100IS (JEOL GmbH, Germany), which were then observed with a JEM-2200 FS (JEOL GmbH, Germany, transmission electron microscope (TEM)).

The diameter of the Hec platelets were measured via scanning electron microscopy (SEM, Zeiss Leo 1530).

A small-angle X-ray "Ganesha AIR" (SAXSLAB, Denmark) equipment was used to record SAXS patterns. It is equipped with a rotating anode X-ray source (copper, MicoMax 007HF, Rigaku Corporation, Japan). A position-sensitive detector (PILATUS 300K, Dectris) was employed to record the diffraction patterns. Prior to the measurements, the PEGHec suspension was centrifuged for 2 h (13000 rpm) to a resulting gel (4.5 wt %) to enhance sensitivity. The measurement of the suspension was performed in 1 mm glass capillaries (Hilgenberg, Germany) at room temperature. The birefringence of the dispersions was shown with a self-made cross polarizer.

The infrared (IR) spectra of the PEGHec composites were recorded with a JASCO FTIR 6100 spectrometer (range: 400-4000 cm^{-1}; resolution: 4 cm^{-1}).

X-ray diffraction (XRD) patterns were measured using nickel filtered Cu-K_α radiation (λ = 1.54187 Å) with a Bragg-Brentano-type diffractometer (Empyrean) equipped with a Pixcel detector. The dispersions were dropped onto glass platelets and dried for 1 week in a vacuum chamber (10^{-3} bar). The X-ray diffraction patterns were analyzed with Panalytical's software Highscore Plus.

The semi-crystalline morphology of neat PEG and PEGHec nanocomposites were examined with polarized light optical microscopy (PLOM) with an OLYMPUS BX51 microscope equipped with an OLYMPUS SC50 camera and a hot-stage (Mettler FP82HT) with liquid nitrogen flow. Samples were prepared by heating them in between glass slides to a temperature of 30 °C above their melting temperatures to erase thermal crystalline history. After 5 min at this temperature, the samples were cooled at 50 °C min^{-1} until the desired isothermal T_c value, which was selected based on prior DSC measurements.

Thermal Analysis. A PerkinElmer 8000 DSC equipment with a cooling accessory (an Intracooler II) was used. Ultrapure nitrogen was used as purge gas, and calibration with indium and tin standards was performed. Sample weight was approximately 5 mg. Non-isothermal scans were performed after melting for 3 min at 80 °C to erase thermal history. Employing scanning rates of 20 °C min^{-1}, a cooling scan from the melt was recorded (down to 0 °C) followed by a subsequent heating scan (from 0 °C to the 80 °C).

We followed the procedure for DSC recommended by Lorenzo et al. [24] to obtain the overall isothermal crystallization rate of the samples, which includes primary nucleation and growth processes. The samples were heated to 80 °C and kept at this temperature for 3 min. Then the samples were rapidly cooled at 60 °C min^{-1} to the isothermal crystallization temperature (T_c). The T_c range employed was previously determined by ensuring that no crystallization occurred during the cooling step. In this way, the minimum isothermal T_c value was chosen when the subsequent heating step showed no melting peak [18].

Self-Nucleation (SN) was performed according to the protocol of

Fillon et al. [25]. In this test, the following steps are carried out at 20 °C min^{-1}: (i) heating the sample to 80 °C and keeping at this temperature for 1 min to erase thermal history; (ii) the sample is then cooled from 80 °C to 0 °C; (iii) heating to a temperature that is denoted self-nucleation temperature (T_s), and the sample remains at this T_s temperature for 5 min; (iv) cooling from T_s to 0 °C to record any changes in T_c due to SN; and (v) a final heating scan is performed from 0 °C to 80 °C. There are three different SN *Domains* that are well-defined in the literature [25,26], which will be explained in the results and discussion section below.

3. Results and discussion

Melt synthesized sodium fluorohectorite ($[Na_{0.5}]^{inter}[Mg_{2.5}Li_{0.5}]^{oct}[Si_4]^{tet}O_{10}F_2$, Hec) [21] comes in high lateral dimensions (20 μm) and shows the rare phenomenon of osmotic swelling delivering ≈ 1 nm thick nanosheets of huge aspect ratio (≈20 000). The latter renders it ideally suited as filler for polymer composite barriers as needed e.g. in (food) packaging [27–29]. By immersing Hec into deionized water, osmotic swelling allows for complete and gentle delamination [21,30,31]. As Hec has a very large aspect ratio, the rotation of the nanosheets is stalled and instead of isotropic suspensions, rather liquid crystalline, lamellar lyotropic phases are obtained. The separation of adjacent nanosheets is well defined and determined by its concentration [32].

Mixing the lamellar lyotropic Hec dispersion with different amounts of an aqueous PEG solution, allows the polymer to uniformally diffuse between adjacent Hec nanosheets yielding perfectly homogeneous ternary lamellar lyotropic dispersions, as evidenced by SAXS (Fig. 1). For instance, the dispersion PEGHec-75 represents a lamellar lyotropic suspension with 42 nm separation of the nanosheets. Reaggregation of Hec nanosheets to stacks can be excluded by the absence of a reflection typical for crystalline hydrated Hec phases at q = 0.65–0.41 $Å^{-1}$ (1.51 nm, indicated as blue line in Fig. 1) [21,32].

These suspensions were cast into Teflon shells and then slowly but thoroughly dried (Fig. S1) whereupon composite films with Hec contents varying from 20 to 75 wt% were obtained. Regardless of the filler content, a d_{001} peak at 1.77 nm (2θ = 4.97°) was observed by XRD for all composites (Fig. 2). The highly rational *(00l)*-series with sharp and intense basal reflections visible up to the sixth order indicate a well-defined, 1-dimensional (1D) order [33,34]. For a Hec layer thickness

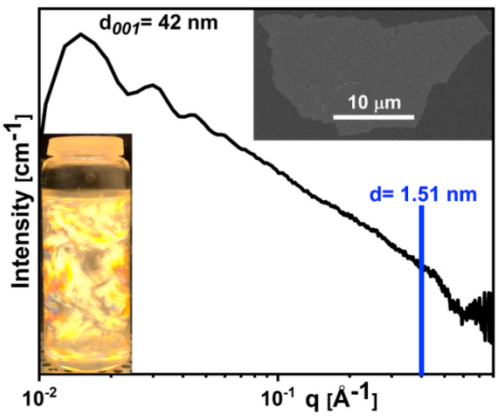

Fig. 1. SAXS pattern of the ternary dispersion (PEG, Hec (75 wt%), water) showing completely separated single nanosheets without any reaggregation of the Hec nanosheets evidenced by absence of a reflection at d = 1.51 nm (blue line) [32]. The insets show a SEM picture of a Hec platelet exhibiting an lateral dimension of >20 μm and the birefringence of the PEGHec-20 hybrid in a self-made cross polarizer. (For interpretation of the references to color in this figure legend, the reader is referred to the Web version of this article.)

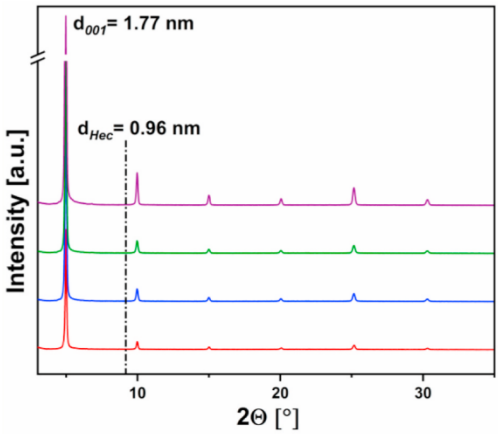

Fig. 2. XRD patterns of PEGHec nanocomposites (red: 20 wt% filler, blue: 40 wt%, green: 60 wt%, purple: 75 wt%). The dotted line at 0.96 nm indicates the d-spacing of neat, completely dry Hec (d_{Hec}). (For interpretation of the references to color in this figure legend, the reader is referred to the Web version of this article.)

of 0.96 nm, a PEG:Hec volume ratio of 45:55 can be deduced for the crystalline domains. Assuming in a first approximation that the intercalated PEG has the same density as bulk PEG (1.1 g/cm^3) and applying the Hec density of 2.7 g/cm^3, a filler content of 75 wt% can be estimated for these crystalline domains. The sample with 75 wt% Hec corresponds to this estimated composition of the crystalline hybrid phase.

When starting with lamellar lyotropic suspensions of large diameter synthetic clays, nanocomposite films show translational symmetry perpendicular to the film, as indicated by Bragg reflections (Fig. 2). The volume ratio of such ordered domains, as found here for PEGHec, are in most cases higher than reflected in the average composition of the composite indicating segregation into an intercalated phase and neat polymer domains [28,29,31,35]. For very few composite systems and only at specific filler contents, single phases of ordered nanocomposites have been observed [23].

TEM images (Fig. 3a) of the highly filled PEGHec nanocomposite (75 wt%) showed extended ordered domains (strictly alternating order of Hec and PEG over a wide range > 200 nm). The interlayer height of 0.81 nm observed by XRD and TEM (Fig. 3b) agrees with published values for PEG layered silicate nanocomposites [36–38]. This 1D ordered intercalated hybrid seems to be a thermodynamically favored phase irrespective of the type and lateral extension of the layered silicate/clay applied as filler.

A closer inspection of the TEM images, however, reveals some few-layer-thick Hec defects. Apparently, the PEG:Hec ratio applied does not perfectly meet the ratio requested for the hybrid material and consequently some Hec-only domains (Fig. 3a, white arrow) are forced to segregate despite thermodynamics favoring the hybrid structure as recently suggested by Walther et al. [39]. However, these Hec domains are far thinner than the coherence length of the X-ray beam and therefore do not show up in the diffraction pattern.

All other samples prepared with lower Hec content display the opposite phenomenon. PEG is available in surplus of the stoichiometry of the hybrid phase and consequently needs to segregate in PEG-only domains. As the evaporation progresses, however, a tortuous path is built up in the casted film making mass transport increasingly more difficult and thus severely limits the length scale of the segregated domains. Moreover, these domains are inherently 2D and occur as anisotropic elliptical lenses (Fig. 4a) because the silicate layers with 20 μm lateral extension all orient in parallel in the film. The limited diffusion

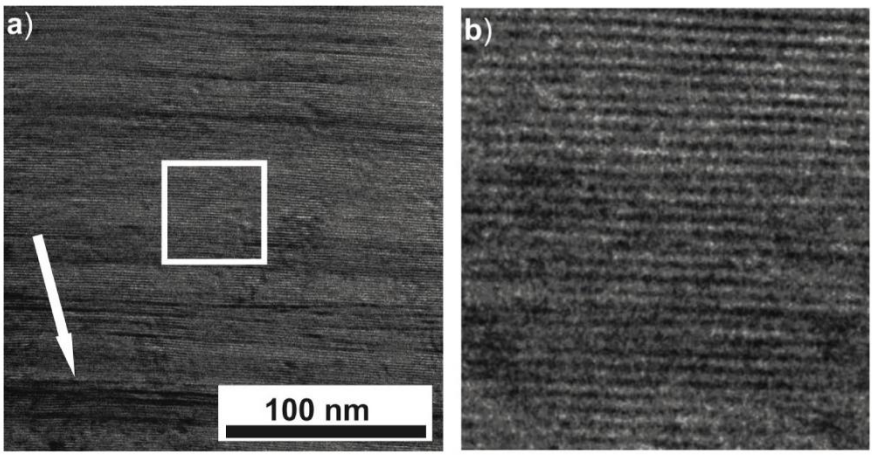

Fig. 3. a) TEM image of the highly filled PEGHec nanocomposite (75 wt%) showing extended ordered domains. White arrow indicates partial restacked Hec phase. White inset is shown in b) as close up indicating the equidistant ordering of the Hec nanosheets in the polymer matrix.

which defines the kinetics of mass transport, and thus the typical size of the segregated domains, according to Cussler is directly dependant on $\frac{\theta^2}{1-\theta}$ (θ = filler content) [31,40]. The slabs of segregated PEG between intercalated hybrid domains therefore are expected to become thicker with decreasing Hec content.

For PEGHec-40, typical slab heights in the range of 35 nm are observed (Fig. 4b). These segregated PEG domains therefore still sense some degree of confinement. Consequently, confinement effects are expected for the segregated PEG domains since they are far from the bulk state but rather experience a severe confinement between the intercalated domains (Fig. 4b). The degree of confinement can be systematically varied with the filler content applied. The PEGHec composites thus represent ideal model systems to study the influence of heterogeneous nucleation surface and confinement on the crystallization behavior of PEG.

These structural results are in line with the non-isothermal DSC scans performed in this work reported in Fig. 5. As can be seen in the DSC scans, the addition of Hec increases the peak crystallization temperature. The results are consistent with a nucleating effect that is maximum at 20 wt% filler content (as T_c is the highest) and progressively reduces as the amount of Hec is increased. The peak crystallization temperature (T_c) increases from 22 °C to 34 °C upon 20 wt% Hec addition (Fig. 5). With further increases in the amount of Hec (40, 60 and 75 wt%), confinement increases. A competition occurs between the nucleating effect of Hec (which tends to increase T_c) and its confinement effect on PEG (which tends to decrease T_c). The 1D-crystalline intercalation compound obtained at 75 wt% Hec even shows a T_c of 19 °C, which is below the T_c of neat PEG (22 °C), and an extremely low crystallinity degree (see Fig. 5b). This low crystallinity value (about 3%) indicates the presence even at these high Hec contents of some very small regions of segregated PEG that were not observed by TEM (Fig. 3). It is clear that strong confinement is the main dominant behavior. This conclusion is in agreement with recent results obtained by Walther et al. and published in Reference 39, where they confirmed the presence of a crystalline phase of PEO in all nanocomposite samples.

Fig. 6 summarizes the non-isothermal DSC results by plotting T_c, T_m, and the degree of crystallinity (X_c) versus Hec content in the composites (see Table S1). As can clearly be seen, the crystallinity of the PEGHec composites strongly decreases with an increasing amount of Hec. This effect leads to a crystallinity of <4% in PEGHec-75. As previously discussed, the space for segregated PEG-only domains between the perfectly ordered hybrid phase is affected by the amount of Hec, which

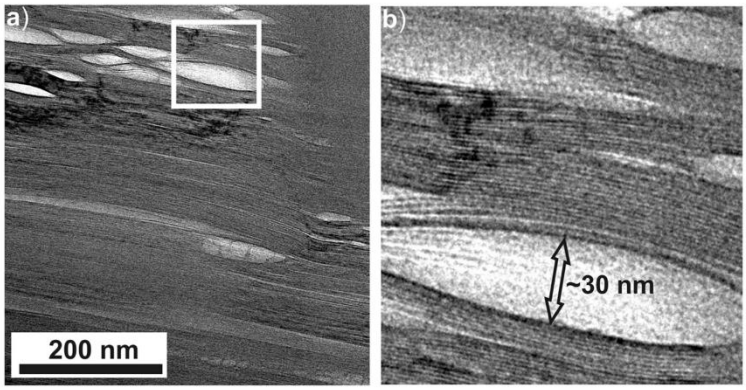

Fig. 4. a) TEM image of PEGHec-40 nanocomposite showing neat PEG domains (white box) between the ordered hybrid domains. b) Close up of white box in a) showing the size of the PEG slabs between the hybrid domains matrix.

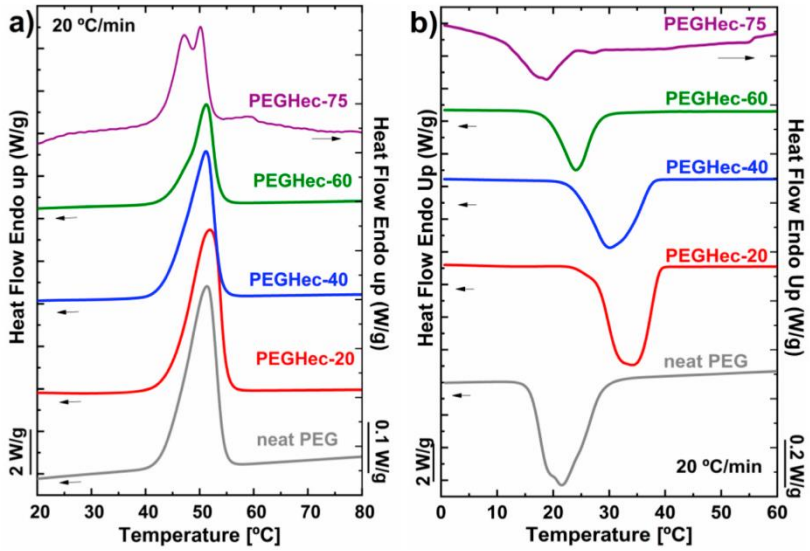

Fig. 5. DSC scans (a,b) of the different nanocomposites (red: 20 wt% filler, blue: 40 wt%, green: 60 wt%, purple: 75 wt%) in comparison with neat PEG (grey). (For interpretation of the references to color in this figure legend, the reader is referred to the Web version of this article.)

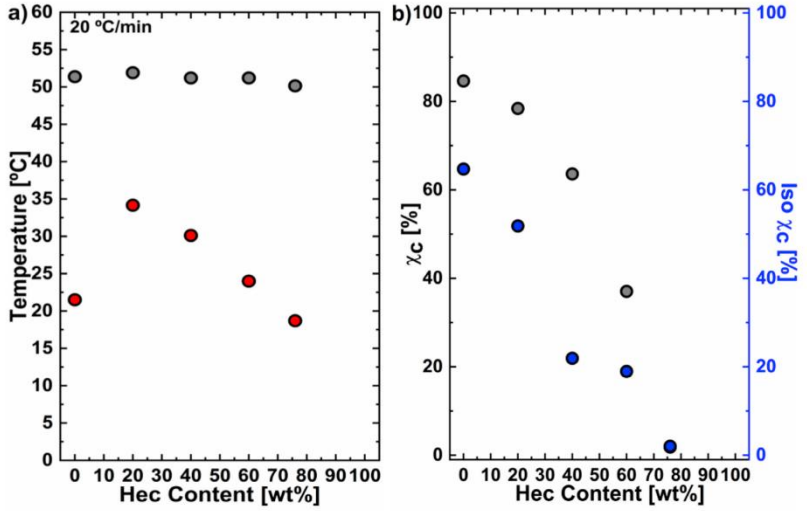

Fig. 6. a) Experimental melting temperatures (grey circles) and crystallization temperatures (red circles); b) calculated degree of crystallinity developed during non-isothermal crystallization (grey circles) and during isothermal crystallization (blue circles) determined as a function of the Hec content in the composites. (For interpretation of the references to color in this figure legend, the reader is referred to the Web version of this article.)

could significantly hinder crystallization of PEG. Within confined space, PEG is not able to crystallize and thus the crystallinity represents the separated PEG phase outside the galleries of Hec. Compared to other publications in the field of polymer-filler crystallinity studies, we observed a large decrease of crystallinity with increasing filler content (Fig. 6b) up to very high loadings [41]. The hybrid materials even keep a significant crystallinity at filler contents as high as 60 wt% .

By employing polarized light optical microscopy (PLOM, Fig. 7), the nucleating effect of Hec can be observed. For neat PEG, the isothermal growth of negative spherulites at 40 °C was easily observed, as PEG develops large spherulites with diameters of around 400 μm (see Fig. 7a). In the case of the sample with 20% Hec, the birefringent colors observed in Fig. 7b and c are due to Hec nanosheets that are viewed edge-on. Fig. 7c shows that birefringent crystals nucleate directly around the areas where the Hec nanosheets are located. They are acting as nuclei for the surrounding PEG matrix crystallization. From these starting points, PEG chains nucleate and PEG crystal aggregates grow (resembling irregular axialites), impinging on one another.

To calculate the efficiency of Hec as a nucleating agent for PEG, we employ the self nucleation (SN) technique (Fig. 8, Table 1). Müller et al.

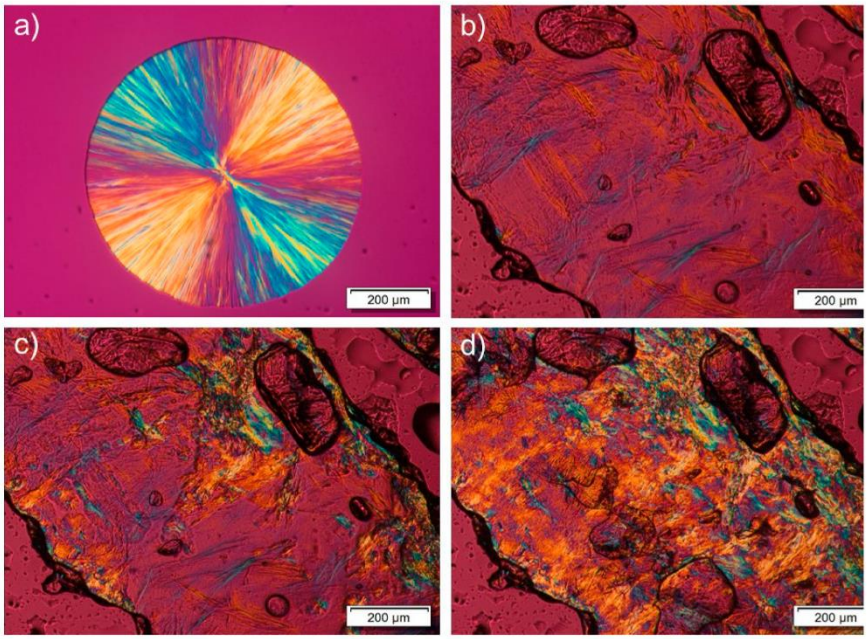

Fig. 7. PLOM micrographs of a) a single PEG spherulite crystallized isothermally at 40 °C and the time-dependant crystallization of PEGHec-20 sample crystallized at 40 °C at b) t = 0 s, c) t = 20 s, d) t = 60 s.

have applied SN protocols to study the confined crystallization in co-polymers and nanocomposites/hybrids, among other polymeric systems [25,26,42]. The protocol used here is detailed in the experimental section.

Fig. 8a presents the cooling scans after SN at the indicated T_s values. Fig. 8b shows the subsequent heating scans from the same T_s values. With the cooling DSC scans of Fig. 8a, the transition between *Domain I* and *II* can be clearly established, while the transition between *Domains II* and *III* can be detected by analyzing the heating DSC scans of Fig. 8b. *Domain I,* or melting domain, (red lines) in Fig. 8 occurs at T_s

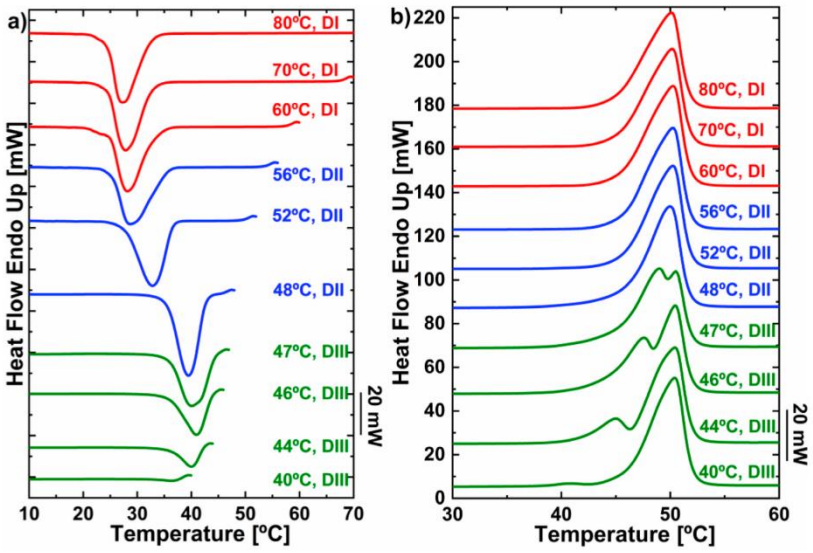

Fig. 8. Cooling (a) and heating (b) scans for neat PEG after SN at different T_s values and presented from top to bottom in decreasing T_s order; *Domain I* (red), *II* (blue), *III* (green) are shown. (For interpretation of the references to color in this figure legend, the reader is referred to the Web version of this article.)

Table 1
Nucleation efficiencies calculated from Equation (1) (see text).

Sample	T_c/°C	NE/%
PEGHec-20	34	67
PEGHec-40	30	44
PEGHec-60	25	17
PEGHec-75	19	0

temperatures where all crystalline memory is erased. This *Domain* is characterized by a constant T_c as is observed in Fig. 6a and invariant T_m value as is observed in Fig. 8b.

Domain I switches to *Domain II* when the T_c increases to higher temperatures (as T_s is lowered). This *Domain* is also called the *exclusive self-nucleation domain*. In *Domain II*, the T_s values are low enough to induce the formation of self-nuclei but high enough to guarantee that annealing does not occur. *Domain II* can be observed in Fig. 8a (DSC scans are plotted with blue lines) and is first detected when T_c values increase in comparison with the standard T_c value observed in *Domain I*. The lowest T_s value within *Domain II* identifies the "ideal self-nucleation temperature" ($T_{s,ideal}$), a temperature that should be carefully measured. The ideal self-nucleation temperature is the T_s temperature that provokes maximum self-nucleation (i.e., maximum increase in the concentration of self-nucleai within *Domain II*) but without producing annealing. According to Fig. 8a, the ideal SN temperature for the PEG employed in this work is 48 °C. If the applied temperature gets too low, melting is incomplete and annealing sets in. This is characteristic for *Domain III* where a second melting peak appears, as can be observed in Fig. 8b (DSC plotted with green lines).

According to Fillon et al. the nucleation efficiency (NE) of a nucleating agent can be easily calculated by using the information obtained by SN measurements [43]. As explained above, self-nuclei are the most efficient nuclei for polymer crystallization. Therefore, the lowest applied temperature in *Domain II* is expected to be the most efficient temperature for SN ($T_{s,ideal}$), since with decreasing temperature, the number of nuclei is increasing. Thereby, the T_c value after SN at 48 °C (i.e., the ideal SN temperature for the PEG employed here, as shown in Fig. 8) or $T_{c,max}$ is taken for the calculation of the different NEs (Equation (1)).

$$NE = \frac{T_{c,NA} - T_{c,P}}{T_{c,\max} - T_{c,P}} \cdot 100 \quad (1)$$

where $T_{c,NA} = T_c$ (PEGHec-X) and $T_{c,P} = T_c$ (neat PEG) = 22 °C, taken from Fig. 5. (For neat PEG, Fig. 8, $T_{c,max} = 40$ °C)

The calculated nucleation efficiencies are reported in Table 1. At 20% Hec, a relatively high nucleation efficiency of 67% is obtained. However, as Hec content increases, the efficiency of Hec as a nucleating agent is offset by its confinement effect and the calculated efficiency decreases dramatically, until it vanishes at very large Hec contents.

Additionally, calorimetry experiments were used to measure the overall isothermal crystallization rate of neat PEG and the PEGHec composites. The overall crystallization rate of a polymer depends on both primary nucleation rate and crystal growth rate. The experimentally measured half-crystallization time ($1/\tau_{1/2}$) is proportional to the overall crystallization rate. The half-crystallization time is defined as the time needed for 50% relative conversion from the melt to the crystalline state.

Fig. 9a shows the overall crystallization rates (expressed as $1/\tau_{1/2}$) for neat PEG and all PEGHec composites as a function of T_c. The curves show the expected trend of a reduction in the overall rate as a function of T_c usually observed at low supercoolings, where the crystallization kinetics is dominated by nucleation effects (i.e., primary and secondary nucleation) and much less affected by diffusion [44].

When 20 wt% Hec is added to PEG, the curve of crystallization rate versus T_c in Fig. 9a is shifted to higher crystallization temperatures, or lower supercoolings. This is a clear acceleration effect of the overall crystallization kinetics provoked by the primary heterogeneous

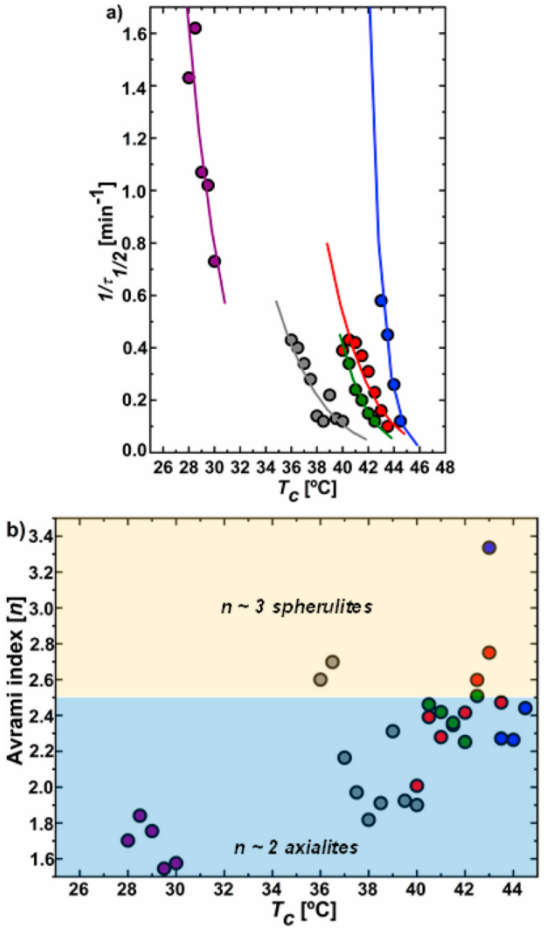

Fig. 9. (a) Inverse of the half-crystallization time ($1/\tau_{1/2}$) as a function of T_c and (b) Avrami index (n) as a function of T_c. (red:20 wt% filler, blue: 40 wt%, green: 60 wt%, purple: 75 wt%, grey: neat PEG). (For interpretation of the references to color in this figure legend, the reader is referred to the Web version of this article.)

nucleation effect of Hec (which in non-isothermal conditions has a 67% nucleation efficiency, see Table 1) on PEG. Increasing the amount of Hec to 40 wt%, increases even further the overall crystallization kinetics. This indicates that primary nucleation is still controlling the overall crystallization kinetics. However, when 60 wt% Hec is added to PEG, confinement effects start to become present. Hec can still nucleate PEG, but Fig. 9a shows that 60 wt% filler content accelerates the overall kinetics less than adding 40 wt% Hec.

Finally, when the amount of Hec increases to 75 wt%, Fig. 9a shows how the overall crystallization rate versus T_c curve is shifted to higher supercoolings with respect to PEG, i.e., relatively slower kinetics are promoted if constant crystallization temperatures are considered (by extrapolation). This result means that confinement effects completely dominate the overall crystallization kinetics and the primary nucleation effect of Hec is less important.

Generally speaking, if we extrapolate all data to a single crystallization temperature in Fig. 9a, the results show that Hec addition increases the overall crystallization rate until a maximum is reached at 40

wt%, then further Hec addition decreases the crystallization rate. The isothermal crystallization kinetics shows remarkable trends that are consistent with an acceleration effect due to primary nucleation enhancement at low hectorite contents, and at higher filler loadings a reduction due to confinement of PEG chains by the filler.

The competition between primary nucleation and confinement in the overall crystallization kinetics results shown in Fig. 9a is very clear. In the last few years similar trends have been reported for similarly confined materials, containing carbon nanotubes and silica nanoparticles, among others [8,18,19,45].

The overall crystallization kinetics data can be modeled by the Avrami equation, even if the fittings to the Avrami equation are usually restricted to low conversions to the crystalline state, i.e., the primary crystallization stage (before crystalline superstructural aggregates impinged on one another during growth) [24,46].

Thereby, the Avrami index (n) (Fig. 9b) provides a useful tool to have a deeper look into the crystallization kinetics with respect to the morphology. As proposed by Müller et al. [45,47,48], the Avrami index can be considered the sum of two parts (Equation (2)):

$$n = n_n + n_{gd} \tag{2}$$

where n_n describes the fraction of the index related to primary nucleation ($n_n = 0$ instantaneous nucleation and $n_n = 1$ sporadic nucleation). The value n_{gd} shows the growth dimensionality (usually 1–3, $n_{gd} = 1$ (one-dimensional crystals), $n_{gd} = 2$ (axialites, 2D) and $n_{gd} = 3$ (spherulites, 3D)).

Fig. 9b shows how the Avrami index varies with crystallization temperature. At low filler contents, the nucleating effect leads to the formation of instantaneously nucleated spherulites or axialites, for which an Avrami index of 3 and 2 respectively should be expected. Within experimental errors and the fact that nucleation is normally not perfectly instantaneous, fractional values of the Avrami index are usually obtained. In samples with a Hec content between 20 and 60 wt%, the Avrami values are around 2.2–2.7. On the other hand, when the Hec content increased to 75 wt%, the Avrami index decreased drastically to values around 1.6–1.8, due to the increasing confinement effect due to Hec. An Avrami index value of 2 would be expected for 2D crystal aggregates instantaneously nucleated, or 1D crystals sporadically nucleated. As it has been observed in literature before in similar nanocomposites/hybrids [18,19], a close correlation exists between Avrami index and confinement. Additionally, as confinement increases the composites need higher degrees of supercooling to crystallize.

As confinement increases, the slow step of the kinetics becomes the nucleation, as growth is usually very fast at high supercoolings and the small spaces where the material crystallizes can be quickly filled by crystal growth once one nucleus is formed. This is the rationale behind the close correlation between decreases in Avrami index and confinement.[38–41]

The Lauritzen and Hoffman (LH) model can be used to fit the isothermal overall crystallization rate data. Further insights into the nucleation versus confinement competition can be gathered from the interpretation of the fitting parameters [49–51]. The LH model applied to DSC data (including both nucleation and growth) is expressed by Equation (3):

$$\frac{1}{\tau_{0.5}}(T) = \frac{1}{\tau_{0.5}}(T=0)\exp\left(\frac{-U^*}{R(T_c - T_\infty)}\right)\exp\left(\frac{-K_g^\tau}{\Delta T f\ T_c}\right) \tag{3}$$

$1/\tau_{0.5}$ represents the overall crystallization rate (nucleation + growth, obtained from DSC).

U^* is a diffusion activation energy (taken as 1500 cal/mol).

R is the gas constant.

T_c is the isothermal crystallization temperature.

T_∞ is a temperature where chain mobility stops (taken as T_g - 30 K).

T_∞ defines the supercooling ($T_m{}^0 - T_c$), and $T_m{}^0$ is the equilibrium melting temperature.

f is defined as: $f = \frac{2T_c}{(T_c + T_m^0)}$

The value K_g^τ is given by the slope of the graph $ln\frac{1}{\tau 0.5} + \frac{U^*}{R(T_c - T\infty)}$ against $(\Delta T f\ T_c)^{-1}$. K_g^τ is proportional to the energy barrier of the overall crystallization. Table 2 shows all relevant parameters that can be obtained by the fitting of the LH model [54].

As shown in Fig. 10 and Table 2, the energy barrier for overall crystallization (proportional to K_g^τ), the fold surface free energy σ_e and the work of chain folding q decrease first with increasing Hec content, passing through a minimum at 40 wt% Hec, as expected in view of the nucleating effect of Hec. A similar effect has also already been observed and examined with the LH theory for PE layered silicate nanocomposites [55]. With further increases of filler loading, the described values increase again and the energy barrier ends up being higher than that for neat PEG at a Hec content of 75 wt%. Ghasemi et al. [55] described an increased surface energy and work of chain folding as hindered re-entry of the polymer chains into the crystal due to the Hec nanosheets. The results presented in Fig. 10 provide additional evidences of the nucleation versus confinement competition that occurs upon Hec addition to PEG.

4. Conclusions

Due to the large diameter (20 μm) of individual silicate layers upon repulsive delamination, liquid crystalline phases are obtained with separations between neighbouring nanosheets of >40 nm. This allows the formation of a homogenous lamellar lyotropic ternary dispersion (water, PEG, Hec). Upon removing the dispersion medium, thermodynamics drives a partial phase segregation. Since mass transport is hindered during the drying process, kinetics of segregation are slowed down and the length scale at which phase segregation can be accomplished varies systematically with filler content.

The DSC results obtained allow us to conclude that a competition was established in the nanocomposites between the nucleation of Hec and its confinement effect on PEG overall crystallization. The nucleating efficiency of Hec at 20% was very high (i.e, NE = 67%) but gradually decreased with increases in loading until it vanished at 75% Hec. The isothermal crystallization kinetics went through a maximum with Hec addition. It increased at low Hec contents (due to nucleation) and then decreased as Hec content increased (due to confinement). The Lauritzen and Hoffman theory successfully modeled the competition between nucleation and confinement, as the energy barrier for the overall crystallization (that includes both nucleation and growth) displayed a clear minimum with Hec content coinciding with the maximum acceleration of the kinetics. Additionally, a clear correlation between filler content and the Avrami index was obtained supporting the increase in confinement as filler loading increased.

Aside of the more fundamental aspects, the PEGHec composites with their tailor-made crystallinity and a very long tortuous path for gas molecules, may have potential as biodegradable barrier systems, particularly of interest as a food packaging material. Work in that direction is in progress.

Table 2
Fitting parameters of the LH theory applied to the overall isothermal crystallization data measured by DSC.

samples	K_g x 10^4 (K^2)	σ_e (erg/cm^2)	q x 10^{-13} (erg)	R^2
neat PEG	4.3	41.3	1.79	0.7826
PEGHec-20	3.1	30.4	1.32	0.8969
PEGHec-40	2.6	25.5	1.11	0.9753
PEGHec-60	3.5	34.2	1.48	0.9875
PEGHec-75	5.2	51.5	2.24	0.8804

Values employed for the L-H fitting: $\rho_c = 1.239$ g/cm^3; $\rho_a = 1.124$ g/cm^3 Å [52]. T_∞ = -97.2 °C; $a_0 = 4.67$ Å $b_o = 4.65$ Å; $U^* = 1500$ Cal/mol; $\Delta h_f = 230$ J/g [53].

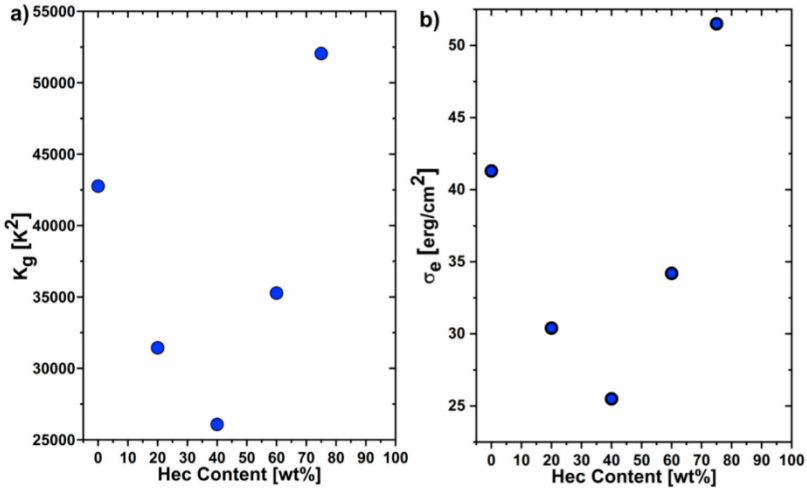

Fig. 10. K_g (a)) and σ (b)) versus Hec Content.

Declaration of competing interest

The authors declare that they have no known competing financial interests or personal relationships that could have appeared to influence the work reported in this paper.

CRediT authorship contribution statement

Christoph Habel: Investigation, Data curation, Formal analysis, Writing - original draft. **Jon Maiz:** Validation, Data curation, Formal analysis, Writing - original draft, Funding acquisition. **Jorge L. Olmedo-Martínez:** Investigation, Data curation. **Juan V. López:** Investigation, Data curation, Formal analysis. **Josef Breu:** Conceptualization, Methodology, Writing - review & editing, Visualization, Supervision, Project administration, Funding acquisition. **Alejandro J. Müller:** Conceptualization, Methodology, Writing - review & editing, Visualization, Supervision, Project administration, Funding acquisition.

Acknowledgements

The authors thank Florian Puchtler for producing the synthetic sodium hectorite, Marco Schwarzmann for the SEM and TEM measurements and sample preparation via cryo ion slicing, Dr. Sabine Rosenfeldt for the SAXS measurements, Maximilian Röhrl for the IR measurements and Renee L. Timmins for proof-reading the manuscript. We appreciate the support of the Keylab for Optical and Electron Microscopy and the Keylab for Small Scale Polymer Processing of the Bavarian Polymer Institute (BPI). This work was supported by the German Science Foundation (DFG) within the collaborative research project SFB 1357. J.M. acknowledges support from the Provincial Council of Gipuzkoa under the program Fellow Gipuzkoa and partial financial support to the IBERDROLA Foundation. J.L.O.M. wish to thank the National Council of Science and Technology (CONACYT) in México for his grant 471837. We acknowledge funding by Mineco MAT2017-83014-C2-1-P project and by the Basque Government through grant IT1309-19. This work has also received funding from the European Union's Horizon 2020 research and innovation program under the Marie Sklodowska-Curie grant agreement No 778092.

Appendix A. Supplementary data

Supplementary data to this article can be found online at https://doi.org/10.1016/j.polymer.2020.122734.

References

[1] M.-C. Popescu, B.-I. Dogaru, D. Sun, E. Stoleru, B. Simionescu, Structural and sorption properties of bio-nanocomposite films based on κ-carrageenan and cellulose nanocrystals, Int. J. Biol. Macromol. 135 (2019) 462–471.
[2] H.S. Nalwa, Handbook of Nanostructured Materials and Nanotechnology, Five-Volume Set, Academic Press, 1999.
[3] P.M. Ajayan, O.Z. Zhou, Applications of Carbon Nanotubes, Carbon Nanotubes, Springer, Berlin, Heidelberg, 2001, pp. 391–425.
[4] A. Arya, A.L. Sharma, Investigation on enhancement of electrical, dielectric and ion transport properties of nanoclay-based blend polymer nanocomposites, Polym. Bull. 77 (6) (2020) 2965–2999.
[5] A.R. Hilmi, N.A. Fauziyah, S. Pratapa, A temperature-dependent storage modulus model for filler-dispersed PEG/silica composites, Compos. B Eng. 173 (2019) 106868.
[6] N.A. Fauziyah, A.R. Hilmi, T.A. Fadly, M.Z. Asrori, M. Mashuri, S. Pratapa, Dynamic tensile and shear storage moduli of PEG/silica-polymorph composites, J. Appl. Polym. Sci. 136 (17) (2019) 47372.
[7] L. Bounabi, N.B. Mokhnachi, A. Djadoun, N. Haddadine, R. Barille, Morphology and thermal properties of clay based biocomposites 38 (8) (2018) 785.
[8] R.M. Michell, A.J. Mueller, Confined crystallization of polymeric materials, Prog. Polym. Sci. 54 (2016) 183–213.
[9] H. Frensch, P. Harnischfeger, B.-J. Jungnickel, Fractionated Crystallization in Incompatible Polymer Blends, Multiphase Polymers: Blends and Ionomers, ACS Publications, 1989, pp. 101–125.
[10] J. Arias-Trujillo, A. Matías-Sanchez, B. Cantero, S. López-Querol, Effect of polymer emulsion on the bearing capacity of aeolian sand under extreme confinement conditions, Construct. Build. Mater. 236 (2020) 117473.
[11] G. Cavallaro, R. De Lisi, G. Lazzara, S. Milioto, Polyethylene glycol/clay nanotubes composites, J. Therm. Anal. Calorim. 112 (1) (2013) 383–389.
[12] D. Hutanu, M.D. Frishberg, L. Guo, C.C. Darie, Recent applications of polyethylene glycols (PEGs) and PEG derivatives, Mod. Chem. Appl. 2 (2) (2014) 1–6.
[13] S. Ghyati, M. Benhamou, M. El-Jai, I. Akhrif, Polymer nanocomposites from natural clay: understanding clay-PEG interaction and their effect on spacing between clay-plates, OAJ Mater. Dev. 3 (2018) 1103.
[14] Y. Liu, H. Meng, S. Konst, R. Sarmiento, R. Rajachar, B. Lee, Injectable dopamine-modified poly(ethylene glycol) nanocomposite hydrogel with enhanced adhesive property and bioactivity, ACS Appl. Mater. Interfaces 6 (2014) 16982–16992.
[15] H. Papananou, E. Perivolari, K. Chrissopoulou, S.H. Anastasiadis, Tuning polymer crystallinity via the appropriate selection of inorganic nanoadditives, Polymer 157 (2018) 111–121.
[16] L. Zhu, B.R. Mimnaugh, Q. Ge, R.P. Quirk, S.Z. Cheng, E.L. Thomas, B. Lotz, B. S. Hsiao, F. Yeh, L. Liu, Hard and soft confinement effects on polymer crystallization in microphase separated cylinder-forming PEO-b-PS/PS blends, Polymer 42 (21) (2001) 9121–9131.

[17] Z. Huang, S. Wang, S. Kota, Q. Pan, M.W. Barsoum, C.Y. Li, Structure and crystallization behavior of poly(ethylene oxide)/Ti3C2Tx MXene nanocomposites, Polymer 102 (2016) 119–126.
[18] A.J. Müller, M.L. Arnal, M. Trujillo, A.T. Lorenzo, Super-nucleation in nanocomposites and confinement effects on the crystallizable components within block copolymers, miktoarm star copolymers and nanocomposites, Eur. Polym. J. 47 (4) (2011) 614–629.
[19] X. Wen, Y. Su, Y. Shui, W. Zhao, A.J. Müller, D. Wang, Correlation between grafting density and confined crystallization behavior of poly (ethylene glycol) grafted to silica, Macromolecules 52 (4) (2019) 1505–1516.
[20] F. Kawai, Microbial degradation of polyethers, Appl. Microbiol. Biotechnol. 58 (1) (2002) 30–38.
[21] H. Kalo, M.W. Möller, M. Ziadeh, D. Dolejš, J. Breu, Large scale melt synthesis in an open crucible of Na-fluorohectorite with superb charge homogeneity and particle size, Appl. Clay Sci. 48 (1-2) (2010) 39–45.
[22] H. Kalo, M.W. Möller, D.A. Kunz, J. Breu, How to maximize the aspect ratio of clay nanoplatelets, Nanoscale 4 (18) (2012) 5633–5639.
[23] Z. Wang, K. Rolle, T. Schilling, P. Hummel, A. Philipp, B.A. Kopera, A.M. Lechner, M. Retsch, J. Breu, G. Fytas, Tunable thermoelastic anisotropy in hybrid Bragg stacks with extreme polymer confinement, Angew. Chem. 132 (3) (2020) 1302–1310.
[24] A.T. Lorenzo, M.L. Arnal, J. Albuerne, A.J. Müller, DSC isothermal polymer crystallization kinetics measurements and the use of the Avrami equation to fit the data: guidelines to avoid common problems, Polym. Test. 26 (2) (2007) 222–231.
[25] B. Fillon, J. Wittmann, B. Lotz, A. Thierry, Self-nucleation and recrystallization of isotactic polypropylene (α phase) investigated by differential scanning calorimetry, J. Polym. Sci., Polym. Phys. Ed. 31 (10) (1993) 1383–1393.
[26] A.J. Müller, M.L. Arnal, Thermal fractionation of polymers, Prog. Polym. Sci. 30 (5) (2005) 559–603.
[27] E.S. Tsurko, P. Feicht, C. Habel, T. Schilling, M. Daab, S. Rosenfeldt, J. Breu, Can high oxygen and water vapor barrier nanocomposite coatings be obtained with a waterborne formulation? J. Membr. Sci. 540 (2017) 212–218.
[28] E.S. Tsurko, P. Feicht, F. Nehm, K. Ament, S. Rosenfeldt, I. Pietsch, K. Roschmann, H. Kalo, J. Breu, Large scale self-assembly of smectic nanocomposite films by doctor blading versus spray coating: impact of crystal quality on barrier properties, Macromolecules 50 (11) (2017) 4344–4350.
[29] E. Doblhofer, J. Schmid, M. Rieß, M. Daab, M. Suntinger, C. Habel, H. Bargel, C. Hugenschmidt, S. Rosenfeldt, J. Breu, Structural insights into water-based spider silk protein–nanoclay composites with excellent gas and water vapor barrier properties, ACS Appl. Mater. Interfaces 8 (38) (2016) 25535–25543.
[30] M. Stöter, D.A. Kunz, M. Schmidt, D. Hirsemann, H. Kalo, B. Putz, J. Senker, J. Breu, Nanoplatelets of sodium hectorite showing aspect ratios of≈ 20 000 and superior purity, Langmuir 29 (4) (2013) 1280–1285.
[31] D.A. Kunz, J. Schmid, P. Feicht, J. Erath, A. Fery, J. Breu, Clay-based nanocomposite coating for flexible optoelectronics applying commercial polymers, ACS Nano 7 (5) (2013) 4275–4280.
[32] S. Rosenfeldt, M. Stöter, M. Schlenk, T. Martin, R.Q. Albuquerque, S. Förster, J. Breu, in-depth insights into the key steps of delamination of charged 2D nanomaterials, Langmuir 32 (41) (2016) 10582–10588.
[33] D.M. Moore, R.C. Reynolds, X-ray Diffraction and the Identification and Analysis of Clay Minerals, Oxford university press, Oxford, 1989.
[34] S.W. Bailey, Nomenclature for regular interstratifications, Am. Mineral. 67 (1982) 394–398.
[35] T. Verho, M. Karesoja, P. Das, L. Martikainen, R. Lund, A. Alegría, A. Walther, O. Ikkala, Hydration and dynamic state of nanoconfined polymer layers govern toughness in nacre-mimetic nanocomposites, Adv. Mater. 25 (36) (2013) 5055–5059.
[36] P. Aranda, E. Ruiz-Hitzky, Poly (ethylene oxide)-silicate intercalation materials, J. Mater. Chem. 4 (6) (1992) 1395–1403.
[37] J. Wu, M.M. Lerner, Structural, thermal, and electrical characterization of layered nanocomposites derived from sodium-montmorillonite and polyethers, J. Mater. Chem. 5 (6) (1993) 835–838.
[38] D.J. Chaiko, New poly (ethylene oxide)– clay composites, Chem. Mater. 15 (5) (2003) 1105–1110.
[39] A. Eckert, M. Abbasi, T. Mang, K. Saalwächter, A. Walther, Structure, mechanical properties, and dynamics of polyethylenoxide/nanoclay nacre-mimetic nanocomposites, Macromolecules 53 (2020) 1716–1725.
[40] G. Choudalakis, A. Gotsis, Permeability of polymer/clay nanocomposites: a review, Eur. Polym. J. 45 (4) (2009) 967–984.
[41] K. Chrissopoulou, K. Andrikopoulos, S. Fotiadou, S. Bollas, C. Karageorgaki, D. Christofilos, G. Voyiatzis, S. Anastasiadis, Crystallinity and chain conformation in PEO/layered silicate nanocomposites, Macromolecules 44 (24) (2011) 9710–9722.
[42] R.M. Michell, A. Mugica, M. Zubitur, A.J. Müller, Self-nucleation of crystalline phases within homopolymers, polymer blends, copolymers, and nanocomposites, in: Polymer Crystallization I, Springer, 2015, pp. 215–256.
[43] B. Fillon, B. Lotz, A. Thierry, J. Wittmann, Self-nucleation and enhanced nucleation of polymers. Definition of a convenient calorimetric "efficiency scale" and evaluation of nucleating additives in isotactic polypropylene (α phase), J. Polym. Sci., Polym. Phys. Ed. 31 (10) (1993) 1395–1405.
[44] L. Mandelkern, Crystallization of Polymers: Volume 2, Kinetics and Mechanisms, Cambridge University Press, 2004.
[45] R.M. Michell, I. Blaszczyk-Lezak, C. Mijangos, A.J. Mueller, Confinement effects on polymer crystallization: from droplets to alumina nanopores, Polymer 54 (16) (2013) 4059–4077.
[46] A.J. Müller, R.M. Michell, A.T. Lorenzo, Isothermal crystallization kinetics of polymers, polymer morphology: principles, characterization, processing, 2016, pp. 181–203.
[47] A.J. Müller, V. Balsamo, M.L. Arnal, Nucleation and Crystallization in Diblock and Triblock Copolymers, Block Copolymers II, Springer, 2005, pp. 1–63.
[48] R.M. Michell, A.J. Müller, Confined crystallization of polymeric materials, Prog. Polym. Sci 54 (2016) 183–213.
[49] A. Lorenzo, A.J. Müller, M.-C. Lin, H.-L. Chen, U.-S. Jeng, D. Priftis, M. Pitsikalis, N. J.M. Hadjichristidis, Influence of macromolecular architecture on the crystallization of (PCL2)-b-(PS2) 4-miktoarm star block copolymers in comparison to linear PCL-b-PS diblock copolymer analogues, Macromolecules 42 (21) (2009) 8353–8364.
[50] M. Trujillo, M.L. Arnal, A.J. Müller, M.A. Mujica, C.U. de Navarro, B. Ruelle, P.J. P. Dubois, Supernucleation and crystallization regime change provoked by MWNT addition to poly (ε-caprolactone) 53 (3) (2012) 832–841.
[51] Q. Guo, Polymer Morphology: Principles, Characterization, and Processing, John Wiley & Sons, 2016.
[52] J. Brandrup, E. Immergut, E. Grulke, Polymer Handbook, John Wiley & Sons Inc, New York, 1999.
[53] J.E. Mark, Polymer Data Handbook, Oxford University Press, 1999.
[54] R. Castillo, A. Müller, Crystallization and morphology of biodegradable or biostable single and double crystalline block copolymers, Prog. Polym. Sci. 34 (6) (2009) 516–560.
[55] H. Ghasemi, P.J. Carreau, M.R. Kamal, Isothermal and non-isothermal crystallization behavior of PET nanocomposites, Polym. Eng. Sci. 52 (2) (2012) 372–384.

SUPPORTING INFORMATION

Competition between nucleation and confinement in the crystallization of poly(ethylene glycol)/ large aspect ratio hectorite nanocomposites

Christoph Habel[a,1], Jon Maiz[b,1], Jorge L. Olmedo-Martínez[b], Juan V. López[c], Josef Breu[a,**], Alejandro J. Müller[b,d,*]

[a] Bavarian Polymer Institute and Department of Chemistry, University of Bayreuth, Universitätsstraße 30, Bayreuth, 95447, Germany

[b] POLYMAT and Polymer Science and Technology Department, Faculty of Chemistry, University of the Basque Country UPV/EHU, Paseo Manuel de Lardizábal 3, 20018 Donostia-San Sebastián, Spain

[c] USB Polymer Group, Department of Materials Science, University Simón Bolívar, Apartado 89000, Caracas 1080-A, Venezuela

[d] IKERBASQUE, Basque Foundation for Science, Bilbao, Spain

[1] These authors contributed equally to this work.

[*,**] Corresponding Authors

E-Mail address: alejandrojesus.muller@ehu.es (*)

josef.breu@uni-bayreuth.de (**)

Figure

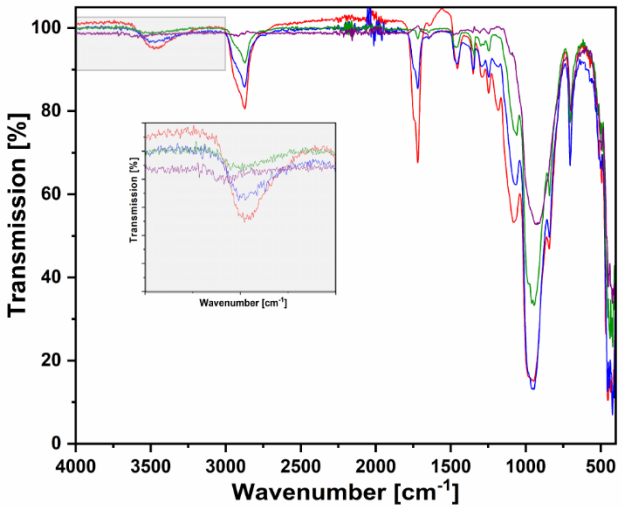

Figure S1. IR Spectra of the PEGHec composites (red: 20wt% filler, blue: 40wt%, green: 60wt%, purple: 75 wt%) showing the residual water content.

Table

Table S1. Melting enthalpy values (ΔH (J/g)) obtained for each corresponding isothermal crystallization temperature (T_c (ºC) of the different samples.

Sample	T_c (ºC)	ΔH (J/g)	Sample	T_c (ºC)	ΔH (J/g)
PEG	36	119	PEGHec-40	43	25
	36.5	120		43.5	26
	37	121		44	22
	37.5	124		44.5	17
	38	124	PEGHec-60	40.5	15
	38.5	127		41	14
	39	128		41.5	14
	39.5	126		42	14
	40	125		42.5	13
PEGHec-20	40	66	PEGHec-75	28	1
	40.5	79		28.5	1
	41	82		29	1
	41.5	82		29.5	1
	42	80		30	1
	42.5	75			
	43	67			
	43.5	55			

7 Publikationsliste

7.1 Publikationen

[1] Jian Zhu, **Christoph Habel**, Theresa Schilling, Andreas Greiner, Josef Breu, Seema Agarwal; Filter-Through Method of Making Highly Efficient Polymer-Clay Nanocomposite Membranes
Erschienen in: *Macromol. Mater. Eng.* **2019**, *304* (7), 1800779.

[2] **Christoph Habel**, Marius Schöttle, Matthias Daab, Natalie J. Eichstaedt, Daniel Wagner, Hadi Bakhshi, Seema Agarwal, Marcus A. Horn, Josef Breu; High-barrier, Biodegradable Food Packaging
Erschienen in: *Macromol. Mater. Eng.* **2018**, *303* (10), 1800333.

[3] **Christoph Habel**, Evgeny S. Tsurko, Julia Hutschenreuther, Raphael Kunz, Dominik Schuchardt, Sabine Rosenfeldt, Volker Altstädt, Josef Breu; Lightweight Ultra-High Barrier Liners for Helium and Hydrogen
Erschienen in: *ACS Nano* **2020***, 14* (6)*,* 7018-7024.

[4] Theresa Schilling, **Christoph Habel**, Sabine Rosenfeldt, Maximilian Röhrl, Josef Breu; Impact of Ultraconfinement on Composite Barriers
Erschienen in: *ACS Appl. Polym. Mater.* **2020**, *2* (7), 3010-3015.

[5] **Christoph Habel**, Jon Maiz, *Jorge L. Olmedo-Martínez,* Juan V. López, Josef Breu, Alejandro J. Müller; Competition between nucleation and confinement in the crystallization of poly(ethylene glycol)/ large aspect ratio hectorite composites
Erschienen in: *Polymer* **2020**, *202*, 122734.

Die Dissertation beruht auf den Veröffentlichungen [1] - [5].

Weitere Publikationen:

[6] Elena Doblhofer, Jasmin Schmid, Martin Rieß, Matthias Daab, Magdalena Suntinger, **Christoph Habel**, Hendrik Bargel, Christoph Hugenschmidt, Sabine Rosenfeldt, Josef Breu, Thomas Scheibel; Structural Insights into Water-Based Spider Silk Protein–Nanoclay Composites with Excellent Gas and Water Vapor Barrier Properties, *ACS Appl. Mater. Interfaces* **2016**, *8* (38), 25535-25543.7

[7] Evgeny S. Tsurko, Patrick Feicht, **Christoph Habel**, Theresa Schilling, Matthias Daab, Sabine Rosenfeldt, Josef Breu; Can high oxygen and water vapor barrier nanocomposite coatings be obtained with a waterborne formulation? *J. Membr. Sci.* **2017**, *540*, 212-218.

[8] Matthias Daab, Natalie J. Eichstaedt, **Christoph Habel**, Sabine Rosenfeldt, Hussein Kalo, Hubert Schießling, Stephan Förster, Josef Breu; The Onset of Osmotic Swelling in Highly Charged Clay Minerals, *Langmuir* **2018**, *34* (28), 8215-8222.

[9] Venkateshaiah, Abhilash, Cheong, Jun Young, **Habel, Christoph**, Wacławek, Stanisław, Lederer, Tomáš Cernik, Miroslav, Kim, Il-Doo, V. T. Padil, Vinod, Agarwal, Seema; Tree Gum-Graphene Oxide Nanocomposite Films as Gas Barriers, *ACS Appl. Nano Mater.* **2020**, *3* (1), 633-640.

[10] Jian Zhu, Anil Kumar, Pin Hu, **Christoph Habel**, Josef Breu, Seema Agarwal; Layering-triggered delayering with exfoliated high-aspect ratio layered silicate for enhanced gas barrier, mechanical properties, and degradability of biodegradable polymers, *Global Challenges* **2020**, *4*, 2000030.

7.2 Konferenzbeiträge

[1] Ordered Functional Heterostructures via Simple Intercalation Reactions, **Christoph Habel**, Matthias Stöter, Bernhard Biersack, Rainer Schobert, Josef Breu, Euroclay **2015**, Edinburgh, Posterpräsentation.

[2] Silicate polymer nanocomposites acting as Helium barrier, **Christoph Habel**, Evgeny Tsurko, Josef Breu, GdCh-Festkörpertagung **2016**, Innsbruck, Posterpräsentation.

[3] Spray Coating of Layered Silicate Nanocomposites Acting as Ultrahigh Gas Barrier Systems, **Christoph Habel**, Josef Breu, International Clay Conference **2017**, Granada, Vortragsgestaltung.

[4] Spray Coating of Layered Silicate Nanocomposites Acting as Ultrahigh Gas Barrier Systems, **Christoph Habel**, Josef Breu, Travelling Seminar **2017**, Russland, Vortrag.

[5] Spray Coating of Clay-Based (Ultra) High Gas Barrier Systems, **Christoph Habel**, Evgeny Tsurko, Theresa Schilling, Sabine Rosenfeldt and Josef Breu, ISRS **2018**, Bayreuth, Posterpräsentation.

[6] Bionanocomposites as “green” alternatives for commercial food packaging materials, **Christoph Habel**, Marius Schöttle, Matthias Daab, Natalie J. Eichstaedt, Daniel R. Wagner, Jasmin Schmid, Evgeny Tsurko, Elena Doblhofer, Hadi Bakhshi, Seema Agarwal, Marcus A. Horn, Josef Breu, Euroclay **2019**, Paris, Vortrag.

[7] Bionanocomposites – green alternatives for commercial food packaging materials?, **Christoph Habel**, Theresa Schilling, Marius Schöttle, Matthias Daab, Natalie J. Eichstaedt, Daniel R. Wagner, Jasmin Schmid, Evgeny Tsurko, Elena Doblhofer, Hadi Bakhshi, Seema Agarwal, Marcus A. Horn, Josef Breu, Bayreuth Polymer Symposium **2019**, Bayreuth, Posterpräsentation mit Kurzvortrag.

8 Danksagung

Mein besonderer Dank gilt meinem Doktorvater Prof. Dr. Josef Breu. Nicht nur für die Tatsache, dass er mir eine höchst anwendungsbezogene Thematik als Forschungsschwerpunkt ermöglicht hat, sondern auch für die vielen Gelegenheiten Forschungsanträge mitzugestalten und Vorträge zu halten, wodurch ich vieles abseits der „klassischen Forschung“ lernen konnte. Das wird mir in Zukunft sicher zu Gute kommen. So knackig manche Diskussionen auch gewesen sind, es hat mich gelehrt meine Meinungen zu vertreten und dahinter zu stehen. Vielen Dank für diese Erfahrungen, Josef, vielen Dank für das „Zügel-Locker-Lassen“, getreu dem Motto: „Fördern und Fordern“!

Ein weiterer großer Dank gilt meiner Laborfamilie, meinen Freunden im „roten Labor + x“! Danke Sonja, Pätrick, Matthias, Raphael, Michl, Sebastian und auch unseren „Neuerrungenschaften“ Renee, Radha und Maxi für viele sehr kurzweilige Arbeitstage. Aus Kollegen sind doch tatsächlich Freunde geworden. Großer Dank auch an alle weiteren Kollegen für die offene Art, die konstruktiven Diskussionen und die lehrreichen und lustigen Konferenzfahrten. Herzlichen Dank natürlich auch an unsere Technischen Assistenten am Lehrstuhl, die die Arbeit unbestritten angenehmer machen. Allen Voran Marco- unser Lehrstuhlmusikant: Danke für die unzähligen TEM und IonSlicer-Stunden mit deiner sympathischen, positiven Art. Weiterhin ein großes Dankeschön an Lena und Florian für euer Engagement und eure Hilfsbereitschaft. Danke auch an Wolfgang für deinen unermüdlichen Einsatz für uns Doktoranden und für die angenehmen Saalpraktika an deiner Seite. Dank gilt auch dem Sekretariat um Sieglinde, Petra und Iris, für das Ermöglichen eines reibungslosen Tagesablaufs.

An die SFB-Mitstreiter der „Nachbarlehrstühle“, Julia, Christoph und Elmar: Danke für das produktive Zusammenarbeiten- zu jeglicher Tageszeit. Weiterhin danke ich allen Kooperationspartnern (vor allem Prof. Dr. S. Agarwal, Dr. S. Rosenfeldt, Prof. Dr. V. Altstädt, Prof. Dr. A. J. Müller, Prof. Dr. M. A. Horn, Dr. J. Maiz, Dr. J. Zhu) für die stets angenehme, zuverlässige und produktive Zusammenarbeit. Nur so geht kooperative, progressive Forschung und macht auch Spaß! Danke vor allem auch an meine tollen Kollegen in Donostia-San Sebastian, die mich dort wunderbar aufgenommen haben. Gracias por todos mis amigos! Im Zuge dessen

auch ein großes Dankeschön an das Elitenetzwerk Bayern, das mir, im Zuge des Elitestudienprogramms „Macromolecular Science“, diese und viele weitere Erfahrungen ermöglicht hat.

Zu guter Letzt die **wichtigsten Personen** in meinem Leben; meinem kleinen, aber sehr feinen Freundeskreis, meiner Partnerin und natürlich meiner stets hinter mir stehenden Familie:

Meinen **Freunden**- natürlich allen voran meinen ehemaligen Mitbewohnern und besten Freunden Jonas, Uli und Pääs. Ihr habt nicht nur die Studienzeit unvergesslich gemacht, sondern habt stets ein offenes Ohr und wertvolle Ratschläge. Auf euch ist einfach immer, zu jeder Zeit, Verlass! Vielen Dank natürlich auch an alle weiteren engen Freunde- es ist schön einen so stets ein bisschen „Kind-gebliebenen“ Freundeskreis an meiner Seite zu wissen. Solche Freunde wie euch zu haben ist Gold wert und macht mich stolz!

An meine Partnerin **Nathalie:** Danke für deinen Rückhalt! Du gibst mir Kraft und bringst unheimlich viel Schwung in mein Leben. Durch deine spontane und ab und an verträumte Art ergänzt du mich sehr, sehr gut. Hartnäckigkeit zahlt sich nicht nur in der Forschung aus. Schön, dass es dich gibt!

Zu guter Letzt, meine über alles geliebte Familie:

Meinen Geschwistern, **Johanna** und **Matthias:** Hanna, du bist einen langen und sehr harten Weg gegangen um dort anzukommen wo du nun bist - darauf kannst du unbändig stolz sein! Da bist du für mich ein Vorbild! Und Matze- das Gleiche gilt für dich. Du hast den Berufszweig gefunden in dem du deine Stärken vollauf zeigen kannst und hast dich dort nach oben gearbeitet- da kann ich mir einiges von dir abschauen. Und dann noch 3 Frauen daheim, davon zwei so wundervolle Töchter – liebe **Jasmin**, liebe **Isabella,** euch wünsche ich nur das Beste!

Danke **Mama**, danke **Papa** für eure unbändige Unterstützung. Es ist schön zu wissen, dass ihr immer hinter mir steht und mich auf meinem Weg unterstützt - ob in beruflicher Sicht oder im Privatleben. Eure liebenswerte und unvergleichliche Art gibt uns Kindern (egal wie alt wir sind) immer das Gefühl, dass ihr für uns da seid', wenn Not am Mann/Frau ist. Egal in welchem Alter, die Fahrt nach Cham ist immer der Weg *nach Hause* - und das wird immer so sein! Genießt euer Renten/Pensions-Dasein - ihr habt es euch redlich verdient! Diese Arbeit widme ich euch!

9 Erklärung des Verfassers

(Eidesstattliche) Versicherungen und Erklärungen

(§ 8 Satz 2 Nr. 3 PromO Fakultät)

Hiermit versichere ich eidesstattlich, dass ich die Arbeit selbstständig verfasst und keine anderen als die von mir angegebenen Quellen und Hilfsmittel benutzt habe (vgl. Art. 64 Abs. 1 Satz 6 BayHSchG).

(§ 8 Satz 2 Nr. 3 PromO Fakultät)

Hiermit erkläre ich, dass ich die Dissertation nicht bereits zur Erlangung eines akademischen Grades eingereicht habe und dass ich nicht bereits diese oder eine gleichartige Doktorprüfung endgültig nicht bestanden habe.

(§ 8 Satz 2 Nr. 4 PromO Fakultät)

Hiermit erkläre ich, dass ich Hilfe von gewerblichen Promotionsberatern bzw. –vermittlern oder ähnlichen Dienstleistern weder bisher in Anspruch genommen habe noch künftig in Anspruch nehmen werde.

(§ 8 Satz 2 Nr. 7 PromO Fakultät)

Hiermit erkläre ich mein Einverständnis, dass die elektronische Fassung der Dissertation unter Wahrung meiner Urheberrechte und des Datenschutzes einer gesonderten Überprüfung unterzogen werden kann.

(§ 8 Satz 2 Nr. 8 PromO Fakultät)

Hiermit erkläre ich mein Einverständnis, dass bei Verdacht wissenschaftlichen Fehlverhaltens Ermittlungen durch universitätsinterne Organe der wissenschaftlichen Selbstkontrolle stattfinden können.

Bayreuth, März 2021 ……

Ort, Datum Christoph Habel